frontiers
RESEARCH TOPICS

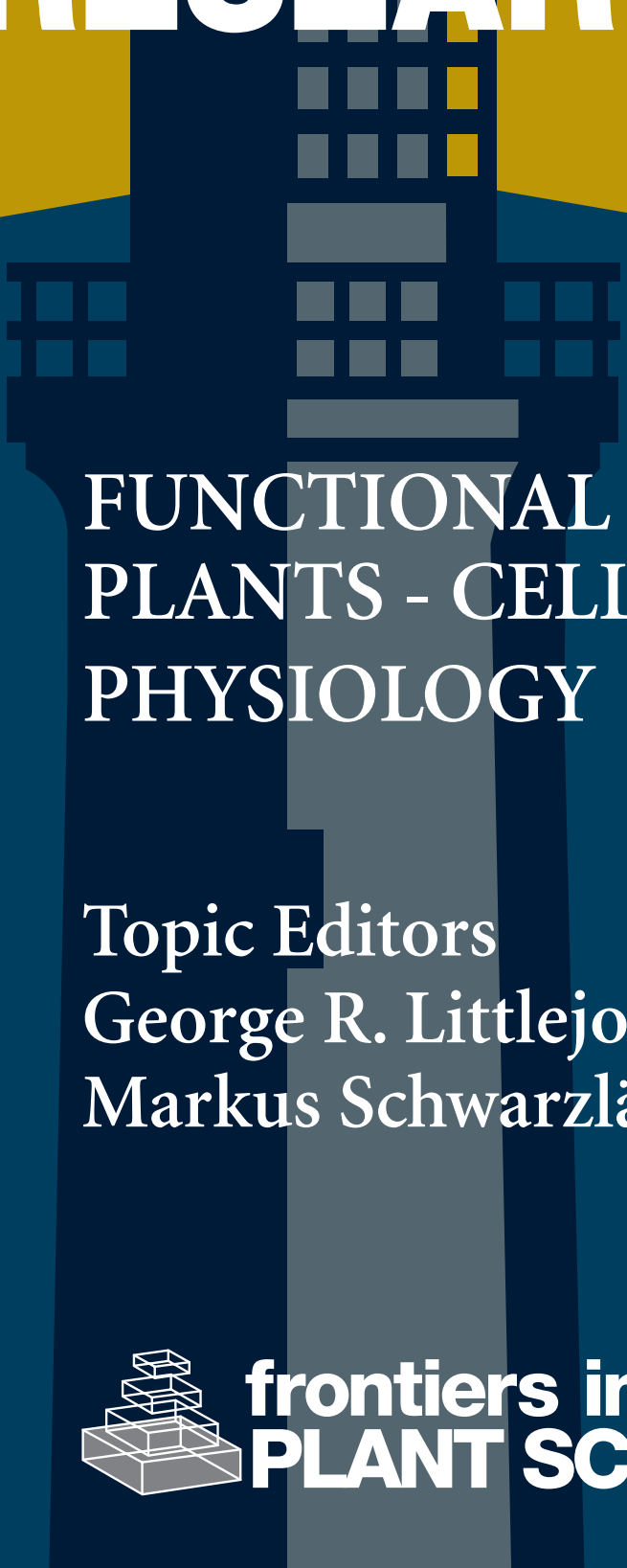

FUNCTIONAL IMAGING IN LIVING PLANTS - CELL BIOLOGY MEETS PHYSIOLOGY

Topic Editors
George R. Littlejohn, Tobias Meckel,
Markus Schwarzländer and Alex Costa

frontiers in
PLANT SCIENCE

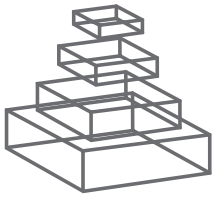

frontiers

FRONTIERS COPYRIGHT STATEMENT

© Copyright 2007-2015
Frontiers Media SA.
All rights reserved.

All content included on this site, such as text, graphics, logos, button icons, images, video/audio clips, downloads, data compilations and software, is the property of or is licensed to Frontiers Media SA ("Frontiers") or its licensees and/or subcontractors. The copyright in the text of individual articles is the property of their respective authors, subject to a license granted to Frontiers.

The compilation of articles constituting this e-book, wherever published, as well as the compilation of all other content on this site, is the exclusive property of Frontiers. For the conditions for downloading and copying of e-books from Frontiers' website, please see the Terms for Website Use. If purchasing Frontiers e-books from other websites or sources, the conditions of the website concerned apply.

Images and graphics not forming part of user-contributed materials may not be downloaded or copied without permission.

Individual articles may be downloaded and reproduced in accordance with the principles of the CC-BY licence subject to any copyright or other notices. They may not be re-sold as an e-book.

As author or other contributor you grant a CC-BY licence to others to reproduce your articles, including any graphics and third-party materials supplied by you, in accordance with the Conditions for Website Use and subject to any copyright notices which you include in connection with your articles and materials.

All copyright, and all rights therein, are protected by national and international copyright laws.

The above represents a summary only. For the full conditions see the Conditions for Authors and the Conditions for Website Use.

Cover image provided by Ibbl sarl, Lausanne CH

ISSN 1664-8714
ISBN 978-2-88919-465-0
DOI 10.3389/978-2-88919-465-0

ABOUT FRONTIERS

Frontiers is more than just an open-access publisher of scholarly articles: it is a pioneering approach to the world of academia, radically improving the way scholarly research is managed. The grand vision of Frontiers is a world where all people have an equal opportunity to seek, share and generate knowledge. Frontiers provides immediate and permanent online open access to all its publications, but this alone is not enough to realize our grand goals.

FRONTIERS JOURNAL SERIES

The Frontiers Journal Series is a multi-tier and interdisciplinary set of open-access, online journals, promising a paradigm shift from the current review, selection and dissemination processes in academic publishing.
All Frontiers journals are driven by researchers for researchers; therefore, they constitute a service to the scholarly community. At the same time, the Frontiers Journal Series operates on a revolutionary invention, the tiered publishing system, initially addressing specific communities of scholars, and gradually climbing up to broader public understanding, thus serving the interests of the lay society, too.

DEDICATION TO QUALITY

Each Frontiers article is a landmark of the highest quality, thanks to genuinely collaborative interactions between authors and review editors, who include some of the world's best academicians. Research must be certified by peers before entering a stream of knowledge that may eventually reach the public - and shape society; therefore, Frontiers only applies the most rigorous and unbiased reviews.
Frontiers revolutionizes research publishing by freely delivering the most outstanding research, evaluated with no bias from both the academic and social point of view.
By applying the most advanced information technologies, Frontiers is catapulting scholarly publishing into a new generation.

WHAT ARE FRONTIERS RESEARCH TOPICS?

Frontiers Research Topics are very popular trademarks of the Frontiers Journals Series: they are collections of at least ten articles, all centered on a particular subject. With their unique mix of varied contributions from Original Research to Review Articles, Frontiers Research Topics unify the most influential researchers, the latest key findings and historical advances in a hot research area!
Find out more on how to host your own Frontiers Research Topic or contribute to one as an author by contacting the Frontiers Editorial Office: researchtopics@frontiersin.org

FUNCTIONAL IMAGING IN LIVING PLANTS - CELL BIOLOGY MEETS PHYSIOLOGY

Topic Editors:
George R. Littlejohn, University of Exeter, United Kingdom
Tobias Meckel, Technische Universität Darmstadt, Germany
Markus Schwarzländer, University of Bonn, Germany
Alex Costa, University of Milan, Italy

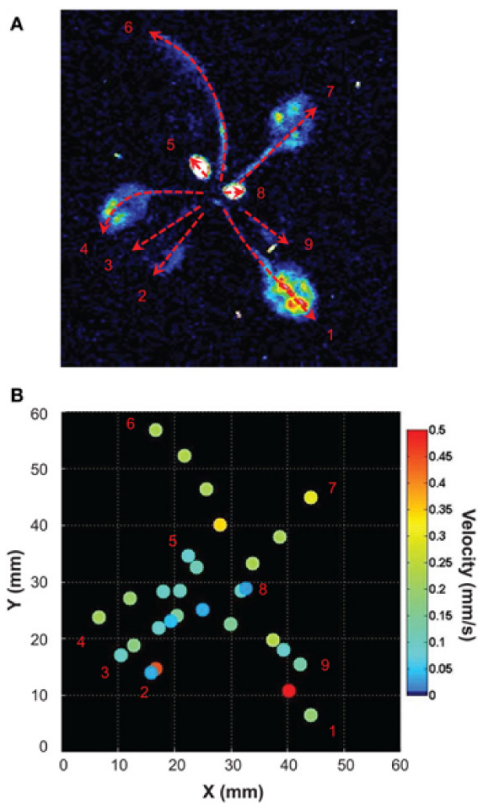

Analysis of the propagation of Ca^{2+} elevations induced by high salt stimulus applied to roots. (A) Free Ca^{2+} elevations on each leaf were analyzed with ImageJ. Velocities (mm/s) of Ca^{2+} responses were determined for each leaf along paths figured by red dashed arrows (values of Ca^{2+} response velocity are presented on Table 1). (B) Propagation speeds along the main leaf vain are indicated for selected points (same space scale as in A). False color scale is in mm/s.

The study of plant cell physiology is currently experiencing a profound transformation. Novel techniques allow dynamic in vivo imaging with subcellular resolution, covering a rapidly growing range of plant cell physiology. Several basic biological questions that have been inaccessible by the traditional combination of biochemical, physiological and cell biological approaches now see major progress. Instead of grinding up tissues, destroying their organisation, or describing cell- and tissue structure, without a measure for its function, novel imaging approaches can provide the critical link between localisation, function and dynamics. Thanks to a fast growing collection of available fluorescent protein variants and sensors, along with innovative new microscopy technologies and quantitative analysis tools, a wide range of plant biology can now be studied in vivo, including cell morphology & migration, protein localization, topology & movement, protein-protein interaction, organelle dynamics, as well as ion, ROS & redox dynamics. Within the cell, genetic targeting of fluorescent protein probes to different organelles and subcellular locations has started to reveal the stringently compartmentalized nature of cell physiology and its sophisticated spatiotemporal regulation in response to environmental stimuli. Most importantly, such cellular processes can be monitored in their natural 3D context, even in complex tissues and organs – a condition not easily met in studies on mammalian cells. Recent new insights into plant cell physiology by functional imaging have been largely driven by technological developments, such as the design of novel sensors, innovative microscopy & imaging techniques and the quantitative analysis of complex image data. Rapid further advances are expected which will require close interdisciplinary interaction of plant biologists with chemists, physicists, mathematicians and computer scientists. High-throughput approaches will become increasingly important, to fill genomic data with 'life' on the scale of cell physiology. If the vast body of information generated in the -omics era is to generate actual mechanistic understanding of how the live plant cell works, functional imaging has enormous potential to adopt the role of a versatile standard tool across plant biology and crop breeding. We welcome original research papers, methodological papers, reviews and mini reviews, with particular attention to contributions in which novel imaging techniques enhance our understanding of plant cell physiology and permits to answer questions that cannot be easily addressed with other techniques.

Table of Contents

05 ***Functional Imaging in Living Plants – Cell Biology meets Physiology***
George R. Littlejohn, Tobias Meckel, Markus Schwarzländer and Alex Costa

08 ***Quantification of Förster Resonance Energy Transfer by Monitoring Sensitized Emission in Living Plant Cells***
Sara M. Müller, Helena Galliardt, Jessica Schneider, B. George Barisas and Thorsten Seidel

28 ***Perspectives for Using Genetically Encoded Fluorescent Biosensors in Plants***
Sisse K. Gjetting, Alexander Schulz and Anja T. Fuglsang

37 ***Development and Properties of Genetically Encoded pH Sensors in Plants***
Alexandre Martinière, Guilhem Desbrosses, Hervé Sentenac and Nadine Paris

43 ***Development of roGFP2-Derived Redox Probes for Measurement of the Glutathione Redox Potential in the Cytosol of Severely Glutathione-Deficient rml1 Seedlings***
Isabel Aller, Nicolas Rouhier and Andreas J. Meyer

55 ***Imaging Long Distance Propagating Calcium Signals in Intact Plant Leaves with the BRET-Based GFP-Aequorin Reporter***
Tou Cheu Xiong, Elsa Ronzier, Frédéric Sanchez, Claire Corratgé-Faillie, Christian Mazars, and Jean-Baptiste Thibaud

68 ***Photosynthesis in a Different Light: Spectro-Microscopy for in Vivo Characterisation of Chloroplasts***
Sébastien Peter, Martina B. Zell, Christian Blum, Alexander Stuhl, Kirstin Elgass, Marucs Sackrow, Vinod Subramaniam, Alfred J. Meixner, Klaus Harter, Veronica G. Maurino and Frank E. Schleifenbaum

75 ***Spectral Analysis Combined With Advanced Linear Unmixing Allows for Histolocalization of Phenolics in Leaves of Coffee Trees***
Geneviève Conéjéro, Michel Noirot, Pascale Talamond and Jean-Luc Verdeil

82 ***An Update: Improvements in Imaging Perfluorocarbon-Mounted Plant Leaves with Implications for Studies of Plant Pathology, Physiology, Development and Cell Biology***
George R. Littlejohn, Jessica C. Mansfield, Jacqueline T. Christmas, Eleanor Witterick, Mark D. Fricker, Murray R. Grant, Nicholas Smirnoff, Richard M. Everson, Julian Moger and John Love

90 ***Arabidopsis Myosin XI Sub-Domains Homologous to the Yeast myo2p Organelle Inheritance Sub-Domain Target Subcellular Structures in Plant Cells***
Amirali Sattarzadeh, Elmon Schmelzer and Maureen R. Hanson

102 ***Plant Cell Shape: Modulators and Measurements***
Alexander Ivakov and Staffan Persson

frontiers in
PLANT SCIENCE

EDITORIAL
published: 19 December 2014
doi: 10.3389/fpls.2014.00740

Functional imaging in living plants—cell biology meets physiology

George R. Littlejohn[1†], Tobias Meckel[2†], Markus Schwarzländer[3†] and Alex Costa[4,5*†]

[1] Division of Plant and Microbial Sciences, School of Biosciences, University of Exeter, Exeter, UK
[2] Membrane Dynamics, Department of Biology, Technische Universität Darmstadt, Darmstadt, Germany
[3] Chemical Signalling, Institute of Crop Science and Resource Conservation, University of Bonn, Bonn, Germany
[4] Department of Biosciences, University of Milan, Milan, Italy
[5] Milan Division, Institute of Biophysics, National Research Council, Milan, Italy
*Correspondence: alex.costa@unimi.it

† These authors have contributed equally to this work.

Edited and reviewed by:
Simon Gilroy, University of Wisconsin - Madison, USA

Keywords: *in vivo* imaging, plants, organelles, cell physiology, dynamics, fluorescent protein sensors, quantitative microscopy

The last quarter of a century has brought major developments in the acquisition of images from plants through improvements in microscopy equipment, software and technique. Likewise, step changes in image analysis tools and the utilization and iterative redesign of fluorescent protein based markers and probes has revolutionized the ability of researchers to ask fundamental questions in cell biology and physiology. This research topic gives a snapshot of the current shape of the field in the plant sciences.

The articles contributed to this research topic are indicative of the work emerging from the plant imaging community and cover, variously, the characterization of individual protein functions; localization and interactions; the use of physiological biosensors; spectroscopic techniques, which utilize autofluorescence of plant tissues and label-free approaches; developmental studies and software engineering. These reflect the broad areas in which imaging is currently being used to functionally dissect plant processes.

A focus in this research topic is the quantitative imaging of fluorescent sensors to explore cell function.

Förster resonance energy transfer (FRET) and how sensitized emission may be used for quantification *in vivo* imaging is reviewed by Müller et al. (2013) who discuss a set of methods that allows for the analysis of molecular interactions, in the light of recent developments in fluorescence microscopy, which have achieved higher spatial and temporal resolution as well as a much-improved sensitivity. A comprehensive overview of FRET imaging is given with a focus on fluorescent proteins and the procedure and analysis of sensitized emission, which allows for a fast and repetitive monitoring of FRET efficiencies as required for the investigation of dynamic plant cells.

A perspective on the use of genetically encoded fluorescent biosensors (including FRET-based probes) in plants is given by Gjetting et al. (2013). The authors discuss the development of a rapidly growing repertoire of genetically encoded fluorescent sensors and how these developments have been a key driver for functional imaging over the last two decades as well as how new sensors have been adopted by plant biology and future opportunities. Autofluorescence from photosynthetic pigments and secondary metabolites, mounting techniques affecting physiological status, sensor silencing and plant specific compartments, such as the apoplast, are identified as technical burdens that can hamper straightforward sensor usage in plants. Plant-adjusted sensor design, such as the usage of new fluorescent protein variants, and imaging techniques, like fluorescent lifetime imaging (FLIM), are recognized as technical opportunities to advance *in vivo* sensing in plants. Biological promise comes from bespoke sensing approaches in which the sensor is matched current questions of plant metabolism, physiology and signaling, such as sugar homeostasis, hormone regulation and pH dynamics of acidic compartments.

The development and properties of pH probes as one group of the genetically encoded sensors discussed by Gjetting et al. (2013) is given detailed attention and set in biological context by Martinière et al. (2013). Imaging of intracellular pH dates back to the early efforts to exploit fluorescent proteins as sensors for *in vivo* physiology. A still growing repertoire of sensor variants for pH has been extensively applied in plant cells to understand subcellular pH milieus and proton gradients across membranes. Nevertheless pH dynamics on a cellular scale are far from understood and potential functional roles of pH as a central physiological parameter are often elusive. In their perspective article, Martinere et al. shine a spotlight on the opportunities and the persisting technical constraints of pH imaging in plants. Insights gained from *in vivo* pH imaging are discussed with respect to exocytotic function, root apoplast responses to changing environments and growth. The highly dynamic nature of the archipelago of subcellular pH islands is exemplified for the physiological transition within the endomembrane system between endoplasmic reticulum (ER) and vacuole.

These three review articles set the scene for two original research articles, contributed by Aller et al. (2013) and Xiong et al. (2014) who report the development of new tools for *in vivo* imaging of glutathione redox status and Ca^{2+}, respectively. Aller et al. (2013) introduce a new member of the redox sensitive GFP family, named roGFP2-iL. roGFP sensors have been extensively used for the *in vivo* monitoring of glutathione redox potential in both animal and plant cells. The founding members of the family, roGFP1 and roGFP2, have midpoint potentials of −290 and −280 mV

respectively, compatible with the monitoring glutathione redox status in plasmatic compartments such as cytosol, mitochondria and peroxisomes. The newly developed roGFP2-iL, which shows a midpoint potential of −238 mV, now enables measurement of glutathione redox status under more oxidizing circumstances, such as in genetic backgrounds with impaired thiol redox maintenance (here exemplified for the glutathione deficient *Arabidopsis rml1* mutant) or in the ER, where both roGFP1 and roGFP2 are completely oxidized. This makes a powerful enhancement of the toolset of glutathione redox sensors and shifts the redox frontier allowing to explore new biology not only in plants.

Addressing another hub of regulation, Xiong et al. (2014) introduce a Bioluminescence Resonance Energy Transfer (BRET) sensor for Ca^{2+} in *Arabidopsis*. The BRET sensor "re-unites" old partners from the jellyfish *Aequoria victoria*—aequorin and GFP, enabling imaging of Ca^{2+} dynamics in entire seedlings and mature leaves of *Arabidopsis* without the necessity of illumination, as required for other popular Ca^{2+} sensor classes, such as the Yellow Cameleons, the GCaMPs and Case12. Instead the GFP-aequorin (G5A) sensor harnesses the photons emitted by the aequorin-coelenterazine complex upon binding of Ca^{2+} to excite the adjacent GFP, via BRET, the fluorescence of which can be detected with a cooled charge-coupled device camera (CCD). This approach allows for increased sensitivity as compared to standard aequorin-based Ca^{2+} sensing and enabled the authors to monitor long-distance Ca^{2+} waves propagating throughout the entire plant body after salt stress treatment applied to the root. This new Ca^{2+} imaging approach will complement other recently developed tools for the *in vivo* analysis of this central second messenger.

Instead of applying fluorescent dyes or introducing recombinant sensor proteins, the same autofluorescence by endogenous plant compounds highlighted as a burden for quantitative imaging by Gjetting et al. (2013) may be actively exploited to provide valuable physiological insight. New spectroscopic techniques for label-free imaging to investigate plant physiology are presented by Peter et al. (2014) and Conejero et al. (2014).

Peter et al. (2014) use spectro-microscopy and Statistical Analysis of Room Temperature Emission Spectra (SART) to characterize *in vivo* function of photosystems PSI and PSII in chloroplasts. This non-invasive technique exploits the natural light absorbance properties of chloroplasts and has the ability to deliver photosynthetic parameters for single chloroplasts at normal growth conditions. As this technique requires only moderate modification of a confocal microscope, it may be readily implemented by well-resourced laboratories.

Conejero et al. (2014) present a method combining spectral analysis with linear unmixing to facilitate histolocalization of phenolics in coffee leaves. Their protocol involves two-photon excitation, spectral characterization of pure chemicals and advanced linear unmixing. Conejero et al. (2014) are able to follow the amount and distribution of key phenolic compounds throughout the development of leaves of various *Coffea* species. By obviating the need for any staining, truly non-invasive histochemical analysis based on quantitative imaging is achieved.

Label-free SRS microscopy is used by Littlejohn et al. (2014) to delimit the negative-space in plant leaves in their paper updating the use of perfluorocarbon mounting media in plants leaves. Functional imaging in intact, living leaves as the main organ of photosynthesis, is often particularly desirable. Much work has been performed on leaf epidermis, while high quality imaging of the mesophyll or vascular bundle cells can prove challenging, due to the optical complexity of the tissue with multiple stacked cell layers and air spaces. Littlejohn et al. (2014) empirically assess the usage of perfluorocarbons, as non-aqueous and non-toxic mounting media for *in vivo* microscopy. A systematic comparison of yet untested perfluorocarbons with four state-of-the-art microscopy techniques pinpoints strong advantages for image quality from the use of perfluoroperhydrophenanthrene. This methodological advance goes far beyond producing "prettier images" and opens a new window for the quantitative *in vivo* study of a defining plant tissue. A particular benefit may be anticipated for ratiometric sensing approaches of physiology where increasing noise and chromatic aberrations in deeper tissue layers can hamper accurate quantitation.

Sattarzadeh et al. (2013) provide an example of how the use of confocal and spinning disc microscopy and *in vivo* imaging facilitates the definition of subcellular localization of proteins through the generation of chimeric fusion constructs between a fluorescent protein (e.g. GFP, YFP, RFP) and the full protein of interest or a functional domain. The authors identify conserved 42 amino-acid PAL domains present in 12 of the 13 *Arabidopsis* class XI myosin isoforms. YFP translational fusions for 11 different myosin PAL sub-domains allowed determination of their subcellular localization at Golgi, mitochondria, nuclear envelope, the plasma membrane and unidentified vesicles. Interestingly, the simultaneous expression of three PAL sub-domains resulted minimal or negligible movement of Golgi and mitochondria, allowing the authors not only to demonstrate that different YFP-PAL sub-domains localize to different subcellular compartments, but also that their overexpression can interfere with the mobility of the marked compartments in the cell. This work illustrates the elegance of *in vivo* imaging in exploring dynamic cell biological processes.

To extract the relevant information out of the highly complex dataset that is an image quantitative evaluation is essential, but far from trivial. In the field of plant cell morphology, cell shapes are irregular and highly variable, which requires the use of quantitative techniques to accurately define shape and provide well-defined phenotypic descriptions. In their review Ivakov and Persson (2013) present the current state of knowledge on cell shape formation in plants, focusing on the use of new quantitative tools and algorithms required to quantify and compare cell shapes in 2D and 3D obtained from microscope images.

This research topic reflects the breadth of approaches developed, adjusted and followed by the plant community in terms of sample preparation and image acquisition and analysis. A major driver behind the recent progress on the burning questions in plants sciences have been technological advances in imaging. Yet the field is far from maturity and progresses quickly with the promise of keeping delivering fundamental new insights in the years to come.

REFERENCES

Aller, I., Rouhier, N., and Meyer, A. J. (2013). Development of roGFP2-derived redox probes for measurement of the glutathione redox potential in the cytosol of severely glutathione-deficient rml1 seedlings. *Front. Plant Sci*. 4:506. doi: 10.3389/fpls.2013.00506

Conejero, G., Noirot, M., Talamond, P., and Verdeil, J.-L. (2014). Spectral analysis combined with advanced linear unmixing allows for histolocalization of phenolics in leaves of coffee trees. *Front. Plant Sci*. 5:39. doi: 10.3389/fpls.2014.00039

Gjetting, S. K., Schulz, A., and Fuglsang, A. T. (2013). Perspectives for using genetically encoded fluorescent biosensors in plants. *Front. Plant Sci*. 4:234. doi: 10.3389/fpls.2013.00234

Ivakov, A., and Persson, S. (2013). Plant cell shape: modulators and measurements. *Front. Plant Sci.* 4:39. doi: 10.3389/fpls.2013.00439

Littlejohn, G. R., Mansfield, J. C., Christmas, J. T., Witterick, E., Fricker, M. D., Grant, M. R., et al. (2014). An update: improvements in imaging perfluorocarbon-mounted plant leaves with implications for studies of plant pathology, physiology, development and cell biology. *Front. Plant Sci.* 5:140. doi: 10.3389/fpls.2014.00140

Martinière, A., Desbrosses, G., Sentenac, H., and Paris, N. (2013). Development and properties of genetically encoded pH sensors in plants. *Front. Plant Sci.* 4:523. doi: 10.3389/fpls.2013.00523

Müller, S. M., Galliardt, H., Schneider, J., Barisas, B. G., and Seidel, T. (2013). Quantification of Förster resonance energy transfer by monitoring sensitized emission in living plant cells. *Front. Plant Sci.* 4:413. doi: 10.3389/fpls.2013.00413

Peter, S. B., Zell, M. B., Blum, C., Stuhl, A., Elgass, K., Sackrow, M., et al. (2014). Photosynthesis in a different light: spectro-microscopy for *in vivo* characterization of chloroplasts. *Front. Plant Sci.* 5:292. doi: 10.3389/fpls.2014.00292

Sattarzadeh, A., Schmelzer, E., and Hanson, M. R. (2013). Arabidopsis myosin XI sub-domains homologous to the yeast myo2p organelle inheritance subdomain target subcellular structures in plant cells. *Front. Plant Sci.* 4:407. doi: 10.3389/fpls.2013.00407

Xiong, T. C., Ronzier, E., Sanchez, F., Corratgé-Faillie, C., Mazars, C., and Thibaud, J.-B. (2014). Imaging long distance propagating calcium signals in intact plant leaves with the BRET-based GFP-aequorin reporter. *Front. Plant Sci.* 5:43. doi: 10.3389/fpls.2014.00043

Conflict of Interest Statement: The authors declare that the research was conducted in the absence of any commercial or financial relationships that could be construed as a potential conflict of interest.

Received: 19 November 2014; accepted: 04 December 2014; published online: 19 December 2014.

Citation: Littlejohn GR, Meckel T, Schwarzländer M and Costa A (2014) Functional imaging in living plants—cell biology meets physiology. Front. Plant Sci. ***5****:740. doi: 10.3389/fpls.2014.00740*

This article was submitted to Plant Cell Biology, a section of the journal Frontiers in Plant Science.

Copyright © 2014 Littlejohn, Meckel, Schwarzländer and Costa. This is an open-access article distributed under the terms of the Creative Commons Attribution License (CC BY). The use, distribution or reproduction in other forums is permitted, provided the original author(s) or licensor are credited and that the original publication in this journal is cited, in accordance with accepted academic practice. No use, distribution or reproduction is permitted which does not comply with these terms.

frontiers in
PLANT SCIENCE

REVIEW ARTICLE
published: 29 October 2013
doi: 10.3389/fpls.2013.00413

Quantification of Förster resonance energy transfer by monitoring sensitized emission in living plant cells

Sara M. Müller[1], Helena Galliardt[1], Jessica Schneider[2], B. George Barisas[3] and Thorsten Seidel[1]*

[1] Dynamic Cell Imaging, Faculty of Biology, Bielefeld University, Bielefeld, Germany
[2] Bioinformatic Resource Facility, Center for Biotechnology, Bielefeld University, Bielefeld, Germany
[3] Chemistry Department, Colorado State University, Fort Collins, CO, USA

Edited by:
Tobias Meckel, Technische Universität Darmstadt, Germany

Reviewed by:
Ram Dixit, Washington University in St. Louis, USA
Takashi Murata, National Institute for Basic Biology, Japan

***Correspondence:**
Thorsten Seidel, Dynamic Cell Imaging, Faculty of Biology, Bielefeld University, Universitätsstraße 25, 33501 Bielefeld, Germany
e-mail: thorsten.seidel@uni-bielefeld.de

Förster resonance energy transfer (FRET) describes excitation energy exchange between two adjacent molecules typically in distances ranging from 2 to 10 nm. The process depends on dipole-dipole coupling of the molecules and its probability of occurrence cannot be proven directly. Mostly, fluorescence is employed for quantification as it represents a concurring process of relaxation of the excited singlet state S_1 so that the probability of fluorescence decreases as the probability of FRET increases. This reflects closer proximity of the molecules or an orientation of donor and acceptor transition dipoles that facilitates FRET. Monitoring sensitized emission by 3-Filter-FRET allows for fast image acquisition and is suitable for quantifying FRET in dynamic systems such as living cells. In recent years, several calibration protocols were established to overcome to previous difficulties in measuring FRET-efficiencies. Thus, we can now obtain by 3-filter FRET FRET-efficiencies that are comparable to results from sophisticated fluorescence lifetime measurements. With the discovery of fluorescent proteins and their improvement toward spectral variants and usability in plant cells, the tool box for *in vivo* FRET-analyses in plant cells was provided and FRET became applicable for the *in vivo* detection of protein-protein interactions and for monitoring conformational dynamics. The latter opened the door toward a multitude of FRET-sensors such as the widely applied Ca^{2+}-sensor Cameleon. Recently, FRET-couples of two fluorescent proteins were supplemented by additional fluorescent proteins toward FRET-cascades in order to monitor more complex arrangements. Novel FRET-couples involving switchable fluorescent proteins promise to increase the utility of FRET through combination with photoactivation-based super-resolution microscopy.

Keywords: Förster resonance energy transfer, fluorescence microscopy, quantitative imaging, fluorescent protein

INTRODUCTION

BACKGROUND THEORY

Energy can be transferred from one molecule to another by radiationless energy transfer between two coupled dipoles. This process has been described precisely by Theodor Förster (1946, 1948) and hence has been termed Förster Resonance Energy Transfer (FRET). If the acceptor is in range of an excited donor's electric field, their dipoles can couple resulting in transfer of quantized excitation energy. More specifically, FRET describes a relaxation process from donor singlet state S_1 to singlet state S_0 and thus, competes with thermal relaxation (internal conversion) and with intersystem crossing toward the triplet state T_1 followed by phosphorescence or even retrograde intersystem crossing (delayed fluorescence). The rate k_T of FRET contributes to the deactivation of the donor molecule (Lakowicz, 2006) and this overall deactivation rate is related to the sum of the rates of all mechanisms deactivating the excited state (**Figure 1**), including FRET, light emission by fluorescence, delayed light emission by phosphorescence subsequent intersystem crossing, and heat dissipation by internal conversion (Cheung, 1991; Watrob et al., 2003). The prerequisites for FRET relaxation are a close distance of the molecules, typically below 10 nm, to enable coupling of the oscillating dipole moments of both molecules in their near field, and a significant overlap of the emission spectrum of the excited molecule and the absorption spectrum of the energy accepting molecule (**Figure 2**), so that the donor frequency matches the acceptor frequency as the energy amounts are quantized (**Table 1**; Lakowicz, 2006).

FRET also requires that the absorbing molecule undergoes a singlet-singlet transition. The efficiency E of energy transfer is related to the sixth power of the ratio of the distance R between donor and acceptor and the Förster radius R_0 (**Table 1**). The Förster radius R_0 corresponds in turn to the critical distance between two fluorophores at which the energy transfer is half-maximal (Hink et al., 2002). R_0 is usually in the range of 1.5–6 nm and depends on factors including quantum yield of the donor, absorption of the acceptor and spectral overlap integral and on an orientation factor κ^2 (**Table 1**; Patterson et al., 2000; Lakowicz, 2006; Lam et al., 2012).

The influence of κ^2 becomes significant if rotational relaxation is slower than the fluorescence lifetime of the donor. κ^2 varies in a range of 0–4 being 0, if the electric field of the excited donor

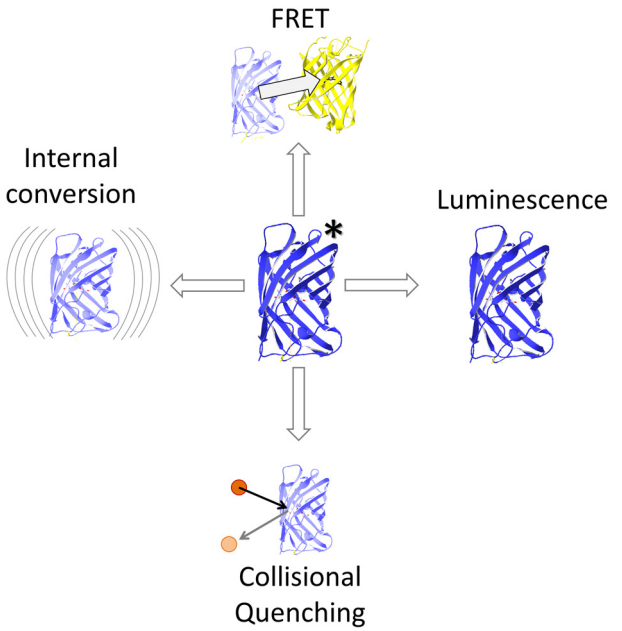

FIGURE 1 | FRET and competing events. FRET competes with internal conversion by heat dissipation, collisional quenching e.g., with halogens and luminescence. The latter comprises fluorescence as well as forbidden transitions such as phosphorescence and delayed fluorescence.

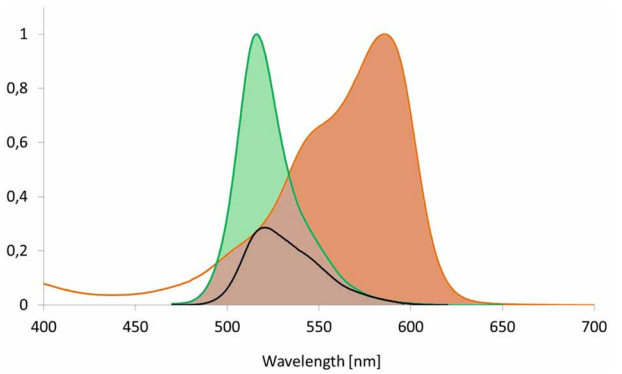

FIGURE 2 | Spectral overlap as prerequisite for FRET. The integral of acceptor's absorption spectrum and the integral of the excited donor's emission spectrum have to show significant overlap to allow for FRET to occur. The overlap integral is shown for the fluorescent proteins Dronpa and mCherry that serve as donor and acceptor, respectively. The black line corresponds to the product of both spectra and reflects the spectral overlap.

Table 1 | Basal equations for FRET.

(1) **Definition of energy transfer rate k_T**

R_0 depends on the refractive index of the medium n, the orientation factor κ^2, the fluorescence quantum yield Φ_D, the normalized fluorescence spectrum of the donor $F_D(\bar{\lambda})$ and the molar absorptivity of the acceptor $\varepsilon_A(\bar{\lambda})$, and the wavelength λ in cm:

$$R_0 = \frac{9000 \ln 10 \kappa^2 \Phi_D}{128\pi^5 n^4 N_A} \int_0^\infty \frac{F_D(\lambda)\varepsilon_A(\lambda)\, d\lambda}{\lambda^4}$$

(2) **Distance-dependency of energy transfer efficiency E**

The efficiency E of energy transfer is the product of k_T times the unperturbed donor lifetime τ_D and varies as the inverse sixth power of the ratio of the distance R between donor and acceptor and the Förster radius R_0:

$$E = \frac{k_T \tau_D}{1 + k_T \tau_D} = \frac{1}{1 + (R/R_0)^6}$$

(3) **Definition of energy transfer rate k_T**

k_T depends on the Förster radius R_0, the distance R separating the chromophores and the unperturbed donor fluorescence lifetime τ_D:

$$k_T = \frac{1}{\tau_D}\left(\frac{R_0}{R}\right)^6$$

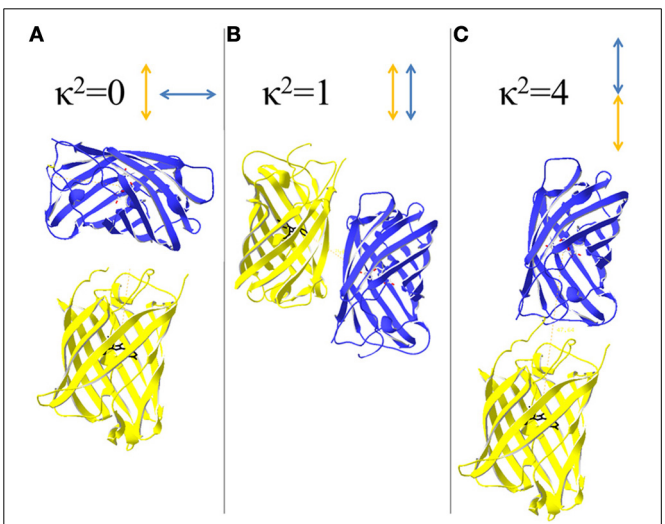

FIGURE 3 | Orientation of donor and acceptor and its influence on the orientation factor κ2. κ^2 depends on the relative arrangements of excited donor's electric field and acceptors absorption dipole. **(A)** A perpendicular arrangements of the transition dipoles results in $\kappa^2 = 0$ and prevents energy transfer between donor and acceptor. **(B)** If the dipoles are arranged side-by-side, κ^2 becomes 1. **(C)** A head to tail arrangement of the dipoles favors FRET as $\kappa^2 = 4$, the highest value that is possible for κ^2.

and acceptor's absorption dipole are perpendicular, and 4, if they are parallel and head to tail orientated (**Figure 3**). The probability of possible arrangements favors a $\kappa^2 = 0$ and there is only low probability for $\kappa^2 = 4$ (Vogel et al., 2012). For the calculation of R_0 it is assumed that rotational diffusion of the dyes is faster than the donor's fluorescence lifetime so that $\kappa^2 = 2/3$. To this end, it is a helpful requirement if the donor is a rather small molecule allowing for fast rotation and donor and acceptor are not linked to each other so that the orientation is not fixed. For fluorescent proteins the rotation correlation time is about 20–30 ns whereas the fluorescent lifetime is in a range of 1–3 ns (Vogel et al., 2012). Thus, the assumption that $\kappa^2 = 2/3$ appears not applicable for the calculation of R_0 of fluorescent protein FRET-couples, but actually no alternative is available. Thus, the calculated R_0-values are useful for comparison of FRET-pairs, if it is kept in mind that calculated distances do not correspond to the real situation. Usually, R_0 is determined based on Equation 1 (Patterson et al., 2000). Calculations based on the acceptor's

excitation spectrum instead of its absorption spectrum can also be performed (Rizzo et al., 2006), although this ignores possible dark states of the acceptor. For fluorescent protein couples R_0 can also be determined by examining fusion constructs of donor and acceptor possessing a linker identical to that of an ECFP/EYFP fusion protein of known R_0 (He et al., 2005). Thus, new R'_0-values can be back-calculated from the known ECFP-EYFP distance R_0 and the measured FRET-efficiency for the couples:

$$R'_0 = \frac{R}{\sqrt[6]{\frac{1}{E}-1}} \quad (4)$$

The distance range that is accessible through FRET-measurements is $\sim 0.5\ R_0 \leq R \leq 1.5\ R_0$ (Gadella et al., 1999) (**Figure 4**). If R is two times of R_0, the FRET-efficiency becomes less than 0.016 and thus negligible, if $R = 0.5\ R_0$, the FRET efficiency becomes larger than 0.984 (Vogel et al., 2012). The higher the spectral overlap and wavelength range, the higher is the Förster radius of a given FRET-pair (Patterson et al., 2000). Also a high quantum yield of the donor yields increased R_0 (Goedhart et al., 2007; Lam et al., 2012). Furthermore, R_0 is sensitive to acceptor stability since blinking of the acceptor affects R_0 (Vogel et al., 2012). In the case of multiple (n) acceptors proximal to a single donor, the operational R_0 becomes n-times R_0 (Jares-Erijman and Jovin, 2003).

The rate of FRET can be estimated both from the loss of fluorescence of the donor or an increase of fluorescence of an acceptor molecule. Alternatively, FRET decreases the lifetime of donor's excited state τ_D and results in a decrease of polarization of the emitted light (Lidke et al., 2003; Lakowicz, 2006). In the life sciences a misleading differentiation between FRET and bioluminescence resonance energy transfer (BRET) has arisen, although both represent FRET (Gandía et al., 2008). Therefore, RET was suggested to be used for FRET as the underlying phenomenon, FRET if the donor is a fluorophore, and BRET if bioluminescence is involved (Lakowicz, 2006).

The most important feature of RET for analysis of protein-protein interactions is the distance dependency. RET occurs in the range of ~0.5–10 nm (Clegg, 2009) and the diameter of a globular protein with a molecular weight of 30 kDa is ~3 nm so that the distance range critical for RET matches the dimension of proteins and turns RET to be a suitable tool for the analyses of conformational dynamics and interactions of proteins (Hink et al., 2002).

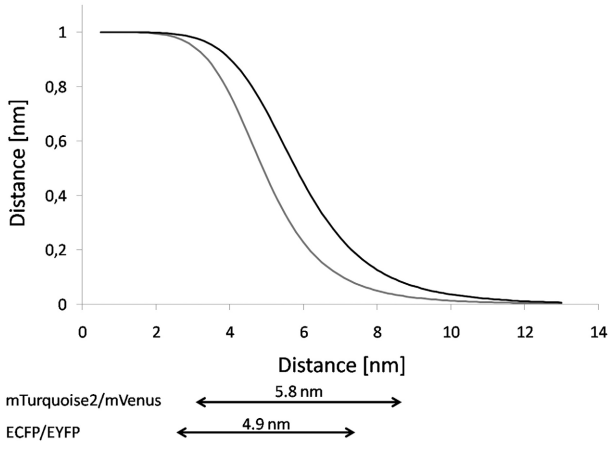

FIGURE 4 | Comparison of Distance-dependency of ECFP/EYFP and mTurquoise2/mVenus. Based on the R_0-values the FRET-efficiency was plotted against the distance. The graph shows the curves for the FRET-pairs ECFP/EYFP (gray line, source of R_0: Patterson et al., 2000) and mTurquoise2/mVenus (black line, source of R_0: Goedhart et al., 2012). Underneath, the dynamic range is given for both FRET-pairs. The dynamic range corresponds to $0.5\ R_0 - 1.5 R_0$.

FLUORESCENT PROTEINS FOR FRET

The discovery of various fluorescent proteins and the engineering of spectrally distinct variants and their improvement regarding photostability, folding efficiency, codon usage, quantum yield, insensitivity to the cellular environment and monomeric forms has enabled non-invasive FRET-measurements in living plant cells. In particular in plants, the employment of the green fluorescent protein was delayed in comparison to its use in mammals due to cryptic splicing resulting in a non-functional protein (Haseloff et al., 1997). The application of fusions of fluorescent proteins in living cells is still challenging due to differences in the sensitivity of fluorescent proteins to the (sub-)cellular environment, sensitivity of detectors that demands high expression levels, expression of proteins in cell types that do not provide their native environment, and required tolerance of proteins to N- or C-terminal fusions (Duncan, 2006). The first described FRET-pair consisted of GFP and its blue-shifted variant blue fluorescent protein (BFP) (Cubitt et al., 1995). This FRET-pair suffered from the low photostability and quantum yield of BFP (Miyawaki and Tsien, 2000), so that the combination of cyan fluorescent protein (CFP) and yellow fluorescent protein (YFP) appeared more promising. However, CFP as well as YFP were found to have major limitations in their applicability due to YFP's sensitivity to pH and halides affecting YFP's absorption, and CFP's multiple fluorescent states and its pH-dependent and low quantum yield (Miyawaki and Tsien, 2000). The pH-sensitivity of YFPs is tightly coupled to halides binding (Seward et al., 2013). In contrast to BFP-GFP this FRET-pair has been subjected to re-engineering in the recent years resulting in vastly improved variants. Basically, the folding mutations F64L, V68L, S72A, M153T, V163A, and S175G resulted in faster maturation especially at 37°C, reflecting folding mutations aimed at enhanced maturation in mammals. The extent to which these mutations are of relevance for an expression in plant cells is unclear. EYFP has been improved to yield halide- and pH-insensitive monomeric variants such as Citrine that bears the additional mutation Q69M conferring reduced sensitivity to acidosis and halides (Heikal et al., 2000; Griesbeck et al., 2001). Venus was designed for fast and complete folding so that it mainly contains the folding mutations F64L, M153T, V163A, S175G but also the mutation F46L resulting in accelerated oxidation of the fluorophore again at 37°C (Nagai et al., 2002). Recently, the kinetics of halide binding have been analyzed and confirmed the reduced halide affinity of Citrine and Venus in comparison to YFP (Seward et al., 2013). Finally, the mutation A206K

affects the dimerization and turns Venus monomeric (mVenus, **Figure 5**). In SYFP2 the mutation V68L was reversed in the background of mVenus and resulted in a slightly brighter fluorescent protein (Kremers et al., 2006). In the case of ECFP, donor fluorescence lifetime measurements revealed a bi-exponential decay curve that hampers data evaluation, so that following improvements gained at a mono-exponential decay. Further aims were increasing the quantum yields and the absorption coefficients of CFPs. Two branches of CFPs were designed that involve similar mutations but that based on different GFP-derivatives: On the one hand CFPs of the Cerulean-branch are based on ECFP and on the other hand, CFPs derive from the SCFP-branch. The latter rely on mVenus (Kremers et al., 2006). The variant Cerulean is characterized by the mutations S72A, Y145A, and H148D and shows a significant increase in brightness compared to ECFP. Also the quantum yield and the absorption coefficient were improved. Both these aromatic amino acid residues were responsible for two different conformational states that caused the bimodal behavior of ECFP. Consequently, their replacement resulted in a CFP that showed mono-exponential decay (Rizzo et al., 2004). Nevertheless, Cerulean undergoes reversible photo-switching that strongly affects long-term measurements and bleaching experiments. Next improvements relied on mutations in β-strands 7 and 8 (S147H, D148G, K166G, I167L, R168N, H169C) and reversing the early mutation S65T to the wildtype serine that lead to Cerulean3 (Markwardt et al., 2011). Cerulean3 shows high photostability and reduced photoswitching behavior, a high quantum yield of 0.87, and only a slightly reduced absorption coefficient compared to Cerulean. Reversing only S65T stabilized the H-bonding status of the hydroxyl group and resulted in a Cerulean with increased photostability and pH-resistance, high quantum yield, and reduced reversible photoswitching (Fredj et al., 2012).

The second branch of CFPs originates from the YFP mVenus. The conversion of mVenus into SCFP1 required reversing the mutations F46L and T203Y and introduction of G65T, Y66W, and N146I. SCFP1 is characterized by a slightly red-shifted emission, low quantum yield, and short fluorescence lifetime. Next, the mutation V68L was reversed so that the red-shift of the emission disappeared and the quantum yield was improved by introducing H148D as described for mCerulean before. The resulting variant SCFP3A has an improved quantum yield of 0.56 and a slightly elongated lifetime (Kremers et al., 2006). Again, mutation S65T was reversed to increase the quantum yield to 0.84 in mTurquoise (Goedhart et al., 2010). Based on the crystal structures of SCFP3A and mTurquoise the amino acid residue Ile146 was identified as target for further improvement. Replacing it by phenylalanine creates a network of van der Waals forces stabilizing the fluorophore. The novel mTurquoise2 (**Figure 5**) has a unique quantum yield of 0.93, a fluorescence lifetime of 3.8 ns, is highly photostable in living cells and matures faster than mTurquoise (Goedhart et al., 2012).

An alternative CFP is the monomeric teal fluorescent protein (mTFP1) from *Clavularia* that shows a quantum yield and photostability superior to Cerulean even in its original version cFP484. Further improvements resulted in the present monomeric form mTFP1 with an absorption coefficient of 64,000 $Mol^{-1}cm^{-1}$ and a quantum yield of 0.85 (Ai et al., 2006). Taken together with its absorption maximum at 462 nm that fits quite well with 458 nm laser lines, mTFP1 appears to be a promising but up to now only rarely applied CFP of high potential for FRET applications.

Pairs of green and red fluorescent proteins represent another group couples commonly applied in FRET-analysis. These provide the advantage of a high R_0 due to the increased wavelength of the spectral overlap, so that the R_0 ranges up to 6.4 nm for the FRET-pair mKo/mCherry (Goedhart et al., 2007). Initially, GFP and DsRed were employed but DsRed proved to be unsatisfactory in FRET-analyses due to its slow maturation (in the range of days) accompanied by a yellowish intermediate, a complex absorption spectrum and a strong tendency to oligomerization, although the intermediate state can be counteracted by pulsed expression followed by an elongated incubation (Baird et al., 2000; Mizuno et al., 2001; Erickson et al., 2003). Intermediate state and oligomerization combine to yield intermolecular FRET potentially interfering with FRET-measurements using DsRed as acceptor, also dark states were observed for DsRed that affect FRET (Blum et al., 2011). Nevertheless, many improvements have been accomplished for DsRed and have resulted in a complete family of spectrally distinct fluorescent proteins, the mFruits-family (Shaner et al., 2004). Initially, mutations addressed the folding efficiency and aimed at monomeric forms of DsRed. The final product with altogether 33 mutations was the monomeric red fluorescent protein 1 (mRFP1) that folds 10 times faster than DsRed (Campbell et al., 2002). Unfortunately, the improvements were achieved on the expense of the quantum yield. Whereas DsRed has a high quantum yield of 0.79 it dropped to 0.25 in mRFP1. Addition of the N- and C-termini of GFP improved its tolerance to N- and C-terminal protein fusions and mutations in the environment of the fluorophore resulted in novel red fluorescent proteins such as dTomato, mStrawberry, and mCherry, but also in the yellow to orange fluorescent proteins mBanana and mOrange (Shaner et al., 2004). In the recent years mCherry

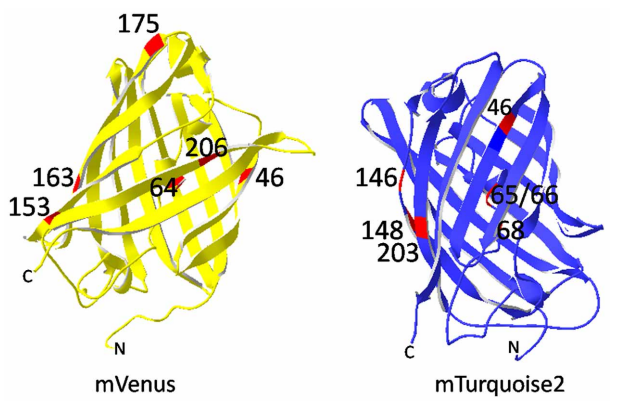

FIGURE 5 | Mutations resulting in mVenus and mTurquoise2. mVenus bears mainly folding mutations (F64L, M153T, V163A, S175G) and F46L for optimized oxidation of the fluorophore. A206K turned Venus monomeric. Cyan emission of the mVenus derivative mTurquoise was achieved by the mutations L46F, Y203T, T65S, Y66W, and N146I. The mutations are highlighted in red. Images were processed with SwissPdb Viewer (Guex and Peitsch, 1997).

became frequently applied although it has the disadvantage of a very low quantum yield of only 0.22 and two fluorescent states were reported for mCherry that result in a biexponential fluorescence decay with EGFP as donor (Shaner et al., 2004; Wu et al., 2009). But its maturation half time of 15 min is superior to any other fluorescent protein and mCherry showed extremely high photostability in single molecule analysis (Shaner et al., 2004; Seefeldt et al., 2008). Another red fluorescent protein that served as FRET-acceptor is mRuby2, an improved monomeric variant of eqFP611 with a comparatively high quantum yield of 0.38 and an absorption coefficient of 113,000 $Mol^{-1}cm^{-1}$ (Lam et al., 2012).

Mostly, EGFP serves as donor for red fluorescent proteins (Erickson et al., 2003; Peter et al., 2005; Padilla-Parra et al., 2008, 2009) due to its monoexponential fluorescence lifetime decay and insensitivity to photobleaching, high quantum yield and short maturation time (Padilla-Parra et al., 2009). The blue-shifted excitation spectrum of the neutral phenol GFP-variant T-Sapphire shows negligible acceptor spectral bleed through (ASBT) in combination with orange and red fluorescent proteins (Mizuno et al., 2001; Zapata-Hommer and Griesbeck, 2003; Bayle et al., 2008), but blue light excitation likely results in high autofluorescence background in plant cells.

Most substances contributing to autofluorescence background in plants share an excitation maximum in the violet/blue range, whereas the emission maxima are distinct between the fluorophores and, thus, affect spectral variants of fluorescent proteins to different extents (Roshchina, 2012; **Table 2**). Between these substances are secondary metabolites that accumulate in the vacuole, but also ubiquitously distributed molecules such as flavins. The main sources of autofluorescence are chlorophylls in the plant cell. Chlorophylls are characterized by a broad absorption and emission spectrum nearly affecting any fluorescent protein. The fluorescence emission spectrum of chloroplasts shows a prominent peak at 670 nm that corresponds to chlorophyll (**Figure 6**). However, chlorophylls are restricted to the thylakoid region of plastids so that their fluorescence is not critical for analyses in other compartments (**Figure 6**).

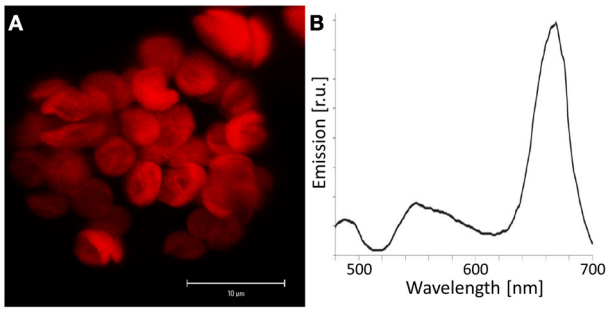

FIGURE 6 | Chlorophyll autofluorescence in Arabidopsis protoplasts. **(A)** Autofluorescence was detected in the range of 650–700 nm using a 458 nm laser line for excitation by confocal laser scanning microscopy of an Arabidopsis mesophyll protoplast. A z-stack was performed and an average projection is shown. The detected emission is restricted to chloroplasts. **(B)** Subsequently, emission spectra of mesophyll protoplasts were recorded by CLSM. The minimum of emission at 514 nm was caused by the applied main beam splitter that is designed for simultaneous excitation at 458 and 514 nm. Autofluorescence emission could be observed in a broad wavelength range with a highly dominant peak at 670 nm.

Table 2 | Sources of autofluorescence in plant cells.

Molecule	Localization	Emission wavelength	References
Chlorophyll	Plastids	450–700 nm, 675–680 nm	Agati, 1998; Vitha and Osteryoung, 2011
UV-VIOLET FLUORESCENT PROTEINS			
Lignin	Cell wall	358 nm; 440 nm	Albinsson et al., 1999; Djikanović et al., 2007
BLUE FLUORESCENT PROTEINS			
Cellulose	Cell wall	420–430 nm	Pöhlker et al., 2011
NAD(P)H	Plastids	450 nm	Poot et al., 2002
Pterins/folates	Vacuole, mitochondria, plastids, cytosol	450 nm	Wolfbeis, 1985; Hossain et al., 2004
CYAN FLUORESCENT PROTEINS–GREEN FLUORESCENT PROTEINS			
Terpenes	(Flowers)	470–525 nm	Roshchina, 2012
Flavonoids	Ubiquitous	470–525 nm	Roshchina, 2012
Lipofuscin-like	(Pollen)	475–480 nm	Roshchina and Karnaukhov, 1999
GREEN–YELLOW FLUORESCENT PROTEINS			
Phenols	Vacuole, cell wall, chloroplasts	490–560 nm	Roshchina, 2012
Flavins	Ubiquitous	520 nm	Wolfbeis, 1985
Betaxanthins	Flowers	530–560 nm	Gandía-Herrero et al., 2005
β-carotin	Chloroplast, lipid globules	560 nm	Gillbro and Cogdell, 1989; Kleinegris et al., 2010
YELLOW–ORANGE FLUORESCENT PROTEINS			
Polyacetylene	Vacuole	530–595 nm	Roshchina, 2012
Isoquinoline	Vacuole	530–595 nm	Otani et al., 2005; Roshchina, 2012
Acridone alkaloids	Vacuole, (idioblasts)	530–595 nm	Eilert et al., 1986; Roshchina, 2012
RED FLUORESCENT PROTEINS			
Anthocyanins	Vacuole, (pollen)	600–630	Roshchina, 2012
Azulenes	(Pollen)	600–630	Roshchina, 2012

Yellow and orange fluorescent proteins are characterized by a higher and more red-shifted spectral overlap with red fluorescent proteins. Accordingly, they enable high R_0-values and thus a high dynamic distance range (**Table 3**; Goedhart et al., 2007; Akrap et al., 2010). However, Lam et al. (2012) suggested the green fluorescent protein Clover and the red fluorescent protein mRuby2 as ideal FRET-pair for expansion of the dynamic range due to their high $R_0 = 6.3$ nm, absorption coefficients and quantum yields. Although the application of yellow donors is still in its infancy, these materials have a high potential for suppressing autofluorescence background, e.g., in plastids. Another interesting aspect is the development of photoswitchable green fluorescent proteins such as Dronpa for FRET. The emission spectrum of Dronpa shows significant overlap with the absorption spectrum of mCherry (**Figure 2**), resulting in an $R_0 = 5.58$ nm. The advantage of this FRET-pair is the possibility to adjust the (active) donor to acceptor ratio. This permits, for example, identification of saturated acceptors in the presence of multiple donors and thus, improvement of donor to acceptor ratio, if donors form a homo-oligomer that interacts with a single acceptor. In 2-step FRET-cascades, photoswitchable mediators should enable to consider energy transfer from donor to acceptor that bypasses the mediator. On the other hand, photoswitchable donors provide a perspective for the combination of FRET and super resolution microscopy, if stability and reproducibility of switching is given. For Dronpa, the initial emission was fully recovered at least after 10 cycles of inactivation and activation (**Figure 7**). However, this number of repetitions is far from the number of repetitions required for photoactivation-dependent sub-diffraction microscopy. Moreover, donor persistence has to arise from single molecules rather than from ensembles. For an additional proof of concept, a fusion protein of Dronpa and mCherry was constructed and the intramolecular FRET-efficiency was determined as 0.53 (**Figure 8**). Next, ratio-imaging has been performed to analyse the robustness of FRET between both proteins while the donor fraction is gradually reduced in a time series. If ASBT is not considered, the ratio increases over time reflecting the increasing contribution of ASBT to the emission in the FRET-channel (**Figure 9A**), but subtraction of ASBT results in a stable ratio over time. In a second set of experiment, Dronpa was stabilized by irradiation with 405 nm before recording the emission at individual time points. In this case, the ratio was constant even if ABST was not considered and fluctuations were less pronounced than in the previous measurement (**Figure 9B**).

Table 3 | Förster-radii of fluorescent protein FRET-pairs.

Fluorophores	Förster radius R_0	Dynamic range	References
BLUE DONOR			
EBFP/ECFP	3.8 nm	1.9–5.7 nm	Patterson et al., 2000
EBFP/EGFP	4.1 nm	2.1–6.2 nm	Patterson et al., 2000
EBFP/EYFP	3.8 nm	1.9–5.7 nm	Patterson et al., 2000
EBFP/DsRed	3.2 nm	1.6–4.8 nm	Patterson et al., 2000
CYAN DONOR			
ECFP/EGFP	4.8 nm	2.4–7.2 nm	Patterson et al., 2000
ECFP/EYFP	4.9 nm	2.5–7.3 nm	Patterson et al., 2000
ECFP/mVenus	5.0 nm	2.5–7.5 nm	Rizzo et al., 2006
mCerulean/EYFP	5.4 nm	2.7–8.1 nm	Rizzo et al., 2006
mCerulean/mVenus	5.4 (5.2) nm	2.7–8.1 nm	Rizzo et al., 2006; Markwardt et al., 2011
mCerulean/mCitrine	5.4 nm	2.7–8.1 nm	Rizzo et al., 2006
mCerulean3/mVenus	5.7 nm	2.9–8.6 nm	Markwardt et al., 2011
SCFP3/SYFP2	5.4 nm	2.7–8.1 nm	Goedhart et al., 2007
mTurquoise/mVenus	5.7 nm	2.9–8.6 nm	Markwardt et al., 2011
mTurquoise2/mVenus	5.8 nm	2.9–8.7 nm	Goedhart et al., 2012
ECFP/DsRed	4.2 (5.1) nm	2.1–6.3 nm (2.6–7.7 nm)	Patterson et al., 2000; Erickson et al., 2003
ECFP/mCherry	3.5 nm	1.8–5.3 nm	He et al., 2005
GREEN DONOR			
EGFP/EYFP	5.6 nm	2.8–8.4 nm	Patterson et al., 2000
EGFP/DsRed	4.7 (5.8) nm	2.4–7.1 nm (2.9–8.7 nm)	Erickson et al., 2003
EGFP/mRFP1	4.7 nm	2.4–7.1 nm	Peter et al., 2005
Clover/mRuby2	6.3 nm	3.2–9.5 nm	Lam et al., 2012
Kaede/Kaede	5.8 nm	2.9–8.7 nm	Wolf et al., 2013a
Dronpa/mCherry	5.6 nm	2.8–8.4 nm	This work
YELLOW/ORANGE DONOR			
EYFP/DsRed	4.9 nm	2.5–7.4 nm	Patterson et al., 2000
EYFP/mCherry	5.7 nm	2.9–8.6 nm	Akrap et al., 2010
SYFP2/mStrawberry	6.3 nm	3.2–9.5 nm	Goedhart et al., 2007
mKo/mCherry	6.4 nm	3.2–9.6 nm	Goedhart et al., 2007

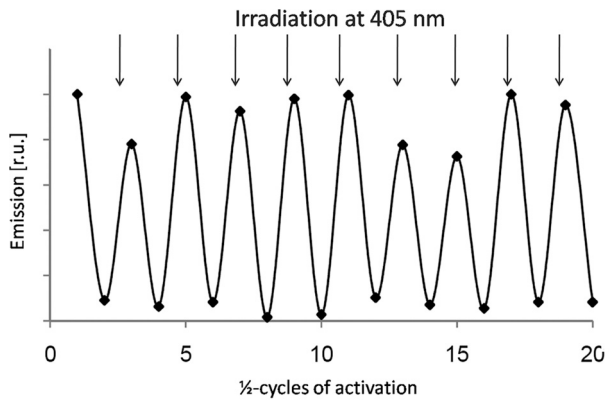

FIGURE 7 | Activation and inactivation cycles of Dronpa in plant cells. Switching of Dronpa was analyzed by confocal laser scanning microscopy of Arabidopsis protoplasts. Emission was detected between 500 and 600 nm using excitation of 488 nm. Intensive illumination with 488 nm was performed to switch Dronpa off. Subsequent irradiation at 405 nm fully recovered the fluorescent state. The procedure was repeated for 10 times without significant loss in emission intensity.

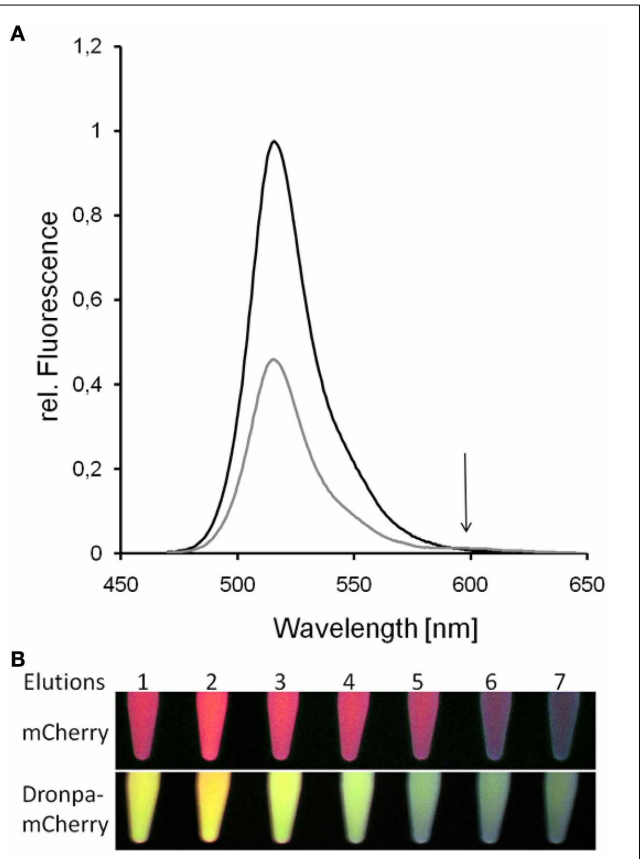

FIGURE 8 | Donor-quenching of Dronpa in the presence of mCherry. The comparison of emission spectra of Dronpa and the fusion protein Dronpa-mCherry revealed the quenching of Dronpa in the presence of mCherry **(A)**. In the emission spectrum of Dronpa-mCherry the emission of mCherry is less pronounced due to the low quantum yield of mCherry. The same effect can be observed by the emission of eluted fluorescent proteins **(B)**: whereas mCherry showed red fluorescence, the emission of the fusion protein is dominated by the yellowish Dronpa fluorescence.

Recently, the photoconvertible fluorescent protein Kaede was used as both donor and acceptor for analysis of homo-oligomerization and conformational alterations. Kaede can be irreversibly converted from a green form to a red form by irradiation at 405 nm. Both forms show high degree of spectral overlap and thus a high $R_0 = 5.74$ nm (Wolf et al., 2013a). The green form of Kaede was gradually converted to the red form and donor-, acceptor- as well as FRET-images (see 3-filter FRET) were obtained while conversion was in progress (Wolf et al., 2013a). Thus, the application of Kaede for the generation of transgenic plants enables multiple analyses in plants ranging from localization experiments with improved separation from autofluorescence, observation of protein dynamics and last but not least monitoring aggregation or conformational dynamics via FRET (Wolf et al., 2013a).

APPLICATION OF FRET IN LIVING CELLS

NANOSENSORS

FRET-based nanosensors are synthetic constructs that share high similarity in their structural design. Usually fluorescent proteins are applied as donor and acceptor that are linked by a sensing domain. Upon binding of the respective ligand the sensing domain undergoes a conformational alteration that can be read out as alteration of FRET-derived emission. Here, the dynamic range of a sensor was defined as range of FRET-efficiency over which the sensor operates (Lam et al., 2012). The function of the sensors might be sensitive to ionic strength and pH, development and application of sensors of low and high affinity for the ligand discriminates between unwanted environmental effects and true sensor response (Chaudhuri et al., 2011). The most prominent sensors are the Ca^{2+}-sensor of the cameleon-type (Miyawaki et al., 1997). Their sensing domain consists of calmodulin and the calmodulin-binding domain M13. Ca^{2+}-binding results in a conformational alteration that favors FRET (Nagai et al., 2004). Although cameleons cause calcium-buffering in the cell, the interference with endogenous calmodulin and M13-domains is negligible (Miyawaki et al., 1999). The frequently applied cameleon YC3.6 represents a low affinity variant and consists of ECFPΔC11 and cpVenus which are linked by calmodulin and the calmodulin-binding M13-domain. Recently, compartment specific variants of YC3.6 were constructed and successfully expressed in plant cells (Krebs et al., 2012). A comprehensive overview of available sensors and their ground-lying design, properties, and limitations has been summarized in Okumoto et al. (2012).

CONFORMATIONAL ALTERATIONS

During their life time proteins principally undergo multiple structural alterations beginning with initial folding, posttranslational modification in terms of regulation and finally degradation. Intramolecular FRET can be applied to visualize protein folding or degradation, if the tertiary structure of the protein positions its termini in a way allowing for FRET in the fully folded mature protein. Structural flexibility of the unfolded conformation or

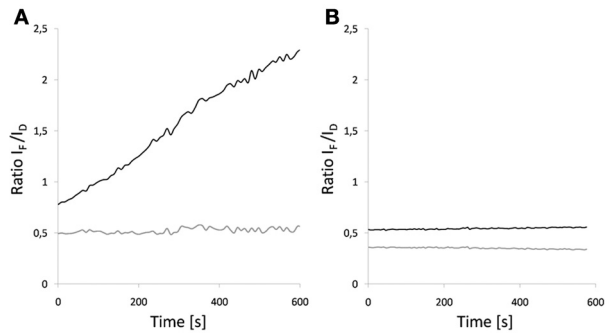

FIGURE 9 | Influence of photoswitching on FRET-ratio of a Dronpa-mCherry fusion. Ratio imaging was performed as a time series. Images were obtained every 6–8 s for 10 min. **(A)** Dronpa was inactivated during the time series. **(B)** Dronpa was reactivated at the time points by irradiation with a 405 nm diode laser. The black line shows data that has not been corrected for acceptor spectral bleed through while the gray curve shows the corrected data.

proteolytic processing due to degradation would result in loss of FRET as it has been reported for *Escherichia coli* proteins (Philipps et al., 2003).

Proteolytic activation of the membrane bound transcription factor ANAC089 was observed in *A. thaliana*. To this end, ECFP was fused to its C-terminus, labeling the membrane integral domain, and EYFP to its N-terminus, labelling the cytosolic domain. Under reducing conditions loss of FRET demonstrated the release of the cytosolic domain that subsequently translocated to the nucleus (Klein et al., 2012).

Alterations of the redox environment affect the conformation of many proteins, e.g., by post translational modifications such as disulfide formation. The structure of the typical 2-cysteine peroxiredoxin was found to be responsive to alterations in the plastidic redox state as two populations of FRET-efficiencies were observed that correspond to the reduced and the oxidized state, respectively, and the protein reacted reversibly to the supply of reduced dithiothreitol (DTT) or hydrogenperoxide. Similar to the previously described constructs, 2-Cys Prx was fused to ECFP at its N-terminus, while the transit peptide was maintained at the extreme N-terminus, and EYFP was fused to its C-terminus (Muthuramalingam et al., 2009). Conformational changes can also be observed in larger complexes such as the 800 kDa vacuolar H^+-ATPase. ATP-depletion by deoxyglucose-supply resulted in a movement of the cytosolic sector V_1 relative to the membrane integral sector V_0 and an altered arrangement of peripheral subunits within the cytosolic V_1-sector (Schnitzer et al., 2011).

PROTEIN-PROTEIN-INTERACTIONS

Complex formation is a common feature of many proteins for forming holo-enzymes, cooperative motifs or microenvironments for a successive sequence of reactions. On the other hand, protein-protein interactions are often involved in protein regulation, either in a short-term or in a long-term manner. FRET enables the visualization and quantitative analysis of protein-protein interactions between at least two proteins, if a protein is genetically fused to the donor and its putative interaction partner to the acceptor. By doing so, many proteins have been analyzed for interaction, just some recent examples are listed: (i) phosphorylation-dependent homo-dimerization has been detected for the response regulator ARR18 (Veerabagu et al., 2012), whereas (ii) GAGA-binding factors BBR/BPC dimerize constitutively in nucleus and nucleolus (Wanke et al., 2011). (iii) Competitive binding of flavonol synthase 1 to chalcone synthase and dihydroflavonol-4-reductase has been demonstrated in *A. thaliana* (Crosby et al., 2011). (iv) The mitochondrial serine acetyltransferase interacts reversibly with O-acetylserine (thiol) lyase to regulate the sulfur homeostasis in tobacco (Wirtz et al., 2012).

MEASURING FRET IN LIVING PLANT CELLS

METHODS FOR FRET-ANALYSIS—AN OVERVIEW

In the last decade several methods and experimental setups were applied for the analysis of FRET in living cells that rely on the property of RET to affect the excited state of donor and acceptor. Comparatively monitoring the donor's fluorescence or fluorescence lifetime in absence and presence of the acceptor, recording the acceptor's emission due to FRET and analysis of donor anisotropy were recruited for the analysis and quantification of FRET. In all cases the obtained FRET-efficiency is a function of energy transfer between donor and acceptor and of the donor fraction taking part in complex formation with acceptors (Xia and Liu, 2001). It turned out that different methods gave results that correlated quite well by tendency, but the exact values differed (Domingo et al., 2007).

ACCEPTOR BLEACHING

The donor transfers energy to the acceptor so that the donor emission is quenched. Upon intensive or prolonged irradiation of the acceptor the fluorophore becomes irreversible inactivated and emission of the donor is recovered. The advantage of this method is the reproducibility of obtained FRET-efficiencies independent of the experimental setup. In 2003, a comprehensive and reliable procedure was suggested for determining FRET by acceptor bleaching (**Figure 10**). The protocol involves positive controls such as donor-acceptor fusions, negative controls such as donor only and analysis of non-bleached regions of interest (Karpova et al., 2003). A fundamental prerequisite is the correction for donor bleaching that might occur in parallel with acceptor bleaching (Daelemans et al., 2004; van Munster et al., 2005). Therefore, the combination of less stable acceptor and a stable donor is favorable (Bhat, 2009). Problematic is the application of acceptor bleaching in living cells. Acceptor bleaching by a laser usually takes ∼1 min, therefore exclusively fixed cells or immobile proteins can be analyzed (Piston and Kremer, 2007). The attempt to overcome the long exposure by high light intensities is accompanied by high photo-toxicity (Xia and Liu, 2001). In particular highly pigmented cells suffer from high level of irradiation. Also, the abundance of fluorophores contributes to photo-toxicity (Dixit and Cyr, 2003). Another possibility that has been developed for conventional fluorescence microscopy relies on gradual acceptor bleaching and fit of the decay curve (van Munster et al., 2005). However, FRET is a mechanism of relaxation of excited molecules that represents a change in the electronic environment

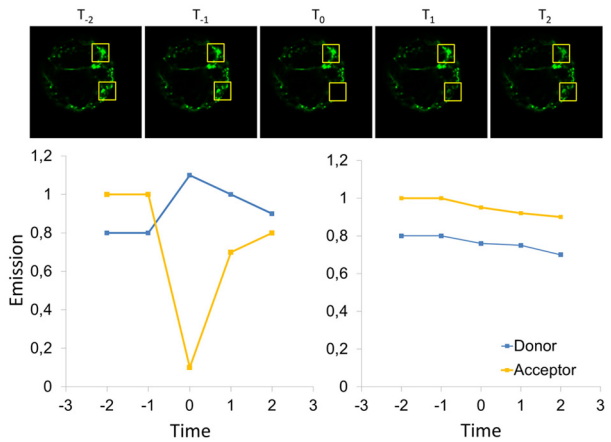

FIGURE 10 | Scheme for FRET-measurement by acceptor bleaching. For determination of the FRET-efficiency by acceptor bleaching, the acceptor is bleached in a defined area of the cell before time point T_0, and the emission of donor and acceptor is recorded subsequent bleaching. In addition, a region of interest is considered that has not been bleached (upper row) and allows for correction of fluctuations of the cellular fluorescence, e.g., it is expected that some bleaching occurs in the entire cells (right panel). In the bleached area, the acceptor emission decreases and the emission of the donor increases since FRET does not contribute to relaxation of the donor anymore. At later time points (T_1 and T_2) fluorescence recovery might be observable depending on the diffusional properties of the analyzed proteins, so that acceptor bleaching connects FRET to mobility measurements by fluorescence recovery after photobleaching (FRAP). Accordingly, highly mobile proteins prevent FRET-measurements by acceptor bleaching, if the recovery is faster than image acquisition subsequent bleaching.

of the donor. Living cells and fixed differ in the environment of the fluorophores, resulting in distinct behavior of fluorophores. Photostability of CFP decreased in fixed cells while Venus showed increased stability. On the other hand, the photostability of mTFP1 and Cerulean increased subsequent fixation whereas YFP was unaffected (Malkani and Schmid, 2011). This indicates that donors such as mTFP1 and Cerulean are suitable for acceptor bleaching in fixed cells in combination with Venus as acceptor. Additional drawbacks are the tendency of fluorescent proteins to undergo photoconversion that is hard to separate from photobleaching (Kremers and Goedhart, 2009), potential changes in cell morphology and focal position (Zal and Gascoigne, 2004) as well as the incomplete bleaching in particular in living cells (Zal and Gascoigne, 2004; Wallrabe and Periasamy, 2005), although corrections were provided for incomplete bleaching (Dinant et al., 2008). In detail, the commonly applied fluorescent protein FRET-couple CFP/YFP suffers from photoconversion of YFP to a cyan form especially in fixed cells putatively due to dehydration and reduced heat dissipation (Valentin et al., 2005; Raarup et al., 2009). On the other hand, photoactivation of CFP and Cerulean has been reported upon bleaching of YFP so that increase of cyan emission is not restricted to the absence of the acceptor but contains a photoactivation-related portion with hard to determine contribution (Malkani and Schmid, 2011). Nevertheless, acceptor bleaching has been reported to be more precise than FLIM-FRET in the case of multi-exponential decaying donors (Goedhart et al., 2007). Accordingly, discrepancies among results from acceptor bleaching and FRET-FLIM were reported for the FRET-pair CFP/YFP due to a four component exponential decay curve (Vermeer et al., 2004). Rarely, acceptor bleaching experiments were followed by fluorescence recovery after photobleaching (FRAP) so that diffusion of intact acceptors into the bleached area resulted in recovery of donor quenching and gave insights into the mobility of the acceptor (Vermeer et al., 2004).

DONOR BLEACHING

The detection of donor bleaching allows for qualitative analysis of FRET and relies on the increased stability of the donor in presence of an acceptor. Hence the bleaching constant increases and it takes longer to bleach the donor completely (Schmid et al., 2001; Daelemans et al., 2004; Szentesi et al., 2005). The time constant of donor bleaching is inversely related to the quantum yield of the donor (Jares-Erijman and Jovin, 2003). The donor decay curve is bimodal due to the fraction of donor that is associated with the acceptors and the fraction that emits directly (Clayton et al., 2005). Donor bleaching experiments require a labile donor and photo stable acceptor that is not necessarily fluorescent, and allow for the quantification of the donor fraction that transfers its energy to the acceptor (Jares-Erijman and Jovin, 2003; Clayton et al., 2005). According to acceptor bleaching, recording the complete bleaching curve might be critical in living cells since morphology and fluorophore distribution may vary at different time points, but data evaluation can be performed based on single steps of bleaching (Clayton et al., 2005).

FLUORESCENCE LIFETIME OF THE DONOR

The fluorescence lifetime of a fluorophore depends on the electronic nano environment so that fluorescence lifetime imaging microscopy (FLIM) is suitable for the analysis of local environmental conditions and can be used for the detection of interactions between proteins and lipids or DNA, respectively (Lakowicz, 2006). If an appropriate acceptor is close to a potential donor, the fluorescence lifetime of the fluorophore decreases due to FRET to the acceptor. Based on the difference in lifetime the FRET-efficiency can be calculated:

$$E = 1 - \frac{\tau_{da}}{\tau_d} \tag{5}$$

Whereas the nano environment is equal for all donor molecules and result in an identical electronic state and thus monoexponential decay, the presence of acceptors leads to a fraction of donors that undergo FRET and donors that do not. This results in a bi-exponential decay curve that has to be fitted for two species (**Figure 11**; Padilla-Parra et al., 2008). Thus, FLIM depends on the decay curve and its exponential behavior to separate interacting and non-interacting donors (Duncan, 2006). The fraction of donor showing FRET relies on the photostability of the acceptor (Padilla-Parra et al., 2009). Two approaches are routinely used for the measurement of the donor fluorescence lifetime: (i) Time domain FLIM depends on a pulsed laser source and time-gated detectors those allow for the observation of the time point of emission (Gerritsen et al., 2009). (ii) On the other hand frequency domain method relies on modulation of the frequency

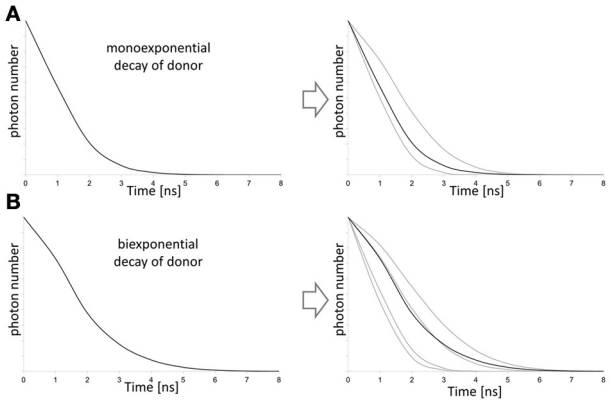

FIGURE 11 | Influence of the donor decay function on FLIM-FRET evaluation. On the left mixtures of decays (black curve) are shown that are separated in the lifetime decays (gray curves) of the contributing states of the putative donor on the right. For donor fluorophores that show a monoexponential fluorescence decay, a bi-exponential fit is required for data evaluation to consider donor fraction that transfer energy to the acceptor and the donor fraction that emits directly **(A)**. If the donor already shows a biexponential behavior fluorescence decay behavior, four contributing fractions of donor have to be considered for the fit of the lifetime decay **(B)**. The fit also provides information on the fraction of donor that undergoes energy transfer to the acceptor.

of the excitation light and modulated detection (Verveer and Hanley, 2009). Unfortunately, the comparison of lifetimes gained by different methods may be hampered by distinct fit-algorithms (Padilla-Parra et al., 2008). Time-correlated single photon counting (TCSPC) is commonly applied on confocal laser scanning microscopes. Here, photons are counted over a defined time interval in a pixelwise manner so that measurements of the fluorescence lifetime in the nucleus were reported to take 3 min. During this time morphological changes in the cell and dynamics in protein localization are likely (Piston and Kremer, 2007; Padilla-Parra et al., 2008). The limitation in speed can potentially be overcome by reduced image resolution and analyzing small regions of interest (Duncan, 2006). Time-gated detection and frequency-domain FLIM in combination with spinning disc microscopy enable high imaging speed (Domingo et al., 2007; Padilla-Parra et al., 2008). However, TCSPC has the advantage of comparatively low excitation light and hence less impact on the cells and less bleaching of the donor (Tramier et al., 2006).

Besides the requirement for specific experimental setups, the usage in the living cell is partially hampered by the requirement for fluorophores with monoexponential fluorescence decay, so that the commonly used FRET-pair ECFP/EYFP is less suitable for FLIM-FRET. CFP undergoes photoconversion leading to multiple lifetime species (**Figure 11**; Tramier et al., 2006). In particular appropriate fluorescent proteins are EGFP that is characterized by insensitivity to photobleaching, mTFP1 with high photostability, AmCyan that unfortunately aggregates, (Padilla-Parra et al., 2009), T-Sapphire (Bhat, 2009), Cerulean (Duncan, 2006), and mKO (Kremers and Goedhart, 2009), SCFP3A and SYFP2 (Kremers et al., 2006). On the other hand, blinking of the acceptor results in multiple lifetime states of the donor and affects data evaluation (Vogel et al., 2012). Also, long lived-acceptors may become saturated by FRET so that acceptors of short fluorescence lifetime are of advantage not exclusively for FLIM-FRET but also for FRET in general (Jares-Erijman and Jovin, 2003). For the donor, a long lifetime increases the probability of FRET (Vogel et al., 2012). Since GFP and YFP represent a highly efficient FRET-couple but with the difficulty of spectral separation (Dinant et al., 2008), non-fluorescent acceptors were designed based on YFP to improve the spectral overlap of donor emission and acceptor absorption without the need for spectral separation of the emission. This resulted in the non-fluorescent variants REACh, REACh2, and sREACh of EYFP (Ganesan et al., 2006; Murakoshi et al., 2008). These proteins serve as donors for EGFP. The residual fluorescence of these proteins is less than 3% of the YFP-fluorescence. However, if concentration is high e.g., in proteasomes, REACh's fluorescence might be detectable (Ganesan et al., 2006).

SPECTRAL IMAGING

Confocal laser scanning microscope allow for recording emission spectra, either by stepwise recording of the emission or by simultaneous detection with an array of detectors or sections of a CCD-chip (Rizzo et al., 2006; Megías et al., 2009). These measurements were termed fluorescence spectral imaging microscopy (FSPIM; Vermeer et al., 2004). The stepwise recording suffers from low acquisition speed as it takes several seconds to obtain a spectrum (Megías et al., 2009). For the detection of FRET at least one spectrum is recorded that covers the emission of both donor and acceptor upon excitation of the donor. A second spectrum covering the acceptor emission upon its excitation provides information on the acceptor abundance, since acceptor signal and FRET-signal are identical in shape and cannot be separated by linear unmixing (Chen et al., 2007). Spectral imaging was reported to be insensitive to autofluorescence and high degree of spectral overlap since the contribution of individual fluorophores can be separated (Megías et al., 2009). In the past, spectral imaging has been combined with acceptor bleaching resulting in a long-lasting procedure that appears not applicable for analysis with subcellular resolution or mobile cytosolic proteins (Kluge et al., 2004; Raicu et al., 2005).

DETECTING SENSITIZED EMISSION BY RATIO-IMAGING

Ratio imaging represents the simplest approach to observe FRET since only two channels are required. The emission of the donor I_D is recorded in the first channel, the FRET-derived emission of the acceptor I_F upon donor excitation in the second channel. FRET results in decreased donor emission and increased acceptor emission so that the ratio I_D/I_F decreases (Miyawaki and Tsien, 2000). Typically, the ratio R_{FRET} of the emissions in the resulting channels is calculated. Neither donor-crosstalk nor direct acceptor excitation are considered:

$$R_{\mathrm{FRET}} = \frac{I_F}{I_D} \tag{6}$$

Calculating the ratio gives consistent values with less variation, but normalization to donor and acceptor expression level is not included (Xia and Liu, 2001). Therefore, the

method depends strongly on the ratio of donor and acceptor and is exclusively suitable for monitoring intramolecular FRET so that donor and acceptor ratio is constant and known (Gordon et al., 1998; Domingo et al., 2007). Thus, it is frequently applied for FRET-analysis of FRET-sensors that consists of donor and acceptor linked by a sensing peptide.

3-FILTER FRET (SENSITIZED EMISSION)

The main drawback of ratio-imaging is the inability to correct for variations in donor to acceptor ratio and for ASBT that is caused by direct excitation at the donor excitation wavelength. Supplementing the ratio imaging by a third channel that detects the fluorescence emission of the acceptor I_A upon acceptor excitation enables for the quantification of the fraction of detected emission that is exclusively related to FRET. The direct excitation of acceptor or ASBT is linearly related to the emission intensity I_A detected in the acceptor channel and linearity is described by the proportionality factor α. The relative amount of donor spectral bleed through (DBST) depends on detector settings and the detection range and is given by the correction factor β (van Rheenen et al., 2004). Both correction factors can be determined experimentally applying cells that express solely donor (Equation 8 for determination of β, **Figure 12**) or acceptor (Equation 7 for determination of α, **Figure 12**). Hoppe et al. (2002) estimated α and β with recombinant purified protein besides the determination in living cells. The obtained values were reported to be in good agreement with data derived from cells expressing the fluorescent proteins.

$$\alpha = \frac{I_F}{I_A} \tag{7}$$

$$\beta = \frac{I_F}{I_D} \tag{8}$$

Finally, the FRET-derived emission intensity I_{corr} is given by Equation 9:

$$I_{\text{corr}} = I_F - \alpha I_A - \beta I_D \tag{9}$$

Several calculations can be found in the literature that are linked to the FRET-efficiency but mostly give values that are linear related to and correlate well with the FRET-efficiency but do not match it exactly. In general, acceptor-related and donor-related equations can be distinguished for calculating apparent FRET-efficiencies, depending on if acceptor emission or donor emission contributes to the nominator (van Rheenen et al., 2004). Most acceptor-based equations are highly sensitive to the detection of acceptor's emission and its capability to be excited at donor's excitation wavelength. The simplest equation relies on relating the FRET-signal to the acceptor emission and is robust to a lack of ABST (Domingo et al., 2007).

$$E = \frac{I_F - \beta I_D - \alpha I_A}{I_A} \tag{10}$$

This equation might be applicable for conventional fluorescence microscopy, but critical with a confocal laser scanning microscope that offers the possibility to adjust excitation intensities independently. Alternatively, the acceptor emission in presence of donor can be related to acceptor emission in absence of the donor so that differences in excitation intensities are considered by α (Wolf et al., 2013a):

$$E = \left(\frac{I_F - \beta I_D}{\alpha I_A} - 1 \right) \tag{11}$$

Here, significant ASBT of acceptor is strictly required and the correction factor α depends on the laser intensity ratio of donor and acceptor excitation (van Rheenen et al., 2004). If ASBT is absent, the nominator becomes 0 and thus undefined.

Donor-based quantifications seem to be more robust to variations of the correction factors. In a simple way, apparent FRET-efficiency can be expressed as FRET-derived emission intensity I_{corr} related to the sum of I_{corr} and I_D. This relies on the assumption that the donor is quenched if FRET occurs, and the sum of I_{corr} and I_D is linearly related to the unquenched donor emission (Seidel et al., 2005; Schnitzer et al., 2011).

$$E = \frac{I_F - \beta I_D - \alpha I_A}{(I_F - \beta I_D - \alpha I_A) + I_D} \tag{12}$$

In another approach, normalization to both donor and acceptor was applied to reduce the variation of filter FRET-measurements.

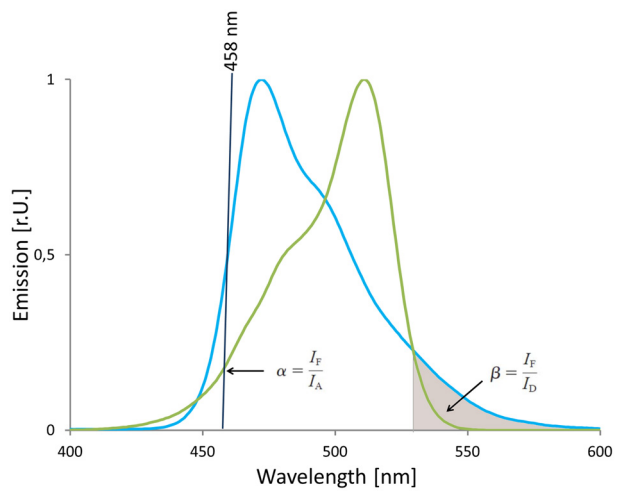

FIGURE 12 | Estimation of correction factors for donor cross talk and acceptor's direct excitation. The absorption spectrum of mVenus and the emission spectrum of mTurquoise2 are shown. The 458 nm laser line (black line) that is used for excitation of mTurquoise2 is in the wavelength range that is covered by the absorption spectrum of mVenus, too. On the other hand, the emission spectrum of mTurquoise2 overlaps with the emission spectrum of mVenus and is also detected in the FRET-channel as indicated by the gray area below the mTurquoise2 emission spectrum. Thus, the factors α and β correct for acceptor's direct excitation at donor's excitation wave length and donor crosstalk into the FRET-channel. The correction factors α and β are calculated based on data sets from cells that express solely mVenus or mTurquoise2, respectively.

This was achieved by calculating the square root of the product of donor and acceptor emission and normalizing I_{corr} to the obtained value (Xia and Liu, 2001):

$$E = \frac{I_F - \beta I_D - \alpha I_A}{\sqrt{I_D I_A}} \quad (13)$$

However, all these equations result in apparent FRET-efficiencies at least qualitatively proving a protein-protein interaction, since its relationship to the true FRET-efficiency is not known due to the lack of calibration of the experimental setup and correction for the cellular environment. Expression of freely diffusing donors and acceptors has been suggested as negative control for occasionally occurring FRET between fluorescent protein donors and acceptors, in particular under conditions of overexpression (Xia and Liu, 2001; Erickson et al., 2003). The obtained apparent FRET-efficiency represents a threshold for accepting the hypothesis of interaction that can be verified by statistical analysis. Overexpression is known to cause spurious FRET that is enhanced by aggregating fluorescent proteins (Erickson et al., 2003). Thus, the avoidance of highly expressing cells further reduces the probability of unspecific interaction (Xia and Liu, 2001). Nevertheless, the apparent FRET-efficiencies are suitable for monitoring conformational dynamics inside complexes and *de novo* complex formation or complex decomposition as long as the structural alterations result in a significant shift of fluorophore's distance or relative orientation.

CALIBRATION AND QUANTIFICATION PROCEDURES FOR FILTER FRET

There are several reasons for calibrating FRET-data. The obtained data vary in the FRET-efficiency due to the application of FRET-pairs with distinct R_0 and thus, different dynamical range, heterogeneity of experimental setups and experimental procedures and variety of methods for data evaluation. Comparing data obtained with different FRET-pairs is quite simply enabled, if FRET-efficiencies are expressed as their corresponding distances so that R_0 is considered and used to normalize FRET-measurements performed with distinct FRET-pairs, even though the calculation of distances is principally incorrect due to lack of information on the chromophores' orientation:

$$R = R_0 \sqrt[6]{\frac{1}{E} - 1} \quad (14)$$

The detection of donor and acceptor signals allows for crosstalk and direct excitation correction of both fluorophores and enables relative FRET-measurements to draw conclusions on structural alterations, but the obtained values are widely irreproducible with other experimental setups. The emission depends strongly on excitation intensity, detector sensitivity, and donor's and acceptor's concentration (Jalink and van Rheenen, 2009). Therefore, several corrections were suggested to consider different quantum yields and absorption coefficients of donor and acceptor, spectral transmission of required filters, and fluctuations in excitation intensities (Gordon et al., 1998; Hoppe et al., 2002; van Munster et al., 2005; Beemiller et al., 2006; Chen et al., 2006). The formulas have to be robust even if the stoichiometry and subcellular microenvironment of fluorescent proteins is unknown (Jares-Erijman and Jovin, 2003). Most of the corrections involved standardization of FRET by e.g., expression of reference constructs of known FRET-efficiency and fluorophore stoichiometry (Hoppe et al., 2002; Zal and Gascoigne, 2004; Beemiller et al., 2006; Chen et al., 2006) or gradual acceptor bleaching (van Munster et al., 2005). Typically, the reference constructs consists of donor and acceptor linked by a short amino acid sequence ranging from 5 to 32 amino acids. A possible arrangement of such a reference construct in comparison to the native GFP-dimer is given in **Figure 13**. In particular for the construction of cyan and YFP reference constructs linkers of 5, 17, and 32 amino acids were frequently applied (Koushik et al., 2006; Chen et al., 2007; Megías et al., 2009). Based on a length of 2.8 Å per amino acid this corresponds to linkers of 1.4–8.96 nm. Since the linkers do not possess a rigid secondary structure, the flexibility increases with increasing linker length so that the relative orientation of the fluorophores becomes highly variable and is more and more influencing and limiting FRET. This increasing complexity has to be considered if calibration is based on reference constructs of high linker length. Furthermore, fluorescent proteins are characterized by heterogeneity such as wide differences in their maturation. Whereas mCherry has a maturation-half time of 15 min its wildtype DsRed needs more than 10 h to maturate (Shaner et al., 2004) and the temperature optima of maturation differs e.g., between GFP and DsRed (Mizuno et al., 2001). Last but not least, different photo-stabilities of donor and acceptor, sensitivity to the environment, or combination of short lived donors with long lived acceptors have to affect intramolecular FRET within reference constructs (Padilla-Parra et al., 2009; Vogel

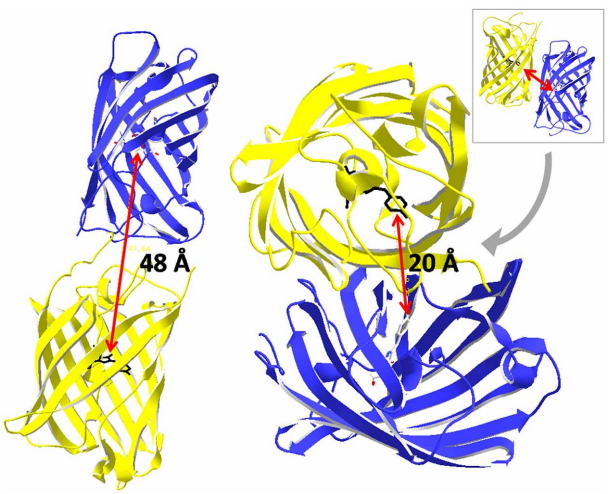

FIGURE 13 | Approximation of nearest neighbor distances between fluorescent proteins. The fluorophore is located on the central α-helix inside the β-can structure. Thus, the fluorophores of two fluorescent proteins are separated by at least 30 Å. Based on the crystal structure of a GFP dimer (pdb 1 GFL, Yang et al., 1996) the distance is 20 Å. The distance was 48 Åin a head to tail arrangement as it is most probably the case for fusion proteins that are frequently applied for FRET standardization.

et al., 2012). All these are reasonable explanations for variations in the spectroscopic behavior of donor-acceptor-fusions that result in e.g., an apparent deviation from the expected amount of donor undergoing FRET (Padilla-Parra et al., 2009). For obtaining the true FRET-efficiency of reference constructs by FLIM, Koushik et al. (2006) suggested fusing the non-fluorescent β-can protein Amber to the donor for recording its lifetime in the absence of the acceptor, since fusion proteins showed a distinct fluorescence lifetime than donor only. Comparing reference constructs for the FRET-pairs ECFP/EYFP and mTurquoise2/mVenus demonstrated the influence of higher quantum yield on the R_0 and thus on the FRET-efficiency (**Figure 14**). The reduction in donor emission is significantly higher for mTurquoise2 in the presence of mVenus ($E = 0.62$, **Figure 14A**) than for ECFP in the presence of EYFP ($E = 0.46$, **Figure 14B**). If tandem fluorophores such as tdTomato are applied as acceptors, the more complex situation for the fluorophores' spatial arrangement and energy transfer pathways has to be considered, although the presence of multiple acceptors for a single donor represent a way of improving resonance energy transfer, since the operational R_0 increases with the number of acceptors (Jares-Erijman and Jovin, 2003). The presence of two acceptors has also an effect on the FRET-efficiency: if Cerulean was fused to two copies of Venus, the FRET-efficiency increased from 0.45 to 0.6 (Chen et al., 2007; Koushik et al., 2009).

Most calculations and calibrations rely on the linear relationship of donor quenching and sensitized acceptor emission (Gordon et al., 1998; Hoppe et al., 2002; Zal and Gascoigne, 2004; Chen et al., 2006). The required proportionality factor has been termed G (or ξ) and depends in technical terms on the quantum yields Φ of donor and acceptor, the transmission $\text{Filter}_{\text{trans}}$ of the filter sets for donor- and acceptor-detection and the coverage $\text{Filter}_{\text{fract trans}}$ of the emission spectra by the filter transmission that is given by the integral of the product of the fluorescence emission spectrum and the transmission spectrum related to the integral of the fluorescence emission spectrum (Gordon et al., 1998):

$$G = \frac{\phi_A}{\phi_D} \frac{\text{AccFilter}_{\text{trans}}}{\text{DonFilter}_{\text{trans}}} \frac{\text{FRETFilter}_{\text{fracttrans}}}{\text{DonFilter}_{\text{fracttrans}}} \tag{15}$$

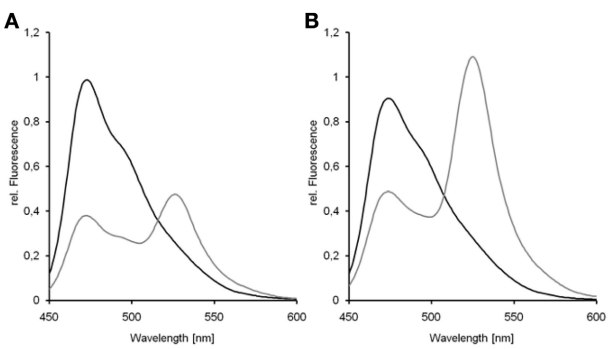

FIGURE 14 | Donor-quenching of ECFP and mTurquoise2 in the presence of an acceptor. Emission spectra of donor only (black) and donor-acceptor fusion (gray) were recorded with a fluorescence spectrometer. Donor quenching of mTurquoise2 was higher in the presence of mVenus **(A)** than the quenching of ECFP in the presence of EYFP **(B)**.

For confocal laser scanning microscopy, an equivalent factor was suggested that is defined by the ratio of the quantum yields of acceptor and donor as well as the ratio of the quantum yields of the photomultipliers at the acceptor's and donor's wavelength (Sun and Periasamy, 2010). Assuming the proper calibration of the detectors with respect to their wavelength dependency at least in a narrow range, the calculation of the coefficient is limited to the ratio of the quantum yields of acceptor and donor. By doing so, the coefficient for e.g., EYFP and ECFP would be 0.66. Finally, the FRET-efficiency is given by Equation 16:

$$E = \frac{\text{coef}\,(I_F - \alpha I_A - \beta I_D)}{\text{coef}\,(I_F - \alpha I_A - \beta I_D) + I_D} \tag{16}$$

However, the factor G can be experimentally determined either by photobleaching of the acceptor or by applying reference constructs. FRET-correction by photobleaching involves two measurements of sensitized emission. The first is performed before acceptor bleaching whereas the second set of images is obtained after acceptor bleaching. The difference of the I_{corr}-values is divided by the difference of the emission in the FRET-channel after bleaching I_F^{post} and the emission in the donor channel before bleaching I_D (Zal and Gascoigne, 2004):

$$G = \frac{(I_F - \alpha I_A - \beta I_D) - \left(I_F^{\text{post}} - \alpha I_A^{\text{post}} - \beta I_D^{\text{post}}\right)}{I_F^{\text{post}} - I_D} \tag{17}$$

Then, the FRET-efficiency is calculated by relating I_{corr} to the FRET-emission I_F and the residual portion of donor fluorescence that has not been transferred to the acceptor by FRET:

$$E = \frac{I_F - \beta I_D - \alpha I_A}{I_F - \alpha I_A + (G - \beta) I_D} \tag{18}$$

Alternatively, G can be calculated based on two reference constructs of different linker length. Chen et al. (2006) applied Cerulean-Venus fusions with a linker of five (Index 1, Equation 19) and 236 amino acids (index 2, Equation 19), respectively. The acceptor emission I_A that is not affected by FRET was used to normalize I_D and I_{corr} for the calculation of G (Equation 19). Finally, the FRET-efficiency is calculated by Equation 18.

$$G = \frac{\frac{I_{F1} - \alpha I_{A1} - \beta I_{D1}}{I_{A1}} - \frac{I_{F2} - \alpha I_{A2} - \beta I_{D2}}{I_{A2}}}{\frac{I_{D2}}{I_{A2}} - \frac{I_{D1}}{I_{A1}}} \tag{19}$$

In the other case, the FRET-efficiency is given by the ratio of the donor emission I_D in the presence of the acceptor and the emission of the donor in the absence of the acceptor (Hoppe et al., 2002):

$$E = 1 - \frac{I_D}{(I_F - \beta I_D - \alpha I_A)\,\xi + I_D} \tag{20}$$

Based on a reference construct, ξ is determined by back calculation. In this case the determinant E is known as well as the correction factors α and β so that ξ is the only remaining unknown factor, if FRET-measurements are performed with the

reference construct expressed in plant cells to obtain I_D, I_F, and I_A. Thus, ξ is given by Equation 21:

$$\xi = \frac{I_D E}{(1-E)\,(I_F - \alpha I_A - \beta I_D)} \tag{21}$$

Since G is used for calculating the sensitized emission based on the donor fluorescence and ξ serves for the calculation of quenched donor fluorescence based on sensitized emission, their relationship is given by:

$$G = \xi^{-1} \tag{22}$$

Hoppe et al. (2002) further suggested a comprehensive approach to calculate the donor and acceptor fractions in the complex and the ratio of both fluorophores to overcome the imperfection of two functions contributing to the apparent FRET-efficiency that are the rate of energy transfer and the fraction of complex bound donor. It should me mentioned that the initially published equations for the determination of R_M and E_D were corrected later (Beemiller et al., 2006). Basically, the ratio of donor and acceptor can be estimated. I_D is linearly related to the donor concentration, if the loss of energy due to FRET is considered. Applying ξ allows for the calculation of the acceptor to donor ratio R_M:

$$R_M = \left(\frac{\xi}{\gamma}\right) \frac{\alpha I_A}{(I_F - \alpha I_A - \beta I_D)\,\xi + I_D} \tag{23}$$

The ratio of ξ and γ can be replaced by the factor k that is estimated based on a dataset obtained with a reference construct of known stoichiometry and calculated by Equation 24 (Chen et al., 2006).

$$k = \frac{\gamma}{\xi} = \frac{I_D + \frac{(I_F - \alpha I_A - \beta I_D)}{G}}{I_A} \tag{24}$$

Once the FRET-efficiency E_c of a given complex is known, the fraction of donor in complex is given by Equation 25 (modified from Hoppe et al., 2002). However, the prerequisite for the true FRET-efficiency E_c of the analyzed protein pair limits the application of the equation widely.

$$f_D = \left(1 - \frac{I_D}{(I_F - \alpha I_A - \beta I_D)\,\xi + I_D}\right) E_c^{-1} \tag{25}$$

The sensitized emission and FRET-efficiency are linearly related, if the sensitized emission is expressed as ratio of acceptor emission in the presence and absence of the donor. In this case, the proportionality factor is given by the ratio of the absorption coefficients of acceptor and donor at donor's excitation wavelength (Gadella et al., 1999).

$$E = \frac{\varepsilon_A}{\varepsilon_D}\left(\frac{I_F - \beta I_D}{\alpha I_A} - 1\right) = \gamma\left(\frac{I_F - \beta I_D}{\alpha I_A} - 1\right) \tag{26}$$

This ratio is principally known and relates the energy absorbed by the donor and transferred to the acceptor to the energy that is directly absorbed by the acceptor (Hoppe et al., 2002). For mTurquoise2 and Venus the absorption coefficients at 458 nm are 28,400 Mol^{-1} cm^{-1} and 16,300 Mol^{-1} cm^{-1}, so that the ratio is 0.574. For ECFP and EYFP the absorption coefficients at 458 nm are 30,700 and 14,700 Mol^{-1} cm^{-1}, respectively, resulting in the ratio 0.479 that is close to an experimentally determined γ of 0.47. However, the theoretical ratio can differ from the real situation in the cell due to the cellular and subcellular environment and its influence on the absorption.

The advantage of this method is its low dependency on differences of filter sets since mainly the emission of the acceptor is considered. Problematic is the requirement for direct excitation of the acceptor as described in the context of Equation 11 that relies on Equation 26.

If the ratio of the absorption coefficients is expressed by the single factor γ, this can be estimated based on a reference construct similar to the calculation of ξ and γ is given by Equation 27:

$$\gamma = \frac{\varepsilon_A}{\varepsilon_D} = \frac{E}{\left(\frac{I_F - \beta I_D}{\alpha I_A}\right) - 1} \tag{27}$$

The recently published data set on the dimer formation of the human transcription factors p50 and RelA in plant cells (Wolf et al., 2013b) was used for calculation of FRET-efficiencies applying the Equation 10 (Domingo et al., 2007), Equation 12 (Seidel et al., 2005), Equation 13 (Xia and Liu, 2001), Equation 18 (Zal and Gascoigne, 2004), Equation 20 (Hoppe et al., 2002), and Equation 16 (Sun and Periasamy, 2010). The non-calibrated apparent FRET-efficiencies were higher than the calibrated. The Equations 10 and 13 resulted in FRET-efficiencies of 0.33, Equation 12 in a lower apparent FRET-efficiency of 0.25. The calibrated FRET-efficiencies were in the same range and statistical analysis did not reveal significant differences among the results. The Equations 18 and 20 gave an identical FRET-efficiency of 0.15, whereas the calculation by Equation 16 gave 0.12 (**Figure 15**). The values for G and ξ were calculated applying a reference construct and were found to be 1.89 and 0.53, respectively. The variability of non-calibrated values and the congruency of the calibrated values indicate the reliability and applicability of the calibrated equations. The acceptor based equation 26 failed due to a low α-value of 0.084 that lead to a FRET-efficiency >1.

For completeness, instead of calculation with the average emission intensities of ROIs or line profiles Heinze et al. (2013) recruited the images directly for quantification and performed pixel-wise calculation of the intensity values of whole images: First of all they divided the FRET image by the donor image and multiplied the result with 100. Next, the obtained image was divided by the donor image and multiplied with 100 again. Finally, the resulting image is divided by the acceptor image, multiplied with 30 and the result is given as intensity-encoded FRET-image. The advantage of this method is the visualization of FRET with respect to the subcellular localization of the analyzed interaction.

Quantification tools of the control software for confocal laser scanning microscopes usually provide text files. The data is either given by statistics of pixel values in a defined region or as an intensity profile along a line through the image. For analysis in plant cell, the usage of enlarged regions of interest is hampered

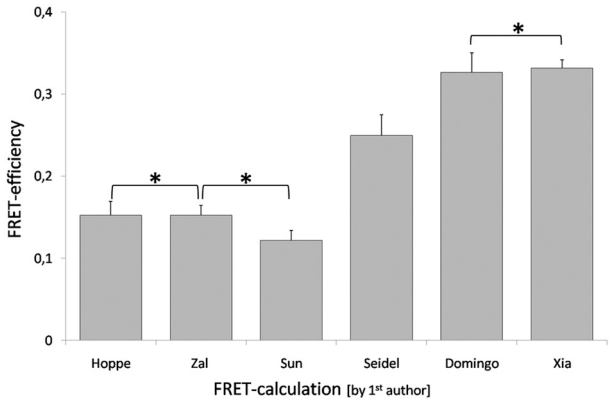

FIGURE 15 | Differences in calculation of FRET-efficiency. The FRET-efficiency was calculated applying data recently published for the interaction between p50 and RelA in plant cells (Wolf et al., 2013b). The FRET-efficiency was calculated by six different methods, the labels correspond to the first authors of the publications that suggested the corresponding equations. An asterisk marks FRET-efficiencies that were not significantly different. The data was analyzed by student's *t*-test. The dataset comprised 22 measurements and mean ± SE are given.

by the central vacuole occupying at least 80 percent of the cellular volume in mature cells. In this case line intensity profiles are of advantage, if spatial correlation of the peaks in the individual channels is considered. To this end a PERL-script has been developed that calculates the FRET-efficiency based on four data sets: (i) dataset from cells expressing the donor to obtain β, (ii) dataset from cells expressing the acceptor to obtain α, (iii) dataset from cells expressing the reference constructs that is required to calculate γ, ξ or G, and finally (iv) the dataset that comprises the measurement of interest. For each dataset a folder has to be created that is named "donor," "acceptor," "reference," or "measurement," respectively. Each folder contains line profiles characterized by only one maximum. The identified maxima in the individual channels are checked for spatial correlation and background noise caused by increased "offset"-values is considered by the intensity of the first data point of each line. For the determination of the correction factors the median was applied instead of the arithmetic mean to rule out overrepresentation of outliers. The output of the PERL-script comprises the median of FRET-efficiencies that are calculated by applying equations 10, 12, 13, 18, 20, and 26. The R_M-value is calculated by Equation 23.

CONCLUSIONS AND FUTURE PERSPECTIVES

Fluorescent proteins allowed for the analysis of protein interactions in living plant cells, either by bimolecular fluorescence complementation or by FRET (Bhat et al., 2006). In the recent years, much effort has been invested in the improvement of these methods and their applicability was vastly improved, although multiple protocols and equations were published in particular for FRET that turned the situation confusing for researchers that want to start with FRET-experiments. Measuring FRET by sensitized emission has the advantage of minimal requirements for the equipment and the possibility to monitor fast intracellular processes. The drawback is its strong dependency on the characteristics of filter sets and detectors. Depending on the aim of the study, it might be sufficient to calculate apparent FRET-efficiency e.g., for documentation of conformational alterations, whereas the comparison of datasets obtained with distinct instruments demands calibration. The obtained FRET-efficiencies further depend on the photostability and spectral properties of the fluorescent protein FRET-pair, so that discussing distances instead of FRET-efficiencies compensates for different FRET-pairs and their characteristic R_0-value.

The complex-formation by proteins is not limited to the interaction of two proteins, but often involves multiple proteins. One current task is the establishment of methods that allow for real time *in vivo* analysis of such complexes. The combination of BiFC and FRET is promising and has been successfully applied to detect ternary complexes of SNAREs by BiFC and FRET between cerulean as donor and folded split-YFP as acceptor (Kwaaitaal et al., 2010). Since BiFC is not limited to proteins of the avGFP-family but also has been demonstrated for mLumin, mRFP1, and mCherry (Jach et al., 2006; Fan et al., 2007; Chu et al., 2009), the combination of BiFC and FRET might be able for both donor and acceptor, if the ground lying requirement is matched that members of the avGFP family are not capable to complement with fragments of other fluorescent proteins, even if the product is not fluorescent. Otherwise, the results would become difficult to interpret.

On the other hand, an advantage of FRET is the ability to supplement a given FRET-pair by additional fluorophores toward a stepwise cascade of energy transfer between three and more fluorophores. This allows for the detection of complex formation by more than two proteins. FRET-cascades are also suitable for long range interactions (Haustein et al., 2003). FRET between three fluorescent proteins has been described before and was denominated 2-step FRET or 3-chromophore FRET (Watrob et al., 2003; Galperin et al., 2004; He et al., 2004, 2005; Seidel et al., 2010; Sun et al., 2010). For such 2-step FRET-measurements in living cells the commonly used FRET-pair CFP-YFP was supplemented by the red fluorescent proteins HcRed (He et al., 2004), mRFP1 (Galperin et al., 2004; He et al., 2005) or mCherry (Seidel et al., 2010). So the energy is ideally transferred from the donor (CFP) via the mediator (YFP) to the acceptor (red fluorescent protein), both steps were analyzed by sensitized emission. However, the situation becomes complex since three distinct FRET-pairs have to be considered, resulting e.g., in direct energy transfer between donor and acceptor bypassing the mediator (Seidel et al., 2010). This can be overcome by control measurements e.g., with REACh as a "mediator" that is no longer capable to transfer energy to the acceptor (Seidel et al., 2010) or by photoswitchable mediators that allow the direct estimation of direct energy transfer between donor and acceptor, although the absence of the mediator's absorption is expected to enhance the probability of FRET between donor and acceptor. Theoretically, FRET measurements by sensitized emission have the potential to be supplied by further fluorescent proteins like UV-fluorescent proteins

such as Sirius (Tomosugi et al., 2009) as donors and infrared-fluorescent proteins as acceptors resulting in a cascade of 3–4 steps of FRET.

Recently Sun et al. (2010) suggested a FLIM-FRET approach for the detection of ternary complexes. They used the fluorophores mVenus and tdTomato as spectral different acceptors for the donor mTFP that showed the lowest fluorescence lifetime in the presence of both acceptors hence reflecting both routes of relaxation. Although this approach is less suitable for the analysis of an elongated linear arrangement of fluorophores that exceed the dimensional limitation of 1.5 R_0 it is suitable for the analysis of compact ternary protein complexes. However, for enlarged complexes, the second step of energy transfer decreases the fluorescent lifetime of the mediator and might prevent its saturation by the donor. This effect has to be reflected by some decrease in the fluorescent lifetime of the donor as well. Since energy that is transferred from mVenus to tdTomato is hard to assign to the decrease in mTFP fluorescence lifetime, Sun et al. (2010) additionally applied spectral imaging and linearly unmixing for the approximation of 2-step FRET. Nevertheless, for the proof, if complexes are formed by more than two proteins, the recruitment of identical fluorescent proteins as additional acceptors should be sufficient for an analysis by FLIM as indicated by donor's lifetimes of the reference constructs consisting of two copies of Venus and one Cerulean (Chen et al., 2007; Koushik et al., 2009).

MATERIALS AND METHODS

ISOLATION AND TRANSFECTION OF PROTOPLASTS

A. thaliana (Columbia) was grown in soil-culture in a growth chamber with 12 h light (240 µmol quanta m^{-2} s^{-1}, 19°C) and 12 h dark (18°C) with 60% relative humidity. For protoplast isolation *A. thaliana* leaves were harvested from soil grown plants at the age of about 4 weeks. The isolation and the polyethylene glycol mediated transfection of *A. thaliana* protoplasts were performed as described before (Seidel et al., 2004).

HETEROLOGOUS EXPRESSION OF FLUORESCENT PROTEINS

ECFP, mTurquoise2, EYFP, mVenus, mCherry, Dronpa as well as the fusion proteins ECFP-EYFP, mTurquoise2-mVenus, Dronpa-mCherry and EYFP-mCherry were heterologously expressed in *E. coli* strain BL21 pLys (DE3). The cultures were grown to $OD_{600} = 0.6$ and expression was induced by supplementing the medium with 1 mM IPTG. Expression was carried out at room temperature overnight. Cells were lysed by lysozyme, treated with supersonic and cell debris were removed by centrifugation at 10,000 g for 30 min. The oligohistidine-tagged proteins were purified by Ni-NTA-affinity chromatography and finally dialyzed against 40 mM phosphate buffer pH 7.

SPECTRAL ANALYSIS OF RECOMBINANT FLUORESCENT PROTEINS

FRET-efficiencies were determined via the reduced fluorescence emission of the donor. The fluorescence and absorption spectra were taken at room temperature (23°C) with a Kontron SFM25 fluorescence spectrometer and a Shimadzu UV-2401 UV/VIS spectrometer, respectively. All measurements were performed in 40 mM potassium phosphate at pH 7. For comparison of CFPs and cyan-yellow fluorescent fusion proteins the molar quantities of the CFP were adjusted equally by the absorption at 400 nm.

CALCULATION OF R_0

The Förster radii were calculated for the FRET-pair Dronpa/mCherry based on the recorded absorption and emission spectra. Calculation was performed as reported before (Patterson et al., 2000; Akrap et al., 2010).

FRET MEASUREMENTS

For FRET measurements, a Leica TCS SP2 confocal system with 40-fold magnification (water immersion objective HCX APO L 40×/0.8W UVI, NA = 0.8) was used. The scan speed was 400 Hz, the image resolution 1024 × 1024 pixels and 12 bit scanning mode was chosen to improve the signal to noise ratio. The transfer efficiency between the fluorophores ECFP, EYFP, mTurquoise2, mVenus, Dronpa, and mCherry was measured within mesophyll protoplasts by sensitized acceptor emission. Emission intensities were recorded sequentially (line by line) in three channels involving photomultipliers 2 and 3 and the excitation wavelengths 458 and 514 nm for cyan and YFP couples as described before (Seidel et al., 2005). PMT 2 detected the ECFP emission in the range of 470–510 nm, PMT 3 the EYFP emission in the range of 530–600 nm. For FRET-couples with mCherry the 488 nm laser line was used for excitation of Dronpa and the 543 nm laser line for excitation of mCherry. Dronpa was detected in the range of 500–530 nm, mCherry between 570 and 620 nm.

ACKNOWLEDGMENTS

This work was funded by the Deutsche Forschungsgemeinschaft (DFG), SFB613 TP A5, and Bielefeld University.

REFERENCES

Agati, G. (1998). Response of the *in vivo* chlorophyll fluorescence spectrum to environmental factors and laser excitation wavelength. *Pure Appl. Opt.* 7, 797–807. doi: 10.1088/0963-9659/7/4/016

Ai, H. W., Henderson, J. N., Remington, S. J., and Campbell, R. E. (2006). Directed evolution of a monomeric, bright and photostable version of Clavularia cyan fluorescent protein: structural characterization and applications in fluorescence imaging. *Biochem. J.* 400, 531–540. doi: 10.1042/BJ20060874

Akrap, N., Seidel, T., and Barisas, B. G. (2010). Förster distances for fluorescent resonance energy transfer between mCherry and other visible fluorescent proteins. *Anal. Biochem.* 402, 105–106. doi: 10.1016/j.ab.2010.03.026

Albinsson, B., Li, S. M., Lundquist, K., and Stomberg, R. (1999). The origin of lignin fluorescence. *J. Mol. Struc.* 508, 19–27. doi: 10.1016/S0022-2860(98)00913-2

Baird, G. S., Zacharias, D. A., and Tsien, R. Y. (2000). Biochemistry, mutagenesis, and oligomerization of DsRed, a red fluorescent protein from coral. *Proc. Natl. Acad. Sci. U.S.A.* 97, 11984–11989. doi: 10.1073/pnas.97.22.11984

Bayle, V., Nussaume, L., and Bhat, R. A. (2008). Combination of novel green fluorescent protein mutant TSapphire and DsRed

variant mOrange to set up a versatile in planta FRET-FLIM Assay. *Plant Physiol.* 148, 51–60. doi: 10.1104/pp.108.117358

Beemiller, P., Hoppe, A. D., and Swanson, J. A. (2006). A phos phatidylinositol-3-kinase-dependent signal transition regulates ARF1 and ARF6 during FCγ receptor-mediated phagocytosis. *PLoS Biol.* 4:e162. doi: 10.1371/journal.pbio.0040162

Bhat, R. A. (2009). FRET and FLIM applications in plants. *Lab. Tech. Biochem. Mol. Biol.* 33, 413–446. doi: 10.1016/S0075-7535(08)00010-7

Bhat, R. A., Lahaye, T., and Panstruga, R. (2006). The visible touch: in planta visualization of protein-protein interactions by fluorophore-based methods. *Plant Methods* 2:12. doi: 10.1186/1746-4811-2-12

Blum, C., Mexiner, A. J., and Subramaniam, V. (2011). Dark proteins disturb multichromophore coupling in tetratmeric fluorescent proteins. *J. Biophotonics* 4, 114–121. doi: 10.1002/jbio.201000075

Campbell, R. E., Tour, O., Palmer, A. E., Steinbach, P. A., Baird, G. S., Zacharias, D. A., et al. (2002). A monomeric red fluorescent protein. *Proc. Natl. Acad. Sci. U.S.A.* 99, 7877–7882. doi: 10.1073/pnas.082243699

Chaudhuri, B., Hörmann, F., and Frommer, W. B. (2011). Dynamic imaging of glucose flux impedance using FRET-sensors in wild-type Arabidopsis plants. *J. Exp. Bot.* 62, 2411–2417. doi: 10.1093/jxb/erq444

Chen, Y. E., Mauldin, J. P., Day, R. N., and Periasamy, A. (2007). Characterization of spectral FRET imaging microscopy for monitoring nuclear protein interactions. *J. Microsc.* 228, 139–152. doi: 10.1111/j.1365-2818.2007.01838.x

Chen, H., Puhl, H. L., Koushik, S. V., Vogel, S. S., and Ikeda, S. R. (2006). Measurement of FRET efficiency and ratio of donor to acceptor concentration in living cells. *Biophys. J.* 91, L39–L41. doi: 10.1529/biophysj.106.088773

Cheung, H. C. (1991). "Resonance energy transfer," in *Topics in Fluorescence Spectroscopy,* Vol. 2, ed J. R. Lakowicz (New York, NY: Plenum Press), 128–176.

Chu, J., Zhang, Z., Zheng, Y., Yang, J., Qin, L., Lu, J., et al. (2009). A novel far-red bimolecular fluorescence complementation system that allows for efficient visualization of protein interactions under physiological conditions. *Biosens. Bioelectron.* 25, 234–239. doi: 10.1016/j.bios.2009.06.008

Clayton, A. H., Klonis, N., Cody, S. H., and Nice, E. C. (2005). Dual-channel photobleaching FRET-microscopy for improved resolution of protein association states in living cells. *Eur. Biophys. J.* 34, 82–90. doi: 10.1007/s00249-004-0427-y

Clegg, R. M. (2009). Förster resonance energy transfer- FRET what it is, why do it, and how it's done. *Lab. Tech. Biochem. Mol. Biol.* 33, 1–58. doi: 10.1016/S0075-7535(08)00001-6

Crosby, K. C., Petraczewska-Bogiel, A., Gadella, T. W. J., and Winkel, B. S. (2011). Förster resonance energy transfer demonstrates a flavonoid metabolon in living plant cells that displays competitive interactions between enzymes. *FEBS Lett.* 585, 2193–2198. doi: 10.1016/j.febslet.2011.05.066

Cubitt, A. B., Heim, R., Adams, S. R., Boyd, A. E., Gross, L. A., and Tsien, R. Y. (1995). Understanding, improving and using green fluorescent proteins. *Trends Biochem. Sci.* 20, 448–455. doi: 10.1016/S0968-0004(00)89099-4

Daelemans, D., Costes, S. V., Cho, E. H., Erwin-Cohen, R. A., Locket, S., and Pavlakis, G. N. (2004). *In vivo* HIV-1 Rev multimerization in the nucleolus and cytoplasm identified by fluorescence resonance energy transfer. *J. Biol. Chem.* 279, 50167–50175. doi: 10.1074/jbc.M407713200

Dinant, C., van Royen, M. E., Vermeulen, W., and Houtsmuller, A. B. (2008). Fluorescence resonance energy transfer of GFP and YFP by spectral imaging and quantitative acceptor bleaching. *J. Microsc.* 231, 97–104. doi: 10.1111/j.1365-2818.2008.02020.x

Dixit, R., and Cyr, R. (2003). Cell damage and reactive oxygen species production induced by fluorescence microscopy: effect on mitosis and guidelines for non-invasive fluorescence microscopy. *Plant J.* 36, 280–290. doi: 10.1046/j.1365-313X.2003.01868.x

Djikanović, D., Kalauzi, A., Jeremić, M., Mićić, M., and Radotić, K. (2007). Deconvolution of fluorescence spectra: contribution to the structural analysis of complex molecules. *Colloids Surf. B Biointerfaces* 54, 188–192. doi: 10.1016/j.colsurfb.2006.10.015

Domingo, B., Sabariegos, R., Picazo, F., and Llopis, J. (2007). Imaging FRET standards by steady-state fluorescence and lifetime methods. *Microsc. Res. Tech.* 70, 1010–1021. doi: 10.1002/jemt.20509

Duncan, R. R. (2006). Fluorescence lifetime imaging microscopy (FLIM) to quantify protein-protein interactions inside cells. *Biochem. Soc. Transactiv.* 34, 679–682. doi: 10.1042/BST0340679

Eilert, U., Wolters, B., and Constabel, F. (1986). Ultrastructure of acridine alkaloid idioblasts in roots and cell cultures of *Ruta graveolens*. *Can. J. Bot.* 64, 1089–1096. doi: 10.1139/b86-149

Erickson, M. G., Moon, D. L., and Yue, D. T. (2003). DsRed as a potential FRET partner with CFP and YFP. *Biophys. J.* 85, 599–611. doi: 10.1016/S0006-3495(03)74504-4

Fan, J. Y., Cui, Z. Q., Wei, H. P., Zhang, Z. P., Zhou, Y. F., Wang, Y. P., et al. (2007). Split mCherry as a new red bimolecular fluorescence complementation system for visualising protein-protein interactions in living cells. *Biochem. Biophys. Res. Commun.* 367, 47–53. doi: 10.1016/j.bbrc.2007.12.101

Förster, T. (1946). Energiewanderung und Fluoreszenz. *Naturwiss* 33, 166–175. doi: 10.1007/BF00585226

Förster, T. (1948). Intermolecular energy migration and fluorescence. *Ann. Phys.* 2, 55–75. doi: 10.1002/andp.19484370105

Fredj, A., Pasquier, H., Demachy, I., Jonasson, G., Levy, B., Derrien, V., et al. (2012). The single T65S mutation generates brighter cyan fluorescent proteins with increased photostability and pH insensitivity. *PLoS ONE* 7:e49149. doi: 10.1371/journal.pone.0049149

Gadella, T. W. J., van der Krogt, G. N., Bisseling, T. (1999). GFP-based FRET microscopy in living plant cells. *Trends Plant Sci.* 4, 287–291. doi: 10.1016/S1360-1385(99)01426-0

Galperin, E., Verkhusha, V. V., and Sorkin, A. (2004). Three-chromophore FRET microscopy to analyze multiprotein interactions in living cells. *Nat. Methods* 1, 209–217. doi: 10.1038/nmeth720

Gandía, J., Lluís, C., Ferré, S., Franco, R., and Ciruela, F. (2008). Light resonance energy transfer-based methods in the study of G protein-coupled receptor oligomerization. *Bioessays* 30, 82–89. doi: 10.1002/bies.20682

Gandía-Herrero, F., Escribano, J., and García-Carmona, F. (2005). Betaxanthines as pigments responsible for visible fluorescence in flowers. *Planta* 222, 586–593. doi: 10.1007/s00425-005-0004-3

Ganesan, S., Ameer-beg, S. M., Ng, T. T., Vojnovic, B., and Wouters, F. S. (2006). A dark yellow fluorescent protein (YFP)-based resonance energy accepting chromoprotein (REACh) for Förster resonance energy transfer with GFP. *Proc. Natl. Acad. Sci. U.S.A.* 103, 4089–4094. doi: 10.1073/pnas.0509922103

Gerritsen, H. C., Agronskaia, A. V., Bader, A. N., and Esposito, A. (2009). "Time domain FLIM: theory, instrumentation, and data analysis," in *Laboratory Techniques in Biochemistry and Molecular Biology*, Vol. 33, ed T. W. J. Gadella (Oxford: Elsevier), 95–132.

Gillbro, T., and Cogdell, R. J. (1989). Carotenoid fluorescence. *Chem. Phys. Lett.* 158, 312–316. doi: 10.1016/0009-2614(89)87342-7

Goedhart, J., van Weeren, L., Hink, M. A., Vischer, N. O., Jalink, K., and Gadella, T. W. J. (2010). Bright cyan fluorescent protein variants ideintified by fluorescence lifetime screening. *Nat. Methods* 7, 137–139. doi: 10.1038/nmeth.1415

Goedhart, J., Vermeer, J. E. M., Adjobo-Hermans, M. J. W., van Weeren, L., and Gadella, T. W. J. (2007). Sensitive detection of p65 homodimers using red-shifted and fluorescent protein-based FRET-couples. *PLoS ONE* 10:e1011. doi: 10.1371/journal.pone.0001011

Goedhart, J., von Stetten, D., Noirclerc-Savoye, M., Lelimousin, M., Joosen, L., Hink, M. A., et al. (2012). Structure-guided evolution of cyan fluorescent proteins towards a quantum yield of 93%. *Nat. Commun.* 3,751. doi: 10.1038/ncomms1738

Gordon, G. W., Berry, G., Liang, X. H., Levine, B., and Herman, B. (1998). Quantitative fluorescence resonance energy transfer measurements using fluorescence microscopy. *Biophys. J.* 74, 2702–2713. doi: 10.1016/S0006-3495(98)77976-7

Griesbeck, O., Baird, G. S., Campbell, R. E., Zacharias, D. A., and Tsien, R. Y. (2001). Reducing the environmental sensitivity of yellow fluorescent protein. Mechanism and application. *J. Bio. Chem.* 276, 29188–29194. doi: 10.1074/jbc.M102815200

Guex, N., and Peitsch, M. C. (1997). SWISS-MODEL and the Swiss-Pdb-Viewer: an environment for comparative protein modeling. *Electrophoresis* 18, 2714–2723. doi: 10.1002/elps.1150181505

Haseloff, J., Siemering, K. R., Prasher, D. C., and Hodge, S. (1997). Removal of a cryptic intron and subcellular localization of green

fluorescent protein are required to mark transgenic Arabidopsis plants brightly. *Proc. Natl. Acad. Sci. U.S.A.* 94, 2122–2127. doi: 10.1073/pnas.94.6.2122

Haustein, E., Jahnz, M., Schwille, P. (2003). Triple FRET: A tool for studying long-range molecular interactions. *Chem. Phys. Chem.* 4, 745–748. doi: 10.1002/cphc.200200634

He, L., Grammer, A. C., Wu, X., and Lipsky, P. E. (2004). TRAF3 forms heterotrimers with TRAF2 and modulates its ability to mediate NF-(kappa)B activation. *J. Biol. Chem.* 279, 55855–55865. doi: 10.1074/jbc.M407284200

He, L., Wu, X., Simone, J., Hewgill, D., and Lipsky, P. E. (2005). Determination of tumor necrosis factor receptor-associated factor trimerization in living cells by CFP->YFP->mRFP FRET detected by flow cytometry. *Nucleic Acid Res.* 33, e61. doi: 10.1093/nar/gni057

Heikal, A. A., Hess, S. T., Baird, G. S., Tsien, R. Y., and Webb, W. W. (2000). Molecular spectroscopy and dynamics of intrinsically fluorescent proteins: coral red (dsRed) and yellow (Citrine). *Proc. Natl. Acad. Sci. U.S.A.* 97, 11996–12001. doi: 10.1073/pnas.97.22.11996

Heinze, M., Herre, M., Massalski, C., Hermann, I., Conrad, U., and Roos, W. (2013). Signal transfer in the plant plasma membrane: phospholipase A2 is regulated via an inhibitory Gα protein and a cyclophylin. *Biochem. J.* 450, 497–509. doi: 10.1042/BJ20120793

Hink, M. A., Bisseling, T., and Visser, A. J. (2002). Imaging protein-protein interactions in living plant cells. *Plant Mol. Biol.* 50, 871–883. doi: 10.1023/A:1021282619035

Hoppe, A. D., Christensen, K., and Swanson, J. A. (2002). Fluorescence Resonance Energy Transfer-based stoichiometry in living cells. *Biophys. J.* 83, 3652–3664. doi: 10.1016/S0006-3495(02)75365-4

Hossain, T., Rosenberg, I., Selhub, J., Kishore, G., Beachy, R., and Schubert, K. (2004). Enhancement of folates in plants through metabolic engineering. *Proc. Natl. Acad. Sci. U.S.A.* 101, 5158–5163. doi: 10.1073/pnas.0401342101

Jach, G., Pesch, M., Richter, K., Frins, S., Uhrig, J. F. (2006). An improved mRFP1 adds red to bimolecular fluorescence complementation. *Nat. Methods* 3, 597–600. doi: 10.1038/nmeth901

Jalink, K., and van Rheenen, J. (2009). "Filter FRET: quantitative imaging of sensitized emission," in *Laboratory Techniques in Biochemistry and Molecular Biology*, Vol. 33, ed T. W. J. Gadella (Oxford: Elsevier), 289–350.

Jares-Erijman, E. A., and Jovin, T. M. (2003). FRET imaging. *Nat. Biotechnol.* 21, 1387–1395. doi: 10.1038/nbt896

Karpova, T. S., Baumann, C. T., He, L., Wu, X., Grammer, A., Lipsky, P., et al. (2003). Fluorescence resonance energy transfer from cyan to yellow fluorescent protein detected by acceptor photo-bleaching using confocal microscopy and a single laser. *J. Microsc.* 209, 56–70. doi: 10.1046/j.1365-2818.2003.01100.x

Klein, P., Seidel, T., Stöcker, B., Dietz, K. J. (2012). The membrane-tethered transcription factor ANAC089 serves as redox-dependent suppressor of stromal ascorbate peroxidase gene expression. *Front. Plant Sci.* 3:247. doi: 10.3389/fpls.2012.00247

Kleinegris, D., van Es, M. A., Janssen, M., Brandenburg, W. A., and Wijffels, R. H. (2010). Carotenoid fluorescnece in *Dunaliella salina*. *J. Appl. Phycol.* 22, 645–649. doi: 10.1007/s10811-010-9505-y

Kluge, C., Seidel, T., Bolte, S., Sharma, S. S., Hanitzsch, M., Satiat-Jeunemaitre, B., et al. (2004). Subcellular distribution of the V-ATPase complex in plant cells, and *in vivo* localisation of the 100 kDa subunit VHA-a within the complex. *BMC Cell Biol.* 5:29. doi: 10.1186/1471-2121-5-29

Koushik, S. V., Blank, P. S., and Vogel, S. S. (2009). Anomalous surplus energy transfer observed with multiple FRET-acceptors. *PLoS ONE* 4:e8031. doi: 10.1371/journal.pone.0008031

Koushik, S. V., Chen, H., Thaler, C., Puhl, H. L., and Vogel, S. S. (2006). Cerulean, Venus and VenusY67C FRET reference standards. *Biophys. J.* 91, L99–L101. doi: 10.1529/biophysj.106.096206

Krebs, M., Held, K., Binder, A., Hashimoto, K., Den Herder, G., Parniske, M., et al. (2012). FRET-based genetically encoded sensors allow high-resolution live cell imaging of Ca^{2+}-dynamics. *Plant J.* 69, 181–192. doi: 10.1111/j.1365-313X.2011.04780.x

Kremers, G. J., and Goedhart, J. (2009). Visible fluorescent proteins for FRET. *Lab. Tech. Biochem. Mol. Biol.* 33, 171–224. doi: 10.1016/S0075-7535(08)00005-3

Kremers, G. J., Goedhart, J., van Munster, E. B., and Gadella, T. W. J. (2006). Cyan and yellow fluorescent proteins with improved brightness, protein folding, and FRET Förster radius. *Biochem.* 45, 6570–6580. doi: 10.1021/bi0516273

Kwaaitaal, M., Keinath, N. F., Pajonk, S., Biskup, C., and Panstruga, R. (2010). Combined bimolecular fluorescence complementation and Förster resonance energy transfer reveals ternary SNARE complex formation in living plant cells. *Plant Physiol.* 152, 1135–1147. doi: 10.1104/pp.109.151142

Lakowicz, J. R. (2006). *Principles of Fluorescent Spectroscopy*, *3rd Edn.* New York, NY: Springer. doi: 10.1007/978-0-387-46312-4

Lam, A., St-Pierre, F., Gong, Y., Marshall, J. D., Cranfill, P. J., Baird, M. A., et al. (2012). Improving FRET dynamic range with bright green and red fluorescent protein. *Nat. Methods* 9, 1005–1012. doi: 10.1038/nmeth.2171

Lidke, D. S., Nagy, P., Barisas, B. G., Heintzmann, R., Post, J. N., Lidke, K. A., et al. (2003). Imaging molecular interactions in cells by dynamic and static fluorescence anisotropy (rFLIM and emFRET). *Biochem. Soc. Trans.* 31, 1020–1027. doi: 10.1042/BST0311020

Malkani, N., and Schmid, J. A. (2011). Some secrets of fluorescent proteins: distinct bleaching in various mounting fluids and photoactivation of cyan fluorescent proteins at yfp-excitation. *PLoS ONE* 6:e18586. doi: 10.1371/journal.pone.0018586

Markwardt, M. L., Kremers, G. J., Kraft, C. A., Ray, K., Cranfill, P. J., Wilson, K. A., et al. (2011). An improved cerulean fluorescent protein with enhanced brightness and reduced reversible photoswitching. *PLoS ONE* 6:e17896. doi: 10.1371/journal.pone.0017896

Megías, D., Marrero, R., Martínez del Peso, B., Garcia, M. A., Bravo-Cordero, J. J., García-Grande, A., et al. (2009). Novel lambda FRET spectral confocal microscopy imaging method. *Microsc. Res. Techn.* 72, 1–11. doi: 10.1002/jemt.20633

Miyawaki, A., Griesbeck, O., Heim, R., and Tsien, R. Y. (1999). Dynamic and quantitative Ca^{2+}-measurements using improved cameleons. *Proc. Natl. Acad. Sci. U.S.A.* 96, 2134–2140. doi: 10.1073/pnas.96.5.2135

Miyawaki, A., and Tsien, R. Y. (2000). Monitoring protein conformations and interactions by fluorescence resonance energy transfer between mutants of green fluorescent protein. *Methods Enzymol.* 327, 427–500. doi: 10.1016/S0076-6879(00)27297-2

Miyawaki, A., Llopis, J., Heim, R., McCaffery, J. M., Adams, J. A., Ikura, M., et al. (1997). Fluorescent indicators for Ca^{2+} based on green fluorescent proteins and calmodulin. *Nature* 388, 882–887. doi: 10.1038/42264

Mizuno, H., Sawano, A., Eli, P., Hama, H., and Miyawaki, A. (2001). Red fluorescent protein from Discosoma as a fusion tag and a partner for fluorescence resonance energy transfer. *Biochemistry*. 40, 2502–2510. doi: 10.1021/bi002263b

Murakoshi, H., Lee, S. J., and Yasuda, R. (2008). Highly sensitive and quantitative FRET-FLIM imaging in single dendritic spines using improved non-radiative YFP. *Brain Cell Biol.* 36, 31–42. doi: 10.1007/s11068-008-9024-9

Muthuramalingam, M., Seidel, T., Laxa, M., Nunes de Miranda, S. M., Gärtner, F., Ströher, E., et al. (2009). Multiple redox and non-redox interactions define 2-Cys peroxiredoxin as a regulatory hub in the chloroplast. *Mol. Plant* 2, 1273–1288. doi: 10.1093/mp/ssp089

Nagai, T., Ibata, K., Park, E. S., Kubota, M., Mikoshiba, K., and Miyawaki, A. (2002). A variant of yellow fluorescent protein with fast and efficient maturation for cell-biological applications. *Nat. Biotechnol.* 20, 87–90. doi: 10.1038/nbt0102-87

Nagai, T., Yamada, S., Tominaga, T., Ichikawa, M., and Miyawaki, A. (2004). Expanded dynamic range of fluorescent indicators for Ca^{2+} by circularly permuted yellow fluorescent proteins. *Proc. Natl. Acad. Sci. U.S.A.* 101, 10554–10559. doi: 10.1073/pnas.0400417101

Okumoto, S., Jones, A., and Frommer, W. B. (2012). Quantitative imaging with fluorescent biosensors. *Annu. Rev. Plant Biol.* 63, 663–706. doi: 10.1146/annurev-arplant-042110-103745

Otani, M., Shitan, N., Sakai, K., Martinoia, E., Sato, F., and Yazaki, K. (2005). Characterization of vacuolar transport of the endogenous alkaloid berberine in *Coptis japonica*. *Plant Physiol.* 138, 1939–1946. doi: 10.1104/pp.105.064352

Padilla-Parra, S., Audugé, N., Coppey-Moisan, M., and Tramier, M. (2008). Quantitative FRET-analysis by fast acquisitions time domain FLIM at high spatial resolution in living cells. *Biophys. J.* 95, 2976–2988. doi: 10.1529/biophysj.108.131276

Padilla-Parra, S., Audugé, N., Lalucque, H., Mevel, J. C., Coppey-Moisan, M., and Tramier, M. (2009). Quantitative comparison of different fluorescent protein couples for fast FRET-FLIM acquisition. *Biophys. J.* 97, 2368–2376. doi: 10.1016/j.bpj.2009.07.044

Patterson, G. H., Piston, D. W., and Barisas, B. G. (2000). Förster distances between green fluorescent protein pairs. *Anal. Biochem*. 284, 438–440. doi: 10.1006/abio.2000.4708

Peter, M., Ameer-Beg, S. M., Hughes, M. K. Y., Keppler, M. D., Prag, S., Marsh, M., et al. (2005). *Biophys. J.* 88, 1224–1237. doi: 10.1529/biophysj.104.050153

Philipps, B., Hennecke, J., and Glockshuber, R. (2003). FRET-based *in vivo* screening for protein folding and increased protein stability. *J. Mol. Biol.* 327, 239–249. doi: 10.1016/S0022-2836(03)00077-9

Piston, D. W., and Kremer, G. J. (2007). Fluorescent protein FRET: the good, the bad and the ugly. *Trends Biochem. Sci.* 32, 407–414. doi: 10.1016/j.tibs.2007.08.003

Pöhlker, C., Huffman, J. A., and Pöschl, U. (2011). Autofluorescence of atmospheric bioaerosols – fluorescent biomolecules and potential interferences. *Atmos. Meas. Tech.* 4, 5857–5933. doi: 10.5194/amtd-4-5857-2011

Poot, M., Pierce, R. H., and Kavanagh, T. J. (2002). "Flow cytometric and fluorometric methods of quantifying and characterizing apoptotic cell death", in *Apoptosis methods in Pharmakology and Toxikology*, ed M. A. Davis (Totowa, NJ: Humana Press), 11–36.

Raarup, M. K., Fjorback, A. W., Jensen, S. M. R., Müller, H. K., Kjærgaard, M. M., Poulsen, H., et al. (2009). Enhanced yellow fluorescent protein photoconversion to a cyan fluorescent protein-like species is sensitive to thermal and diffusion conditions. *J. Biomed. Opt.* 14, 034039. doi: 10.1117/1.3103338

Raicu, V., Jansma, D. B., Miller, R. J. D., and Friesen, J. D. (2005). Protein interaction quantified *in vivo* by spectrally resolved fluorescence resonance energy transfer. *Biochem. J.* 385, 265–277. doi: 10.1042/BJ20040226

Rizzo, M. A., Springer, G., Segawa, K., Zipfel, W. R., and Piston, D. W. (2006). Optimization of pairings and detection conditions for measurement of FRET between cyan and yellow fluorescent proteins. *Microsc. Microanal.* 12, 238–254. doi: 10.1017/S1431927606060235

Rizzo, M. A., Springer, G. H., Granada, B., and Piston, D. W. (2004). An improved cyan fluorescent protein variant useful for FRET. *Nat. Biotechnol.* 22, 445–449. doi: 10.1038/nbt945

Roshchina, V. V. (2012). Vital autofluorescence: application to the study of plant living cells. *Int. J. Spectrosc*. 2012, 1–14. doi: 10.1155/2012/124672

Roshchina, V. V., and Karnaukhov, V. N. (1999). Changes in pollen autofluorescence induced by ozone. *Biol. Plant.* 42, 273–278. doi: 10.1023/A:1002120904588

Schmid, J. A., Scholze, P., Kudlacek, O., Freissmuth, M., Singer, E. A., and Sitte, H. H. (2001). Oligomerization of the human serotonin transporter and of the rat GABA transporter 1 visualized by fluorescence resonance energy transfer microscopy in living cells. *J. Biol. Chem.* 276, 3805–3810. doi: 10.1074/jbc.M007357200

Schnitzer, D., Seidel, T., Sander, T., Golldack, D., and Dietz, K. J. (2011). The cellular energization state affects peripheral stalk stability of plant vacuolar H^+-ATPase and impairs vacuolar acidification. *Plant Cell Physiol.* 52, 946–956. doi: 10.1093/pcp/pcr044

Seefeldt, B., Kasper, R., Seidel, T., Tinnefeld, P., Dietz, K. J., Heilemann, M., et al. (2008). Fluorescent proteins for single-molecule fluorescence applications. *J. Biophotonics* 1, 74–82. doi: 10.1002/jbio.200710024

Seidel, T., Golldack, D., and Dietz, K. J. (2005). Mapping of C-termini of V-ATPase subunits by *in vivo*-FRET measurements. *FEBS Lett.* 579, 4374–4382. doi: 10.1016/j.febslet.2005.06.077

Seidel, T., Kluge, C., Hanitzsch, M., Ross, J., Sauer, M., Dietz, K. J., et al. (2004). Colocalization and FRET-analysis of subunits c and a of the vacuolar H^+-ATPase in living plant cells. *J. Biotech.* 112, 165–175. doi: 10.1016/j.jbiotec.2004.04.027

Seidel, T., Seefeldt, B., Sauer, M., and Dietz, K. J. (2010). *In vivo* analysis of the 2-Cys peroxiredoxin oligomeric state by two-step FRET. *J. Biotechnol.* 149, 272–279. doi: 10.1016/j.jbiotec.2010.06.016

Seward, H. E., Basran, J., Denton, R., Pfuhl, M., Muskett, F. W., and Bagshaw, C. R. (2013). Halide and proton binding kinetics of yellow fluorescent protein variants. *Biochemistry* 52, 2482–2491. doi: 10.1021/bi3016839

Shaner, N. C., Campbell, R. E., Steinbach, P. A., Giepmans, B. N., Palmer, A. E., and Tsien, R. Y. (2004). Improved monomeric red, orange and yellow fluorescent proteins derived from Discosoma sp. red fluorescent protein. *Nat. Biotechnol.* 22, 1567–1572. doi: 10.1038/nbt1037

Sun, Y., and Periasamy, A. (2010). Additional correction for energy transfer efficiency calculation in filter-based resonance energy transfer microscopy for more accurate results. *J. Biomed. Opt.* 15, 020513. doi: 10.1117/1.3407655

Sun, Y., Wallrabe, H., Booker, C. F., Day, R. N., and Periasamy, A. (2010). Three-color spetral FRET microscopy localizes three interacting proteins in living cells. *Biophys. J.* 99, 1274–1283. doi: 10.1016/j.bpj.2010.06.004

Szentesi, G., Vereb, G., Horváth, G., Bodnár, A., Fábián, Á., Matkó, J., et al. (2005). Computer program for analysing donor photobleaching FRET image series. *Cytometry* A 67A, 119–128. doi: 10.1002/cyto.a.20175

Tomosugi, W., Matsuda, T., Tani, T., Nemoto, T., Kotera, I., Saito, K., et al. (2009). An ultramarine fluorescent protein with increased photostability and pH insensitivity. *Nat. Methods* 6, 351–353. doi: 10.1038/nmeth.1317

Tramier, M., Zahid, M., Mevel, J. C., Masse, M. J., and Coppey-Moisan, M. (2006). Sensitivity of CFP/YFP and GFP/mCherry pairs to donor photobleaching on FRET determination by fluorescence lifetime imaging microscopy in living cells. *Microsc. Res. Tech.* 69, 933–939. doi: 10.1002/jemt.20370

Valentin, G., Verheggen, C., Piolot, T., Neel., H., Coppey-Moisan, M., and Bertrand, E. (2005). Photoconversion of YFP into a CFP-like species during acceptor photobleaching FRET experiments. *Nat. Methods* 2, 801. doi: 10.1038/nmeth1105-801

van Munster, E. B., Kremers, G. J., Adjobo-Hermans, M. J. W., and Gadella, T. W. J. (2005). Fluorescence resonance Energy transfer (FRET) measurement by gradual acceptor photobleaching. *J. Microsc.* 218, 253–262. doi: 10.1111/j.1365-2818.2005.01483.x

van Rheenen, J., Langeslag, M., and Jalink, K. (2004). Correcting confocal acquisition to optimize imaging of fluorescence resonance energy transfer by sensitized emission. *Biophys. J.* 86, 2517–2529. doi: 10.1016/S0006-3495(04)74307-6

Veerabagu, M., Elgass, K., Kirchler, T., Huppenberger, P., Harter, K., Chaban, C., et al. (2012). The Arabidopsis B-type response regulator 18 homodimerizes and positively regulates cytokinin responses. *Plant J.* 72, 721–731. doi: 10.1111/j.1365-313X.2012.05101.x

Vermeer, J. E. M., van Munster, E. B., Vischer, N. O., and Gadella, T. W. J. (2004). Probing plasma membrane microdomains in cowpea protoplasts using lipidated GFP-fusion proteins and multimode FRET microscopy. *J. Microsc*. 214, 190–200. doi: 10.1111/j.0022-2720.2004.01318.x

Verveer, P. J., and Hanley, Q. S. (2009). Frequency domain FLIM theory, instrumentation, and data analysis. *Lab. Tech. Biochem. Mol. Biol.* 33, 59–94. doi: 10.1016/S0075-7535(08)00002-8

Vitha, S., and Osteryoung, K. W. (2011). Immunofluorescence microscopy for localization of Arabidopsis chloroplast proteins. *Methods Mol. Biol.* 774, 33–58. doi: 10.1007/978-1-61779-234-2_3

Vogel, S. S., Nguyen, T. A., van der Meer, B. W., and Blank, P. S. (2012). The impact of heterogeneity and dark acceptor states on FRET: implications for using fluorescent protein donors and acceptors. *PLoS ONE* 7:e49593. doi: 10.1371/journal.pone.0049593

Wallrabe, H., and Periasamy, A. (2005). Imaging protein molecules using FRET and FLIM microscopy. *Curr. Opin. Biotechnol.* 16, 19–27. doi: 10.1016/j.copbio.2004.12.002

Wanke, D., Hohenstatt, M. L., Dynowski, M., Bloss, U., Hecker, A., Elgass, K., et al. (2011). Alanine zipper-like coiled-coil domains are necessary for homotypic dimerization of plant GAGA-factors in the nucleus and nucleolus. *PLoS ONE* 6:e16070. doi: 10.1371/journal.pone.0016070

Watrob, H. M., Pan, C. P., and Barkley, M. D. (2003). Two-step FRET as a structural tool. *J. Am. Chem. Soc.* 125, 7336–7343. doi: 10.1021/ja034564p

Wirtz, M., Beard, K. F. M., Lee, C. P., Boltz, A., Schwarzländer, M., Fuchs, C., et al. (2012). Mitochondrial cysteine synthase complex regulates O-Acetylserine biosynthesis in plants. *J. Biol. Chem.* 287,

27941–27947. doi: 10.1074/jbc.M112.372656

Wolf, H., Barisas, B. G., Dietz, K. J., and Seidel, T. (2013a). Kaede for detection of protein oligomerization. *Mol. Plant.* 6, 1453–1462. doi: 10.1093/mp/sst039

Wolf, A., Akrap, N., Marg, B., Galliardt, H., Heiligentag, M., Humpert, F., et al. (2013b). Elements of the transcriptional machinery are compatible among plants and mammals. *PLoS ONE* 8:e53737. doi: 10.1371/journal.pone.0053737

Wolfbeis, O. S. (1985). "The fluorescence of organic natural products," in *Molecular Luminescence Spectroscopy: Methods and Applications,* ed S. G. Schulman (New York, NY: John Wiley and Sons).

Wu, B., Chen, Y., and Müller, J. D. (2009). Fluorescence fluctuation spectroscopy of mCherry in living cells. *Biophys. J.* 96, 2391–2404. doi: 10.1016/j.bpj.2008.12.3902

Xia, Z., and Liu, Y. (2001). Reliable and global measurement of fluorescence resonance energy transfer using fluorescence microscopes. *Biophys. J.* 81, 2395–2402. doi: 10.1016/S0006-3495(01)75886-9

Yang, F., Moss, L. G., and Philipps, Jr. (1996). Structure of the green fluorescent protein. *Nat. Biotechnol.* 14, 1246–1251. doi: 10.1038/nbt1096-1246

Zal, T., and Gascoigne, N. R. J. (2004). Photobleaching-corrected FRET efficiency imaging of live cells. *Biophys. J.* 86, 3923–3939. doi: 10.1529/biophysj.103.022087

Zapata-Hommer, O., Griesbeck, O. (2003). Efficiently folding and circularly permuted variants of the Sapphire mutant of GFP. *BMC Biotechnol.* 3:5. doi: 10.1186/1472-6750-3-5

Conflict of Interest Statement: The authors declare that the research was conducted in the absence of any commercial or financial relationships that could be construed as a potential conflict of interest.

Received: 28 June 2013; accepted: 29 September 2013; published online: 29 October 2013.

*Citation: Müller SM, Galliardt H, Schneider J, Barisas BG and Seidel T (2013) Quantification of Förster resonance energy transfer by monitoring sensitized emission in living plant cells. Front. Plant Sci. **4**:413. doi: 10.3389/fpls.2013.00413*

This article was submitted to Plant Cell Biology, a section of the journal Frontiers in Plant Science.

Copyright © 2013 Müller, Galliardt, Schneider, Barisas and Seidel. This is an open-access article distributed under the terms of the Creative Commons Attribution License (CC BY). The use, distribution or reproduction in other forums is permitted, provided the original author(s) or licensor are credited and that the original publication in this journal is cited, in accordance with accepted academic practice. No use, distribution or reproduction is permitted which does not comply with these terms.

frontiers in
PLANT SCIENCE

MINI REVIEW ARTICLE
published: 12 July 2013
doi: 10.3389/fpls.2013.00234

Perspectives for using genetically encoded fluorescent biosensors in plants

Sisse K. Gjetting*[1], *Alexander Schulz*[1] *and Anja T. Fuglsang*[1,2]

[1] *Transport Biology Section, Department of Plant and Environmental Sciences, University of Copenhagen, Copenhagen, Denmark*
[2] *Center of Excellence for Membrane Pumps and Disease, PUMPKIN, Aarhus, Denmark*

Edited by:
Elison B. Blancaflor, The Samuel Roberts Noble Foundation, USA

Reviewed by:
Elison B. Blancaflor, The Samuel Roberts Noble Foundation, USA
Gabriele B. Monshausen, Pennsylvania State University, USA

***Correspondence:**
Anja T. Fuglsang, Transport Biology Section, Department of Plant and Environmental Sciences, University of Copenhagen, Thorvaldsensvej 40, Copenhagen, DK-1871, Denmark
e-mail: atf@life.ku.dk

Genetically encoded fluorescent biosensors have long proven to be excellent tools for quantitative live imaging, but sensor applications in plants have been lacking behind those in mammalian systems with respect to the variety of sensors and tissue types used. How can this be improved, and what can be expected for the use of genetically encoded fluorescent biosensors in plants in the future? In this review, we present a table of successful physiological experiments in plant tissue using fluorescent biosensors, and draw some conclusions about the specific challenges plant cell biologists are faced with and some of the ways they have been overcome so far.

Keywords: plant bioimaging, genetically encoded biosensors, fluorescence microscopy, calcium sensor, phosphatidylinositol sensor, pH sensors

INTRODUCTION

Genetically encoded fluorescent biosensors are increasingly used as the preferred method to visualize and analyse ion fluxes, signaling components, and metabolites, covering an expanding palette of cellular processes. While fluorescent proteins as such are mainly used for localization and expression studies, genetically encoded fluorescent biosensors in addition allow real time studies of cell metabolism with a similar high spatial and temporal resolution. Cell-specific promoters allow biosensor expression in the target cell of choice in contrast to chemical probes that are inherently dependent on efficient delivery into the cells.

The huge interest and progress in the field is reflected in a large number of recent reviews on fluorescent proteins and genetically encoded sensors, e.g., (Fehr et al., 2004; Lalonde et al., 2005; VanEngelenburg and Palmer, 2008; Frommer et al., 2009; Chudakov et al., 2010; Okumoto, 2010; Mehta and Zhang, 2011; Miyawaki, 2011; Newman et al., 2011; Palmer et al., 2011; Okumoto et al., 2012). Several reviews describe plant specific uses, e.g., (Dixit et al., 2006; Frommer et al., 2009; Swanson et al., 2011; Choi et al., 2012; Ehrhardt and Frommer, 2012; Okumoto, 2012; Okumoto et al., 2012). In addition, http://biosensor.dpb.carnegiescience.edu/ provides a database of selected available biosensors.

In the present context, the term genetically encoded fluorescent biosensors refers to fluorescent proteins coupled with a sensing mechanism that causes a change in fluorescence intensity upon ligand binding. Most sensors can be grouped within two major types of fluorescent biosensors: (1) single fluorescent protein sensors, which can carry the sensing mechanism within the fluorescent protein, such as e.g., pHluorins, or where sensing is coupled to a ligand binding domain. Other options using single fluorescent proteins include protein-protein interactions reported by fluorescent protein reconstitution (biFC) or detection of protein translocation. One notable exception of specific plant relevance is the DII-Venus auxin sensor, where degradation of the fluorescent protein is utilized as sensing mechanism. (2) FRET-based sensors, where ligand binding causes a conformational change of the sensor leading to a change in FRET ratio between two fluorescent proteins, usually CFP/YFP variants. Within these groups many sensor platform designs are possible, which are described in detail elsewhere, see e.g., (Okumoto et al., 2012).

There is general consensus that the field is expanding and far from saturated with respect to sensor targets, the quality and variety of the fluorescent proteins, spatiotemporal resolution, compartmentation, and to imaging techniques. This paper discusses the perspectives for using genetically encoded fluorescent biosensors in plants, summarizing the specific challenges plant cell biologists are faced with and the ways they have been overcome so far. Although, due to space restrictions, this review focuses on fluorescent biosensors, the aspects discussed apply to luminescent biosensors as well. What are the expectations for fluorescent biosensors in plants in the future? Can they help in assigning a function to the many orphan receptor-like kinases or create complete flux maps of metabolite and ions in Arabidopsis and other model organisms as suggested by (Okumoto et al., 2012)? We will point to some challenges that need to be addressed, if biosensors are to be used more widely.

WHY ARE GENETICALLY ENCODED FLUORESCENT BIOSENSORS LESS USED IN PLANTS THAN IN MAMMALIAN CELLS?

The variety of genetically encoded fluorescent sensors is explored primarily in mammalian systems. Although these sensors offer highly attractive advantages for plant cell imaging, reports on physiological measurements in plants have been comparatively few, which might indicate that using these tools for live physiological experiments in plants is not trivial.

Table 1 below is a compilation of genetically encoded fluorescent sensors used for physiological experiments in plants. Several important insights into plant cell biology have been gained from

Table 1 | Genetically encoded fluorescent sensors used for physiological experiments in plants, subdivided by sensor function.

Sensor name	FPs	Kd/pKa	λ_{max} ex./em.	Plant species, tissue	Localization	Stimulus/response	References
CAMELEONS AND OTHER CALCIUM SENSORS							
YC2.1	ECFP-EYFP	100 nM, 4.3 μM (biphasic)	ECFP: 434/477 EYFP: 514/427	*A.t.* guard cells	Cytosol	ABA pathogen elicitors CO2	Allen et al., 1999a,b, 2000, 2001, 2002; Hugouvieux et al., 2001; Klusener et al., 2002; Young et al., 2006; Siegel et al., 2009; **Miyawaki et al., 1999**
				L. longiflorum, *N. tabacum*, pollen tubes	Cytosol, nucleus		Watahiki et al., 2004
nupYC2.1				*M. truncatula* root hairs, wt and symbiotic. defect. mutants	Cytosol, nucleus	Nod factor, mycorrhiza, Mastoparan, JA	Miwa et al., 2006a,b; Sun et al., 2007; Kosuta et al., 2008; Sieberer et al., 2009; Capoen et al., 2011
YC3.1	ECFP-EYFP	1.5 μM		*N. tabacum*, pollen tube	Cytosol		Michard et al., 2008, 2011, **Miyawaki et al., 1999**
				A.t. pollen grain, pollen tubes, papilla cells	Cytosol		Iwano et al., 2004
YC3.6	ECFP-cpVENUS	250 nM		*A.t.* roots	Cytosol	Glu, ATP, Al^{3+}	Haruta et al., 2008; Rincon-Zachary et al., 2010, **Nagai et al., 2004**
				A.t., *N. tabacum*, pollen tubes	Cytosol		Iwano et al., 2009
				A.t. guard cells	Cytosol	Methyl Jasmonate (MeJA)	Weinl et al., 2008; Munemasa et al., 2011
				A.t. rosette leaves	Cytosol	Butyrate, ABA, MeJA	Islam et al., 2010
				A.t. roots, root hairs	Cytosol	Touch, gravitropism, barrier, IAA	Monshausen et al., 2007, 2008, 2009, 2011
				A.t. roots, cotyledons	PM, nucleus, cytosol		Krebs et al., 2012
YC4.6	ECFP-VENUS	58 nM 14.4 μM		*A.t.* pollen tubes	ER		Iwano et al., 2009 **Nagai et al., 2004**

(Continued)

Table 1 | Continued

Sensor name	FPs	Kd/pKa	λ_{max} ex./em.	Plant species, tissue	Localization	Stimulus/response	References
D3cpv-KVK-SKL	ECFP-cpVENUS			*A.t.* leaves, guard cells	Peroxisomes	Ca^{2+}	Costa et al., 2010 **Palmer et al., 2006**
D3cpv		0.6 μM		*A.t.* Roots, cotyledons	Tonoplast		Krebs et al., 2012
pH SENSORS							
pHluorin (ratiometric)	GFP	pKa 6.9		*N. tabacum,* pollen tubes	Cytosol		Certal et al., 2008; Michard et al., 2008 **Miesenbock et al., 1998**
				A.t. roots, *N. benthamiana*	Apoplast, cytosol	Fusicoccin salt, mannitol	Moseyko and Feldman, 2001; Plieth et al., 2001; Gao et al., 2004
PE-pHluorin PR-pHluorin	GFP	pKa 6.6	Ex 395/475 PE:Em 480/512 PR:Em 515	*A.t.* protoplasts PSB-D, PSB-L	Cytosol, vacuole, mitochondria, chloroplast endomembr. compartments		**Shen et al., 2013**
Pt-GFP	Pt-GFP	pKa 7.3 (7.8)	475/390 (ex) 508 (em)	*A.t.* roots, leaves guard cells	Cytosol		**Schulte et al., 2006**
GFP H148D	GFP	pKa 7.8		*A.t.* roots, root hairs	Cytosol	Gravitropism touch, barrier	Fasano et al., 2001; Monshausen et al., 2007, 2009, **Elsliger et al., 1999**
pHusion apo-pHusion	mRFP1-EGFP	pKa 5.8 (6.0)	EGFP: 488/507 mRFP1: 584/607	*A.t.* leaf mesophyll, roots	Cytosol, apoplast	IAA	**Gjetting et al., 2012**
REDOX SENSORS							
Cyt-RoGFP1 Cyt-GRX1-RoGFP1 c-RoGFP1/2 Per-RoGFP1 Pla-RoGFP2 MitRoGFP1+2	GFP	Mid point potential RoGFP1: 288 mV RoGFP2: 272 mV	RoGFP1: λ_{max} oxidized: 396 nm λ_{max} reduced: 468 nm	*A.t.* leaf discs, leaf epidermis, roots	Cytosol, peroxisomes, plastids, mitochondria	Dark, (age), inhibitors/abiotic, stress	Jiang et al., 2006; Schwarzlander et al., 2009; Rosenwasser et al., 2010 **Hanson et al., 2004**

(Continued)

Table 1 | Continued

Sensor name	FPs	Kd/pKa	λ_{max} ex./em.	Plant species, tissue	Localization	Stimulus/response	References
RoGFP1 c-RoGFP1/2 Px-RoGFP2 Cp-RoGFP2 ER-RoGFP2			RoGFP2: λ_{max} oxidized: 398 nm λ_{max} reduced: 492 nm	*N. tabacum*, leaf epidermis, leaf discs	Cytosol, peroxisomes, plastids, ER	Inhibitors/abiotic stress	Schwarzlander et al., 2008, 2009
H_2O_2: HyPer HyPer-KSRM	cpYFP		Ex. 420/500 Em. 516	*N. tabacum* leaves, *A.t.* leaves pre-/post-bolting, guard cells	Cytosol, peroxisomes	Ca^{2+}	Costa et al., 2010 **Belousov et al., 2006**
OTHER SENSORS							
Chloride: Clomeleon	ECFP-EYFP		ECFP: 434/477	*A.t.* roots	Cytosol	Salt stress, Mg^{2+},Ca^{2+},La^{3+}, A9C (anion chan. block.)	Lorenzen et al., 2004; Plieth and Saleh, 2013, **Kuner and Augustine, 2000**
Glucose: FlipGlu600 μ, 2 m, 170 n	ECFP-EYFP	600 μM, 2 mM, 170 nM	EYFP: 514/427	*A.t.* silencing mutants and wildtype, roots, leaves	Cytosol	Glucose flux and levels	**Deuschle et al., 2006**; Chaudhuri et al., 2008, 2011
Sucrose: FlipSuc90 μ	ECFP-EYFP	88 μM		*A.t.* silencing mutants, roots	Cytosol		**Chaudhuri et al., 2008**
Glutamine: D157N	ECFP-Venus	6 mM (8.5 mM)	Venus:515/528	*A.t.* silencing mutants roots	Cytosol		**Yang et al., 2010**
PtdIns3P,4P, (4,5)P_2: YFP-2xFYVE mRFP-PH_{FAPP1} YFP- $PH_{FAPP1/PLC\partial 1}$	EYFP/mRFP1		EYFP: 514/427 mRFP1: 584/607	Protoplasts (cowpea, BY2). *M. truncatula* roots, *A.t.* seedlings	Localization (PM, golgi, cell plate)	PPIs dynamics	Vermeer et al., 2006; Vermeer et al, 2009; van Leeuwen et al., 2007
Auxin: DII-VENUS	Venus		Venus: 515/528	*A.t.* leaves, roots	Nucleus	Gravitropism	**Brunoud et al., 2012**

Details of the sensors: Dissociation constants, (Kd), pKa-values (of the pH sensors), with in vivo values in brackets, type of FP used, tissue, species, and potentially applied stimulus are given, as well as references to the original plant experiments. A.t. refers to Arabidopsis thaliana. References to Kd/pKa values and spectral properties of the sensors are shown in bold.

their use. Notably, applications of the Ca^{2+}-sensing Cameleons have given substantial insight into the role of calcium in stomatal opening (Allen et al., 1999a,b) as well as the role of calcium gradients in growing pollen tubes (Michard et al., 2008), root hairs of Arabidopsis (Monshausen et al., 2007), Nod factor-induced nuclear calcium transients in *M. truncatula* root hair cells (Capoen et al., 2011) and visualization of Ca^{2+}-dynamics in response to auxin during root gravitropism (Monshausen et al., 2011). Also pH sensors have been useful in plants. The pHluorin sensors have been used to document in detail cytosolic pH gradients and oscillations in growing pollen tubes (Michard et al., 2008), and cell wall pH has been measured by use of pHluorins (Gao et al., 2004) or apo-pHusion (Gjetting et al., 2012) secreted to the apoplast.

Looking closer at these experiments, some obvious similarities are seen. It can be argued that successful experiments are often carried out in single cell systems, such as guard cells, root hairs and pollen tubes, where complex cell-to-cell communication is limited. These experiments are all studies of ion signaling, that can be directly correlated with a growth or turgor response, making them attractive experimental setups. Although this is a trend, indeed, several experiments have been successfully carried out in intact tissue, very often in roots, (Fasano et al., 2001; Rincon-Zachary et al., 2010; Monshausen et al., 2011; Gjetting et al., 2012) where autofluorescence is negligible and access is not hindered by the waxy cuticle. Sensors that were successfully used for physiological measurements in intact tissue were often developed specifically for use in plants (e.g., the auxin sensor, DII-Venus, and the apoplastic pH-sensor apo-pHusion). Secondly, it is noted that overall only few sensor platforms and targets were used, again reflecting the fact that many sensors are originally designed for mammalian purposes. Thirdly, sensors were most often expressed in the cytosol, which is the default expression if not specifically targeted to other compartments, and finally most experiments were carried out in Arabidopsis or tobacco, which may not be surprising, since these are easy to manipulate. These observations emphasize some specific challenges that have to be addressed in order to broaden the palette of successful sensor applications in plants.

PLANT-SPECIFIC FEATURES THAT LIMIT THE APPLICABILITY OF GENETICALLY ENCODED FLUORESCENT SENSORS

AUTOFLUORESCENCE FROM CHLOROPLASTS AND CELL WALLS

Plants are complex, multicellular organisms to work with, and fluorescent probes do not always penetrate multiple cell layers, largely due to the barrier formed by the waxy cuticle and the cell wall. Therefore, genetically encoded sensors are ideally suited for plant cell imaging. However, in plants autofluorescence is a major challenge, particularly in photosynthesizing tissue (chlorophyll ex. 420–460 nm/em. 600–700 nm) and from the cell wall (various components are excited by UV to blue wavelengths, emitting mainly blue light), which can be addressed by the choice of fluorophores in sensor design, or may be circumvented, when lower photon counts/densities can be tolerated, by the use of bioluminescent proteins, such as Aequorin (Mehlmer et al., 2012), where excitation is caused by a chemical reaction instead of light, thus avoiding excitation of autofluorescence.

PRECAUTIONS FOR MOUNTING PROCEDURES AND STUDYING EXTERNALLY APPLIED CHEMICAL STIMULI

Genetically encoded sensors as such are non-invasive, but their application to study cellular responses to chemical stimuli requires a perfusion setup and immobilization for microscopy, which can potentially harm the cells. The cuticle covering aerial tissues is an entrance barrier for many compounds, and sometimes even for the ligand itself, making *in vivo* calibrations difficult when using such sensors. Efficient immobilization methods ensure that no movement of the specimen takes place, while at the same time allowing for perfusion of the chemical stimulus and plant growth. It was, however, recently shown that the commonly used method to immobilize Arabidopsis tissue with a medical adhesive severely impairs cell viability of root cells (Gjetting et al., 2012), making alternative methods necessary. An alternative could be the newly developed root chip (Grossmann et al., 2011) or more simply mounting roots on agarose (Gjetting et al., 2012). Another common method used e.g., for cross-fixing pollen tubes on polylysine slides (Michard et al., 2008) was also shown to disrupt Arabidopsis root cells. In general, the act of handling living tissue under a microscope will inevitably cause disturbance of the tissue and induce various stress responses and tropisms. This of course affects live imaging methods of genetically encoded fluorescent sensors as well as other methods.

GENE SILENCING MAY BE CAUSED BY CHOICE OF PROMOTER OR TANDEM FLUORESCENT PROTEINS

Gene silencing has often been mentioned as a particular problem for plant expression of genetically encoded fluorescent biosensors, particularly when used in tandem repeats, or driven by the 35S promoter (Miyawaki et al., 1997; Deuschle et al., 2006; Krebs et al., 2012). This problem was solved in one case by replacing the 35S-promoter of viral origin with the plant-derived UBQ10 promoter in Arabidopsis (Krebs et al., 2012), or by expressing the sensor in transgene silencing mutants (Deuschle et al., 2006). The use of silencing mutants however, is not optimal, since their general growth pattern is changed, and may influence the measurements in unpredictable ways. In our lab, the 35S-promoter did not provoke inhibitory gene silencing when driving the expression of either FRET-based sensors or ratiometric pH sensors (Gjetting et al., 2012 and unpublished results). Transgene silencing in root tips and seedlings was reported to cause a reduction in fluorescence intensity and thus undetectable FRET changes after 10–15 days of growth (Deuschle et al., 2006; Chaudhuri et al., 2011). In contrast, we were able to monitor pH changes in leaves of 1–2 months old plants which were not subject to silencing (Gjetting et al., 2012).

THE APOPLAST

This plant-specific extracellular compartment plays a major role in transport regulation, but obviously only plant scientists are interested in developing tools to study its dynamics. Sensors for apoplastic measurements must deal with the low pH values,

which are disruptive to many fluorescent proteins, and also be able to measure large differences in ion or solute concentration in the much less buffered apoplast. Apoplastic pH sensors have been used to measure salt stress (Schulte et al., 2006) and the effect of externally applied auxin (Gjetting et al., 2012), but the targeting of sensor protein to the apoplast results in accumulation in the ER, which should be taken into account when measuring the ratio. However, this accumulated protein could potentially be used as an internal pH reference or even as a tool to study pH in the endomembrane system as well. Another issue with apoplastic measurements relate to the structure of GFP in that an oxidizing environment, such as the cell wall and ER can impair proper folding of the fluorescent protein. The use of superfolder GFP (sfGFP) variants may in time be helpful in plants for solving this problem (Aronson et al., 2011).

IMPROVEMENT OF SENSOR APPLICATIONS IN PLANTS

INCREASING SENSOR TARGET RANGE TO INCLUDE, E.G., HORMONES AND KINASES

There are many possibilities to expand the range of sensor targets in plants. Developing sensors for central, plant-specific signaling events, like hormone action or activity of plant-specific receptor-like kinases would be major landmarks. An example is a recently developed auxin sensor, which is a fusion of the YFP variant Venus to the Aux/IAA auxin-interaction domain DII (Brunoud et al., 2012), targeted to the nucleus. Using this sensor, auxin distribution was mapped during gravity sensing and lateral shoot formation in Arabidopsis. For mammalian cells, e.g., a variety of GFP-based biosensors exist for kinases, GTPases, phosphatidylinositols (PtdIns) (Kimber et al., 2002; Yoshizaki et al., 2006; Zhang and Allen, 2007). Such sensors (PtdIns) have only recently emerged in the plant community (Munnik and Nielsen, 2011), probably because plants use different signaling components that cannot be targeted by sensors developed for mammalian systems.

pH MEASUREMENTS IN ACIDIC COMPARTMENTS

Sensors in plants have so far mainly been expressed in the cytosol, although several other compartments have also been explored (see **Table 1**). Indeed, targeted sensors are desirable, e.g., to study cell wall pH-dynamics (Gao et al., 2004; Gjetting et al., 2012). Sensor secretion to the apoplast involves accumulation of protein in transit in the endomembrane system, which is a problem to be considered carefully. This may be the reason that some researchers prefer pH-sensitive, small molecular weight fluorescent probes for surface pH measurements in Arabidopsis (Bibikova et al., 1998; Monshausen et al., 2011; Geilfus and Muhling, 2012). However, an apoplastic sensor, stably expressed in cells throughout the tissue, and not just the surface is preferable e.g., in roots to study details of the extracellular pH signature of gravitropic responses and auxin signaling (Swarup et al., 2005). The localization of pH sensors in the acidic compartment of the apoplast or vacuole is also hindered by the sensitivity of GFP to acidity (Tsien, 1998). The pH sensor *pt*GFP, derived from the Orange Seapen, *Ptilosarcus gurneyi* showed increased acid stability compared with avGFP derived pHluorins. PtGFP fluorescence could be fully restored after exposure to pH 3.5, and partially restored down to pH 2.5 and may therefore be more suitable for acidic measurements. In contrast, pHluorins were completely denatured at pH 3.5 (Schulte et al., 2006). Recently, a pHluorin-derived sensor, based on a solubility-modified GFP (sm-GFP) was targeted to the vacuole, and to other endomembrane compartments and used to determine pH of the different compartments (Shen et al., 2013).

VARIETY OF FPs AND TECHNOLOGY

Expanding the variety of sensor fluorescent proteins, e.g., by the development of different FRET donor/acceptors would facilitate the study of several ions/metabolites simultaneously, e.g., the commonly linked signaling cascade of intracellular calcium/apoplastic pH, as well as same ion fluxes in several compartments or complex protein-protein interactions. Multiplexed FRET (Piljic and Schultz, 2008) and fluorescence lifetime imaging (FLIM)-FRET (Grant et al., 2008) are becoming more feasible as the variety of spectral variants increases. In *N. benthamiana* leaves a FRET-FLIM assay was used to detect known protein interactions using a FRET pair of the GFP variant TSapphire as donor, and mOrange as acceptor (Bayle et al., 2008). A similar approach was used to detect a flavonoid metabolon in Arabidopsis protoplasts (Crosby et al., 2011). These examples are not using genetically encoded sensors as such, and are based on transient expression in single cell systems, but further illustrate the possibilities of using fluorescent protein technology in plants and may be useful for sensor construction at a later stage.

IDENTIFICATION OF NEW GENES AND GENE FUNCTION

Genetically encoded sensors may also be used to identify the role of genes of unknown function. A new class of glucose efflux transporters, SWEETs was identified by FRET-based glucose sensors (Chen et al., 2010), and repeated with a sucrose sensor, identifying a subclade of SWEET efflux transporters involved in sucrose transport, indicating a role in phloem loading (Chen et al., 2011). Another promising sensor application known from animal systems, addressed the functional identification of unknown signaling components. This idea was elegantly adapted to Arabidopsis, where the luminescent calcium sensor Aequorin was used to identify an extracellular signaling peptide, AtRALF1, (rapid alkalinization factor) by its ability to induce a cytosolic Ca^{2+}-increase (Haruta et al., 2008). The effect of this peptide was subsequently analysed in detail in Arabidopsis roots expressing the Cameleon sensor YC3.6.

CONCLUDING REMARKS

The use of genetically encoded sensors in plants faces some specific challenges not shared with the mammalian world, which need to be addressed by plant scientists. Nevertheless, the continuous development and refinement of fluorescent proteins, sensor design and bioimaging techniques make genetically encoded sensors very promising tools for elucidating metabolic networks and signaling events in plant cells in the future.

REFERENCES

Allen, G. J., Chu, S. P., Harrington, C. L., Schumacher, K., Hoffmann, T., Tang, Y. Y., et al. (2001). A defined range of guard cell calcium oscillation parameters encodes stomatal movements. *Nature* 411, 1053–1057. doi: 10.1038/35082575

Allen, G. J., Chu, S. P., Schumacher, K., Shimazaki, C. T., Vafeados, D., Kemper, A., et al. (2000). Alteration of stimulus-specific guard cell calcium oscillations and stomatal closing in Arabidopsis *det3* mutant. *Science* 289, 2338–2342. doi: 10.1126/science.289.5488.2338

Allen, G. J., Kuchitsu, K., Chu, S. P., Murata, Y., and Schroeder, J. I. (1999a). Arabidopsis *abi1-1* and *abi2-1* phosphatase mutations reduce abscisic acid-induced cytoplasmic calcium rises in guard cells. *Plant Cell* 11, 1785–1798.

Allen, G. J., Kwak, J. M., Chu, S. P., Llopis, J., Tsien, R. Y., Harper, J. F., et al. (1999b). Cameleon calcium indicator reports cytoplasmic calcium dynamics in Arabidopsis guard cells. *Plant J.* 19, 735–747. doi: 10.1046/j.1365-313x.1999.00574.x

Allen, G. J., Murata, Y., Chu, S. P., Nafisi, M., and Schroeder, J. I. (2002). Hypersensitivity of abscisic acid-induced cytosolic calcium increases in the Arabidopsis farnesyltransferase mutant *era1-2*. *Plant Cell* 14, 1649–1662. doi: 10.1105/tpc.010448

Aronson, D. E., Costantini, L. M., and Snapp, E. L. (2011). Superfolder GFP is fluorescent in oxidizing environments when targeted via the Sec translocon. *Traffic* 12, 543–548. doi: 10.1111/j.1600-0854.2011.01168.x

Bayle, V., Nussaume, L., and Bhat, R. A. (2008). Combination of novel green fluorescent protein mutant TSapphire and DsRed variant mOrange to set up a versatile in planta FRET-FLIM assay. *Plant Physiol.* 148, 51–60. doi: 10.1104/pp.108.117358

Belousov, V. V., Fradkov, A. F., Lukyanov, K. A., Staroverov, D. B., Shakhbazov, K. S., Terskikh, A. V., et al. (2006). Genetically encoded fluorescent indicator for intracellular hydrogen peroxide. *Nat. Methods* 3, 281–286. doi: 10.1038/nmeth866

Bibikova, T. N., Jacob, T., Dahse, I., and Gilroy, S. (1998). Localized changes in apoplastic and cytoplasmic pH are associated with root hair development in Arabidopsis thaliana. *Development* 125, 2925–2934.

Brunoud, G., Wells, D. M., Oliva, M., Larrieu, A., Mirabet, V., Burrow, A. H., et al. (2012). A novel sensor to map auxin response and distribution at high spatio-temporal resolution. *Nature* 482, 103–106. doi: 10.1038/nature10791

Capoen, W., Sun, J., Wysham, D., Otegui, M. S., Venkateshwaran, M., Hirsch, S., et al. (2011). Nuclear membranes control symbiotic calcium signaling of legumes. *Proc. Natl. Acad. Sci. U.S.A.* 108, 14348–14353. doi: 10.1073/pnas.1107912108

Certal, A. C., Almeida, R. B., Carvalho, L. M., Wong, E., Moreno, N., Michard, E., et al. (2008). Exclusion of a proton ATPase from the apical membrane is associated with cell polarity and tip growth in *Nicotiana tabacum* pollen tubes. *Plant Cell* 20, 614–634. doi: 10.1105/tpc.106.047423

Chaudhuri, B., Hormann, F., and Frommer, W. B. (2011). Dynamic imaging of glucose flux impedance using FRET sensors in wild-type Arabidopsis plants. *J. Exp. Bot.* 62, 2411–2417. doi: 10.1093/jxb/erq444

Chaudhuri, B., Hormann, F., Lalonde, S., Brady, S. M., Orlando, D. A., Benfey, P., et al. (2008). Protonophore- and pH-insensitive glucose and sucrose accumulation detected by FRET nanosensors in Arabidopsis root tips. *Plant J.* 56, 948–962. doi: 10.1111/j.1365-313X.2008.03652.x

Chen, L. Q., Hou, B. H., Lalonde, S., Takanaga, H., Hartung, M. L., Qu, X. Q., et al. (2010). Sugar transporters for intercellular exchange and nutrition of pathogens. *Nature* 468, 527–532. doi: 10.1038/nature09606

Chen, L. Q., Qu, X. Q., Hou, B. H., Sosso, D., Osorio, S., Fernie, A. R., et al. (2011). Sucrose efflux mediated by SWEET proteins as a key step for phloem transport. *Science* 335, 207–211. doi: 10.1126/science.1213351

Choi, W. G., Swanson, S. J., and Gilroy, S. (2012). High-resolution imaging of Ca^{2+}, redox status, ROS and pH using GFP biosensors. *Plant J.* 70, 118–128. doi: 10.1111/j.1365-313X.2012.04917.x

Chudakov, D. M., Matz, M. V., Lukyanov, S., and Lukyanov, K. A. (2010). Fluorescent proteins and their applications in imaging living cells and tissues. *Physiol. Rev.* 90, 1103–1163. doi: 10.1152/physrev.00038.2009

Costa, A., Drago, I., Behera, S., Zottini, M., Pizzo, P., Schroeder, J. I., et al. (2010). H2O2 in plant peroxisomes: an *in vivo* analysis uncovers a Ca^{2+}-dependent scavenging system. *Plant J.* 62, 760–772. doi: 10.1111/j.1365-313X.2010.04190.x

Crosby, K. C., Pietraszewska-Bogiel, A., Gadella, T. W. Jr., and Winkel, B. S. (2011). Forster resonance energy transfer demonstrates a flavonoid metabolon in living plant cells that displays competitive interactions between enzymes. *FEBS Lett.* 585, 2193–2198. doi: 10.1016/j.febslet.2011.05.066

Deuschle, K., Chaudhuri, B., Okumoto, S., Lager, I., Lalonde, S., and Frommer, W. B. (2006). Rapid metabolism of glucose detected with FRET glucose nanosensors in epidermal cells and intact roots of Arabidopsis RNA-silencing mutants. *Plant Cell* 18, 2314–2325. doi: 10.1105/tpc.106.044073

Dixit, R., Cyr, R., and Gilroy, S. (2006). Using intrinsically fluorescent proteins for plant cell imaging. *Plant J.* 45, 599–615. doi: 10.1111/j.1365-313X.2006.02658.x

Ehrhardt, D. W., and Frommer, W. B. (2012). New technologies for 21st century plant science. *Plant Cell* 24, 374–394. doi: 10.1105/tpc.111.093302

Elsliger, M. A., Wachter, R. M., Hanson, G. T., Kallio, K., and Remington, S. J. (1999). Structural and spectral response of green fluorescent protein variants to changes in pH. *Biochemistry* 38, 5296–5301. doi: 10.1021/bi9902182

Fasano, J. M., Swanson, S. J., Blancaflor, E. B., Dowd, P. E., Kao, T. H., and Gilroy, S. (2001). Changes in root cap pH are required for the gravity response of the Arabidopsis root. *Plant Cell* 13, 907–921.

Fehr, M., Ehrhardt, D. W., Lalonde, S., and Frommer, W. B. (2004). Minimally invasive dynamic imaging of ions and metabolites in living cells. *Curr. Opin. Plant Biol.* 7, 345–351. doi: 10.1016/j.pbi.2004.03.015

Frommer, W. B., Davidson, M. W., and Campbell, R. E. (2009). Genetically encoded biosensors based on engineered fluorescent proteins. *Chem. Soc. Rev.* 38, 2833–2841. doi: 10.1039/b907749a

Gao, D., Knight, M. R., Trewavas, A. J., Sattelmacher, B., and Plieth, C. (2004). Self-reporting Arabidopsis expressing pH and Ca^{2+} indicators unveil ion dynamics in the cytoplasm and in the apoplast under abiotic stress. *Plant Physiol.* 134, 898–908. doi: 10.1104/pp.103.032508

Geilfus, C. M., and Muhling, K. H. (2012). Transient alkalinization in the leaf apoplast of *Vicia faba L.* depends on NaCl stress intensity: an *in situ* ratio imaging study. *Plant Cell Environ.* 35, 578–587. doi: 10.1111/j.1365-3040.2011.02437.x

Gjetting, K. S., Ytting, C. K., Schulz, A., and Fuglsang, A. T. (2012). Live imaging of intra- and extracellular pH in plants using pHusion, a novel genetically encoded biosensor. *J. Exp. Bot.* 63, 3207–3218. doi: 10.1093/jxb/ers040

Grant, D. M., Zhang, W., McGhee, E. J., Bunney, T. D., Talbot, C. B., Kumar, S., et al. (2008). Multiplexed FRET to image multiple signaling events in live cells. *Biophys. J.* 95, L69–L71. doi: 10.1529/biophysj.108.139204

Grossmann, G., Guo, W. J., Ehrhardt, D. W., Frommer, W. B., Sit, R. V., Quake, S. R., et al. (2011). The RootChip: an integrated microfluidic chip for plant science. *Plant Cell* 23, 4234–4240. doi: 10.1105/tpc.111.092577

Hanson, G. T., Aggeler, R., Oglesbee, D., Cannon, M., Capaldi, R. A., Tsien, R. Y., et al. (2004). Investigating mitochondrial redox potential with redox-sensitive green fluorescent protein indicators. *J. Biol. Chem.* 279, 13044–13053. doi: 10.1074/jbc.M312846200

Haruta, M., Monshausen, G., Gilroy, S., and Sussman, M. R. (2008). A cytoplasmic Ca^{2+} functional assay for identifying and purifying endogenous cell signaling peptides in Arabidopsis seedlings: identification of AtRALF1 peptide. *Biochemistry* 47, 6311–6321. doi: 10.1021/bi8001488

Hugouvieux, V., Kwak, J. M., and Schroeder, J. I. (2001). An mRNA cap binding protein, ABH1, modulates early abscisic acid signal transduction in Arabidopsis. *Cell* 106, 477–487. doi: 10.1016/S0092-8674(01)00460-3

Islam, M. M., Hossain, M. A., Jannat, R., Munemasa, S., Nakamura, Y., Mori, I. C., et al. (2010). Cytosolic alkalization and cytosolic calcium oscillation in arabidopsis guard cells response to ABA and MeJA. *Plant Cell Physiol.* 51, 1721–1730. doi: 10.1093/pcp/pcq131

Iwano, M., Entani, T., Shiba, H., Kakita, M., Nagai, T., Mizuno, H., et al. (2009). Fine-tuning of the cytoplasmic Ca^{2+} concentration is essential for pollen tube growth. *Plant Physiol.* 150, 1322–1334. doi: 10.1104/pp.109.139329

Iwano, M., Shiba, H., Miwa, T., Che, F. S., Takayama, S., Nagai, T., et al. (2004). Ca^{2+} dynamics in a pollen grain and papilla cell during pollination of Arabidopsis. *Plant Physiol.* 136, 3562–3571. doi: 10.1104/pp.104.046961

Jiang, K., Schwarzer, C., Lally, E., Zhang, S., Ruzin, S., Machen, T., et al. (2006). Expression and characterization of a redox-sensing green fluorescent protein (reduction-oxidation-sensitive green fluorescent protein) in Arabidopsis. *Plant Physiol.* 141, 397–403. doi: 10.1104/pp.106.078246

Kimber, W. A., Trinkle-Mulcahy, L., Cheung, P. C., Deak, M., Marsden, L. J., Kieloch, A., et al. (2002). Evidence that the tandem-pleckstrin-homology-domain-containing protein TAPP1 interacts with Ptd(3, 4)P_2 and the multi-PDZ-domain-containing protein MUPP1 *in vivo*. *Biochem. J.* 361, 525–536. doi: 10.1042/0264-6021:3610525

Klusener, B., Young, J. J., Murata, Y., Allen, G. J., Mori, I. C., Hugouvieux, V., et al. (2002). Convergence of calcium signaling pathways of pathogenic elicitors and abscisic acid in Arabidopsis guard cells. *Plant Physiol.* 130, 2152–2163. doi: 10.1104/pp.012187

Kosuta, S., Hazledine, S., Sun, J., Miwa, H., Morris, R. J., Downie, J. A., et al. (2008). Differential and chaotic calcium signatures in the symbiosis signaling pathway of legumes. *Proc. Natl. Acad. Sci. U.S.A.* 105, 9823–9828. doi: 10.1073/pnas.0803499105

Krebs, M., Held, K., Binder, A., Hashimoto, K., Den Herder, G., Parniske, M., et al. (2012). FRET-based genetically encoded sensors allow high-resolution live cell imaging of Ca^{2+} dynamics. *Plant J.* 69, 181–192. doi: 10.1111/j.1365-313X.2011.04780.x

Kuner, T., and Augustine, G. J. (2000). A genetically encoded ratiometric indicator for chloride: capturing chloride transients in cultured hippocampal neurons. *Neuron* 27, 447–459. doi: 10.1016/S0896-6273(00)00056-8

Lalonde, S., Ehrhardt, D. W., and Frommer, W. B. (2005). Shining light on signaling and metabolic networks by genetically encoded biosensors. *Curr. Opin. Plant Biol.* 8, 574–581. doi: 10.1016/j.pbi.2005.09.015

Lorenzen, I., Aberle, T., and Plieth, C. (2004). Salt stress-induced chloride flux: a study using transgenic Arabidopsis expressing a fluorescent anion probe. *Plant J.* 38, 539–544. doi: 10.1111/j.0960-7412.2004.02053.x

Mehlmer, N., Parvin, N., Hurst, C. H., Knight, M. R., Teige, M., and Vothknecht, U. C. (2012). A toolset of aequorin expression vectors for in planta studies of subcellular calcium concentrations in *Arabidopsis thaliana*. *J. Exp. Bot.* 63, 1751–1761. doi: 10.1093/jxb/err406

Mehta, S., and Zhang, J. (2011). Reporting from the field: genetically encoded fluorescent reporters uncover signaling dynamics in living biological systems. *Annu. Rev. Biochem.* 80, 375–401. doi: 10.1146/annurev-biochem-060409-093259

Michard, E., Dias, P., and Feijo, J. (2008). Tobacco pollen tubes as cellular models for ion dynamics: improved spatial and temporal resolution of extracellular flux and free cytosolic concentration of calcium and protons using pHluorin and YC3.1 Cameleon. *Sex Plant Reprod.* 21, 169–181. doi: 10.1007/s00497-008-0076-x

Michard, E., Lima, P. T., Borges, F., Silva, A. C., Portes, M. T., Carvalho, J. E., et al. (2011). Glutamate receptor-like genes form Ca^{2+} channels in pollen tubes and are regulated by pistil D-serine. *Science* 332, 434–437. doi: 10.1126/science.1201101

Miesenbock, G., De Angelis, D. A., and Rothman, J. E. (1998). Visualizing secretion and synaptic transmission with pH-sensitive green fluorescent proteins. *Nature* 394, 192–195. doi: 10.1038/28190

Miwa, H., Sun, J., Oldroyd, G. E., and Downie, J. A. (2006a). Analysis of Nod-factor-induced calcium signaling in root hairs of symbiotically defective mutants of *Lotus japonicus*. *Mol. Plant Microbe Interact.* 19, 914–923. doi: 10.1094/MPMI-19-0914

Miwa, H., Sun, J., Oldroyd, G. E., and Downie, J. A. (2006b). Analysis of calcium spiking using a Cameleon calcium sensor reveals that nodulation gene expression is regulated by calcium spike number and the developmental status of the cell. *Plant J.* 48, 883–894. doi: 10.1111/j.1365-313X.2006.02926.x

Miyawaki, A. (2011). Proteins on the move: insights gained from fluorescent protein technologies. *Nat. Rev. Mol. Cell Biol.* 12, 656–668. doi: 10.1038/nrm3199

Miyawaki, A., Griesbeck, O., Heim, R., and Tsien, R. Y. (1999). Dynamic and quantitative Ca^{2+} measurements using improved Cameleons. *Proc. Natl. Acad. Sci. U.S.A.* 96, 2135–2140. doi: 10.1073/pnas.96.5.2135

Miyawaki, A., Llopis, J., Heim, R., McCaffery, J. M., Adams, J. A., Ikura, M., et al. (1997). Fluorescent indicators for Ca^{2+} based on green fluorescent proteins and calmodulin. *Nature* 388, 882–887. doi: 10.1038/42264

Monshausen, G. B., Bibikova, T. N., Messerli, M. A., Shi, C, and Gilroy, S. (2007). Oscillations in extracellular pH and reactive oxygen species modulate tip growth of Arabidopsis root hairs. *Proc. Natl. Acad. Sci. U.S.A.* 104, 20996–21001. doi: 10.1073/pnas.0708586104

Monshausen, G. B., Bibikova, T. N., Weisenseel, M. H., and Gilroy, S. (2009). Ca^{2+} regulates reactive oxygen species production and pH during mechanosensing in Arabidopsis roots. *Plant Cell* 21, 2341–2356. doi: 10.1105/tpc.109.068395

Monshausen, G. B., Messerli, M. A., and Gilroy, S. (2008). Imaging of the Yellow Cameleon 3.6 indicator reveals that elevations in cytosolic Ca^{2+} follow oscillating increases in growth in root hairs of Arabidopsis. *Plant Physiol.* 147, 1690–1698. doi: 10.1104/pp.108.123638

Monshausen, G. B., Miller, N. D., Murphy, A. S., and Gilroy, S. (2011). Dynamics of auxin-dependent Ca^{2+} and pH signaling in root growth revealed by integrating high-resolution imaging with automated computer vision-based analysis. *Plant J.* 65, 309–318. doi: 10.1111/j.1365-313X.2010.04423.x

Moseyko, N., and Feldman, L. J. (2001). Expression of pH-sensitive green fluorescent protein in *Arabidopsis thaliana*. *Plant Cell Environ.* 24, 557–563. doi: 10.1046/j.1365-3040.2001.00703.x

Munemasa, S., Hossain, M. A., Nakamura, Y., Mori, I. C., and Murata, Y. (2011). The Arabidopsis calcium-dependent protein kinase, CPK6, functions as a positive regulator of methyl jasmonate signaling in guard cells. *Plant Physiol.* 155, 553–561. doi: 10.1104/pp.110.162750

Munnik, T., and Nielsen, E. (2011). Green light for polyphosphoinositide signals in plants. *Curr. Opin. Plant Biol.* 14, 489–497. doi: 10.1016/j.pbi.2011.06.007

Nagai, T., Yamada, S., Tominaga, T., Ichikawa, M., and Miyawaki, A. (2004). Expanded dynamic range of fluorescent indicators for Ca^{2+} by circularly permuted yellow fluorescent proteins. *Proc. Natl. Acad. Sci. U.S.A.* 101, 10554–10559. doi: 10.1073/pnas.0400417101

Newman, R. H., Fosbrink, M. D., and Zhang, J. (2011). Genetically encodable fluorescent biosensors for tracking signaling dynamics in living cells. *Chem. Rev.* 111, 3614–3666. doi: 10.1021/cr100002u

Okumoto, S. (2010). Imaging approach for monitoring cellular metabolites and ions using genetically encoded biosensors. *Curr. Opin. Biotechnol.* 21, 45–54. doi: 10.1016/j.copbio.2010.01.009

Okumoto, S. (2012). Quantitative imaging using genetically encoded sensors for small molecules in plants. *Plant J.* 70, 108–117. doi: 10.1111/j.1365-313X.2012.04910.x

Okumoto, S., Jones, A., and Frommer, W. B. (2012). Quantitative imaging with fluorescent biosensors: advanced tools for spatiotemporal analysis of biodynamics in cells. *Annu. Rev. Plant Biol.* 63, 663–706. doi: 10.1146/annurev-arplant-042110-103745

Palmer, A. E., Giacomello, M., Kortemme, T., Hires, S. A., Lev-Ram, V., Baker, D., et al. (2006). Ca^{2+} indicators based on computationally redesigned calmodulin-peptide pairs. *Chem. Biol.* 13, 521–530. doi: 10.1016/j.chembiol.2006.03.007

Palmer, A. E., Qin, Y., Park, J. G., and McCombs, J. E. (2011). Design and application of genetically encoded biosensors. *Trends Biotechnol.* 29, 144–152. doi: 10.1016/j.tibtech.2010.12.004

Piljic, A., and Schultz, C. (2008). Simultaneous recording of multiple cellular events by FRET. *ACS Chem. Biol.* 3, 156–160. doi: 10.1021/cb700247q

Plieth, C., and Saleh, L. (2013). A9C sensitive Cl(-)-accumulation in *A. thaliana* root cells during salt stress is controlled by internal and external calcium. *Plant Signal. Behav.* [Epub ahead of print].

Plieth, C., Sattelmacher, B., Trewavas, A., Hansen, U., and Knight, M. (2001). Engineering plants expressiong calcium and pH indicators in the cytoplasm and the apoplast. *Plant Nutri.* 92, 252–253. doi: 10.1007/0-306-47624-X_121

Rincon-Zachary, M., Teaster, N. D., Sparks, J. A., Valster, A. H., Motes, C. M., and Blancaflor, E. B. (2010). Fluorescence resonance energy transfer-sensitized emission of yellow Cameleon 3.60 reveals root zone-specific calcium signatures in Arabidopsis in response to aluminum and other trivalent cations. *Plant Physiol.* 152, 1442–1458. doi: 10.1104/pp.109.147256

Rosenwasser, S., Rot, I., Meyer, A. J., Feldman, L., Jiang, K., and Friedman, H. (2010). A fluorometer-based method for monitoring oxidation of

redox-sensitive GFP (roGFP) during development and extended dark stress. *Physiol. Plant* 138, 493–502. doi: 10.1111/j.1399-3054.2009.01334.x

Schulte, A., Lorenzen, I., Bottcher, M., and Plieth, C. (2006). A novel fluorescent pH probe for expression in plants. *Plant Methods* 2, 7. doi: 10.1186/1746-4811-2-7

Schwarzlander, M., Fricker, M. D., Muller, C., Marty, L., Brach, T., Novak, J., et al. (2008). Confocal imaging of glutathione redox potential in living plant cells. *J. Microsc.* 231, 299–316. doi: 10.1111/j.1365-2818.2008.02030.x

Schwarzlander, M., Fricker, M. D., and Sweetlove, L. J. (2009). Monitoring the *in vivo* redox state of plant mitochondria: effect of respiratory inhibitors, abiotic stress and assessment of recovery from oxidative challenge. *Biochim. Biophys. Acta* 1787, 468–475. doi: 10.1016/j.bbabio.2009.01.020

Shen, J., Zeng, Y., Zhuang, X., Sun, L., Yao, X., Pimpl, P., et al. (2013). Organelle pH in the Arabidopsis endomembrane system. *Mol. Plant*. doi: 10.1093/mp/sst079. [Epub ahead of print].

Sieberer, B. J., Chabaud, M., Timmers, A. C., Monin, A., Fournier, J., and Barker, D. G. (2009). A nuclear-targeted Cameleon demonstrates intranuclear Ca^{2+} spiking in Medicago truncatula root hairs in response to rhizobial nodulation factors. *Plant Physiol.* 151, 1197–1206. doi: 10.1104/pp.109.142851

Siegel, R. S., Xue, S., Murata, Y., Yang, Y., Nishimura, N., Wang, A., et al. (2009). Calcium elevation-dependent and attenuated resting calcium-dependent abscisic acid induction of stomatal closure and abscisic acid-induced enhancement of calcium sensitivities of S-type anion and inward-rectifying K channels in Arabidopsis guard cells. *Plant J.* 59, 207–220. doi: 10.1111/j.1365-313X.2009.03872.x

Sun, J., Miwa, H., Downie, J. A., and Oldroyd, G. E. (2007). Mastoparan activates calcium spiking analogous to Nod factor-induced responses in Medicago truncatula root hair cells. *Plant Physiol.* 144, 695–702. doi: 10.1104/pp.106.093294

Swanson, S. J., Choi, W. G., Chanoca, A., and Gilroy, S. (2011). *In vivo* imaging of Ca^{2+}, pH, and reactive oxygen species using fluorescent probes in plants. *Annu. Rev. Plant Biol.* 62, 273–297. doi: 10.1146/annurev-arplant-042110-103832

Swarup, R., Kramer, E. M., Perry, P., Knox, K., Leyser, H. M., Haseloff, J., et al. (2005). Root gravitropism requires lateral root cap and epidermal cells for transport and response to a mobile auxin signal. *Nat. Cell Biol.* 7, 1057–1065. doi: 10.1038/ncb1316

Tsien, R. Y. (1998). The green fluorescent protein. *Annu. Rev. Biochem.* 67, 509–544. doi: 10.1146/annurev.biochem.67.1.509

VanEngelenburg, S. B., and Palmer, A. E. (2008). Fluorescent biosensors of protein function. *Curr. Opin. Chem. Biol.* 12, 60–65. doi: 10.1016/j.cbpa.2008.01.020

van Leeuwen, W., Vermeer, J. E., Gadella, T. W. Jr., and Munnik, T. (2007). Visualization of phosphatidylinositol 4, 5-bisphosphate in the plasma membrane of suspension-cultured tobacco BY-2 cells and whole Arabidopsis seedlings. *Plant J.* 52, 1014–1026. doi: 10.1111/j.1365-313X.2007.03292.x

Vermeer, J. E., Thole, J. M., Goedhart, J., Nielsen, E., Munnik, T., and Gadella, T. W., Jr. (2009). Imaging phosphatidylinositol 4-phosphate dynamics in living plant cells. *Plant J.* 57, 356–372. doi: 10.1111/j.1365-313X.2008.03679.x

Vermeer, J. E., van Leeuwen, W., Tobena-Santamaria, R., Laxalt, A. M., Jones, D. R., Divecha, N., et al. (2006). Visualization of PtdIns3P dynamics in living plant cells. *Plant J.* 47, 687–700. doi: 10.1111/j.1365-313X.2006.02830.x

Watahiki, M. K., Trewavas, A. J., and Parton, R. M. (2004). Fluctuations in the pollen tube tip-focused calcium gradient are not reflected in nuclear calcium level: a comparative analysis using recombinant yellow Cameleon calcium reporter. *Sex. Plant Reprod.* 17, 125–130. doi: 10.1007/s00497-004-0224-x

Weinl, S., Held, K., Schlucking, K., Steinhorst, L., Kuhlgert, S., Hippler, M., et al. (2008). A plastid protein crucial for Ca^{2+}-regulated stomatal responses. *New Phytol.* 179, 675–686. doi: 10.1111/j.1469-8137.2008.02492.x

Yang, H., Bogner, M., Stierhof, Y. D., and Ludewig, U. (2010). H-independent glutamine transport in plant root tips. *PLoS ONE* 5:e8917. doi: 10.1371/journal.pone.0008917

Yoshizaki, H., Aoki, K., Nakamura, T., and Matsuda, M. (2006). Regulation of RalA GTPase by phosphatidylinositol 3-kinase as visualized by FRET probes. *Biochem. Soc. Trans.* 34, 851–854. doi: 10.1042/BST0340851

Young, J. J., Mehta, S., Israelsson, M., Godoski, J., Grill, E., and Schroeder, J. I. (2006). CO_2 signaling in guard cells: calcium sensitivity response modulation, a Ca^{2+}-independent phase, and CO(2) insensitivity of the gca2 mutant. *Proc. Natl. Acad. Sci. U.S.A.* 103, 7506–7511. doi: 10.1073/pnas.0602225103

Zhang, J., and Allen, M. D. (2007). FRET-based biosensors for protein kinases: illuminating the kinome. *Mol. Biosyst.* 3, 759–765. doi: 10.1039/b706628g

Conflict of Interest Statement: The authors declare that the research was conducted in the absence of any commercial or financial relationships that could be construed as a potential conflict of interest.

Received: 29 April 2013; accepted: 13 June 2013; published online: 12 July 2013.

*Citation: Gjetting SK, Schulz A and Fuglsang AT (2013) Perspectives for using genetically encoded fluorescent biosensors in plants. Front. Plant Sci. **4**:234. doi: 10.3389/fpls.2013.00234*

This article was submitted to Frontiers in Plant Cell Biology, a specialty of Frontiers in Plant Science.

Copyright © 2013 Gjetting, Schulz and Fuglsang. This is an open-access article distributed under the terms of the Creative Commons Attribution License, which permits use, distribution and reproduction in other forums, provided the original authors and source are credited and subject to any copyright notices concerning any third-party graphics etc.

frontiers in
PLANT SCIENCE

PERSPECTIVE ARTICLE
published: 18 December 2013
doi: 10.3389/fpls.2013.00523

Development and properties of genetically encoded pH sensors in plants

Alexandre Martinière[1]*, Guilhem Desbrosses[2], Hervé Sentenac[1] and Nadine Paris[1]*

[1] *Biochimie et Physiologie Moléculaire des Plantes, Institut de Biologie Intégrative des Plantes, UMR 5004 CNRS/UMR 0386 INRA/Montpellier SupAgro/Université Montpellier 2, Montpellier, France*
[2] *Laboratory of Tropical and Mediterranean Symbioses (UMR113, Université Montpellier 2, Institut de Recherche pour le Développement, Cirad Montpellier SupAgro, Institut National de la Recherche Agronomique), Université Montpellier 2, Montpellier, France*

Edited by:
Markus Schwarzländer, University of Bonn, Germany

Reviewed by:
Peter Pimpl, University of Tuebingen, Germany
Alexander Schulz, University of Copenhagen, Denmark
Melanie Krebs, University of Heidelberg, Germany

****Correspondence:***
Alexandre Martinière and Nadine Paris, Biochimie et Physiologie Moléculaire des Plantes, Institut de Biologie Intégrative des Plantes, UMR 5004 CNRS/UMR 0386 INRA/Montpellier SupAgro/Université Montpellier 2, F-34060 Montpellier Cedex 1, France
e-mail: martinie@supagro.inra.fr; paris@supagro.inra.fr

Fluorescent proteins (FPs) have given access to a large choice of live imaging techniques and have thereby profoundly modified our view of plant cells. Together with technological improvements in imaging, they have opened the possibility to monitor physico-chemical changes within cells. For this purpose, a new generation of FPs has been engineered. For instance, pHluorin, a point mutated version of green fluorescent protein, allows to get local pH estimates. In this paper, we will describe how genetically encoded sensors can be used to measure pH in the microenvironment of living tissues and subsequently discuss the role of pH in (i) exocytosis, (ii) ion uptake by plant roots, (iii) cell growth, and (iv) protein trafficking.

Keywords: pH, GFP, vacuoles, pHluorin, acidic gowth theory, ion transport, endomembrane trafficking

INTRODUCTION

Genetically encoded fluorescent sensors are becoming extremely powerful tools for functional imaging. For instance, the classic calcium sensor introduced by Roger Tsien's lab, cameleon, is now extensively used in the plant field (Miyawaki et al., 1997; Romoser et al., 1997). Such calcium sensors have allowed major breakthroughs regarding, for instance, the molecular dialog between plant roots and symbiotic microorganisms (Sieberer et al., 2012; Singh and Parniske, 2012). More recently, dedicated strategies have led to the development of very promising biosensors, which allow to probe the local concentration of disaccharides, phosphate, amino acid, or ammonium (reviewed in Gjetting et al., 2013; Jones et al., 2013). In this perspective issue, we will focus on a specific type of sensors optimized for pH measurement.

PROPERTIES OF GENETICALLY ENCODED pH SENSORS

Classical fluorescent dyes have been used to estimate pH in plants. For example, fluorescein coupled to dextran allows pH recording in the close vicinity of roots (Monshausen et al., 2009, 2011) or shoots (Geilfus and Mühling, 2012). The 2′,7′-Bis(2-carboxyethyl)-5(6)-carboxyfluorescein (BCECF), which was first introduced by Rink et al. (1982), is also classically used to measure plant vacuolar pH, especially in its membrane permeable form as acetomethyl ester (BCECF-AM; Krebs et al., 2010). Nevertheless, such approaches are invasive and do not allow measuring pH in other intracellular cell structures. Genetically encoded pH sensors have been designed to overcome these limitations.

The chromophore of green fluorescent protein (GFP) is formed by two autocatalytic reactions (cyclization and oxidation) between Ser65, Tyr66, and Gly67 (review in Wachter, 2007). It absorbs light at two maxima: 395 nm when protonated and 475 nm when depronated (Bizzarri et al., 2009). This shift in absorption has been extensively used to record pH in living organisms (Kneen et al., 1998; Llopis et al., 1998), and optimized versions of GFP for pH measurement have been generated. Ecliptic and superecliptic pHluorins display almost no fluorescence when protonated, allowing sensitive detection of biological processes associated with pH increase (**Table 1**; Miesenböck et al., 1998; Sankaranarayanan and Ryan, 2001). However, the equilibrium between the protonated and deprotonated states of these proteins is also affected by temperature and ionic strength. Furthermore, the light emitted by such sensor protein is dependent on its own concentration. Thus a variation in fluorescence signal can result either from a change in pH or in concentration of the sensor. To circumvent this issue, ratiometric pH sensors have been developed providing a pH readout independent of the probe concentration. Among such sensors, one of the most popular is pHluorin. It was generated by introducing point mutations in *Aequorea victoria* GFP (AvGFP) sequence, especially S202H, which conferred ratiometric behavior to the sensor (Miesenböck et al., 1998; Bizzarri et al., 2009). For example, pHluorin displays a strong increase in absorption at 475 nm

Table 1 | Selected genetically encoded pH sensors available for *in vivo* pH measurements.

Constructs	Type	Excitation(nm)	Emission(nm)	pH range	pKa	Delta ratio	Reference
pHluorin, pHluorin2*, RaVC**, PRpHluorin***, pHGFP****	Ratiometric	395/475	510	5.4–8.4	6.9	2.5	Miesenböck et al. (1998)
Ecliptic pHluorin, PEpHluorin***	Ecliptic	395/477	510	6.5–8	7.2	13.5	Miesenböck et al. (1998)
Superecliptic pHluorin	Ecliptic	477	510	5.5–8.5	7.2	13	Sankaranarayanan and Ryan (2001)
deGFP3	Ratiometric	396	460/515	6–9	7.3	20	Hanson et al. (2002)
E2GFP	Ratiometric	458/488	500/560	5–8.5	6.9/7.5	10	Bizzarri et al. (2006)
ptGFP	Ratiometric	390/475	540	3.8–8.2	7.3	36	Schulte et al. (2006)
pHlameleon 6	FRET-based ratiometric	458	481/533	5–7.5	5.6	9	Esposito et al. (2008)
pHusion	Ratiometric	488/558	510/600	4.5–8	5.8	6	Gjetting et al. (2012)
pHlash	BRET	n.a.	475/525	5.4–9	n.a.	3.3	Zhang et al. (2012)

**Eightfold brighter version of pHluorin (Mahon, 2011)*
***pHluorin with optimize codon usage for Aspergillus (Bagar et al., 2009)*
****pHluorin with optimize codon usage for Arabidopsis (Shen et al., 2013)*
*****pHGFP, chimera between smGFP (Davis and Vierstra, 1998) and pHluorin to prevent splicing (Moseyko and Feldman, 2001)*

and, simultaneously, a strong decrease in absorption at 395 nm when the pH is shifted from 7.5 to 5.5. The pHluorin sensor has a pKa of 6.9 and the dynamic range of fluorescent signal is from pH 5.4 to 8.4 (**Table 1**). This pH range is suitable for most plant subcellular compartments, with the exception of the apoplast, which is too acidic, and the vacuole, where GFP is degraded (Tamura et al., 2003). Later, derivatives of this protein were engineered to improve the level of expression. This is the case for ratiometric Venus Citrine (RaVC), whose codon usage has been optimized for expression in *Aspergillus* (Bagar et al., 2009), and the plant-solubility-modified ratiometric pHluorin (*PRpHluorin*), optimized for *Arabidopsis* (Shen et al., 2013). To avoid erroneous pH measurement due to chromatic aberrations, an alternative type of ratiometric sensor was generated from S65T GFP, where the emission is yellow-shifted upon alkalization (**Table 1**). This dual emission GFP (deGFP) contains the point mutations T203C and H148G or H148C (Hanson et al., 2002). In addition, some sensors such as E^2GFP and E^1GFP combine dual emission and dual excitation features (Bizzarri et al., 2006; Arosio et al., 2007).

The major limitation of using pHluorin and its derivates, especially in plant tissues, is their acidic quenching at an apparent pH near 4.5. Two strategies were used to improve pH sensing in acidic environments. The first strategy is to use a fluorescent protein (FP), *Pt*-GFP, from orange sea pen, *Ptilosarcus gurneyi* (Schulte et al., 2006). Although *Pt*-GFP has a pKa similar to that of pHluorin (pK_{PtGFP}: 7.3), this protein has a broader pH response range and is more stable in acidic conditions (Schulte et al., 2006). The second strategy is to make a tandem of FPs with highly different ranges of pH responsiveness. The measure of pH is then either given by Förster resonance energy transfer (FRET) between these two proteins, as for pHlameleon (Esposito et al., 2008) or by the ratio of fluorescence of the proteins. In particular, the tandem of enhanced GFP (eGFP) and monomeric red FP (mRFP1) is suitable for measuring pH in the apoplasm (Gjetting et al., 2012). Finally, a new pH biosensor was developed recently based on bioluminescence resonance energy transfer (BRET). This pHlash sensor is composed of a luciferase as a donor, fused to pH-sensitive Venus as acceptor (Zhang et al., 2012). Use of bioluminescence significantly improves the signal-to-noise ratio making BRET particularly useful for experimentation at the whole tissue or organism scale.

Regardless of the exact type of genetically encoded pH sensors, estimation of the local pH value from the fluorescence data is not straightforward. This requires calibration to characterize the relationship between the fluorescence properties of the sensor and pH. The calibration can be carried out either *in vitro* or *in vivo* (Gao et al., 2004; Schulte et al., 2006; Shen et al., 2013). *In vitro* calibration uses heterologously expressed sensors in buffers of different pH. Such a calibration does not take into account the ionic strength and buffering capacity of the cell and thus can lead to substantial artifacts (Schulte et al., 2006). *In vivo* calibration uses sensor-expressing plant cells that are treated with an ionophore, such as nigericin, in presence of a solution with sufficient buffering capacity to clamp the pH of the cellular environment containing the sensor. This approach should be favored whenever possible, but is still limited for several reasons. First, there is no objective way to ensure that the equilibrium has reached between the bathing media and the cell compartment where the sensor is located. This is especially true when the sensor is in the lumen of intracellular structures, meaning that the ionophore has to be effective on two successive membranes. Secondly, the ionophore modifies the ion content of the cell and consequently the native buffering capacity and ionic strength. Such calibration issues may explain the ongoing debate on the feasibility of measuring absolute pH values with sensors *in vivo* (Schulte et al., 2006; Bizzarri et al., 2009).

ANALYSIS OF EXOCYTOSIS EVENTS WITH pH SENSORS

Genetically encoded pH sensors can be used to investigate processes that give rise to, or rely on, changes in pH. During exocytosis, vesicle lumen undergoes a rapid alkalinization upon fusion to the plasma membrane. Since the pioneering study by Miesenböck et al. (1998), ecliptic pHluorin has been extensively used as an exocytosis indicator (Sankaranarayanan et al., 2000; Gandhi and Stevens, 2003; Taylor et al., 2011). For instance, in the synaptic cleft, Gandhi and Stevens (2003) were able to distinguish three types of vesicle behaviors at the plasma membrane. In another study, ecliptic pHluorin used to describe the dependency of vesicle fusion on actin filaments and cdc42, a protein controlling cell division (Alberts et al., 2006). Similar approaches would appear useful in the plant field. According to the classical view of ligand–receptor trafficking, a difference in pH is expected between the lumen of the *trans*-Golgi network (TGN) and the apoplastic face of the plasma membrane (Robinson et al., 2012). Hence, the luminal pH of exocytic vesicles is predicted to be different before and after fusion with the plasma membrane. In recent reports, TGN compartments have been shown to have the most acidic lumen of the secretory pathway, with a pH around 6 (Martinière et al., 2013; Shen et al., 2013; **Table 2**). On the other side, apoplastic pH is likely to be highly variable and dependent on tissue type and development stage (Gao et al., 2004; Staal et al., 2011; Geilfus and Mühling, 2012; Gjetting et al., 2012). Unfortunately, studies that concomitantly measure the pH in the TGN and in the apoplasm are still lacking.

pH WITHIN THE APOPLAST

In plants, the plasma membrane is energized by P-type proton pump ATPases. Direct evidence has been obtained that proton diffusion within the apoplast away from the membrane can be rate-limiting when compared to proton excretion by the proton pumps. Using weak acid influx for assaying pH, it has been shown that the local pH in the unstirred aqueous layers next to the plasmalemma can be much lower than that of the external bathing solution, by up to 2 pH units under conditions that maximize the rate of net proton excretion (Sentenac and Grignon, 1987; Grignon and Sentenac, 1991). A few studies on the dependency of membrane transport in roots on external pH have quantitatively assessed this steady state pH shift at the membrane surface due to proton excretion by using weak acid influx assays under the same conditions as those used for the transport measurements (Thibaud et al., 1998). Clearly, the results indicated that this shift in pH strongly contributed to energization of the cell membrane and had to be taken into account to explain, for instance, kinetic and thermodynamic features of nitrate, phosphate, or potassium transport (Thibaud et al., 1988), or the effect of HCO_3^-, a buffer that can be naturally present in the external solution (in calcareous soils), on the transport rate of these nutriments (Toulon et al., 1989) or on iron reduction at the cell surface (Toulon et al., 1992).

Different methods have been developed to estimate local pH values, using proton-selective micro-electrodes (Felle, 1998) or impermeable pH-sensitive dyes (Taylor et al., 1996; Monshausen et al., 2009, 2011), or collecting apoplasmic fluids (Mühling and Sattelmacher, 1995). However, such approaches provide estimates of the pH conditions at the organ surface or, at best, of the mean pH within the apoplast, and not of the local pH in close vicinity of the membrane, which is the actual pH sensed by the ion transporters. Another source of difficulties is the possibility of heterogeneities within the apoplast. For example, in the root cortex and for the inner cortical cells, the diffusion barrier that

Table 2 | Summary of pH measurements in plant cells using pH sensors.

	Tobacco epidermis (Martinière et al., 2013)	***Arabidopsis* root tip (Martinière et al., 2013)**	***Arabidopsis* protoplasts (Shen et al., 2013)**
Cytosol	7.8 (pHluorin)	8 (pHluorin)	7.3 (PpHluorin)
ER	7.5 (pHluorin-hdel)	7.7 (pHluorin-hdel)	7.1 (PpHluorin-hdel)
Cis-Golgi			6.8 (ManI-PpHluorin)
Trans-Golgi	6.9 (ST-pHluorin)	6.8 (ST-pHluorin)	
TGN	6.1 (pHluorin-AtVSR2)	6 (pHluorin-AtVSR2)	6.2 (PpHluorin-AtVSR2 trunc)
PVC	6.8 (pHluorin-AtVSR2)		
Late PVC	7.1 (pHluorin-AtVSR2-IMAA)		
TGN plus recycling endosomes	6.5 (pHluorin-AtVSR2-YA)		6.3 (PpHluorin-truncAtVSR2-YA)
Vacuole	6 (BCECF-AM)	5.7 (BCECF-AM)	5.2 (Aleurain-PpHluorin)
Plastid stroma			7.2 (RecaA-PpHluorin)
Peroxisome			8.4 (PpHluorin-SLR)
Mitochondria			8.1 (mito-PpHluorin)
Nucleus			7.2 (NLS-PpHluorin)

The average pH is indicated for each subcellular compartment the pH sensor used for the measurement being indicated between parenthesis. ST, sialyltransferase; ManI, mannosidase 1; AtVSR2, At2g14720; trunc, truncated AtVSR2 with no luminal domain; BCECF-AM, 2′,7′-Bis(2-carboxyethyl)-5(6)-carboxyfluorescein; tetrakis(acetoxymethyl) ester mito, transit peptide of the β-subunit of NpF1-ATP synthase; NLS, nuclear localization signal.

slows proton migration toward the external solution comprises the entire apoplastic continuum, from cortical cells surrounding the endodermis to the root epidermis surface. Furthermore, longitudinal heterogeneities in surface pH have been observed between the root apex, the elongation region and the fully differentiated zone, due to differences in the rate and direction of proton transport. The physiological consequences and roles of such radial and longitudinal differences, in terms of membrane energization and transport activity, have been poorly investigated. Clearly, genetically encoded pH sensors open novel perspectives in this domain of the root structure–function relationship. In this respect, Moseyko and Feldman (2001) and Gao et al. (2004) have developed pioneering approaches. For example, large pH variations were observed in response to salt stress. When challenged with 100 mM NaCl, root cells displayed a more alkaline apoplasm and a more acidic cytosol. These changes in pH might result from specific activation of H^+:Na^+ antiport activity mediated by the plasma membrane Salt-Overly-Sensitive1 (SOS1) antiporter in response to salinity constraint (Quintero et al., 2011). Such analyses clearly indicate that expression of pH sensor proteins in mutant plants could allow rapid progress in investigating the root structure–function relationship and its role in membrane energization, ion transport and plant adaptation to environmental stresses.

CELL WALL pH AND GROWTH

Cell capacity to control the apoplastic pH plays a major role also in plant growth and development. Indeed, according to the acid growth theory, cell wall "loosening" favored by low pH allows cell elongation (Rayle and Cleland, 1992). In a typical sequence of events, auxin stimulates proton secretion by plasmalemma proton pump ATPases, resulting in cell wall acidification, causing activation of expansins, which loosen cellulose microfibrils. As a result, cell walls become more extensible favoring turgor-driven cell elongation. In support to the acid growth theory, the elongation zone of the root generally displays a more acidic apoplasm than the fully differentiated zone (Staal et al., 2011). Intriguingly, a close-up analysis using a pH sensor reveals highly dynamic fluctuations of root surface pH with alkalinization and acidification periods and alkalinization bursts along the root longitudinal axis or alternating between opposing flanks (Monshausen et al., 2011). Such results indicate that a net influx of protons can occur in epidermal cells, as previously reported in other studies (O'Neill and Scott, 1983). Intriguingly, a recent report shows that treatment of root tips with indole-3-acetic acid (IAA) induces an increase in pH by about 0.5–0.8 pH units (Gjetting et al., 2012), which might be related to the periodical alkalinization previously reported in root tips (Monshausen et al., 2011).

pH MAPPING OF ORGANELLES AND PROTEIN TARGETING

Taking advantage of growing knowledge in protein targeting mechanisms, appropriate signal sequences can be fused to the coding sequence of the pH sensor so that this is targeted later to various cell membranes or compartments. Using such an approach, pH in various intracellular compartments was measured *in vivo* in mammalian and, more recently, in *Arabidopsis* protoplasts (Shen et al., 2013), tobacco leaf epidermal cells or *Arabidopsis* root tip cells (Martinière et al., 2013). These studies directly demonstrate a gradual acidification of 1.5–2 pH units in the lumen of the endomembrane system with ER displaying the most alkaline pH and vacuole the most acidic one (see **Table 2**). Interestingly, some pH differences exist for a given compartment between plant species (cytosol, endoplasmic reticulum and vacuole; **Table 2**). These variations could be the result of biological variation between the systems tested (intact cells versus protoplast) or could be due to differences in growing condition. For instance, pH homeostasis is known to be sensitive to light intensity (Martinière et al., 2013). Most compartment markers cycle at least between two subcellular localizations and there is still no way to target a sensor solely to either the lumen of the TGN, the prevacuolar compartment (PVC) or the late PVC. Fusion of pH sensors to the vacuolar sorting receptor (VSR) mutants Y165A and IMAA allowed to partially solve such localization issue, the former mutant being preferentially retained in the TGN and the latter localized in the LPVC. This allowed differentiation between TGN and the PVC and getting pH estimates for these two compartments (Martinière et al., 2013; Shen et al., 2013). However, it should be noted that, in addition to TGN, the Y165A VSR mutant is very likely to also label recycling endosomes and plasma membranes (daSilva et al., 2006; Saint-Jean et al., 2010). Furthermore, accumulation of the IMAA mutant in the LPVC is only transient (Saint-Jean et al., 2010).

In average, the population of VSR labeled compartments has a pH intermediate between the *trans*-Golgi and the vacuole in all the systems tested. But surprisingly, the TGN is actually more acidic, with a pH 6, than the PVC (pH 6.8) or even the late PVC (pH 7.1, see **Table 2**; Martinière et al., 2013). This result fits well with the localization of V-type ATPase involved in pumping protons. Indeed, VHA-a1 protein is preferentially accumulated in the TGN (Dettmer et al., 2006) and is not detected in the multivesicular bodies (MVB; Robinson et al., 2012) or PVC. Accordingly to the proton leak model, while V-type ATPase acidifies a compartment, antiporters could be involved in proton extrusion (Demaurex, 2002). For instance, NHX5 and NHX6 Na^+/H^+ antiports have been proposed to be involved in such a mechanism in plant endosomes (Bassil et al., 2011). Therefore, the relative amount of VHA-a1 and proton antiporters such as NHX5/6, in compartment on the way to the vacuole could have a preponderant role in proton homeostasis and substantial consequence in terms of protein sorting. In support to this hypothesis, is the mistargeting of a soluble vacuolar marker in *nhx5 nhx6* double knockout (Bassil et al., 2011) and the fact that the pH measured in the TGN and the PVC fits well with the distribution of VHA-a1 and NHX5/6 in tobacco leaf epidermal cells (Martinière et al., 2013).

The fact that the PVC is more alkaline than TGN is surprising and in contradiction with the VSR-mediated vacuolar sorting model where acidification in the PVC is thought to be responsible for a release of the ligand by the receptor (Kirsch et al., 1994; Ahmed et al., 2000; Shimada et al., 2003). In fact, the *in vitro* binding curve between VSR and the ligand is bell shaped with an optimum pH at 6 (Kirsch et al., 1994). This value corresponds to the pH measured *in vivo* in the TGN (Martinière et al., 2013)

suggesting that binding of VSR to its ligand would be optimal in the TGN but significantly lower in more acidic and alkaline compartments. The use of ratiometric sensors to measure the endomembrane luminal pH therefore suggests that alkalinization rather than acidification would trigger ligand release from the receptor VSR in the PVC (Martinière et al., 2013). Of course this model does not take into account other environmental parameters in TGN and PVC such as the calcium concentration that is also known to regulate ligand binding for a least some members of the VSR family (Watanabe et al., 2002, 2004). Finally, it is also important to point out that the pH reported for the PVC or the TGN is an average from a large population of independent organelles with some variation of pH values. This difference is either due to technical limitations in imaging or may reflect pH variability between compartments of same identity, e.g., TGN or PVC. A model for VSR-mediated transport is still a matter of debate (Robinson and Pimpl, 2013).

It is likely that pH ratiometric sensors will open new perspectives in our understanding of the mobility, functional heterogeneity and remodeling capacities of organelles. For instance, the TGN has been assumed to undergo maturation as its morphology changes over time (Scheuring et al., 2011). Using pH sensors along with dynamic studies could provide evidence for these maturation events.

CONCLUDING REMARKS

Genetically encoded pH sensors have opened avenues for cell biology. They will provide valuable functional data with respect to cell compartmentation, protein trafficking, acidic growth, or ion diffusion within plant tissue. One of the future challenges will be to improve the definition of pH information provided by the sensor as cell nano-environments are anticipated. For instance, protein and lipid composition of membranes have a substantial effect on proton diffusion. As well, it is reasonable to anticipate a higher proton concentration in the vicinity of ATPase pumps and therefore heterogeneity on membrane surfaces with respect to pH.

REFERENCES

Ahmed, S. U., Rojo, E., Kovaleva, V., Venkataraman, S., Dombrowski, J. E., Matsuoka, K., et al. (2000). The plant vacuolar sorting receptor AtELP is involved in transport of NH(2)-terminal propeptide-containing vacuolar proteins in *Arabidopsis thaliana*. *J. Cell Biol.* 149, 1335–1344. doi: 10.1083/jcb.149.7.1335

Alberts, P., Rudge, R., Irinopoulou, T., Danglot, L., Gauthier-Rouvière, C., and Galli, T. (2006). Cdc42 and actin control polarized expression of TI-VAMP vesicles to neuronal growth cones and their fusion with the plasma membrane. *Mol. Biol. Cell* 17, 1194–1203. doi: 10.1091/mbc.E05-07-0643

Arosio, D., Garau, G., Ricci, F., Marchetti, L., Bizzarri, R., Nifosì, R., et al. (2007). Spectroscopic and structural study of proton and halide ion cooperative binding to gfp. *Biophys. J.* 93, 232–244. doi: 10.1529/biophysj.106.102319

Bagar, T., Altenbach, K., Read, N. D., and Benčina, M. (2009). Live-Cell imaging and measurement of intracellular pH in filamentous fungi using a genetically encoded ratiometric probe. *Eukaryot. Cell* 8, 703–712. doi: 10.1128/EC.00333-08

Bassil, E., Ohto, M., Esumi, T., Tajima, H., Zhu, Z., Cagnac, O., et al. (2011). The *Arabidopsis* intracellular Na+/H+ antiporters NHX5 and NHX6 are endosome associated and necessary for plant growth and development. *Plant Cell* 23, 224–239. doi: 10.1105/tpc.110.079426

Bizzarri, R., Arcangeli, C., Arosio, D., Ricci, F., Faraci, P., Cardarelli, F., et al. (2006). Development of a novel GFP-based ratiometric excitation and emission pH indicator for intracellular studies. *Biophys. J.* 90, 3300–3314. doi: 10.1529/biophysj.105.074708

Bizzarri, R., Serresi, M., Luin, S., and Beltram, F. (2009). Green fluorescent protein based pH indicators for in vivo use: a review. *Anal. Bioanal. Chem.* 393, 1107–1122. doi: 10.1007/s00216-008-2515-9

daSilva, L. L. P., Foresti, O., and Denecke, J. (2006). Targeting of the plant vacuolar sorting receptor BP80 is dependent on multiple sorting signals in the cytosolic tail. *Plant Cell* 18, 1477–1497. doi: 10.1105/tpc.105.040394

Davis, S. J., and Vierstra, R. D. (1998). Soluble, highly fluorescent variants of green fluorescent protein (GFP) for use in higher plants. *Plant Mol. Biol.* 36, 521–528. doi: 10.1023/A:1005991617182

Demaurex, N. (2002). pH Homeostasis of cellular organelles. *News Physiol. Sci.* 17, 1–5.

Dettmer, J., Hong-Hermesdorf, A., Stierhof, Y.-D., and Schumacher, K. (2006). Vacuolar H^+-ATPase activity is required for endocytic and secretory trafficking in *Arabidopsis*. *Plant Cell* 18, 715–730. doi: 10.1105/tpc.105.037978

Esposito, A., Gralle, M., Dani, M. A. C., Lange, D., and Wouters, F. S. (2008). pHlameleons: a family of FRET-based protein sensors for quantitative pH imaging. *Biochemistry* 47, 13115–13126. doi: 10.1021/bi8009482

Felle, H. H. (1998). The apoplastic pH of the *Zea mays* root cortex as measured with pH-sensitive microelectrodes: aspects of regulation. *J. Exp. Bot.* 49, 987–995. doi: 10.1093/jxb/49.323.987

Gandhi, S. P., and Stevens, C. F. (2003). Three modes of synaptic vesicular recycling revealed by single-vesicle imaging. *Nature* 423, 607–613. doi: 10.1038/nature01677

Gao, D., Knight, M. R., Trewavas, A. J., Sattelmacher, B., and Plieth, C. (2004). Self-reporting *Arabidopsis* expressing pH and $[Ca^{2+}]$ indicators unveil ion dynamics in the cytoplasm and in the apoplast under abiotic stress. *Plant Physiol.* 134, 898–908. doi: 10.1104/pp.103.032508

Geilfus, C.-M., and Mühling, K. H. (2012). Transient alkalinization in the leaf apoplast of *Vicia faba* L. depends on NaCl stress intensity: an in situ ratio imaging study. *Plant Cell Environ.* 35, 578–587. doi: 10.1111/j.1365-3040.2011.02437.x

Gjetting, K. S. K., Ytting, C. K., Schulz, A., and Fuglsang, A. T. (2012). Live imaging of intra- and extracellular pH in plants using pHusion, a novel genetically encoded biosensor. *J. Exp. Bot.* 63, 3207–3218. doi: 10.1093/jxb/ers040

Gjetting, S. K., Schulz, A., and Fuglsang, A. T. (2013). Perspectives for using genetically encoded fluorescent biosensors in plants. *Front. Plant Sci.* 4:234. doi: 10.3389/fpls.2013.00234

Grignon, C., and Sentenac, H. (1991). pH and ionic conditions in the apoplast. *Annu. Rev. Plant Physiol. Plant Mol. Biol.* 42, 103–128. doi: 10.1146/annurev.pp.42.060191.000535

Hanson, G. T., McAnaney, T. B., Park, E. S., Rendell, M. E. P., Yarbrough, D. K., Chu, S., et al. (2002). Green fluorescent protein variants as ratiometric dual emission pH sensors. 1. Structural characterization and preliminary application. *Biochemistry* 41, 15477–15488. doi: 10.1021/bi026609p

Jones, A. M., Grossmann, G., Danielson, J. Å., Sosso, D., Chen, L.-Q., Ho, C.-H., et al. (2013). In vivo biochemistry: applications for small molecule biosensors in plant biology. *Curr. Opin. Plant Biol.* 16, 389–395. doi: 10.1016/j.pbi.2013.02.010

Kirsch, T., Paris, N., Butler, J. M., Beevers, L., and Rogers, J. C. (1994). Purification and initial characterization of a potential plant vacuolar targeting receptor. *Proc. Natl. Acad. Sci. U.S.A.* 91, 3403–3407. doi: 10.1073/pnas.91.8.3403

Kneen, M., Farinas, J., Li, Y., and Verkman, A. S. (1998). Green fluorescent protein as a noninvasive intracellular pH indicator. *Biophys. J.* 74, 1591–1599. doi: 10.1016/S0006-3495(98)77870-1

Krebs, M., Beyhl, D., Görlich, E., Al-Rasheid, K. A. S., Marten, I., Stierhof, Y.-D., et al. (2010). *Arabidopsis* V-ATPase activity at the tonoplast is required for efficient nutrient storage but not for sodium accumulation. *Proc. Natl. Acad. Sci. U.S.A.* 107, 3251–3256. doi: 10.1073/pnas.0913035107

Llopis, J., McCaffery, J. M., Miyawaki, A., Farquhar, M. G., and Tsien, R. Y. (1998). Measurement of cytosolic, mitochondrial, and Golgi pH in single living cells with green fluorescent proteins. *Proc. Natl. Acad. Sci. U.S.A.* 95, 6803–6808. doi: 10.1073/pnas.95.12.6803

Mahon, M. J. (2011). pHluorin2: an enhanced, ratiometric, pH-sensitive green florescent protein. *Adv. Biosci. Biotechnol.* 2, 132–137. doi: 10.4236/abb.2011.23021

Martinière, A., Bassil, E., Jublanc, E., Alcon, C., Reguera, M., Sentenac, H., et al. (2013). In vivo intracellular pH measurements in Tobacco and *Arabidopsis* reveal an unexpected pH gradient in the endomembrane system. *Plant Cell* 25, 4028–4043. doi: 10.1105/tpc.113.116897

Miesenböck, G., De Angelis, D. A., and Rothman, J. E. (1998). Visualizing secretion and synaptic transmission with pH-sensitive green fluorescent proteins. *Nature* 394, 192–195. doi: 10.1038/28190

Miyawaki, A., Llopis, J., Heim, R., McCaffery, J. M., Adams, J. A., Ikura, M., et al. (1997). Fluorescent indicators for Ca^{2+} based on green fluorescent proteins and calmodulin. *Nature* 388, 882–887. doi: 10.1038/42264

Monshausen, G. B., Bibikova, T. N., Weisenseel, M. H., and Gilroy, S. (2009). Ca^{2+} regulates reactive oxygen species production and pH during mechanosensing in *Arabidopsis* roots. *Plant Cell* 21, 2341–2356. doi: 10.1105/tpc.109.068395

Monshausen, G. B., Miller, N. D., Murphy, A. S., and Gilroy, S. (2011). Dynamics of auxin-dependent Ca^{2+} and pH signaling in root growth revealed by integrating high-resolution imaging with automated computer vision-based analysis. *Plant J.* 65, 309–318. doi: 10.1111/j.1365-313X.2010.04423.x

Moseyko, N., and Feldman, L. J. (2001). Expression of pH-sensitive green fluorescent protein in *Arabidopsis thaliana*. *Plant Cell Environ.* 24, 557–563. doi: 10.1046/j.1365-3040.2001.00703.x

Mühling, K. H., and Sattelmacher, B. (1995). Apoplastic ion concentration of intact leaves of field bean (*Vicia faba*) as influenced by ammonium and nitrate nutrition. *J. Plant Physiol.* 147, 81–86. doi: 10.1016/S0176-1617(11)81417-3

O'Neill, R. A., and Scott, T. K. (1983). Proton flux and elongation in primary roots of barley (*Hordeum vulgare* L.). *Plant Physiol.* 73, 199–201. doi: 10.1104/pp.73.1.199

Quintero, F. J., Martinez-Atienza, J., Villalta, I., Jiang, X., Kim, W.-Y., Ali, Z., et al. (2011). Activation of the plasma membrane Na/H antiporter Salt-Overly-Sensitive 1 (SOS1) by phosphorylation of an auto-inhibitory C-terminal domain. *Proc. Natl. Acad. Sci. U.S.A.* 108, 2611–2616. doi: 10.1073/pnas.1018921108

Rayle, D. L., and Cleland, R. E. (1992). The Acid Growth Theory of auxin-induced cell elongation is alive and well. *Plant Physiol.* 99, 1271–1274. doi: 10.1104/pp.99.4.1271

Rink, T. J., Tsien, R. Y., and Pozzan, T. (1982). Cytoplasmic pH and free Mg2+ in lymphocytes. *J. Cell Biol.* 95, 189–196. doi: 10.1083/jcb.95.1.189

Robinson, D. G., and Pimpl, P. (2013). Receptor-mediated transport of vacuolar proteins: a critical analysis and a new model. *Protoplasma* doi: 10.1007/s00709-013-0542-7 [Epub ahead of print].

Robinson, D. G., Pimpl, P., Scheuring, D., Stierhof, Y.-D., Sturm, S., and Viotti, C. (2012). Trying to make sense of retromer. *Trends Plant Sci.* 17, 431–439. doi: 10.1016/j.tplants.2012.03.005

Romoser, V. A., Hinkle, P. M., and Persechini, A. (1997). Detection in living cells of Ca^{2+}-dependent changes in the fluorescence emission of an indicator composed of two green fluorescent protein variants linked by a calmodulin-binding sequence. A new class of fluorescent indicators. *J. Biol. Chem.* 272, 13270–13274. doi: 10.1074/jbc.272.20.13270

Saint-Jean, B., Seveno-Carpentier, E., Alcon, C., Neuhaus, J.-M., and Paris, N. (2010). The cytosolic tail dipeptide Ile-Met of the pea receptor BP80 is required for recycling from the prevacuole and for endocytosis. *Plant Cell* 22, 2825–2837. doi: 10.1105/tpc.109.072215

Sankaranarayanan, S., De Angelis, D., Rothman, J. E., and Ryan, T. A. (2000). The use of pHluorins for optical measurements of presynaptic activity. *Biophys. J.* 79, 2199–2208. doi: 10.1016/S0006-3495(00)76468-X

Sankaranarayanan, S., and Ryan, T. A. (2001). Calcium accelerates endocytosis of vSNAREs at hippocampal synapses. *Nat. Neurosci.* 4, 129–136. doi: 10.1038/83949

Scheuring, D., Viotti, C., Krüger, F., Künzl, F., Sturm, S., Bubeck, J., et al. (2011). Multivesicular bodies mature from the trans-Golgi network/early endosome in *Arabidopsis*. *Plant Cell* 23, 3463–3481. doi: 10.1105/tpc.111.086918

Schulte, A., Lorenzen, I., Böttcher, M., and Plieth, C. (2006). A novel fluorescent pH probe for expression in plants. *Plant Methods* 2, 7. doi: 10.1186/1746-4811-2-7

Sentenac, H., and Grignon, C. (1987). Effect of H excretion on the surface pH of corn root cells evaluated by using weak zacid influx as a pH probe. *Plant Physiol.* 84, 1367–1372. doi: 10.1104/pp.84.4.1367

Shen, J., Zeng, Y., Zhuang, X., Sun, L., Yao, X., Pimpl, P., et al. (2013). Organelle pH in the *Arabidopsis* endomembrane system. *Mol. Plant* 6, 1419–1437. doi: 10.1093/mp/sst079

Shimada, T., Fuji, K., Tamura, K., Kondo, M., Nishimura, M., and Hara-Nishimura, I. (2003). Vacuolar sorting receptor for seed storage proteins in *Arabidopsis thaliana*. *Proc. Natl. Acad. Sci. U.S.A.* 100, 16095–16100. doi: 10.1073/pnas.2530568100

Sieberer, B. J., Chabaud, M., Fournier, J., Timmers, A. C. J., and Barker, D. G. (2012). A switch in Ca^{2+} spiking signature is concomitant with endosymbiotic microbe entry into cortical root cells of *Medicago truncatula*. *Plant J.* 69, 822–830. doi: 10.1111/j.1365-313X.2011.04834.x

Singh, S., and Parniske, M. (2012). Activation of calcium- and calmodulin-dependent protein kinase (CCaMK), the central regulator of plant root endosymbiosis. *Curr. Opin. Plant Biol.* 15, 444–453. doi: 10.1016/j.pbi.2012.04.002

Staal, M., De Cnodder, T., Simon, D., Vandenbussche, F., Van der Straeten, D., Verbelen, J.-P., et al. (2011). Apoplastic alkalinization is instrumental for the inhibition of cell elongation in the *Arabidopsis* root by the ethylene precursor 1-aminocyclopropane-1-carboxylic acid. *Plant Physiol.* 155, 2049–2055. doi: 10.1104/pp.110.168476

Tamura, K., Shimada, T., Ono, E., Tanaka, Y., Nagatani, A., Higashi, S.-I., et al. (2003). Why green fluorescent fusion proteins have not been observed in the vacuoles of higher plants. *Plant J.*35, 545–555. doi: 10.1046/j.1365-313X.2003.01822.x

Taylor, D. P., Slattery, J., and Leopold, A. C. (1996). Apoplastic pH in corn root gravitropism: a laser scanning confocal microscopy measurement. *Physiol. Plant.* 97, 35–38. doi: 10.1111/j.1399-3054.1996.tb00475.x

Taylor, M. J., Perrais, D., and Merrifield, C. J. (2011). A high precision survey of the molecular dynamics of mammalian clathrin-mediated endocytosis. *PLoS Biol.* 9:e1000604. doi: 10.1371/journal.pbio.1000604

Thibaud, J. B., Davidian, J. C., Sentenac, H., Soler, A., and Grignon, C. (1988). H^+ cotransports in corn roots as related to the surface pH shift induced by active H^+ excretion. *Plant Physiol.* 88, 1469–1473. doi: 10.1104/pp.88.4.1469

Toulon, V., Sentenac, H., Thibaud, J. B., Davidian, J. C., Moulineau, C., and Grignon, C. (1992). Role of apoplast acidification by the H(+) pump: effect on the sensitivity to pH and CO2 of iron reduction by roots of *Brassica napus* L. *Planta* 186, 212–218. doi: 10.1007/BF00196250

Toulon, V., Sentenac, H., Thibaud, J.-B., Soler, A., Clarkson, D., and Grignon, C. (1989). Effect of HCO_3^- concentration in the absorption solution on the energetic coupling of H^+-cotransports in roots of *Zea mays* L. *Planta* 179, 235–241. doi: 10.1007/BF00393694

Wachter, R. M. (2007). Chromogenic cross-link formation in green fluorescent protein. *Acc. Chem. Res.* 40, 120–127. doi: 10.1021/ar040086r

Watanabe, E., Shimada, T., Kuroyanagi, M., Nishimura, M., and Hara-Nishimura, I. (2002). Calcium-mediated association of a putative vacuolar sorting receptor PV72 with a propeptide of 2S albumin. *J. Biol. Chem.* 277, 8708–8715. doi: 10.1074/jbc.M109346200

Watanabe, E., Shimada, T., Tamura, K., Matsushima, R., Koumoto, Y., Nishimura, M., et al. (2004). An ER-localized form of PV72, a seed-specific vacuolar sorting receptor, interferes the transport of an NPIR-containing proteinase in *Arabidopsis* leaves. *Plant Cell Physiol.* 45, 9–17. doi: 10.1093/pcp/pch012

Zhang, Y., Xie, Q., Robertson, J. B., and Johnson, C. H. (2012). pHlash: a new genetically encoded and ratiometric luminescence sensor of intracellular pH. *PLoS ONE* 7:e43072. doi: 10.1371/journal.pone.0043072

Conflict of Interest Statement: The authors declare that the research was conducted in the absence of any commercial or financial relationships that could be construed as a potential conflict of interest.

Received: 30 August 2013; accepted: 04 December 2013; published online: 18 December 2013.

*Citation: Martinière A, Desbrosses G, Sentenac H and Paris N (2013) Development and properties of genetically encoded pH sensors in plants. Front. Plant Sci. **4**:523. doi: 10.3389/fpls.2013.00523*

This article was submitted to Plant Cell Biology, a section of the journal Frontiers in Plant Science.

Copyright © 2013 Martinière, Desbrosses, Sentenac and Paris. This is an open-access article distributed under the terms of the Creative Commons Attribution License (CC BY). The use, distribution or reproduction in other forums is permitted, provided the original author(s) or licensor are credited and that the original publication in this journal is cited, in accordance with accepted academic practice. No use, distribution or reproduction is permitted which does not comply with these terms.

frontiers in
PLANT SCIENCE

ORIGINAL RESEARCH ARTICLE
published: 16 December 2013
doi: 10.3389/fpls.2013.00506

Development of roGFP2-derived redox probes for measurement of the glutathione redox potential in the cytosol of severely glutathione-deficient *rml1* seedlings

Isabel Aller*[1], *Nicolas Rouhier*[2] *and Andreas J. Meyer*[1]*

[1] *INRES-Chemical Signalling, University of Bonn, Bonn, Germany*
[2] *Interactions Arbres Microorganismes, IFR 110 EFABA, Faculté des sciences, Université de Lorraine, UMR 1136 Université de Lorraine/INRA, Vandoeuvre, lès-Nancy, France*

Edited by:
Alex Costa, University of Milan, Italy

Reviewed by:
Mirko Zaffagnini, University of Bologna, Italy
Frank E. Schleifenbaum, University of Tuebingen, Germany
Taras P. Pasternak, Albert-Ludwigs-University of Freiburg, Germany

****Correspondence:***
Andreas J. Meyer, INRES-Chemical Signalling, University of Bonn, Friedrich-Ebert-Allee 144, 53113 Bonn, Germany
e-mail: andreas.meyer@uni-bonn.de

Glutathione is important for detoxification, as a cofactor in biochemical reactions and as a thiol-redox buffer. The cytosolic glutathione buffer is normally highly reduced with glutathione redox potentials (E_{GSH}) of more negative than −310 mV. Maintenance of such negative redox potential is achieved through continuous reduction of glutathione disulfide by glutathione reductase (GR). Deviations from steady state glutathione redox homeostasis have been discussed as a possible mean to alter the activity of redox-sensitive proteins through switching of critical thiol residues. To better understand such signaling mechanisms it is essential to be able to measure E_{GSH} over a wide range from highly negative redox potentials down to potentials found in mutants that show already severe phenotypes. With the advent of redox-sensitive GFPs (roGFPs), understanding the *in vivo* dynamics of the thiol-based redox buffer system became within reach. The original roGFP versions, roGFP1 and roGFP2, however, have midpoint potentials between −280 and −290 mV rendering them fully oxidized in the ER and almost fully reduced in the cytosol, plastids, mitochondria, and peroxisomes. To extend the range of suitable probes we have engineered a roGFP2 derivative, roGFP2-iL, with a midpoint potential of about −238 mV. This value is within the range of redox potentials reported for homologous roGFP1-iX probes, albeit with different excitation properties. To allow rapid and specific equilibration with the glutathione pool, fusion constructs with human glutaredoxin 1 (GRX1) were generated and characterized *in vitro*. GRX1-roGFP2-iL proved to be suitable for *in vivo* redox potential measurements and extends the range of E_{GSH} values that can be measured *in vivo* with roGFP2-based probes from about −320 mV for GRX1-roGFP2 down to about −210 mV for GRX1-roGFP2-iL. Using both probes in the cytosol of severely glutathione-deficient *rml1* seedlings revealed an E_{GSH} of about −260 mV in this mutant.

Keywords: glutathione, glutathione redox potential, GRX1-roGFP2, *rml1*, redox imaging

INTRODUCTION

Thiol redox biochemistry is considered to play a fundamental role in cellular processes including signaling and cell fate decisions. The ability to dynamically and quantitatively measure such cellular processes *in vivo* is key to understand the underlying principles and the coordination of redox processes in the context of intact cells. Redox-sensitive GFP (roGFP) allows a direct read-out of the glutathione redox potential (E_{GSH}) particularly in reducing compartments (Meyer and Dick, 2010). However, current variants of roGFPs are largely inadequate in mutants with very low glutathione levels, generally oxidizing conditions like in the ER, or oxidizing conditions triggered by pathological processes. These limitations demand the development of further roGFP variants with less negative midpoint potentials.

The tripeptide glutathione (γ-L-glutamyl-L-cysteinylglycine) constitutes the major low molecular weight thiol in most prokaryotic and virtually all eukaryotic organisms. Glutathione is synthesized in two sequential steps that are catalyzed by two enzymes, glutamate-cysteine ligase (GSH1) and glutathione synthase (GSH2). In plants, glutathione fulfills a broad range of essential functions including detoxification of heavy metals and xenobiotics and serving as an electron donating cofactor in biochemical reactions (Cobbett and Goldsbrough, 2002; Noctor et al., 2011). Moreover glutathione constitutes one of the most important redox buffer systems in the cell. The capacity to act as a redox buffer relies on the reversible convertibility of glutathione between the reduced form of glutathione (GSH) and the oxidized form glutathione disulfide (GSSG). While the glutathione pool in the cytosol, mitochondria, plastids, and peroxisomes is maintained in a highly reduced state by NADPH and glutathione reductase (GR) (Schwarzländer et al., 2008; Marty et al., 2009), the glutathione redox buffer in the endoplasmic reticulum (ER) is highly oxidized (Hwang et al., 1992; Brach et al., 2009). E_{GSH} depends on the absolute glutathione concentration and the ratio

of [GSH]:[GSSG] (Meyer and Hell, 2005). The local E_{GSH} is assumed to affect the glutathionylation status of proteins which is an important means of regulating protein activity (Michelet et al., 2005; Noctor et al., 2011; Zaffagnini et al., 2012).

Conditions of environmental challenge are frequently considered to cause the generation of oxidants in the form of reactive oxygen species (ROS) (Apel and Hirt, 2004; Torres et al., 2006). Apart from potential toxic effects of ROS, the oxidants are increasingly recognized as vital messengers in cellular signaling (Finkel, 2011). Oxidant-dependent signaling may occur either directly by specific recognition of oxidants (Forman et al., 2010) or indirectly through detoxification of oxidants and resulting changes in the cellular redox buffer system providing an opportunity for readout of these changes. Stress-dependent alterations of E_{GSH} caused by a transient draw of electrons from the glutathione redox buffer for oxidant detoxification and coupling of E_{GSH} to target proteins thus may result in altered protein function and hence pronounced metabolic and developmental consequences for individual cells and the whole organism.

Depletion of total GSH also directly impacts on E_{GSH} and thus mutants with defects in GSH biosynthesis may cause constitutive activation or inactivation of respective signaling pathways. Indeed, Arabidopsis *rax1* mutants carrying a mutation in the GSH1 enzyme leading to only 20–50% of wild-type GSH are affected in stress signaling and have induced defense pathways (Ball et al., 2004). Another partially GSH-deficient mutant, *pad2*, is not capable of activating appropriate defense mechanisms against biotic stressors (Parisy et al., 2007; Schlaeppi et al., 2008). The most severe, yet viable, mutant affected in GSH1 is *rml1*, which contains only 2–10% of wild-type glutathione (Vernoux et al., 2000; Cairns et al., 2006). Homozygous *rml1* mutant seedlings show impaired root development, which is assumed to be caused by redox-dependent inhibition of cell cycle components (Vernoux et al., 2000).

Better understanding of redox-regulatory processes mediated by glutathione demands experimental approaches enabling quantitative monitoring of E_{GSH}. The development of roGFPs enables ratiometric thiol redox imaging at subcellular level (Dooley et al., 2004; Hanson et al., 2004). The two excitation maxima of the parental GFP arise from the protonation state of the chromophore and excited state proton transfer that converts the neutral form of the chromophore into the green emitting anionic form (Brejc et al., 1997; Palm et al., 1997). Engineering of two surface-exposed cysteines into the GFP barrel on the two adjacent β-strands 7 and 10 in positions allowing reversible disulfide formation exploits a structure-dependent shift in the protonation status of the chromophore for ratiometric measurements (Dooley et al., 2004; Hanson et al., 2004). The degree of chromophore protonation is also dependent on the type of chromophore: while roGFP1 derived from the wild-type chromophore with the amino acid S65 in the chromophore displays a dominant excitation peak in the UV range, the roGFP2 variant derived from EGFP containing the S65T mutation has a main excitation peak at 490 nm (Hanson et al., 2004). The chromophore type also slightly affects the redox potential of the engineered disulfide with roGFP1 being slightly more negative than roGFP2. It has been shown that glutaredoxin (GRX) catalyzes the oxidation and reduction of roGFP in the presence of glutathione (Meyer et al., 2007; Gutscher et al., 2008). Fusion of GRX to roGFP overcomes kinetic limitations of the GRX/roGFP interaction and possible limitations caused by the absence of appropriate GRXs in some organisms or subcellular compartments (Gutscher et al., 2008; Meyer and Dick, 2010). In addition to kinetic properties, the thermodynamic properties of roGFP probes are similarly important for dynamic measurements and ideally redox sensors with redox potentials adapted to the desired measuring range should be selected. It has been shown that the redox potentials of roGFP variants, roGFP3 and roGFP4, which both contain the engineered disulfide C149/C202, are more negative than the redox potentials of their respective counterparts roGFP1 and roGFP2, which both contain the disulfide C147/C204 (Hanson et al., 2004). The redox potential can also be shifted to less negative values by engineering basic amino acids next to the disulfide-forming cysteines. As a consequence, such probes show an increased pI and hence a significantly enhanced response rate for reductive processes (Cannon and Remington, 2006). In the oxidizing ER lumen and under highly severe stress conditions, however, these probes would still be fully oxidized. To overcome this limitation, Lohman and Remington (2008) further engineered roGFP1 by replacing the chromophore-interacting H148 by serine and inserting an additional amino acid between the disulfide forming C147 and S148. Depending on the amino acid inserted behind C147 the respective members of the so-called roGFP1-iX family had less negative midpoint potentials between −229 and −246 mV (Lohman and Remington, 2008). However, even these less reducing probes appear almost fully oxidized in the ER at steady state of HeLa cells (Birk et al., 2013).

While under highly reducing conditions roGFP1 may have some advantages, roGFP2 has advantages in less reducing conditions as they occur in partially glutathione-deficient mutants (Meyer et al., 2007; Schwarzländer et al., 2008). Specifically, roGFP2 has a larger dynamic range than roGFP1 and it avoids potential illumination-dependent photoisomerization artifacts associated with roGFP1 (Schwarzländer et al., 2008). Because roGFP2 also is less reducing than roGFP1 we asked whether roGFP2-iX probes can be engineered and whether such probes would have an even less negative redox potential than their respective roGFP1-iX counterparts to enable redox imaging in compartments with a less negative E_{GSH}. Inhibition of GSH biosynthesis in wild-type roots by BSO leads to severe oxidation in the cytosol (Meyer et al., 2007). Similarly, E_{GSH} in *rml1* roots has been shown to be far less negative than in wild-type plants (Meyer and Dick, 2010), but the exact value of cytosolic E_{GSH} in this mutant has not been determined because the redox potential is close to the edge or even beyond the usable measuring range of roGFP2. After detailed characterization the novel roGFP2-iL probe was thus used to determine E_{GSH} in the cytosol of *rml1* seedlings in order to define the lower limit of glutathione redox potentials under which viability can be maintained.

MATERIALS AND METHODS

GENE CONSTRUCTION, PROTEIN EXPRESSION AND PURIFICATION

roGFP2 (C48S/S65T/Q80R/F99S/S147C/Q204C, (Dooley et al., 2004; Hanson et al., 2004) was used as a template to generate roGFP2-iL (C48S/S65T/Q80R/F99S/S147CL/H148S/Q204C)

in which a leucine was added after C147. For site-specific insertion of C147CL and substitution of H148S into the roGFP2 sequence the primers 5′-AACTACAACTGC CTGAGCAACGTCTATATCATGGCC-3′ and 5′-GCTCAGGCA GTTGTAGTTGTACTCCAGCTTGTG-3′ were used. N-terminal fusion of human GRX1 and roGFP2-iL was done by PCR using gene-specific primers 5′-TCAGGAGGAGTGAGCAAGGGCGA-3′ and 5′-TCGCCCTTGCTCACTCCTCCTGA-3′. Amplification of full-length product was done with the primer pair 5′-AC CATGATGGCTCAAGAGTTTGTGAA-3′ and 5′-TCTAGACT TGTACAGCTCGTCCATG-3′ generating GRX1-TS$(GGSGG)_6$-roGFP2-iL (GRX1-roGFP2-iL). Both PCR products were cloned into pCAP^s vector (Roche, www.roche-applied-science.com) for sequence confirmation.

The sequence of free roGFP2-iL and GRX1-roGFP2-iL were cloned into the BamHI and NcoI restriction sites of the protein expression vector pQE-30 (Qiagen, www.qiagen.com) for the production of a recombinant protein containing an N-terminal His_6-tag. The restriction sites were introduced by PCR using the primer pairs 5′-TGGATCCGCTCAAGAGTTTGTGAACTG-3′ and 5′-CTAAGCTTTTACTTGTACAGCTCGTCC-3′ for GRX1-roGFP2iL and 5′-AAGGATCCGTGAGCAAGGGCGAGGAGC-3′ and 5′-CTAAGCTTTTACTTGTACAGCTCGTCC-3′ for roGFP2-iL. Recombinant roGFP1 was produced as described earlier (Schwarzländer et al., 2008). pQE-30 plasmids for expression of roGFP1-iL and roGFP1-iE were kindly provided by Dr. J. Remington (Univ. Oregon) and Dr. C. Appenzeller-Herzog (Univ. Basel), respectively.

For stable expression in plants, a modified version of pBinAR vector (Höfgen and Willmitzer, 1990) containing UBQ10 promoter instead of 35S promoter was used. The coding sequence of GRX1-roGFP2iL was amplified by 5′-AG GTACCATGGCTCAAGAGTTTGTGAAC-3′ and 5′-TATGTCG ACTTACTTGTACAGCTCGTCCAT-3′ to add KpnI and SalI restriction sites used for cloning.

ISOLATION OF RECOMBINANT PROTEINS

After transformation of the *E. coli* strain Origami (DE3) (Novagen, www.merckmillipore.de), a pre-culture of 10 ml was grown over night at 37°C. Five mL of the pre-culture were added to 450 ml LB medium and grown at room temperature to an OD_{600} of 0.5–0.8. Expression of the different roGFP variants was induced by addition of isopropyl-β-D-thiogalactopyranoside (IPTG) to a final concentration of 1 mM. Protein expression was performed at room temperature for 24 h. The cells were harvested and resuspended in protein extraction buffer (50 mM Tris-HCl pH 8.0, 250 mM NaCl). The cells were sonicated for 10 min. Cell lysate was centrifuged and the soluble roGFP proteins purified via a Ni^{2+} loaded HiTrap™ Chelating HP Column (GE Healthcare, www.gelifesciences.com).

SPECTROSCOPY

Fluorescence excitation spectra were collected using a LS55 fluorescence spectrophotometer (Perkin Elmer Life Sciences, http://www.perkinelmer.com). Five hundred microliter protein solution was placed in a 1 ml quartz cuvette. Samples contained 0.2 μM protein in reaction buffer (100 mM K_2HPO_4/KH_2PO_4 pH 7.4, 1 mM EDTA) and 10 mM total dithiothreitol (DTT) for full reduction or 10 mM total H_2O_2 for full oxidation of the sensor, respectively. The spectra were collected from 350 to 520 nm with a bandwidth of 10 nm and a scan speed of 500 nm min^{-1}. Fluorescence was detected at 540 nm.

The fluorescence quantum yield (QY) of roGFPs was determined by comparison to Rhodamine 6G (Sigma-Aldrich, www.sigmaaldrich.com) which has a QY of 0.9 when dissolved in water (Magde et al., 2002). Six different dilutions of the respective proteins with absorbances between 0.01 and 0.1 were prepared in aqueous solution. Both, standard and roGFP samples were excited at 488 nm with a bandwidth of 5 nm. Total emission was collected from 505 to 590 nm. Fluorescence quantum yields for roGFPs were calculated from the integrated fluorescence intensities of the spectra after correction for wavelength-dependent photomultiplier sensitivity.

IN VITRO CHARACTERIZATION OF roGFP VARIANTS

In vitro characterization of roGFP2-iL and GRX1-roGFP2-iL fusions by ratiometric time-course measurements with isolated proteins was performed on a fluorescence plate reader (POLARstar Omega; BMG Labtech, www.bmglabtech.com) with filter-based excitation at 390 and 480 nm and detection of emitted light at 520 nm. Phosphate buffer (100 mM K_2HPO_4/KH_2PO_4, 1 mM EDTA, pH 7.4) with 1 μM of the respective roGFP according to the information given in the text were pipetted into the wells of a 96-well plate with a clear bottom (NUNC™ 96, www.thermoscientific.com). Reduced glutathione (in 100 mM K_2HPO_4/KH_2PO_4 buffer, pH 7.0) was automatically injected to the indicated final concentration using the built-in injectors. For maximum achievable reduction of the glutathione buffer, 0.1 μM recombinant *Arabidopsis thaliana* GR1 (*At*GR1) and 100 μM NADPH were added to each well. To allow comparable reduction kinetics, the proteins were pre-oxidized with 10 mM H_2O_2 for 30 min. The remaining H_2O_2 was removed by desalting spin columns according to the manufacturer's manual (Zeba™ Spin Desalting Columns, www.thermoscientific.com). H_2O_2 and DTT to a final concentration of 10 mM were separately used to define maximum oxidation and maximum reduction of the sensors. In the comparative reduction assays with free roGFP1, roGFP1-iL, roGFP2, and roGFP2iL, purified *At*GRX2 to a final concentration of 2 μM was included in the reaction mix.

DETERMINATION OF MIDPOINT POTENTIALS OF roGFP VARIANTS

Both roGFP2-iL and GRX-roGFP2-iL (1 μM final concentration) were allowed to equilibrate (2–3 h) with lipoic acid buffers [reduced form dihydrolipoic acid (DHLA); oxidized form lipoic acid (LA)] (Equation 1). DHLA/LA was used at a total concentration of 2.5 mM in degassed HEPES buffer (100 mM HEPES, 300 mM NaCl, 1 mM EDTA, pH 7.0). The appropriate concentrations of DHLA and LA to set distinct redox potentials were calculated from the Nernst equation based on the standard reduction potential of lipoic acid (E'°_{LA}) of −290 mV at pH 7.0 (Lees and Whitesides, 1993).

$$roGFP_{ox} + DHLA \Leftrightarrow roGFP_{red} + LA \quad (1)$$

The redox potential for each of the two redox pairs is defined by the Nernst equation using the respective midpoint potential and ratios (Q) of oxidized to reduced roGFP and LA to DHLA, respectively (Equation 2).

$$E = E^{\circ\prime} - \frac{RT}{nF} \ln Q \tag{2}$$

In this equation, R is the gas constant (8.314 J K^{-1} mol^{-1}), T is the temperature (298.15 K), n is the number of transferred electrons, and F is Faraday's constant (96,485 C mol^{-1}). After redox equilibration of both redox couples it is possible to equate the two redox potentials (Equation 3):

$$E_{LA} = E^{\circ\prime}_{LA} - \frac{0.0592V}{2} \log \frac{[\text{DHLA}]}{[\text{LA}]} = E^{\circ\prime}_{roGFP} - \frac{0.0592V}{2} \log \frac{[\text{roGFP}_{\text{red}}]}{[\text{roGFP}_{\text{ox}}]} = E_{roGFP} \tag{3}$$

Because $E^{\circ\prime}_{\text{LA}}$ is known this leaves two unknowns, $E^{\circ\prime}_{\text{roGFP}}$ and $[\text{roGFP}_{\text{red}}]/[\text{roGFP}_{\text{ox}}]$. The redox potential of roGFP is dependent on the degree of oxidation (OxD_{roGFP}) of the redox pair $\text{roGFP}_{\text{red}}/\text{roGFP}_{\text{ox}}$according to Equations 4 and 5:

$$OxD_{roGFP} = \frac{[\text{roGFP}_{\text{ox}}]}{[\text{roGFP}_{\text{ox}}] + [\text{roGFP}_{\text{red}}]} \tag{4}$$

$$\frac{[\text{roGFP}_{\text{red}}]}{[\text{roGFP}_{\text{ox}}]} = \frac{1 - OxD_{roGFP}}{OxD_{roGFP}} \tag{5}$$

Substitution of Equation 5 into Equation 3 allows transformation of Equation 3 into Equation 6:

$$E_{LA} = E^{\circ\prime}_{LA} - \frac{0.0592V}{2} \log \frac{[\text{DHLA}]}{[\text{LA}]} = E^{\circ\prime}_{roGFP} - \frac{0.0592V}{2} \log \frac{1 - OxD_{roGFP}}{OxD_{roGFP}} = E_{roGFP} \tag{6}$$

OxD_{roGFP} can be measured *in vitro* by monitoring the fluorescence emission intensities (I) at 520 nm for excitation at 390 and 480 nm. After equilibration in an environment of a defined redox potential, the respective values were used to determine OxD_{roGFP} according to Equation 7:

$$OxD_{roGFP} = \frac{R - R_{red}}{\left(\frac{I480_{\text{ox}}}{I480_{\text{red}}}\right)(R_{ox} - R) + (R - R_{red})} \tag{7}$$

Here, R denotes the ratio of the fluorescence intensities measured at 390 and 480 nm. R_{red} and R_{ox} represent the fluorescence ratios of fully reduced and fully oxidized roGFP, respectively. The raw values of I were always corrected by subtracting the respective blank values.

For determination of the midpoint potentials $E^{\circ\prime}$ of roGFP variants OxD_{roGFP} or, alternatively, the degree of reduction $ReD_{roGFP} = 1 - OxD_{roGFP}$ was plotted against the calculated redox potentials of the respective lipoic acid redox buffers and all data points were fitted to a sigmoidal dose-response curve using GraphPadPrism5 (GraphPad Software, www.graphpad.com). The titration of each protein was carried out three times with 4 technical replicates. Titration of GRX1-roGFP2 and roGFP2 was done with DTT, which has a more negative reduction potential than lipoic acid ($E^{\circ\prime}_{\text{DTT}} = -323$ mV, Shaked et al., 1980).

PLANT MATERIAL AND GROWTH CONDITIONS

Heterozygous Arabidopsis *rml1* mutants were selected by genotyping for the mutant allele and exploiting the fact that the point mutation (Vernoux et al., 2000) generates a new ApoI restriction site. After transformation of heterozygous plants with the respective roGFP constructs transformed plants were first screened for uniform fluorescence on a stereomicroscope equipped with fluorescence optics and a GFP filter. In a subsequent molecular screen heterozygous *rml1* seedlings were selected for further propagation. Seeds from transgenic plants expressing either GRX1-roGFP2 of GRX1-roGFP2-iL were surface sterilized with 70% ethanol twice and resuspended in sterile deionized water. Seeds were plated on nutrient medium [5 mM KNO_3, 2.5 mM KH_2PO_4, 2 mM $MgSO_4$, 2 mM $Ca(NO_3)_2$, 10 µM Fe-EDTA, 0.1% (v/v) micronutrient mix (Somerville and Ogren, 1982), pH 5.8 solidified with 0.8% phytagel]. Plants were kept at 4°C for 1 day before placing them in vertical orientation in a growth chamber with a diurnal cycle of 16 h light at 22°C and 8 h dark at 18°C. The light intensity was 75 µmol photons m^{-2} s^{-1}. Plants were grown for 3 days until the characteristic dwarf phenotype of *rml1* became visible.

CLSM IMAGING

Pre-selected *rml1* seedlings were mounted on a slide in a drop of water and immediately transferred to a Zeiss confocal microscope LSM780 (Carl Zeiss Microscopy, www.zeiss.de/mikro). Images were collected with a 40× lens (Zeiss Objective C-Apochromat 40×/1.2 W Corr M27) in multi-track mode with line switching between 488 nm excitation and 405 nm excitation and taking an average of four readings in case of GRX1-roGFP2 and two readings for GRX1-roGFP2-iL, respectively. The roGFP fluorescence was collected with a 505–530 nm emission band-pass filter. Autofluorescence excited at 405 nm was collected from 430 to 480 nm and values were used to subtract autofluorescence bleeding into the roGFP channel as described previously (Schwarzländer et al., 2008; Samalova et al., 2013).

RATIOMETRIC IMAGE ANALYSIS

Images were imported into a custom written MatLab (The MathWorks, www.mathworks.de) analysis suite (M.D. Fricker, Dept. Plant Sciences, Oxford). The ratio analysis was performed on a pixel-by-pixel basis as $I405/I488$ following spatial averaging in (x,y) using a 3×3 kernel. Correction of $I405$ for autofluorescence bleeding into the 405 nm channel and subtraction of background signals for each channel was performed. The average background signal was typically measured from the vacuole of one of the cells. For pseudocolor display, the ratio was coded on a spectral color scale ranging from blue (fully reduced) to red (fully oxidized), with limits set by the *in situ* calibration. The calibration

was done by incubation of *rml1* seedlings expressing GRX1-roGFP2 or GRX1-roGFP2-iL in 10 mM DTT and 25 mM H_2O_2, respectively, to drive the roGFPs to their fully reduced and fully oxidized forms. *OxD* of GRX1-roGFP2 and GRX1-roGFP2-iL expressed in the cytosol of *rml1* mutants was calculated according to Equation 7 albeit with wavelengths 405 nm and 488 nm used for excitation of roGFPs *in vivo*.

RESULTS

DEVELOPMENT AND CHARACTERIZATION OF roGFP2-iL

To investigate whether roGFP2 can be modified to generate less reducing probe variants, the roGFP2 sequence was further engineered by introducing site-specific mutations thus generating roGFP2-iL (**Figures 1A,B**). Subsequently, roGFP2-iL was fused behind human GRX1 to generate GRX1-roGFP2-iL (**Figure 1C**) to ensure specificity of the novel probe for E_{GSH} similar to other roGFP variants used before (Gutscher et al., 2008; Meyer and Dick, 2010; Albrecht et al., 2013; Birk et al., 2013). IPTG-induction of *E. coli* cultures transformed with roGFP2-iL and GRX1-roGFP2-iL already resulted in bright green cultures suggesting that the introduced mutations did not abolish the fluorescence (not shown). Comparison of roGFP2-iL and roGFP1-iE with the standard Rhodamine 6G resulted in a QY of 0.6 for roGFP2-iL and a QY of 0.4 for roGFP1-iE. This initial observation was further confirmed through side-by-side fluorescence scans of recombinant roGFP2 and roGFP2-iL in buffers containing either 10 mM DTT for full reduction or 10 mM H_2O_2 for full oxidation of the probes, respectively (**Figure 2**). As previously described (Dooley et al., 2004; Hanson et al., 2004), formation of the disulfide upon oxidation of roGFP2 favors the protonated, neutral form of the chromophore causing an increase in fluorescence at 395 nm while the 488 nm peak is decreased (red curve). Conversely, full reduction of roGFP2 leads to a decrease in excitation at 395 nm while the peak at 488 nm is increased (blue curve; **Figure 2A**).

Modification of roGFP2 through the C147CL insertion and H148S exchange does alter the general spectral properties but does not abolish the dual excitation behavior in roGFP2-iL (**Figure 2B**). Full oxidation of the sensor causes an increase of fluorescence at 395 nm and a corresponding decrease in 488 nm excitation while full reduction of roGFP2-iL leads to decreased fluorescence excitation at 395 nm and an increase at 488 nm. A clear isosbestic point at 425 nm separates the two peaks further indicating two equilibrating molecular species (**Figure 2B**). Thus, all spectral properties of roGFP2 are fully retained in the newly-generated roGFP2-iL. In contrast to roGFP2, however, the maximum change in fluorescence intensity between fully oxidized and fully reduced sensor states was significantly lower in roGFP2-iL. The dynamic range (δ) for the maximum change of the fluorescence ratio between the fully oxidized and fully reduced state of the chromophore was calculated from the fluorescence excitation at the wavelengths used for ratiometric imaging (i.e., 405 and 488 nm). While roGFP2 has a $\delta_{405/488}$ of 8.18 the $\delta_{405/488}$ for roGFP2-iL was found to be 2.55 (**Figure 2**; **Table 1**). Further equilibration of roGFP2-iL in redox buffers with varying pH revealed that the fluorescence ratio of roGFP2-iL is pH-insensitive in the physiological range (**Figure 3**).

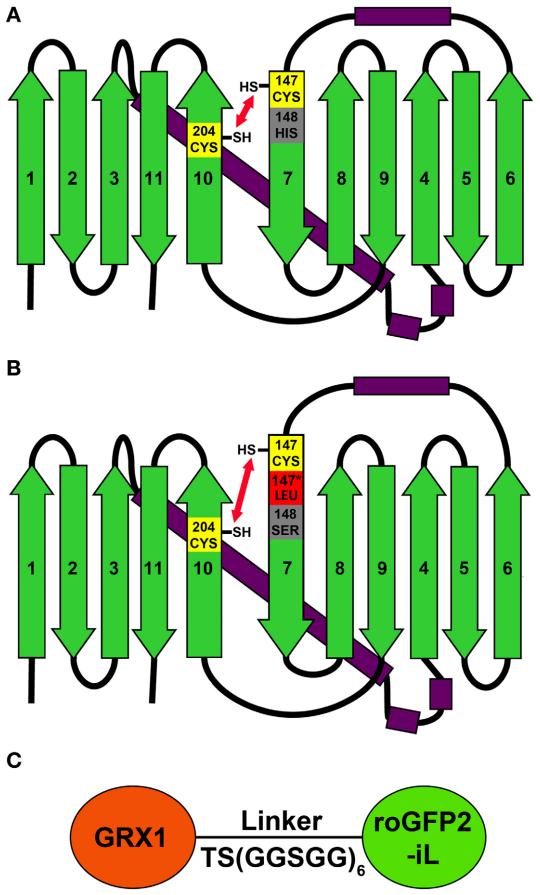

FIGURE 1 | 2D models of roGFP2 and roGFP2-iL illustrate the relative position of disulfide forming Cys147 and Cys204. (A) Cys147 and Cys204 are located on strands 7 and 10, respectively, and are positioned in close proximity so that they can facilitate disulfide formation. **(B)** The introduction of a leucine next to Cys147 (Leu147*) and the substitution of His148 by serine increase the relative distance between Cys147 and Cys204 that causes alterations in the thermodynamic stability of the disulfide. **(C)** Schematic representation of the GRX1-roGFP2-iL fusion protein. GRX1 was fused to the N-terminus of roGFP2-iL by a $TS(GGSGG)_6$ linker.

The standard redox potential ($E^{o\prime}$) strongly depends on the thermodynamic stability between C147 and C204 that is influenced by the nature of the surrounding amino acid residues. It has been described for roGFP1-iL that the insertion C147CL and the substitution H148S lower the thermodynamic stability of the inter-strand disulfide C147–C204 resulting in a less negative $E^{o\prime}$ of the sensor (Lohman and Remington, 2008). To test whether this effect on thermodynamic stability is retained in roGFP2-iL, $E^{o\prime}_{roGFP2\text{-}iL}$ was determined through titration with LA/DHLA. Plotting the degree of reduction of the respective sensor variants against the redox potential of the ambient LA/DHLA buffer allowed to deduce $E^{o\prime}$ values of -237.7 ± 2 mV for roGFP2-iL (**Figure 4A**) and 243.2 ± 5 mV for GRX1-roGFP2-iL (**Figure 4B**). The difference in $E^{o\prime}$ of roGFP2-iL and GRX1-roGFP2-iL suggests that

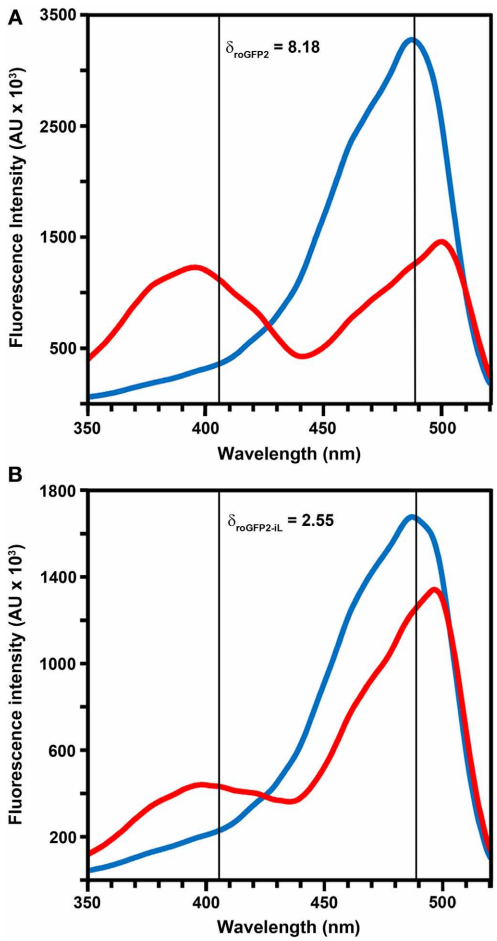

FIGURE 2 | Excitation properties of roGFP2 and roGFP2-iL. Excitation spectra of roGFP2 **(A)** and roGFP2-iL **(B)** in fully oxidized (red curve) and fully reduced (blue curve) state. Emission was monitored at 540 nm. The maximum dynamic ranges (δ) were calculated from the 405/488 nm excitation ratios for fully reduced and fully oxidized probes. Both excitation wavelengths are indicated by vertical lines.

N-terminal fusion of GRX1 influences the thermodynamic properties of the C147–C204 disulfide. To test this hypothesis, the midpoint potential of roGFP2 and GRX1-roGFP2 was determined side-by-side by titration against DTT redox buffers. As depicted in **Figure 5**, free roGFP2 shows an $E^{o\prime}$ of -277.5 ± 1 mV (**Figure 5A**) while $E^{o\prime}$ of GRX1-roGFP2 is shifted to -290.2 ± 3 mV (**Figure 5B**).

To test whether the reduction kinetics of roGFP2-iL is affected by GRX, roGFP2-iL was fused to the C-terminus of *Hs*GRX1 and the catalytic efficiency for the reduction of the resulting fusion protein by GSH was compared to free roGFP2-iL in *in vitro* experiments (**Figure 6**). In the absence of GRX, pre-oxidized roGFP2-iL responds only slowly to injection of 2 mM GSH while the GRX1-roGFP2-iL fusion protein shows a dramatically increased reduction rate.

To further confirm the less negative $E^{o\prime}$ of roGFP2-iL, the sensor was used side-by-side with other roGFP variants in reduction experiments with GSH at physiological concentrations as reducing agent. Since not all compared roGFPs were available as fusion proteins with GRX1, recombinant free GRX was added to the reaction mix. Pre-oxidized roGFP1, roGFP2, roGFP1-iL and roGFP2-iL were all reduced in the presence of GSH which was injected into the roGFP solutions to a final concentration of 5 mM. Subsequently, the reduction kinetics of the sensors were followed over time (**Figure 7A**). Addition of GSH resulted in complete reduction of roGFP1-iL and roGFP2-iL within 3 min while the reduction of roGFP2 was clearly delayed by several minutes and reached only 95% within 21 min. The reduction of the most negative probe roGFP1 was even slower and reached only 81% within 21 min. The rapid change in the degree of reduction of sensors with significantly less negative $E^{o\prime}$ values than $E^{o\prime}$ values of roGFP2 and roGFP1 (**Table 1**) can be further illustrated by the first derivative *dReD/dt* of the degree of reduction. *dRed/dt* of the four different probes plotted against time after injection of GSH shows the most rapid change in the degree of reduction for roGFP1-iL and roGFP2-iL while the values for roGFP2 and roGFP1 are much lower (**Figure 7B**).

Table 1 | Mutations, redox potentials, and dynamic range of GFP derived redox probes.

Probe	Amino acid changes	$E^{o\prime}$	δ[a]
roGFP2	C48S/S65T/Q80R/F99S/S147C/Q204C	−280 mV (consensus)	11.55 (390/480) 8.18 (405/488)
roGFP2-iL	C48S/S65T/Q80R/F99S/S147CL/H148S/Q204C	−240 mV (DHLA/LA)	3.1 (390/480) 2.55 (405/488)
roGFP1[b,c]	C48S/S147C/Q204C	−291 mV (consensus)	6.1 (400/475)[d] 2.58 (405/488)[e]
roGFP1-iL[d]	C48S/Q80R/S147CL/H148S/Q204C	−229 mV (DHLA/LA)[f]	7.2 (400/475)[d]
roGFP1-iE[d]	C48S/Q80R/S147CE/H148S/Q204C	−236 mV (DHLA/LA)[f]	4.5 (400/475)[d]

[a] *Dynamic range determined with the excitation wavelengths given in parenthesis. 405 nm and 488 nm are the excitation wavelengths used for confocal imaging.*
[b] *Hanson et al., 2004.*
[c] *Dooley et al., 2004.*
[d] *Lohman and Remington, 2008.*
[e] *Schwarzländer et al., 2008.*
[f] *Dihydrolipoic acid (DHLA, reduced form), Lipoic acid (LA, oxidized form).*

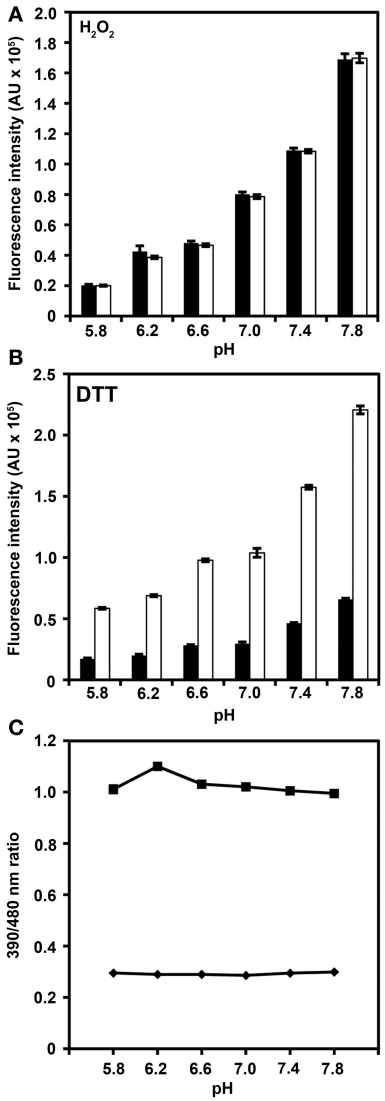

FIGURE 3 | pH-dependence of roGFP2-iL fluorescence. Recombinant roGFP2-iL was incubated in potassium-phosphate buffer at different pH values. The changes in roGFP2-iL fluorescence intensity of the 390 nm (black) and 480 nm channel (white) in buffers of different pH values under full oxidation with 10 mM H_2O_2 **(A)** and full reduction by 10 mM DTT **(B)** is shown. Increasing pH values beyond pH 7.0 equally increase fluorescence intensity in both channels thus the 390/480 nm ratio remains unaffected. Conversely, decreasing pH below pH 7.0 has the opposite effect for fully oxidized and fully reduced roGFP2-iL. Similar pH-dependent effects have been reported for wild-type GFP (Patterson et al., 1997). **(C)** The excitation ratios (390/480 nm) in 10 mM H_2O_2 (♦) and in 10 mM DTT (■) of roGFP2-iL are plotted against the respective pH solution. For several data points, standard error is smaller than data marker ($n = 3$ technical replicates).

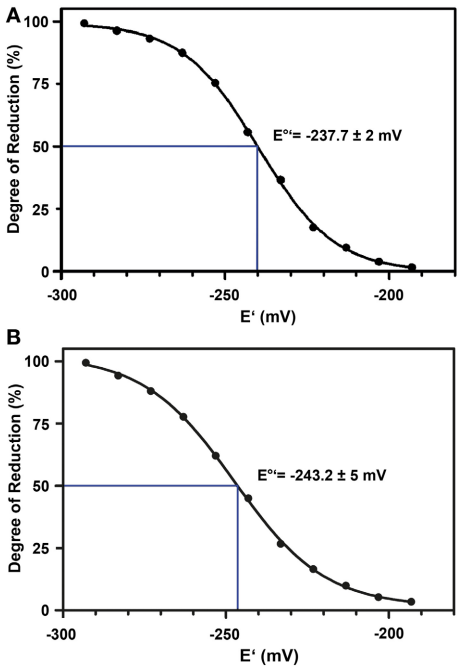

FIGURE 4 | Redox titration of roGFP2-iL and GRX1-roGFP2-iL. The degree of reduction of roGFP2-iL **(A)** and GRX1-roGFP2-iL **(B)** was determined from the excitation ratios plotted against the potential of the ambient redox buffer. Representative measurements of at least 3 independent redox titrations (with 4 replicates each) for both probes are shown.

MEASUREMENT OF THE CYTOSOLIC E_{GSH} IN SEVERELY GLUTATHIONE-DEFICIENT *rml1* MUTANTS

Conventional roGFP1 and roGFP2 are highly reduced when expressed in the cytosol of non-stressed cells (Meyer et al., 2007; Schwarzländer et al., 2008). Therefore, roGFP-iX probes with a less negative midpoint potential would obviously be expected to be also fully reduced, particularly when fused GRX1 ensures specific equilibration with the local E_{GSH}. Severe stress situations and pathological conditions, however, can lead to pronounced oxidation in the cytosol and thus probes with a less negative midpoint potential may be advantageous for redox imaging in the cytosol to fully resolve the dynamic changes in E_{GSH}. Severe depletion of GSH in the Arabidopsis mutant *rml1* has been reported to result in growth inhibition and it has been speculated that this effect may be caused by severe oxidation of cytosolic E_{GSH} and redox-dependent inhibition of the cell cycle (Vernoux et al., 2000). Indeed, roGFP2 has been shown to be largely oxidized in the cytosol of *rml1* seedlings (Meyer and Dick, 2010). To further investigate the effect of severe GSH depletion on the cytosolic E_{GSH}, both probes, GRX1-roGFP2 and GRX1-roGFP2-iL were expressed in the cytosol of *rml1* and used to measure E_{GSH} in root epidermal cells. As expected, the conventional GRX1-roGFP2 was largely oxidized (**Figures 8A,B**). Incubation of *rml1* seedlings with 25 mM H_2O_2 resulted only in minor additional increase in the fluorescence ratio of GRX1-roGFP2 while incubation of seedlings in 10 mM DTT caused a pronounced drop in fluorescence ratio. Expression of GRX1-roGFP2-iL in the cytosol of *rml1* mutants, on the other hand, resulted in a largely reduced probe (**Figures 8A,C**). Full reduction of the probe through incubation of seedlings with 10 mM DTT caused only a small drop in the detected fluorescence ratio. In contrast, incubation with 25 mM H_2O_2 resulted in a pronounced increase in the 405/488 nm fluorescence ratio. The dynamic range of the

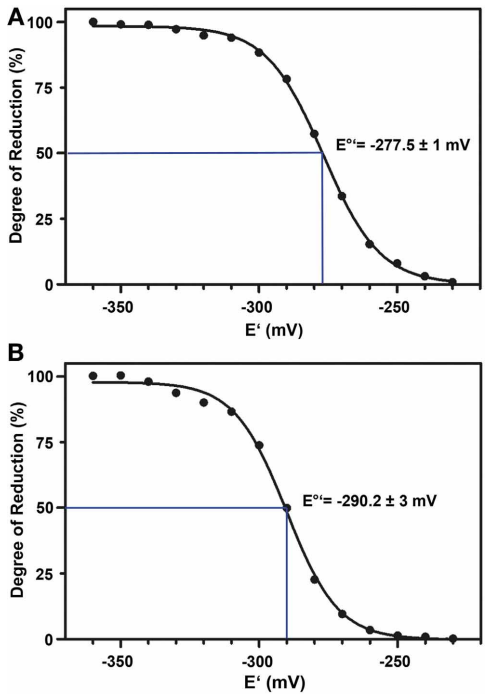

FIGURE 5 | Redox titration of roGFP2 and GRX1-roGFP2. The degree of reduction of roGFP2 **(A)** and GRX1-roGFP2 **(B)** was determined from the excitation ratios plotted against the potential of the ambient redox buffer. Representative measurements of at least 3 independent redox titrations (with 4 replicates each) for both probes are shown.

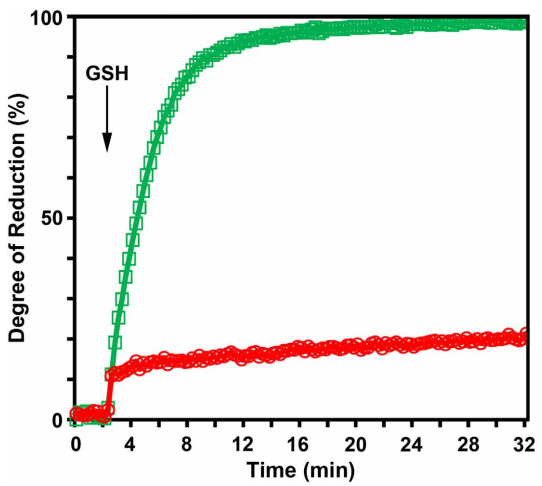

FIGURE 6 | The N-terminally fused glutaredoxin catalyzes the transfer of electrons from glutathione to roGFP2-iL. The excitation ratio 390/480 nm with emission at 520 nm was followed over time. Fully reduced glutathione was added to a solution of oxidized roGFP2-iL (○) or GRX1-roGFP2-iL (□), respectively 2.5 min after the start of the measurement. Change of reduction was recorded over time after injection of 2 mM reduced glutathione. The reaction buffer contained 100 μM NADPH and glutathione reductase at pH 7.4 to maintain full reduction of glutathione over the measured time ($n = 4$).

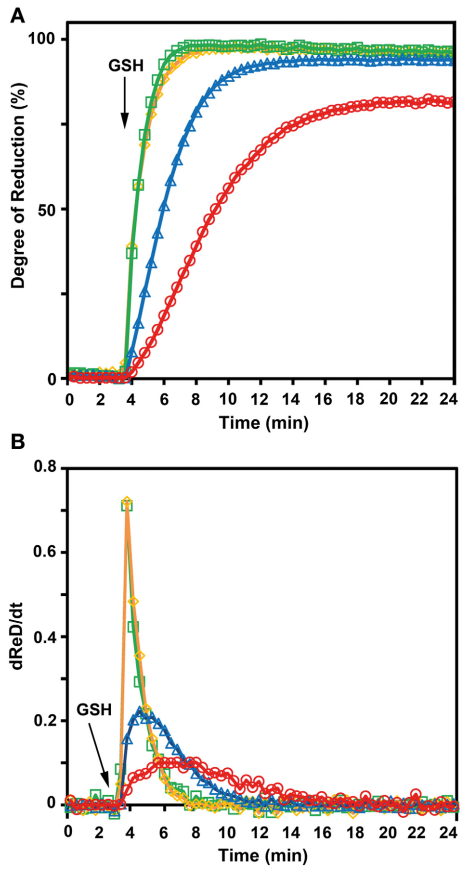

FIGURE 7 | GSH-dependent reduction of roGFP variants. The kinetics for the reduction of roGFP by reduced glutathione strongly depends on redox potential of the disulfide forming cysteines of the respective roGFP sensors. **(A)** The excitation ratio 390/480 nm with emission at 520 nm was followed over time. Fully reduced glutathione (final concentration 5 mM) was added to a solution of pre-oxidized roGFP1-iL (□), roGFP2-iL (◇), roGFP2 (△), and roGFP1 (○) 3.75 min after start of the measurement. The reaction buffer contained 2 μM GRX, 100 μM NADPH, and glutathione reductase at pH 7.4 to maintain maximum reduction of glutathione over the measured time course ($n = 4$). **(B)** *dRed/dt* further illustrates the rapid change in reduction of roGFP1-iL (□) and roGFP2-iL (◇) compared to roGFP2 (△) and roGFP1 (○).

probe in the cytosol calculated from the respective *min* and *max* ratios was about 3-fold (**Figure 8C**), which is similar to the predictions from the spectral analysis of recombinant roGFP2-iL (**Figure 2**).

Calculation of the degree of oxidation (*OxD*) of both probes from the ratiometric imaging data presented in **Figure 8** showed a low *OxD* of only 14% for GRX1-roGFP2-iL and a corresponding high *OxD* of 93% for GRX1-roGFP2 (**Figure 9A**). The measured *OxD* values for both probes can be compared to titration curves for GRX1-roGFP2 (blue) and GRX1-roGFP2-iL (red) that were calculated from the Nernst-Equation using $E^{\circ\prime}$ values determined earlier (**Figure 9B**). The interception points between the titration curves and the *OxD* for GRX1-roGFP2 and GRX1-roGFP2-iL, respectively, suggest an E_{GSH} in the cytosol of *rml1* of about −260 mV.

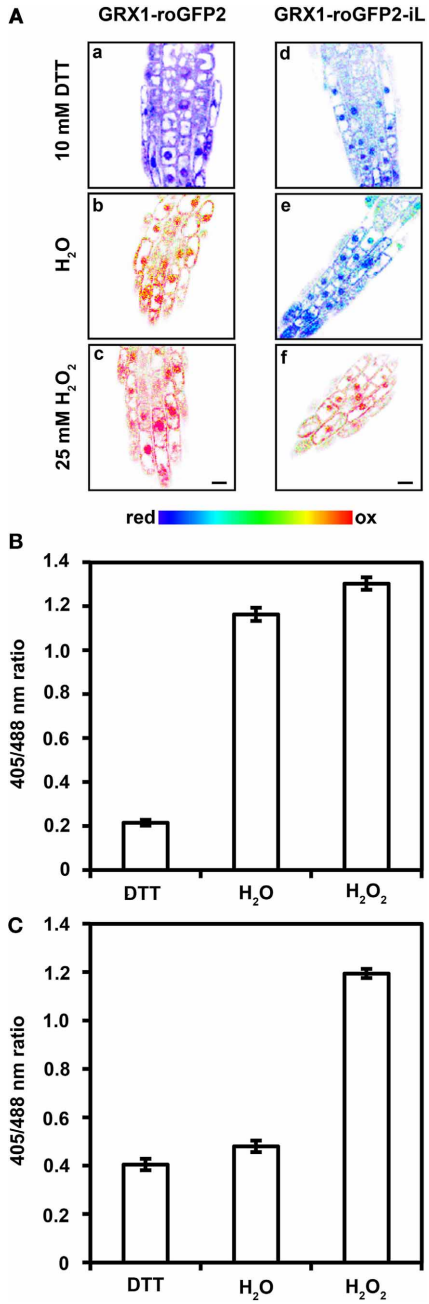

FIGURE 8 | The GRX1-roGFP2-iL probe expressed in the cytosol of homozygous *rml1* mutants is almost completely reduced while GRX1-roGFP2 is highly oxidized. (A) Ratiometric images **(a–f)** show the redox state of GRX1-roGFP2 and GRX-roGFP2-iL in the cytosol of root epidermal cells of *rml1* mutants. Treatment with 10 mM DTT results in full reduction of GRX1-roGFP2 **(a)** and GRX-roGFP2-iL **(d)**, while under resting conditions GRX1-roGFP2 is highly oxidized **(b)** whereas GRX1-roGFP2-iL is in a reduced state **(e)**. Treatment with 25 mM H_2O_2results in complete oxidation of GRX1-roGFP2 **(c)** and GRX-roGFP2-iL **(f)**. Scale bar 10 µm. **(B,C)** Fluorescence ratio of cytosolic GRX1-roGFP2 **(B)** and GRX1-roGFP2-iL **(C)** show complete reduction and oxidation of GRX-roGFP2 and GRX1-roGFP2-iL after treatment with 10 mM DTT and 25 mM H_2O_2, respectively. Under resting conditions in H_2O, GRX1-roGFP2 is highly oxidized while GRX1-roGFP2-iL is highly reduced. Values are calculated as the mean ± SD ($n = 5 - 10$).

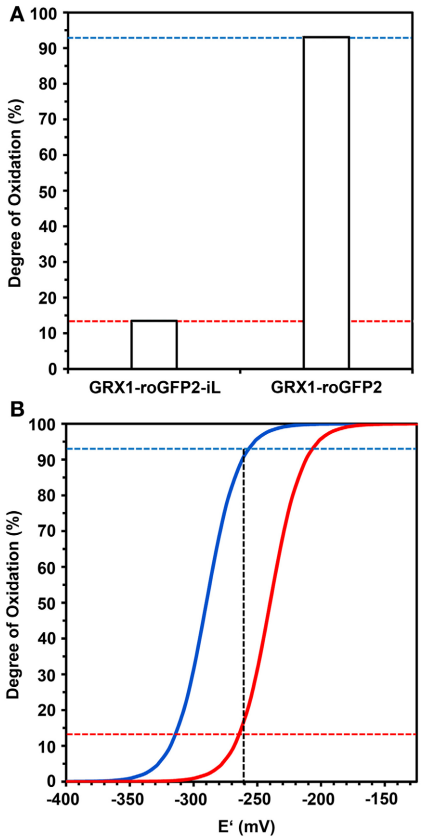

FIGURE 9 | Deduction of the redox potential of the roGFP probes from the Degree of Oxidation (*OxD*) in the cytosol of *rml1* seedlings. (A) GRX1-roGFP2-iL and GRX1-roGFP2 expressed in the cytosol of *rml1* plants as calculated according to equations given in Materials and Methods from the mean fluorescence data presented in **Figure 7**. While GRX1-roGFP2 is highly oxidized only a small fraction of GRX1-roGFP2-iL is in the oxidized state. **(B)** Titration curves drawn for GRX1-roGFP2 (blue) and GRX1-roGFP2-iL (red) were calculated from the Nernst-Equation using the midpoint potentials determined in **Figures 3**, **4**. Dotted horizontal lines refer to *OxD* of GRX1-roGFP2 and GRX1-roGFP2-iL from *rml1* measurements shown in panel **(A)**. The vertical dotted line indicates the interception points for GRX1-roGFP2 (blue) and GRX-roGFP2-iL (red) which suggests an E_{GSH} of about −260 mV in the cytosol of *rml1*.

DISCUSSION

The glutathione redox potential in life cells varies depending on the compartment and on environmental conditions imposing stress situations for the plant. While cytosol, peroxisomes, mitochondria, and plastids in Arabidopsis wild-type plants maintain a highly reduced glutathione buffer with redox potentials of less than −310 mV, the ER is far less reducing with E_{GSH} values of less than −240 mV (Meyer et al., 2007; Schwarzländer et al., 2008). In nominally reducing compartments, severe stress can trigger physiological conditions frequently described as oxidative stress. Better understanding of the underlying molecular processes leading to gradual oxidation and also the downstream processes involved in signal transduction cascades enabling the plant to adapt to a stress situation requires the ability to measure individual components of the cellular redox buffer system in a

dynamic way. The roGFPs, and particularly GRX1-roGFP2 fusion proteins, have been shown to sense the local E_{GSH} with high specificity due to selective mediation of thiol/disulfide exchange reaction between glutathione and roGFP by GRXs (Meyer et al., 2007; Gutscher et al., 2008). The originally introduced variants roGFP1 and roGFP2, however, are particularly suitable only in the reducing compartments of wild-type plants and mutants with limited effects on the amount of glutathione (Meyer et al., 2007; Maughan et al., 2010), or mutants affected in the GSH/GSSG redox equilibrium due to lack of GR (Marty et al., 2009). In more oxidizing compartments or more severe mutants affected in glutathione redox homeostasis, E_{GSH} is outside the measuring range of these probes thus limiting their usability. The need for less reducing probe variants has been partially fulfilled through the introduction of roGFP1-iX variants derived from roGFP1 (Lohman and Remington, 2008). However, even the least reducing variant roGFP1-iL is still largely oxidized in the ER of human cells and thus hardly capable of detecting oxidative processes in the ER. In addition, the most oxidizing roGFP1-iX variant roGFP1-iL has been reported as being relatively dim compared to the parent roGFP1 (Avezov et al., 2013; Birk et al., 2013). Similar to the continuous extension of the range of differentially colored fluorescent proteins (Shaner et al., 2005) there is also a demand for redox reporter proteins with midpoint potentials matching the E_{GSH} in distinct compartments or in mutants with targeted alterations in glutathione homeostasis.

The insertion of amino acids in the GFP backbone may lead to changes in the spectroscopic properties of GFP but still yield functional fluorescent proteins (Topell et al., 1999; Cannon and Remington, 2006; Lohman and Remington, 2008). Insertion of single amino acid residues within the roGFP backbone, adjacent to the reactive cysteine 147, leads to a destabilization of the disulfide formed between Cys147 and Cys204. As a consequence, the resulting roGFP1-iX variants show a less negative midpoint potential compared to the parental roGFP1. However, the substitution of the chromophore phenol(ate) interacting His148 by Ser148 was required to maintain ratiometric behavior (Lohman and Remington, 2008). A roGFP1-iL carrying the mutations S147CL and H148S has been reported to have the least negative midpoint potential (-229 ± 5 mV) of a whole series or roGFP1-iX variants (Lohman and Remington, 2008). Introduction of the same changes into roGFP2 lead to roGFP2-iL. This new variant maintained the general ratiometric behavior of roGFP2 with the excitation peak for the anionic form of the chromophore at 488 nm being more pronounced than the UV excitation peak for the protonated chromophore. However, the dynamic range δ for the maximum change in peak excitation ratio was significantly decreased compared to roGFP2 (see **Figure 2** and **Table 1**). A similar reduction of the dynamic range due to amino acid insertion next to Cys147 has already been reported for several roGFP1-iX variants but not for the roGFP1-iL version (Lohman and Remington, 2008). Similarly to roGFP1-iL, roGFP2-iL is also lower in fluorescence than the respective parent roGFP. Nevertheless, the maintenance of ratiometric properties and a sufficiently large dynamic range to resolve biologically relevant redox changes suggest that roGFP2-iL is generally suitable for *in vivo* measurements.

The roGFP1-iL and roGFP2-iL only differ in the S65T substitution introducing an additional methyl group in roGFP2. This minor change not only affects the protonation of the chromophore leading to pronounced stabilization of the anionic form of the chromophore (Elsliger et al., 1999; Jung et al., 2005) but also shifts the midpoint potential of roGFP2 −10 mV less negative compared to roGFP1. The shift in $E^{o\prime}$ from −280 mV for roGFP2 to −238 mV for roGFP2-iL is lower than the shift for roGFP1-iL which at −229 mV is 62 mV less negative than its parent roGFP1. Different from the original expectation, the modification of roGFP2 did thus not result in a linear additive effect in which the resulting roGFP2-iL was expected to be slightly more negative than roGFP1-iL. The deviation from linearity is probably due to geometric constraints in the roGFP barrel similar to those described for roGFP1-iR which had been expected to be less reducing than roGFP1-iL due to stabilization of the thiolate anion by the introduced adjacent basic arginine residue (Lohman and Remington, 2008). The roGFP1-iR, however, turned out to be more reducing than roGFP1-iL. Whether introduction of basic amino acids in the vicinity of the redox active cysteines may cause a stabilization of thiolates and thus render the redox potential of roGFP2-iL less negative is not known at this stage.

For live cell measurements biosensors should ideally exhibit a strong preference for one specific analyte. By definition, roGFPs undergo thiol/disulfide exchange reactions and it has been shown that specificity for glutathione is achieved through specific interaction with GRXs (Meyer et al., 2007). Fusion of GRX1 to roGFP2 leads to a permanent increase of the local GRX concentration around roGFP and hence this kinetic coupling further increases the likelihood of interaction between roGFP and the fused GRX1 compared to other non-specific interactions with other oxidoreductases (Gutscher et al., 2008; Albrecht et al., 2013). Human GRX1 does also interact with roGFP2-iL and the fusion protein GRX1-roGFP2-iL responds much faster to changes in E_{GSH} than free roGFP2-iL. Interestingly, fusion of GRX1 to the N-termini of different roGFP variants consistently leads to a slight shift of 5–13 mV in the midpoint potentials toward more negative values. A similar shift of 6 mV has also been reported for GRX1-roGFP1-iE (Birk et al., 2013). Consistent with the respective order of redox potentials, Birk et al. (2013) also observed a higher degree of oxidation of GRX1-roGFP1-iE than for free roGFP1-iE expressed in the ER. A possible explanation for the effects of N-terminally fused GRX on the $E^{o\prime}$ of roGFP probes might be a mechanical strain that acts on the GFP barrel slightly affecting the thermodynamic stability of the disulfide. Despite the slightly less negative midpoint potential of roGFP1-iL compared with roGFP2-iL, the kinetic properties of both probes for reduction by GSH are very similar. This suggests that both probes may be equally suitable in compartments with oxidizing conditions. RoGFP2-iL thus extends the range of suitable probes for oxidizing compartments by offering additional spectral features. The dominant excitation peak at 488 nm may be of particular advantage for lifetime imaging of roGFPs with pulsed blue excitation. This imaging approach has been successfully used for the original roGFP2 probe and different roGFP1-iX variants (Wierer et al., 2012; Avezov et al., 2013). For roGFP2-iL, excitation with blue light would maximize the excitation and hence minimize the integration time required

to sample sufficient photons for analysis. Furthermore, it has been reported that roGFP1 under conditions of intense illumination undergoes an irreversible photoswitch reaction that would foster the anionic form of the chromophore and thus may artificially report reducing conditions even though the local environment of the probe is oxidizing (Schwarzländer et al., 2008).

Generally, roGFP probes are appropriate for measuring the thiol/disulfide equilibrium within a linear range of about ±30 mV from their midpoint potential equivalent to an *OxD* between 10 and 90%. RoGFP2-iL may thus be suitable in the range from ∼ −205 to ∼ −275 mV. Recently it was shown that GRX1-roGFP1-iE is still oxidized to more than 90% when expressed in the ER of HeLa cells (Birk et al., 2013). This high degree of oxidation clearly limits the use of the probe in that it would not allow investigating processes leading to increasing oxidation in the ER. Based on the even slightly more negative midpoint potential a very similar response can be expected for GRX1-roGFP2-iL.

Stable expression of GRX1-roGFP2-iL and GRX1-roGFP2 in the cytosol of homozygous *rml1* plants allowed ratiometric measurements of the yet undefined E_{GSH} with both sensors. In both cases the measured values are close to the end of the linear range of the respective probes with GRX1-roGFP2 being even slightly beyond its useful linear measurement range with an oxidation of 93%. GRX1-roGFP2-iL with $OxD = 14\%$ is still in the linear range. Importantly, *OxD* for both sensor variants can be converted to the respective redox potential and in both cases the redox potential is about −260 mV. A combination of both probes thus effectively doubles the useful dynamic range without leaving a gap between the two probes. The concentration of cytosolic glutathione in wild-type Arabidopsis root tips has been shown to be between 2 and 3 mM (Fricker et al., 2000). Assuming a medium concentration of 2.5 mM cytosolic GSH and an OxD_{GSH} of 0.002% (Meyer et al., 2007) the Nernst equation predicts an E_{GSH} of about −310 mV. A remaining GSH level of only 2% in *rml1* would then lead to an E_{GSH} of −260 mV. This calculation assumes a constant OxD_{GSH} which is not necessarily given. Obviously, the *rml1* mutant seedlings are stressed and supply with redox equivalents in form of NADPH may be restricted under these severe metabolic constraints. If indeed OxD_{GSH} was higher in *rml1* than in the wild-type then the total glutathione level in the cytosol would have to be assumed to be slightly above 2% in order to reach an E_{GSH} of −260 mV. This, however, is still well within the measured range of glutathione concentrations in *rml1*.

In conclusion, GRX1-roGFP2-iL further extends the range of roGFP-based probes for measurements of E_{GSH} far less reducing than typical E_{GSH} values normally found in the cytosol. This applies similarly to cell-type specific developmental differences as well as to mutants with low glutathione levels and to generally oxidizing compartments like the ER. GRX1-roGFP2-iL may still be largely oxidized in the ER of non-stressed plants as it has been shown for GRX1-roGFP1-iE in HeLa cells (Birk et al., 2013). The oxidizing redox potential in the lumen supports protein folding whereas deviations from steady-state redox conditions induce an unfolded protein response (Merksamer et al., 2008). Vice versa, malfunction in oxidative protein folding is assumed to affect the redox potential of the lumenal glutathione pool. Under stress situations and in mutants causing a shift in the ER redox potential toward more negative values, GRX1-roGFP2-iL will likely allow dynamic measurement of the glutathione-related redox processes in the ER lumen. Conversely, severe stress situations can cause very strong oxidation in the cytosol, chloroplasts, mitochondria, and peroxisomes and the extent of these reactions may also be dependent on the developmental state of particular cells. Dark-induced senescence has been shown to cause an oxidation of mitochondrial roGFP1 and roGFP2 up to the end of their linear range within only 3 days (Rosenwasser et al., 2010). Under such pathological conditions GRX1-roGFP2-iL will allow to further investigate the most oxidizing phases of the responses.

ACKNOWLEDGMENTS

We thank James Remington for providing pQE-30 with roGFP1-iL and Christian Appenzeller-Herzog for pQE-30 with roGFP1-iE. The UBQ10 promoter was kindly provided by Karin Schumacher. This work was supported by a grant from the Deutsche Forschungsgemeinschaft (DFG) to Andreas J. Meyer (grant ME1567/5-1).

REFERENCES

Albrecht, S. C., Sobotta, M. C., Bausewein, D., Aller, I., Hell, R., Dick, T. P., et al. (2013). Redesign of genetically encoded biosensors for monitoring mitochondrial redox status in a broad range of model eukaryotes. *J. Biomol. Screen.* doi: 10.1177/1087057113499634. [Epub ahead of print].

Apel, K., and Hirt, H. (2004). Reactive oxygen species: metabolism, oxidative stress, and signal transduction. *Annu. Rev. Plant Biol.* 55, 373–399. doi: 10.1146/annurev.arplant.55.031903.141701

Avezov, E., Cross, B. C. S., Kaminski Schierle, G. S., Winters, M., Harding, H. P., Melo, E. P., et al. (2013). Lifetime imaging of a fluorescent protein sensor reveals surprising stability of ER thiol redox. *J. Cell Biol.* 201, 337–349. doi: 10.1083/jcb.201211155

Ball, L., Accotto, G. P., Bechtold, U., Creissen, G., Funck, D., Jimenez, A., et al. (2004). Evidence for a direct link between glutathione biosynthesis and stress defense gene expression in Arabidopsis. *Plant Cell* 16, 2448–2462. doi: 10.1105/tpc.104.022608

Birk, J., Meyer, M., Aller, I., Hansen, H. G., Odermatt, A., Dick, T. P., et al. (2013). Endoplasmic reticulum: reduced and oxidized glutathione revisited. *J. Cell Sci.* 126, 1604–1617. doi: 10.1242/jcs.117218

Brach, T., Soyk, S., Müller, C., Hinz, G., Hell, R., Brandizzi, F., et al. (2009). Non-invasive topology analysis of membrane proteins in the secretory pathway. *Plant J.* 57, 534–541. doi: 10.1111/j.1365-313X.2008.03704.x

Brejc, K., Sixma, T. K., Kitts, P. A., Kain, S. R., Tsien, R. Y., Ormo, M., et al. (1997). Structural basis for dual excitation and photoisomerization of the *Aequorea victoria* green fluorescent protein. *Proc. Natl. Acad. Sci. U.S.A.* 94, 2306–2311. doi: 10.1073/pnas.94.6.2306

Cairns, N. G., Pasternak, M., Wachter, A., Cobbett, C. S., and Meyer, A. J. (2006). Maturation of Arabidopsis seeds is dependent on glutathione biosynthesis within the embryo. *Plant Physiol.* 141, 446–455. doi: 10.1104/pp.106.077982

Cannon, M. B., and Remington, S. J. (2006). Re-engineering redox-sensitive green fluorescent protein for improved response rate. *Protein Sci.* 15, 45–57. doi: 10.1110/ps.051734306

Cobbett, C., and Goldsbrough, P. (2002). Phytochelatins and metallothioneins: roles in heavy metal detoxification and homeostasis. *Annu. Rev. Plant Biol.* 53, 159–182. doi: 10.1146/annurev.arplant.53.100301.135154

Dooley, C. T., Dore, T. M., Hanson, G. T., Jackson, W. C., Remington, S. J., and Tsien, R. Y. (2004). Imaging dynamic redox changes in mammalian cells with green fluorescent protein indicators. *J. Biol. Chem.* 279, 22284–22293. doi: 10.1074/jbc.M312847200

Elsliger, M. A., Wachter, R. M., Hanson, G. T., Kallio, K., and Remington, S. J. (1999). Structural and spectral response of green fluorescent protein variants to changes in pH. *Biochemistry* 38, 5296–5301. doi: 10.1021/bi9902182

Finkel, T. (2011). Signal transduction by reactive oxygen species. *J. Cell Biol.* 194, 7–15. doi: 10.1083/jcb.201102095

Forman, H. J., Maiorino, M., and Ursini, F. (2010). Signaling functions of reactive oxygen species. *Biochemistry* 49, 835–842. doi: 10.1021/bi9020378

Fricker, M. D., May, M., Meyer, A. J., Sheard, N., and White, N. S. (2000). Measurement of glutathione levels in intact roots of Arabidopsis. *J. Microsc.* 198, 162–173. doi: 10.1046/j.1365-2818.2000.00696.x

Gutscher, M., Pauleau, A., Marty, L., Brach, T., Wabnitz, G., Samstag, Y., et al. (2008). Real-time imaging of the intracellular glutathione redox potential. *Nat. Methods* 5, 553–559. doi: 10.1038/nmeth.1212

Hanson, G. T., Aggeler, R., Oglesbee, D., Cannon, M., Capaldi, R. A., Tsien, R. Y., et al. (2004). Investigating mitochondrial redox potential with redox-sensitive green fluorescent protein indicators. *J. Biol. Chem.* 279, 13044–13053. doi: 10.1074/jbc.M312846200

Höfgen, R., and Willmitzer, Z. (1990). Biochemical and genetic analysis of different patatin isoforms expressed in various organs of potato (*Solanum tuberosum*). *Plant Sci.* 66, 221–230. doi: 10.1016/0168-9452(90)90207-5

Hwang, C. C., Sinskey, A. J., and Lodish, H. F. (1992). Oxidized redox state of glutathione in the endoplasmic reticulum. *Science* 257, 1496–1502. doi: 10.1126/science.1523409

Jung, G., Wiehler, J., and Zumbusch, A. (2005). The photophysics of green fluorescent protein: influence of the key amino acids at positions 65, 203, and 222. *Biophys. J.* 88, 1932–1947. doi: 10.1529/biophysj.104.044412

Lees, W. J., and Whitesides, G. M. (1993). Equilibrium constants for thiol-disulfide interchange reactions: a coherent, corrected set. *J. Org. Chem.* 58, 642–647. doi: 10.1021/jo00055a016

Lohman, J., and Remington, S. (2008). Development of a family of redox-sensitive green fluorescent protein indicators for use in relatively oxidizing subcellular environments. *Biochemistry* 47, 8678–8688. doi: 10.1021/bi800498g

Magde, D., Wong, R., and Seybold, P. (2002). Fluorescence quantum yields and their relation to lifetimes of rhodamine 6G and fluorescein in nine solvents: improved absolute standards for quantum yields. *Photochem. Photobiol.* 75, 327–334. doi: 10.1562/0031-8655(2002)075<0327:FQYATR>2.0.CO;2

Marty, L., Siala, W., Schwarzländer, M., Fricker, M. D., Wirtz, M., Sweetlove, L. J., et al. (2009). The NADPH-dependent thioredoxin system constitutes a functional backup for cytosolic glutathione reductase in Arabidopsis. *Proc. Natl. Acad. Sci. U.S.A.* 106, 9109–9114. doi: 10.1073/pnas.0900206106

Maughan, S. C., Pasternak, M., Cairns, N., Kiddle, G., Brach, T., Jarvis, R., et al. (2010). Plant homologs of the *Plasmodium falciparum* chloroquine-resistance transporter, PfCRT, are required for glutathione homeostasis and stress responses. *Proc. Natl. Acad. Sci. U.S.A.* 107, 2331–2336. doi: 10.1073/pnas.0913689107

Merksamer, P., Trusina, A., and Papa, F. (2008). Real-time redox measurements during endoplasmic reticulum stress reveal interlinked protein folding functions. *Cell* 135, 933–947. doi: 10.1016/j.cell.2008.10.011

Meyer, A., and Dick, T. (2010). Fluorescent protein-based redox probes. *Antioxid. Redox Signal.* 13, 621–650. doi: 10.1089/ars.2009.2948

Meyer, A. J., Brach, T., Marty, L., Kreye, S., Rouhier, N., Jacquot, J.-P., et al. (2007). Redox-sensitive GFP in *Arabidopsis thaliana* is a quantitative biosensor for the redox potential of the cellular glutathione redox buffer. *Plant J.* 52, 973–986. doi: 10.1111/j.1365-313X.2007.03280.x

Meyer, A. J., and Hell, R. (2005). Glutathione homeostasis and redox-regulation by sulfhydryl groups. *Photosynth. Res.* 86, 435–457. doi: 10.1007/s11120-005-8425-1

Michelet, L., Zaffagnini, M., Marchand, C., Collin, V., Decottignies, P., Tsan, P., et al. (2005). Glutathionylation of chloroplast thioredoxin f is a redox signaling mechanism in plants. *Proc. Natl. Acad. Sci. U.S.A.* 102, 16478–16483. doi: 10.1073/pnas.0507498102

Noctor, G., Mhamdi, A., Chaouch, S., Han, Y., Neukermans, J., Marquez-Garcia, B., et al. (2011). Glutathione in plants: an integrated overview. *Plant Cell Environ.* 35, 454–484. doi: 10.1111/j.1365-3040.2011.02400.x

Palm, G., Zdanov, A., Gaitanaris, G., Stauber, R., Pavlakis, G., and Wlodawer, A. (1997). The structural basis for spectral variations in green fluorescent protein. *Nat. Struct. Biol.* 4, 361–365. doi: 10.1038/nsb0597-361

Parisy, V., Poinssot, B., Owsianowski, L., Buchala, A., Glazebrook, J., and Mauch, F. (2007). Identification of PAD2 as a γ-glutamylcysteine synthetase highlights the importance of glutathione in disease resistance of Arabidopsis. *Plant J.* 49, 159–172. doi: 10.1111/j.1365-313X.2006.02938.x

Patterson, G. H., Knobel, S. M., Sharif, W. D., Kain, S. R., and Piston, D. W. (1997). Use of the green fluorescent protein and its mutants in quantitative fluorescence microscopy. *Biophys. J.* 73, 2782–2790. doi: 10.1016/S0006-3495(97)78307-3

Rosenwasser, S., Rot, I., Meyer, A. J., Feldman, L., Jiang, K., and Friedman, H. (2010). A fluorometer-based method for monitoring oxidation of redox-sensitive GFP (roGFP) during development and extended dark stress. *Physiol. Plant.* 138, 493–502. doi: 10.1111/j.1399-3054.2009.01334.x

Samalova, M., Meyer, A. J., Gurr, S. J., and Fricker, M. D. (2013). Robust anti-oxidant defences in the rice blast fungus *Magnaporthe oryzae* confer tolerance to the host oxidative burst. *New Phytol.* doi: 10.1111/nph.12530. [Epub ahead of print].

Schlaeppi, K., Bodenhausen, N., Buchala, A., Mauch, F., and Reymond, P. (2008). The glutathione-deficient mutant *pad2-1* accumulates lower amounts of glucosinolates and is more susceptible to the insect herbivore *Spodoptera littoralis*. *Plant J.* 55, 774–786. doi: 10.1111/j.1365-313X.2008.03545.x

Schwarzländer, M., Fricker, M., Müller, C., Marty, L., Brach, T., Novak, T., et al. (2008). Confocal imaging of glutathione redox potential in living plant cells. *J. Microsc.* 231, 299–316. doi: 10.1111/j.1365-2818.2008.02030.x

Shaked, Z., Szajewski, R., and Whitesides, G. (1980). Rates of thiol-disulfide interchange reactions involving proteins and kinetic measurements of thiol pK_a values. *Biochemistry* 19, 4156–4166. doi: 10.1021/bi00559a004

Shaner, N., Steinbach, P., and Tsien, R. (2005). A guide to choosing fluorescent proteins. *Nat. Methods* 2, 905–909. doi: 10.1038/nmeth819

Somerville, C. R., and Ogren, W. L. (1982). "Isolation of photorespiration mutants in Arabidopsis," in *Methods in Chloroplast Molecular Biology*, eds M. Edelman, R. B. Hallick, and N. H. Chua (Amsterdam: Elsevier Biomedical Press), 129–138.

Topell, S., Hennecke, J., and Glockshuber, R. (1999). Circularly permuted variants of the green fluorescent protein. *FEBS Lett.* 457, 283–289. doi: 10.1016/S0014-5793(99)01044-3

Torres, M. A., Jones, J. D. G., and Dangl, J. L. (2006). Reactive oxygen species signaling in response to pathogens. *Plant Physiol.* 141, 373–378. doi: 10.1104/pp.106.079467

Vernoux, T., Wilson, R. C., Seeley, K. A., Reichheld, J. P., Muroy, S., Brown, S., et al. (2000). The ROOT MERISTEMLESS1/CADMIUM SENSITIVE2 gene defines a glutathione-dependent pathway involved in initiation and maintenance of cell division during postembryonic root development. *Plant Cell* 12, 97–110. doi: 10.2307/3871032

Wierer, S., Peter, S., Elgass, K., Mack, H., Bieker, S., Meixner, A., et al. (2012). Determination of the *in vivo* redox potential by one-wavelength spectro-microscopy of roGFP. *Anal. Bioanal. Chem.* 403, 737–744. doi: 10.1007/s00216-012-5911-0

Zaffagnini, M., Bedhomme, M., Marchand, C., Couturier, J., Gao, X., Rouhier, N., et al. (2012). Glutaredoxin s12: unique properties for redox signaling. *Antioxid. Redox Signal.* 16, 17–32. doi: 10.1089/ars.2011.3933

Conflict of Interest Statement: The authors declare that the research was conducted in the absence of any commercial or financial relationships that could be construed as a potential conflict of interest.

Received: 03 September 2013; accepted: 26 November 2013; published online: 16 December 2013.

*Citation: Aller I, Rouhier N and Meyer AJ (2013) Development of roGFP2-derived redox probes for measurement of the glutathione redox potential in the cytosol of severely glutathione-deficient rml1 seedlings. Front. Plant Sci. **4**:506. doi: 10.3389/fpls.2013.00506*

This article was submitted to Plant Cell Biology, a section of the journal Frontiers in Plant Science.

Copyright © 2013 Aller, Rouhier and Meyer. This is an open-access article distributed under the terms of the Creative Commons Attribution License (CC BY). The use, distribution or reproduction in other forums is permitted, provided the original author(s) or licensor are credited and that the original publication in this journal is cited, in accordance with accepted academic practice. No use, distribution or reproduction is permitted which does not comply with these terms.

frontiers in
PLANT SCIENCE

METHODS ARTICLE
published: 18 February 2014
doi: 10.3389/fpls.2014.00043

Imaging long distance propagating calcium signals in intact plant leaves with the BRET-based GFP-aequorin reporter

***Tou Cheu Xiong*[1,2,3,4]*, *Elsa Ronzier*[1,2,3,4], *Frédéric Sanchez*[1,2,3,4], *Claire Corratgé-Faillie*[1,2,3,4], *Christian Mazars*[5,6] and *Jean-Baptiste Thibaud*[1,2,3,4]**

[1] *Biochimie et Physiologie Moléculaire des Plantes, Institut National de la Recherche Agronomique, UMR 386, Montpellier, France*
[2] *Biochimie et Physiologie Moléculaire des Plantes, Centre National de la Recherche Scientifique, UMR 5004, Montpellier, France*
[3] *Biochimie et Physiologie Moléculaire des Plantes, SupAgro, Montpellier, France*
[4] *Biochimie et Physiologie Moléculaire des Plantes, UM2, Montpellier, France*
[5] *Laboratoire de Recherche en Sciences Végétales, Université de Toulouse, UPS, UMR 5546, Castanet-Tolosan, France*
[6] *Centre National de la Recherche Scientifique, UMR 5546, Castanet-Tolosan, France*

Edited by:
Alex Costa, University of Milan, Italy

Reviewed by:
Zhi Qi, Inner Mongolia University-Hohhot, China
Nathalie Leborgne-Castel, Université de Bourgogne, France
Markus Schwarzländer, University of Bonn, Germany

****Correspondence:***
Tou Cheu Xiong, Biochimie et Physiologie Moléculaire des Plantes, Institut National de la Recherche Agronomique, UMR 386/Centre National de la Recherche Scientifique, UMR 5004/Montpellier SupAgro/Université Montpellier 2, Campus INRA-SupAgro, Place Pierre Viala, F34060 Montpellier Cedex 2, France
e-mail: xiong@supagro.inra.fr

Calcium (Ca^{2+}) is a second messenger involved in many plant signaling processes. Biotic and abiotic stimuli induce Ca^{2+} signals within plant cells, which, when decoded, enable these cells to adapt in response to environmental stresses. Multiple examples of Ca^{2+} signals from plants containing the fluorescent yellow cameleon sensor (YC) have contributed to the definition of the Ca^{2+} signature in some cell types such as root hairs, pollen tubes and guard cells. YC is, however, of limited use in highly autofluorescent plant tissues, in particular mesophyll cells. Alternatively, the bioluminescent reporter aequorin enables Ca^{2+} imaging in the whole plant, including mesophyll cells, but this requires specific devices capable of detecting the low amounts of emitted light. Another type of Ca^{2+} sensor, referred to as GFP-aequorin (G5A), has been engineered as a chimeric protein, which combines the two photoactive proteins from the jellyfish *Aequorea victoria*, the green fluorescent protein (GFP) and the bioluminescent protein aequorin. The Ca^{2+}-dependent light-emitting property of G5A is based on a bioluminescence resonance energy transfer (BRET) between aequorin and GFP. G5A has been used for over 10 years for enhanced *in vivo* detection of Ca^{2+} signals in animal tissues. Here, we apply G5A in Arabidopsis and show that G5A greatly improves the imaging of Ca^{2+} dynamics in intact plants. We describe a simple method to image Ca^{2+} signals in autofluorescent leaves of plants with a cooled charge-coupled device (cooled CCD) camera. We present data demonstrating how plants expressing the G5A probe can be powerful tools for imaging of Ca^{2+} signals. It is shown that Ca^{2+} signals propagating over long distances can be visualized in intact plant leaves and are visible mainly in the veins.

Keywords: *Arabidopsis thaliana*, calcium imaging, cooled CCD camera, GFP-aequorin, leaf, long distance calcium signaling, calcium waves, salt stress

INTRODUCTION

Calcium (Ca^{2+}) has long been established as a second messenger. Transgenic expression of fluorescence resonance energy transfer (FRET)-based fluorescent Ca^{2+} reporters such as the popular yellow cameleon (YC) or of the bioluminescent aequorin has permitted non-invasive monitoring of free Ca^{2+} levels and enabled real-time imaging of Ca^{2+} levels in different cell-types and organisms, including plants (Knight et al., 1991; Perez Koldenkova and Nagai, 2013). The YC has been used extensively for imaging Ca^{2+} signals in specific plant cell types such as guard cells (Allen et al., 1999), germinating pollen tubes (Iwano et al., 2012), and root hairs (Miwa et al., 2006; Monshausen et al., 2008). YC is also well suitable for Ca^{2+} sensing in subcellular compartments (Krebs et al., 2012; Bonza et al., 2013). However, YC requires excitation by exogenous light, which limits its relevance in plant photosynthetic tissues due to high background emission from auto-fluorescent cell walls, chlorophyll, and secondary metabolites. Indeed, wide autofluorescent spectrum of plant leaf pigments that overlap YC emission limits visualization of changes in intensity of YC fluorescence emission upon Ca^{2+} elevation. Moreover, Ca^{2+} imaging at plant tissue level requires strong and long excitation to detect fluorescence signals. Long term Ca^{2+} measurements would result in some YC photo-bleaching and/or tissue damage, this limiting long term Ca^{2+} measurements, over 24 h for example. On the other hand, the bioluminescent Ca^{2+} reporter aequorin does not require exogenous excitation light and very little background signal is produced resulting in a high signal-to-noise ratio throughout long acquisition periods. Aequorin has the largest dynamic range among Ca^{2+} reporters, allowing the monitoring of Ca^{2+} signals over several days and over a wide range of Ca^{2+} concentrations (Alonso and Garcia-Sancho, 2011). Aequorin has been introduced into several plant species (Knight et al., 1991; Webb et al., 2010) and has enabled photon counting based monitoring of Ca^{2+} in intact plant leaves. Many reports of aequorin application in plants have been published, where photon counting with luminometers was used to

describe Ca^{2+} signaling under several stress conditions. However, to image photons emitted by aequorin with good resolution in both space and time requires sophisticated detection devices such as image photon detectors (IPDs) (Webb et al., 2010) or cameras fitted with an Intensified Charge-Coupled Device (ICCD) (Webb et al., 2010) or Electron Multiplying Charge-Coupled Device (EMCCD) (Rogers et al., 2008; Webb et al., 2010). This is a significant limitation to *in planta* Ca^{2+} imaging which could be overcome by using the G5A probe, an engineered fusion between the green fluorescent protein (GFP) and aequorin (**Figures 1A,C**) initially developed for Ca^{2+} imaging in animal cells (Baubet et al., 2000; Rogers et al., 2005). Through a bioluminescence resonance energy transfer (BRET) from aequorin to GFP, the wavelength of the emitted photon is 510 nm, instead of 470 nm and detection yield by CCD is found optimized, compared to aequorin, with a better signal/noise ratio (Baubet et al., 2000; Rogers et al., 2005, 2008).

Here, (i) we applied G5A in Arabidopsis, (ii) we show that, in comparison to aequorin, G5A enhances *in vitro* and *in vivo* detection of weak Ca^{2+} events in intact plants, including in photosynthetic tissues and (iii) we describe a simple method that only requires a cooled-CCD camera to visualize Ca^{2+} signals in plant leaves as, for example, Ca^{2+} waves propagating along leaf veins of intact plants after imposing a salt stress to roots of these plants. It is concluded that G5A reporter is an interesting alternative to aequorin.

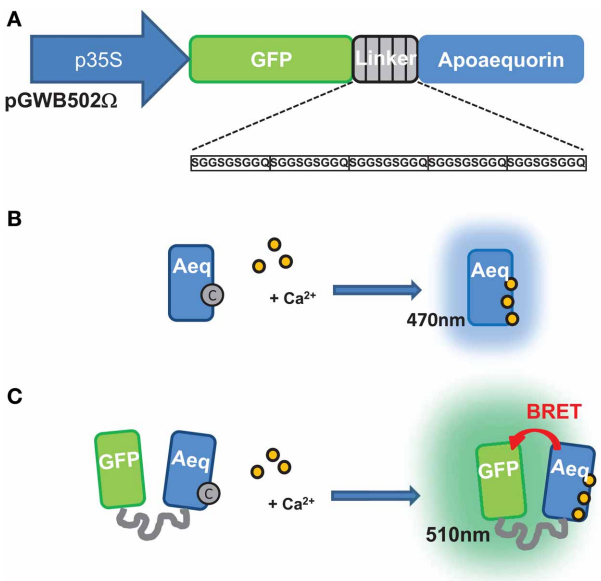

FIGURE 1 | Construction and operating principle of the G5A Ca^{2+} reporter. (A) Structure of the chimeric gene encoding the G5A sensor. The open-reading frame (*ORF*) encoding the green fluorescent protein (GFP) is linked to the *ORF* encoding the apo-aequorin by five repeats of a short sequence encoding a SGGSGSGGQ oligopeptide. The structure and length of this linker ensures efficient bioluminescence resonance energy transfer (BRET) between the aequorin and the GFP (Baubet et al., 2000). Using the pGWB502Ω vector, constitutive G5A expression is driven by a 35S promoter. **(B)** Principle of the aequorin bioluminescence emission upon binding of Ca^{2+}. In the presence of the coelenterazine cofactor ("C"), the apo-aequorin is reconstituted as a functional aequorin. Upon binding of three Ca^{2+} ions, the cofactor is released with emission of light at ~470 nm. **(C)** Principle of G5A fluorescence emission upon binding of Ca^{2+}. Thanks to the tight molecular coupling between the aequorin and GFP moieties of G5A, a BRET phenomenon between aequorin and GFP leads to excitation of and fluorescence emission at 510 nm by the latter.

MATERIALS AND METHODS

CLONING G5A AND ENGINEERING G5A-EXPRESSING PLANTS

The original vector harboring the *G5A* construct (Baubet et al., 2000) was kindly provided by Dr. Philippe Brûlet's group (CNRS, Gif-sur-Yvette, France). The G5A coding sequence was cloned into the Gateway® entry vector pDONR™ by two sequential PCRs amplification using a *G5A* forward primer 5′-GGAGATAGAACC**ATGAGCAAGGGCGAGGAGCTGTTCA**-3′ and a *G5A* reverse primer 5′-TCCACCTCCGG**ATCAGGGGAC AGCTCCACCGTAG**-3′, followed by a second PCR using a U5 forward primer 5′-GGGGACAAGTTTGTACAAAAA AGCAGGCTTCGAAGGAGAT-AGAACCATG-3′ and a U3 reverse primer 5′-AGATTGGGGACCACTTTGTACAAGAAA GC-TGGGTCTCCACCTCCGGATC-3′. Next step was a transfer, by LR Gateway® recombination, of the *G5A* construct into the expression vector pGWB502Ω (Nakagawa et al., 2007).

The pGWB502Ω-*G5A* construct was introduced in *Agrobacterium tumefaciens* (GV3101), for transformation of *Arabidopsis thaliana* ecotype Col-0 by the floral dip method (Clough and Bent, 1998). G5A expressing transgenic plants were selected using hygromycin selective media and checked for GFP fluorescence emission under direct excitation of GFP at 488 nm (see **Figure 2**). Homozygous G5A expressing T3 and T4 plants (here below denoted *G5A* plants) were used and compared to transgenic plants expressing aequorin in the cytoplasm (Col-0 ecotype, denoted below *Aeq* plants) obtained from Prof. Marc Knight (Durham, UK).

PLANT MATERIAL AND GROWTH CONDITIONS

Seeds from *Aeq* and *G5A* plants were surface-sterilized and placed on half-strength Murashige and Skoog plate medium supplemented with sucrose 1% (w/v) and with hygromycin (15 μg/mL)(*G5A*) or kanamycin (50 μg/mL)(*Aeq*), and stratified at 4°C for 2 days in the dark. Seedlings were subsequently grown in a growth chamber at 22°C with a 70% relative humidity, in long-day conditions (150 $\mu E/m^2/s$ light for 16 h a day) for 7 days. These 7-day old seedlings were either used directly or further grown in soil under short day conditions (200 $\mu E/m^2/s$ light for 8 h a day) for 3–7 weeks, as indicated.

LUMINESCENCE MEASUREMENT AND IMAGING

Seedlings

In vivo reconstitution of functional aequorin was performed by incubating 7 day-old seedlings for 4 h at 22°C in the dark with a 2.5 μM aqueous solution of coelenterazine HCP (Interchim). For imaging, coelenterazine-treated seedlings were placed within a dark chamber over a gelosed layer (water with 1% agar) in large Petri dishes. A cooled-CCD camera (Hamamatsu 4880-30), fitted at the top of the chamber, collected photons. Sequential image acquisition was carried out using the Hipic 5.1.0 software with an exposure time per image in the 15–60 s range (as indicated in the

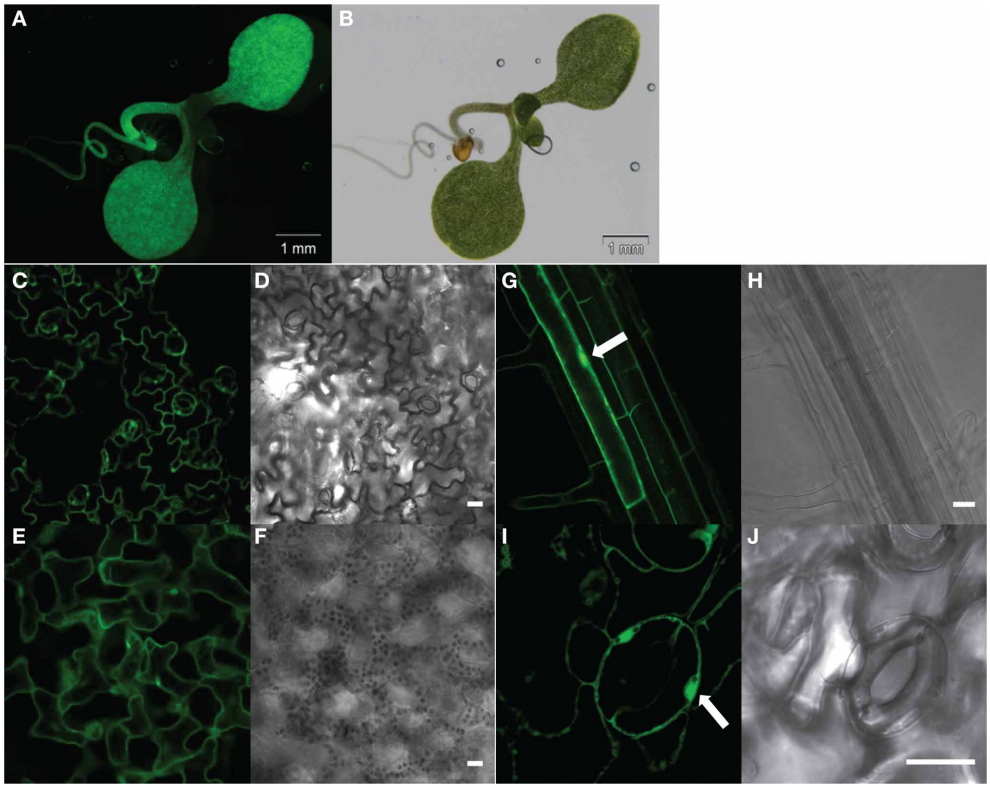

FIGURE 2 | Constitutive expression of the G5A fusion protein in all tissues of *Arabidopsis thaliana* seedlings. Seven **(A–F)** or 21 day-old **(G–J)** plants of the *G5A* line were checked for reporter expression by excitation of GFP (at λ_{ex} = 488 nm) under a stereo microscope **(A,B)** or a confocal microscope **(C–J)**. Fluorescence emission by GFP is shown in **(A,C,E,G,I)** and corresponding bright field images are shown respectively in **(B,D,F,H,J)**. Fluorescent stereo microscope observation of intact seedlings allowed detection of GFP signals in cotyledons and the primary root **(A,B)**. Confocal microscopy observation of leaf epidermal cells **(C,D)** and mesophyll cells **(E,F)** showed good expression of G5A in leaf tissues. G5A fluorescence was observed in both the cytosol and the nucleus (arrows) of root cells **(G,H)** and of stomatal guard cells **(I,J)**. Scale bar = 20 μm.

Figure legends). Images were analyzed in ImageJ (Schneider et al., 2012). The first 5 min in each sequence were discarded because of chlorophyll autofluorescence decay.

Older soil-grown plants

At the end of the day, the soil was gently removed from the roots and the whole plants were incubated for 4 h at 22°C in the dark in a 2.5 μM aqueous solution of coelenterazine HCP. Plants were then placed with the roots in Qualibact® (CEB) tubes filled with water through a hole in the cap of the tube to separate leaves from roots. Plants were left for 1 h in the dark at room temperature for recovery. Images of the rosette were acquired as described above for seedlings, with a 30 s integration time. NaCl at a final concentration of 200 mM was injected with a remotely controlled syringe at the root level after 25 min of acquisition.

Excised mature leaves

Mature leaves were excised from 6–7-week old plants grown as described above and incubated at 22°C in the dark for 4 h in a 2.5 μM aqueous solution of coelenterazine HCP. The treated excised leaf was then transferred to a dark chamber under the cooled-CCD camera for G5A imaging as described above with 15 s exposure time by frame. For salt stress, 100 μL of 200 mM NaCl was pipetted onto the excised leaf petiole (see **Figure 8A** arrow) and subsequent light emission was acquired.

IMAGE ANALYSIS

All images were analyzed in ImageJ. Shading correction of all images was performed by subtraction of a dark field image (acquisition without sample) acquired with the same exposure time. Backgrounds of each image were normalized by subtraction of ROIs of non-plant pixels. ROIs of plant pixels were then quantified and the average values are plotted over the time. Background noise after chlorophyll fluorescence decay was determined by imaging light emission from wild-type plant leaves and then subtracted for data obtained from *G5A* or *Aeq* plants. Ca^{2+} signal velocity was determined with the MtrackJ plugin of ImageJ and the localization (x,y) of each velocity value was plotted with Matlab® software (R2006a).

AEQUORIN IMMUNOBLOTTING

Soluble protein was extracted from 50 pooled seedlings (Mithofer and Mazars, 2002) and separated by SDS-PAGE. Immunoblotting was carried out using an anti-aequorin rabbit polyclonal antibody (Novus Biological, NB100-1877) as described by the manufacturer. Signals of immunodetection were acquired with

LAS-3000 imager (Fujifilm) and quantified with Multi-Gauge v3.2 (Fujifilm).

CALIBRATION OF THE TWO PROBES G5A AND AEQUORIN

Soluble proteins were extracted from *G5A* and *Aeq* plants as described by Mithofer and Mazars (2002) and were diluted in a buffer (Tris-HCl 200 mM, pH 7.4, EGTA 5 mM, NaCl 0.5 M, β-mercaptoethanol 5 mM) containing the coelenterazine HCP cofactor for 2 h in the dark at 4°C. Relative amounts of G5A and aequorin reporters in these crude extracts were estimated by immunoblotting (**Figure 3A**). So-called *G5A* and *Aeq* buffers were prepared by diluting soluble protein crude extracts from *G5A* and *Aeq* plants in Tris-HCl 200 mM, pH 7.0, EGTA 5 mM at a protein content of 0.1 μg/μL and 0.15 μg/μL respectively (to ensure that subsequent *in vitro* comparison of both reporters was made with equal quantities of them). Wells of 96-well plates were filled with 50 μL of different Ca^{2+} solutions, of which the free Ca^{2+} concentration was estimated by MaxChelator Software (http://www.stanford.edu/~cpatton/downloads.htm). To start probe calibration, 50 μL of either *G5A* or *Aeq* buffer was dispensed into each well and maximum light emitted per second (L) was measured. In a second step, 100 μL of a 2 M $CaCl_2$ solution was dispensed into each well for discharging the remaining reconstituted G5A or aequorin reporters. Light emitted at this time (L_{total}) allowed the total amount of functional Ca^{2+} reporter to be estimated. All light measurements were made with a plate-spectrophotometer Victor^2 (Perkin Elmer). Collected photons were integrated over 1 s lapses during 180 s. Results are expressed as the ratio ±SE of maximum light over total light (L/L_{total}).

RESULTS

Effective transformation using the pGWB502Ω-*G5A* construct was expected to yield a broad constitutive expression pattern of the G5A probe. This was checked in a Ca^{2+}-independent manner by direct excitation, at 488 nm, of the GFP moiety of the chimera probe (**Figure 2**).

A strong ubiquitous GFP signal was observed in 7 day-old seedlings. The subcellular pattern of the GFP signal suggested cytosolic and nuclear localization (arrows in **Figures 2G,I**).

An anti-aequorin polyclonal antibody (Novus Biological, USA) was used to evaluate the amount of G5A and aequorin proteins in the soluble protein fraction (**Figure 3A**). This antibody revealed strong bands at 22 kDa and 52 kDa in both protein extracts from *Aeq* and *G5A* plants. The G5A/aequorin ratio (protein level) was estimated at 1.48 ± 0.14.

Calibration curves were performed with soluble protein extracts from *G5A* or *Aeq* plants. Equal amounts of G5A and aequorin reporters were used for *in vitro* calibration curves. Data are expressed as maximum light emitted per second (denoted "L") (Fricker et al., 1999) over total light (denoted "L_{total}") ratio (**Figure 3B** see "Methods" section). G5A and aequorin showed similar responses to free Ca^{2+} concentration and calibration curves in **Figure 3B** do not differ significantly over the 10^{-8} to 10^{-6} M free Ca^{2+} range. Linear regression between 10^{-8} to 10^{-6} M free Ca^{2+} reveals a straight line with a slope of 1.065 ± 0.016 ($R^2 = 0.988$) and 0.888 ± 0.015 ($R^2 = 0.987$) for G5A and aequorin respectively (**Figure 3B**). The reciprocal relationship, i.e., between free Ca^{2+} concentration and the rate of consumption of G5A or aequorin, can be represented by the equation:

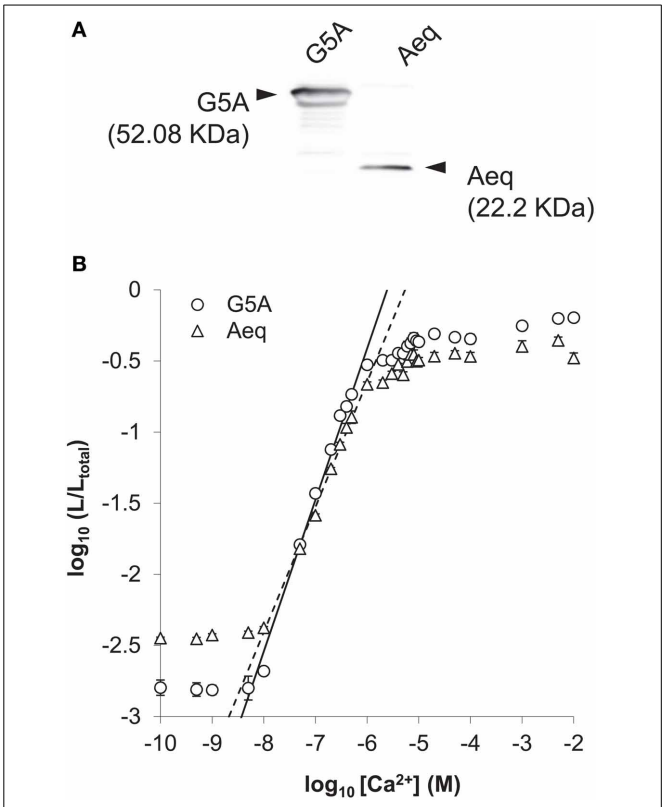

FIGURE 3 | *In vitro* calibration of G5A and aequorin as Ca^{2+} reporters. **(A)** Immunoblotting of soluble protein fractions from fifty 14 day-old plants of the *G5A* and *Aeq* lines with an anti-aequorin polyclonal antibody. Signals of immunoblotting were quantified and indicated as a G5A/aequorin ratio of protein accumulation of 1.48 ± 0.14 (average of one hundred seedlings obtained in two independent experiments ± SE, $n = 2$). **(B)** *In vitro* calibration curves of G5A and aequorin in soluble protein extracts from *G5A* and *Aeq* plants. Equivalent amounts of Ca^{2+} reporters were used for the comparison (based on assay reported in **A**) and incubated in a buffer containing 2.5 μM coelenterazine HCP cofactor for 2 h in the dark at 4°C prior light emission assay in the presence of various free Ca^{2+} amounts (see Materials and Methods). Results are expressed as the ratio ± SE ($n = 6$ in two independent experiments) of maximum light over total light (L/L_{total}). The linear range of L/L_{total} ratio as a function of free Ca^{2+} concentration is shown for G5A (full line) and aequorin (dashed line).

$$-\log([Ca^{2+}]) = a * -\log(\frac{L}{L_{\text{Total}}}) + b \text{ (Fricker et al., 1999)}$$

Coefficients a and b in the above equation are 0.93919 and 5.61289 for G5A, and 1.13646 and 5.26608 for aequorin.

The bioluminescent reporter aequorin has very low noise and high signal/noise ratio (Brini, 2008; Webb et al., 2010). No signal from G5A and aequorin was detected under *in vitro conditions*, in the absence of coelenterazine HCP. In the presence of coelenterazine HCP and without Ca^{2+}, G5A and aequorin noise levels were respectively 271.16 ± 10.76 and 198.67 ± 11.52 RLU (Relative

Light Unit). This difference is, however, negligible compared to signal after injection of free Ca^{2+}. At the basal level of cytosolic free Ca^{2+} (0.1 μM), maximum light level was increased to $6.61 \times 10^3 \pm 0.32 \times 10^3$ and $1.72 \times 10^3 \pm 0.29 \times 10^3$ RLU for G5A and aequorin respectively. At 1 μM free Ca^{2+}, light levels increased up to $90.14 \times 10^3 \pm 7.44 \times 10^3$ and $20.25 \times 10^3 \pm 1.65 \times 10^3$ RLU for G5A and aequorin respectively. Data expressed as signal/noise ratio for the two reporters (**Figure 4A**) show that G5A is approximately 3–5 times better than aequorin. For instance, the signal/noise ratio of aequorin with 1 μM free Ca^{2+} is reached with only 300 nM free Ca^{2+} with G5A reporter.

In parallel, comparison of the two Ca^{2+} reporters was performed *in planta*. Different time lapses were tested for collecting photons emitted by *G5A* and *Aeq* plants (**Figure 4B**). The threshold for signal detection for basal level of free Ca^{2+} was approximately 10 s and 30 s with G5A and aequorin respectively. A 30 s time lapse allowed sufficient light to be collected from *G5A* plants while 1 min was hardly sufficient in the case of *Aeq* plants.

Sudden light-dark transition has been reported to induce weak Ca^{2+} signals in photosynthetic tissues (Johnson et al., 1995; Sai and Johnson, 2002; Dodd et al., 2006). To assess the capability of G5A to detect weak Ca^{2+} events in intact plant tissues, we challenged Arabidopsis plants with darkness: the reactions of *G5A* plants upon light-dark transition were compared to those of *Aeq* plants (**Figure 5**). Significantly more photons could be collected from *G5A* plants than from the *Aeq* plants over this period (**Figure 5B**). Successive integrations of photons over 1 min time lapses provided an overview of the Ca^{2+} signal kinetics (**Figure 5C**). Dark-induced Ca^{2+} signals displayed by G5A and aequorin had parallel kinetics (**Figure 5C** and inset), with a maximal light emission between 40 and 60 min. However, approximately five times more photons were detected from plants of the *G5A* line.

This interesting G5A feature allowed us to follow the dynamics of free Ca^{2+} in leaves triggered by a salt stress applied to roots of intact plants (**Figure 6** and **Supplementary videos S1**, **S2**). The stress was sensed by roots and propagated to leaves, suggesting that Ca^{2+} waves might contribute to plant adaptation to salt stress. A time series of representative results (from video S1) is presented in **Figure 6A**. It shows that a 30 s delay after the

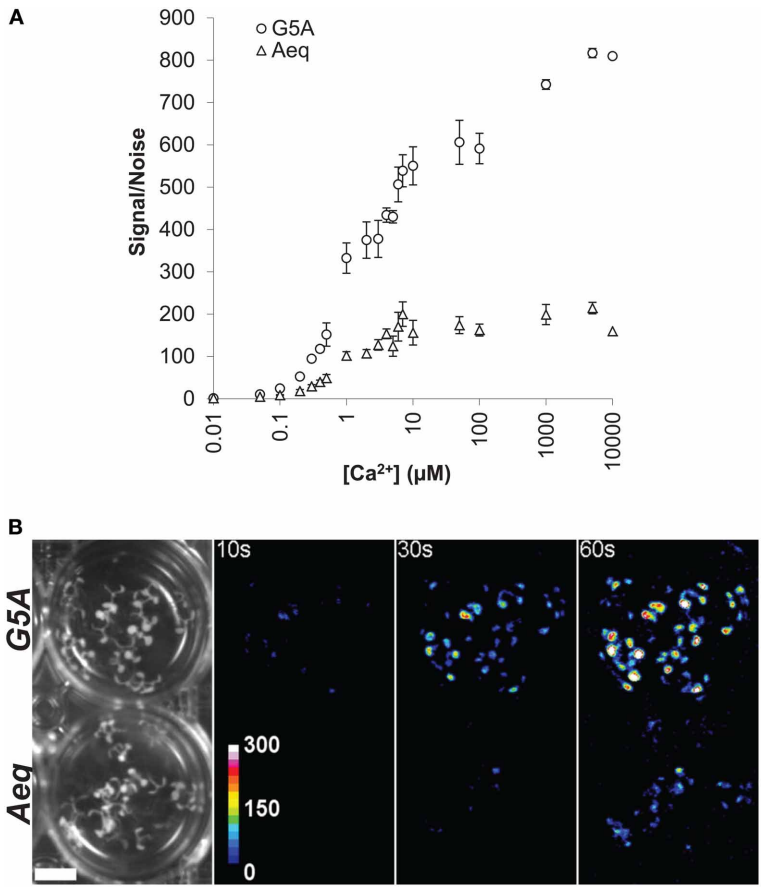

FIGURE 4 | *In vitro* and *in vivo* comparison of light emission by G5A and aequorin (A) *In vitro* assay of light emission from equal amounts of Ca^{2+} reporters G5A and aequorin is plotted against buffer free Ca^{2+} concentration. Results (mean ± SE, $n = 6$) are expressed as the ratio of signal (maximum emitted light) over noise. **(B)** Representative *in vivo* Ca^{2+} signals emitted from 7 day-old *G5A* (top) and *Aeq* (bottom) plants over different exposition time lapses (10, 30, and 60 s). Left panel shows bright field view (scale bar = 1 cm) of the imaged plants. The other panels display cumulative Ca^{2+} responses in false colors (color scale in the 10 s-labeled panel).

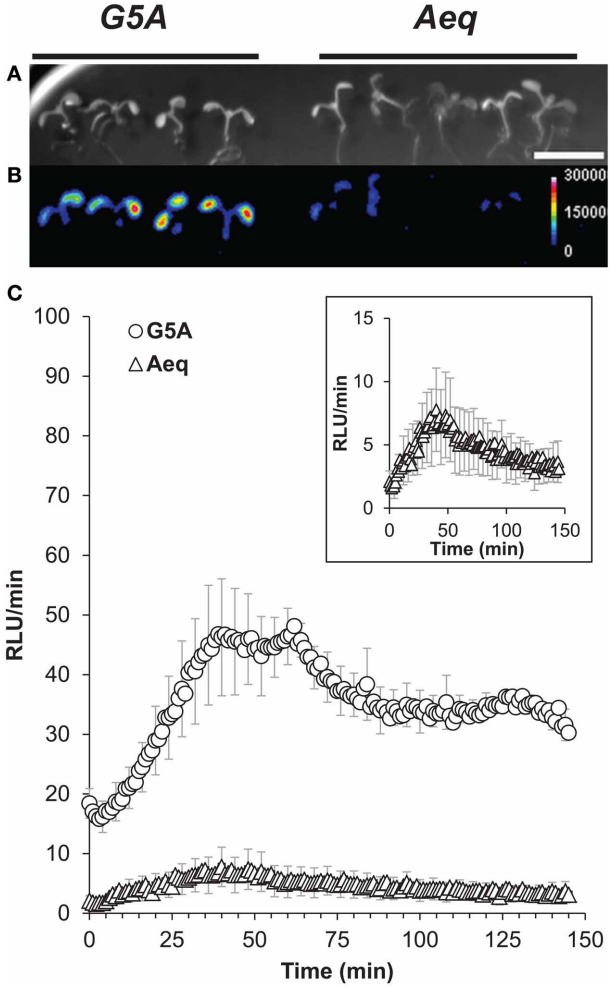

FIGURE 5 | Ca^{2+} dynamics detected in response to dark onset from plants expressing G5A or aequorin. (A) Bright field view of batches of 7 day-old *G5A* (left) and *Aeq* (right) Arabidopsis reporter lines. Scale bar = 1 cm. **(B)** Cumulative amount of light emitted from these plants after dark onset, over 150 min, expressed in false colors (scale shown at right, in device-dependent arbitrary unit or "RLU," standing for "relative light unit"). Representative results of 10 independent measurements of dark-induced Ca^{2+} released. **(C)** 150 min time course of the cumulative light emission over 60 s time lapses from plants in **(A,B)** (data are means ± SE of 10 independent experiments with four *G5A* and five *Aeq* plants). Ca^{2+} dynamics from the *Aeq* plants show kinetics (inset) similar to *G5A* plants but with approximately five times less light emission.

application of NaCl (at time = 0) was required before Ca^{2+} levels increased in the petioles. Elevated calcium levels then propagated to the rest of the leaves. It is interesting to note that the Ca^{2+} responses of mature and young leaves differed in terms of kinetics. Mature leaves responded by an initial rapid, transient, Ca^{2+} peak (**Figure 6A**, time = 1–2 min) followed by a second very slow, wave-like, increase and subsequent decrease of free Ca^{2+} level lasting more than 50 min (from 6 to 60 min) with a maximum at 12–13 min. The young leaves displayed a single rapid Ca^{2+} transient peak (**Figure 6A** red arrows), similar to that observed in mature leaves although slightly later (3.5–4.5 min after salt stress application). Defining the whole plant as an ROI and plotting the time course of the signal summed over each 30 s lapse (in RLU/30 s) for 60 min after salt stress application yielded a dynamic view of these Ca^{2+} events at leaf level (**Figure 6B**). It was found that both the Ca^{2+} peaks (observed for mature and young leaves) and the Ca^{2+} wave had a maximum at 19–20 RLU/30 s (**Figure 6B**). Despite inevitable variations from a plant to another one, an analogous pattern of distribution in space and time of Ca^{2+} events was observed when challenging a plant with a salt stress at the root level (**Supplementary video S2**).

Light emitted by G5A in intact plants facing a salt stress therefore appeared to be sufficiently intense to image the propagation of Ca^{2+} signals in leaves with good time resolution. We performed a simple analysis of Ca^{2+} waves on each leaf of plants subjected to a salt stress applied to roots. Ca^{2+} signal velocities were then calculated for each leaf of the plant shown in **Figure 6** (red dashed arrows, **Figure 7**). This shows that velocity was not constant within a given leaf (it decreased at leaf tip) and differed depending on the leaf. Detailed numerical values are given (**Table 1**): maximum and minimum of velocities were 0.52 and 0.03 mm/s respectively.

Further applications of G5A were investigated by imposing similar salt stress on mature leaves excised from 7–8 week-old plants (**Figure 8**). Application of 100 µL of 200 mM NaCl onto the petiole end of an excised leaf (**Figure 8A**, white arrow) was enough to generate detectable elevations in free calcium after 1 min. They started immediately after the exposure to the NaCl solution at the site of application before they spread throughout the rest of the leaf (**Figure 8A** and **Supplementary videos S3**, **S4**). The propagation of free calcium elevation seems to be different in the basal third part of the leaf (denoted by ∗ in **Figure 8C**) as compared to the rest of the leaf (denoted by ∗∗ in **Figure 8C**). In the early phase of response to the applied stress, increase in free Ca^{2+} were observed in the peripheral regions of the basal third part of the leaf and not in the middle vein. Subsequently, Ca^{2+} responses seem to propagate throughout the leaf, firstly, along the vascular tissues (primary and secondary veins) and later in the mesophyll tissue. Quantification of increase in free Ca^{2+} from the entire leaf shows that salt stress induced two different peaks of Ca^{2+}, which correspond to these two successive episodes of Ca^{2+} increase, firstly in the basal part of the leaf, subsequently in the rest of the leaf (as indicated by asterisks in **Figure 8B** as described for **Figure 8C**).

In this example (representative of five independent leaves), elevation of free Ca^{2+} induced by NaCl needed 315 s (image at 1:00 to 6:15) to travel through a 57 mm-long leaf. Thus, in this example the average velocity was 0.181 mm/s. A further analysis was performed on the primary vein of this leaf (**Figure 8C**, red dashed line X–Y), a kymographic representation of velocity value on the axis X–Y shows that there were three different Ca^{2+} response velocities (**Figure 8D**). Two of them (red dashed and orange dashed arrows) spread acropetally (from X to Y) whereas one propagated the opposite way (Y–X, cyan dashed arrow). Interestingly, between the first third and the second third of the leaf, was observed a region where no Ca^{2+} signals were detected with G5A. Despite this gap, Ca^{2+} signal propagation was observed all along the XY axis (**Figure 8C** and **Supplementary video S3**).

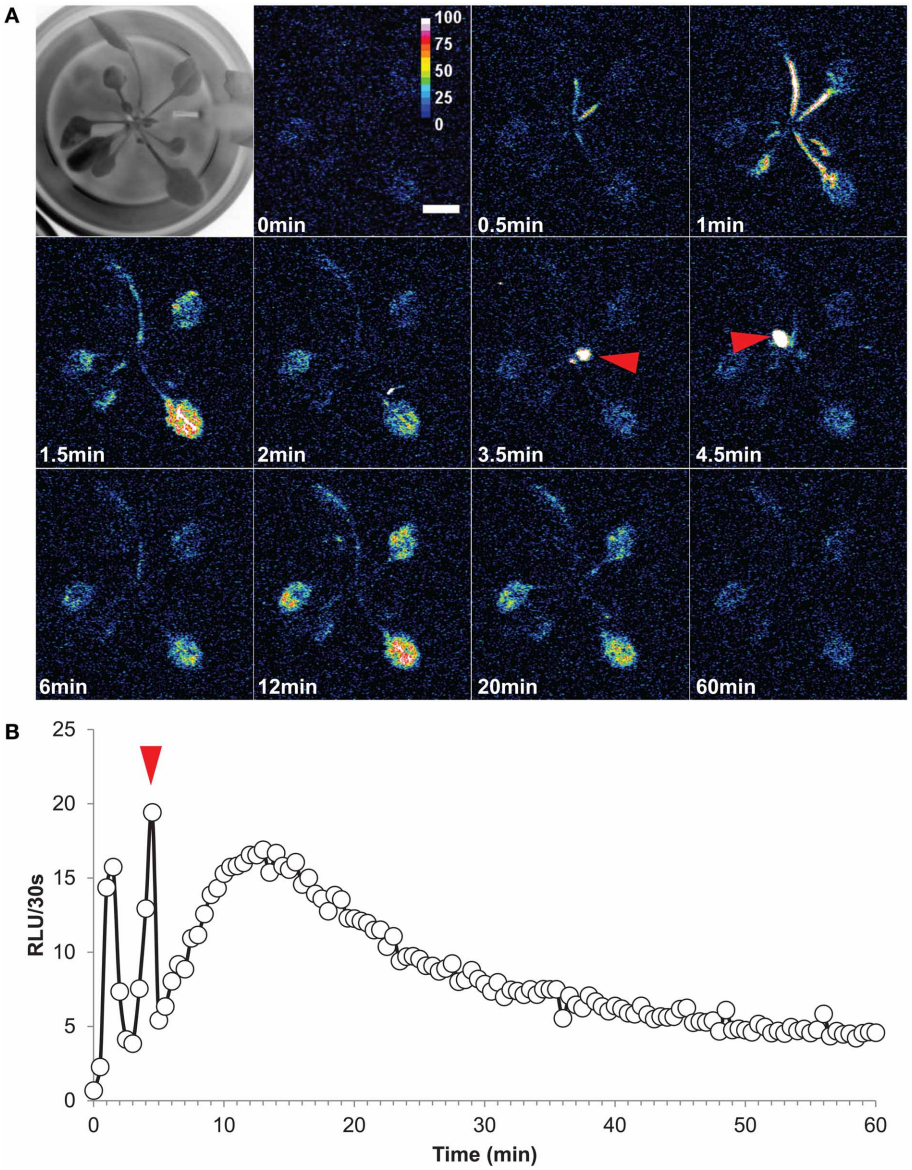

FIGURE 6 | High salt exposition of roots elicits long distance Ca^{2+} dynamics in leaves. (A) Time series of images (time of capture indicated in the left bottom corner of each image) showing propagation of Ca^{2+} elevation in aerial part of an intact plant (Representative result of five independent plants). First image of the series is a bright-field view of the plant. At time = 0, a solution of NaCl (200 mM final concentration) was applied to roots and light subsequently emitted from leaves was accumulated over 60 min (each image shows cumulative light intensity over a 30 s time lapse). After 0.5 min, Ca^{2+} elevations were detected on petioles and propagation of Ca^{2+} responses to the end of each mature leaf were observed. Young leaves responded only at 3.5–4.5 min after NaCl stress (red arrows) **(B)** Quantification of light signals from the whole plant over 60 min. As in **(A)** the red arrow indicates the short Ca^{2+} response in young leaves.

Analyses of Ca^{2+} waves on this excised leaf (representative of five leaves) show that Ca^{2+} signal velocities along different veins (**Figure 9A** dashed arrows) were different. Local velocity values were plotted on the image (as spots in false-color scale, **Figure 9B**). Higher velocities in the center of the leaf and slower velocities at leaf borders were found (**Figure 9B**). Details of velocities of Ca^{2+} signals in leaf veins, including on X–Y axis (#1, #8, and #16) are presented in **Table 2** below. Despite inevitable variation from a leaf excised from a plant to another leaf excised from another plant, the nature and pattern (both in space and time) was essentially reproducible (see **Supplemental video S4**).

DISCUSSION

Since the successful use of aequorin as a Ca^{2+}-signaling reporter in plant tissues (Knight et al., 1991), examples of aequorin imaging in plants have relied on the use of ultra-sensitive camera devices (intensified-CCD or electron-multiplying-CCD) to detect the few photons emitted by aequorin. They have revealed, for

example, that Ca^{2+} oscillations occur during diurnal rhythms in plant leaves (Johnson et al., 1995; Sai and Johnson, 2002; Dodd et al., 2006). Optimized imaging of aequorin signals in plants has been reported recently that, with integration time down to 40 s, showed stimulus- and tissue-specific Ca^{2+} signatures in seedlings (Zhu et al., 2013). In these examples of aequorin imaging in plants, however, low light detection relied upon sophisticated and costly equipment. Another interesting development of aequorin-based approach to *in planta* Ca^{2+} signaling has recently been reported: expression of aequorin in specific cell types of Arabidopsis was used to determine which cell types release calcium into the cytosol in response to a given stimulus (Marti et al., 2013). Photometry (with high time resolution) of aequorin emission from plants expressing the Ca^{2+}-sensor in specific leaf cell–types (mesophyll cells, guard cells, [peri-]vascular cells, epidermal cells, and trichomes) may be used to follow various stresses. These experimental conditions allowed the collected information to be ascribed to a given cell-type, without spatial localization of the measured signals.

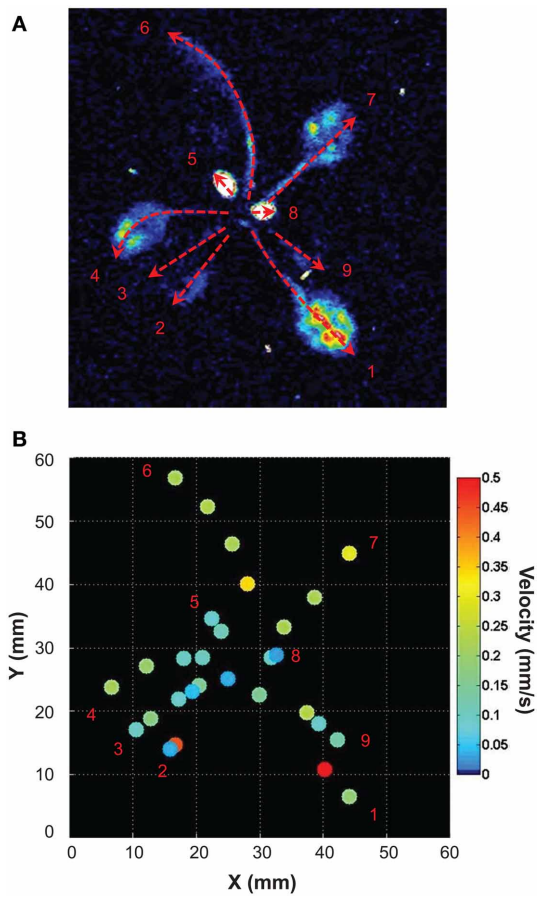

FIGURE 7 | Analysis of the propagation of Ca^{2+} elevations induced by high salt stimulus applied to roots. (A) Free Ca^{2+} elevations on each leaf were analyzed with ImageJ. Velocities (mm/s) of Ca^{2+} responses were determined for each leaf along paths figured by red dashed arrows (values of Ca^{2+} response velocity are presented on **Table 1**). **(B)** Propagation speeds along the main leaf vain are indicated for selected points (same space scale as in **A**). False color scale is in mm/s.

The G5A-based method we report here provides an interesting complement to these recent improvements of aequorin-based methods. In the *Aequoria victoria* jellyfish, a naturally evolved BRET phenomenon between aequorin and GFP occurs. Several artificial proteins assembling aequorin with GFP-derived proteins have been engineered to mimic the natural BRET observed in *Aequoria victoria*. Performance of these artificial Ca^{2+} reporters depends on the linker motif placed in between the BRET partner proteins (Baubet et al., 2000; Gorokhovatsky et al., 2004). Comparison of different linkers in GFP-aequorin protein fusions has demonstrated that the five repeat motifs used here in the so-called G5A artificial reporter (see **Figure 1**) allows a high BRET efficiency (Baubet et al., 2000). Subsequently, the G5A reporter has been successfully used to monitor Ca^{2+} elevation at cellular and organ levels in animals (Baubet et al., 2000; Chiesa et al., 2001; Cassidy and Radda, 2005; Rogers et al., 2005, 2008; Martin et al., 2007; Naumann et al., 2010). To date, however, no G5A application in plants has been reported.

Although our *in vitro* assays show similar calibration curves for both reporters (**Figure 3B**), there was a significantly better signal/noise ratio for G5A than for aequorin (**Figure 4A**) corresponding to a 3–5 fold increase in light collected from the former compared to the latter. Such an amplification is consistent with the data obtained *in planta* (**Figures 4B**, **5**) where small changes of free Ca^{2+} concentration were more easily detected with G5A than with aequorin. The (up to) 5-fold amplification of light in plants expressing G5A is similar to the 5.7-fold increase

Table 1 | Ca^{2+} wave properties in different leaves of an intact plant.

Leaf number	Total length (mm)	Velocity mean (mm/s)	Velocity minimum (mm/s)	Velocity maximum (mm/s)	Duration* (s)	Latency* (s)
1	25.96	0.29 ± 0.10	0.15	0.52	90	30
2	15.55	0.17 ± 0.12	0.03	0.45	90	30
3	16.87	0.11 ± 0.02	0.05	0.18	150	60
4	18.50	0.15 ± 0.03	0.10	0.23	120	30
5	5.84	0.10 ± 0.01	0.08	0.11	60	240
6	30.81	0.26 ± 0.03	0.23	0.34	120	30
7	22.19	0.25 ± 0.02	0.22	0.30	90	30
8	3.68	0.06 ± 0.03	0.03	0.09	60	210
9	13.67	0.15 ± 0.04	0.09	0.24	90	90

**Time resolution is limited by the time acquisition (30 s).*

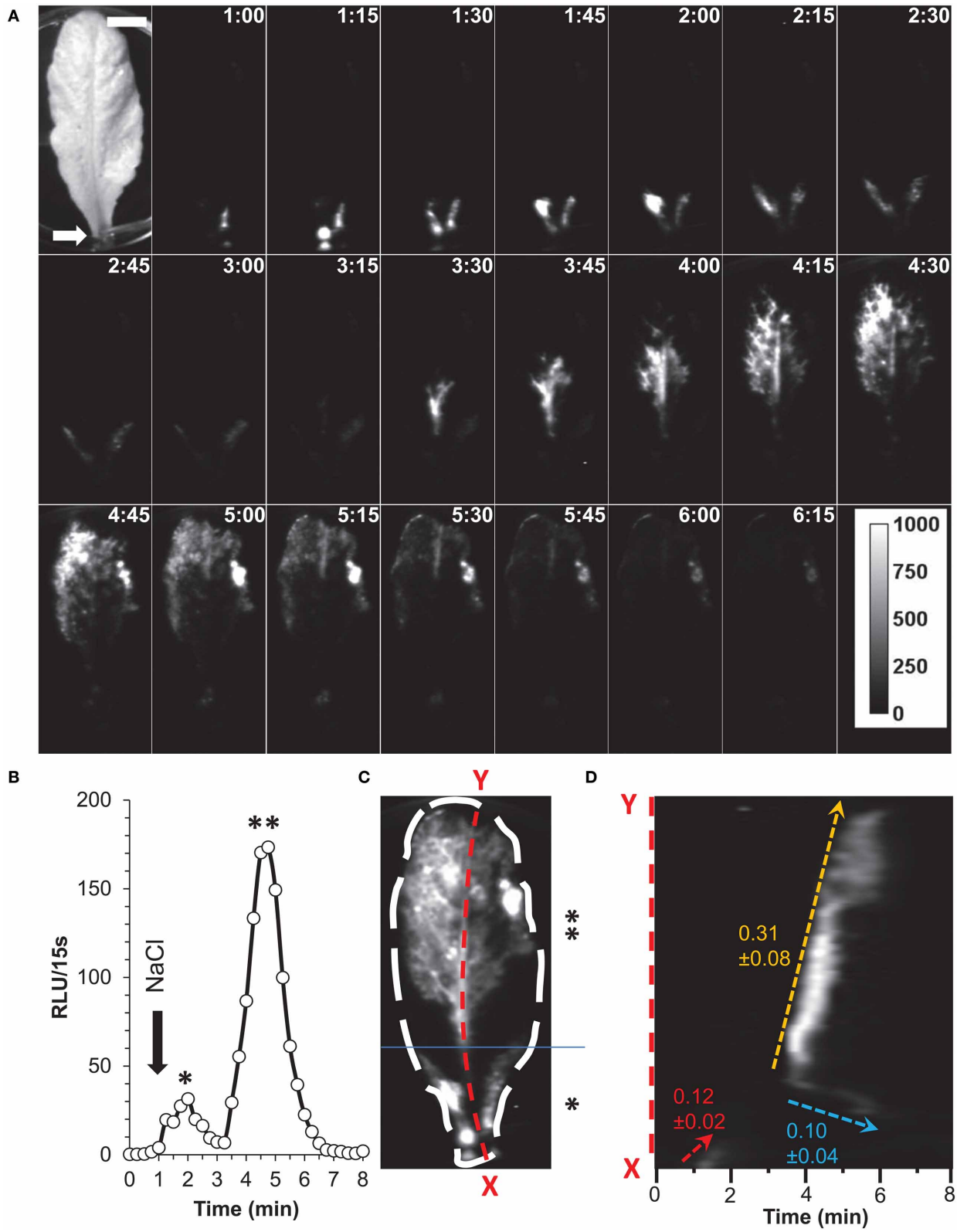

FIGURE 8 | Salt application on detached leaf elicits Ca^{2+} waves along the vascular tissue. (A) Time series of images (time of capture indicated in the right top corner of each image in min:s) showing propagation of Ca^{2+} responses in a detached leaf. First image of the series is a bright-field view of the plant. At time = 1 min, 100 μL of a solution of NaCl (200 mM) was dispensed onto the petiole (white arrow) and light subsequently emitted from leaves was integrated over 7 min (each image shows cumulative light over

(Continued)

FIGURE 8 | Continued
a 15 s time lapse). Ca^{2+} responses were immediately detected on petioles and propagation of Ca^{2+} responses to the end of leaf was observed. Scale bar = 1 cm. Calibration bar in gray scale is shown in the last image (RLU). Representative result of five independent experiments. **(B)** Quantification of light signals from ROI for the whole leaf (see **C**) over 8 min (in RLU per 15 s). At time = 1 min, NaCl was applied onto the petiole (black arrow). The two peaks denoted by ∗ and ∗∗ correspond to a Ca^{2+} increase in the basal third and the rest of the leaf respectively. **(C)** Localization of Ca^{2+} responses is represented by a z-stack of standard deviation of Ca^{2+} signals over the 8 min of measurement. Ca^{2+} signals seem to take place in leaf veins. The basal third of the leaf is indicated by ∗ and the rest of the leaf by ∗∗. Line scan of primary vein (red dashed line X–Y) is analyzed in **(D)**. **(D)** Kymographic representation of Ca^{2+} signals in the primary vein (X–Y from **C**). Three different velocities of Ca^{2+} signals could be measured and are indicated.

in the light signal resulting from BRET between luciferin and GFP in *Renilla reniformis* (Ward and Cormier, 1976). It is interesting to note however that the improved detection of light emission from aequorin through BRET is still not completely understood (Webb et al., 2010). In the jellyfish *Aequorea victoria*, aequorin is associated with the GFP that allows the amplification of light by BRET phenomena. *In vitro*, the binding between aequorin and GFP does not occur, even at high concentration and no BRET events was observed (Baubet et al., 2000). Fusion of aequorin and GFP is a prerequisite to observe such natural light amplification seen in jellyfish. Baubet et al. have designed an optimized linker that results in sufficient high quantum yield to visualize Ca^{2+} induced light emission from G5A (Baubet et al., 2000).

An issue for plant cell physiologists is the autofluorescence of chlorophyll and other organic pigments which hinders the use of fluorescent probes with overlapping spectroscopic properties. For instance chlorophyll *b* and carotenoids (lutein, neoxanthin, and violaxanthin) have major absorption peaks between 469 and 490 nm (Rivadossi et al., 2004; Taylor et al., 2006) and may absorb photons emitted at ∼470 nm by aequorin in leaf cells. As a consequence of the efficient BRET between its aequorin and GFP moieties, G5A emits photons at∼510 nm (Baubet et al., 2000; Rogers et al., 2005, 2008), thus reducing absorbance by plant tissues and resulting in better detection by cameras or luminometers. This also could contribute to the better performance of G5A compared to aequorin in the present *in planta* experiments (**Figure 5C**).

In addition to these considerations, the G5A-based results that we report here exemplify the possibilities that this Ca^{2+} reporter holds for plant biologists. Comparison of *Aeq* and *G5A* plants subjected to darkness shows that similar responses could be visualized with both Ca^{2+} reporters, but five times more light was emitted from *G5A* plants (**Figure 5**). This suggests that G5A is an alternative tool to aequorin for Ca^{2+} imaging when signals are either too low or if ultra-sensitive camera is not available. Moreover, further examples of potential application of G5A are introduced here, showing the analysis of long-distance Ca^{2+} signaling (potentially involved in the coordination of the integrative responses of plant to stresses, here salt stress, **Figures 6–9**).

Long distance propagation of Ca^{2+} signals ("Ca^{2+} waves") is attracting increasing interest in the plant biology community (Steinhorst and Kudla, 2013) and in this context, G5A seems to be a complementary tool, along with fluorescent Ca^{2+} reporters, to investigate complex cell to cell communication within plants. Most of Ca^{2+} imaging experiments in intact tissue with a fluorescent reporter have been carried out in roots (Fasano et al., 2001; Monshausen et al., 2011; Gjetting et al., 2012), where auto-fluorescence is much less of an obstacle than in leaves. It is by using FRET-confocal laser scanning microscopy that Ca^{2+} imaging on leaves with YC has recently been reported (Benikhlef et al., 2013; Verrillo et al., 2014). Aequorin imaging requires ultra-sensitive cameras (intensified-CCD or electron-multiplied-CCD) while G5A imaging does not. The high dynamics and intensity of G5A light emission upon Ca^{2+} events open opportunities to detect low Ca^{2+} signals and to analyse their propagation with good time resolution, using a "regular" cooled CCD camera. In practical terms, time resolution is the time required to make an image (a frame) with an acceptably high signal/noise ratio. Under the present experimental conditions, integration time for a frame was well under 1 min: depending on amplitude of the Ca^{2+} signal this integration time ranged from 30 s (**Figure 6**) down to 15 s (**Figure 8**) for whole seedlings or mature leaves and even down to 5 s in the most favorable case (wounding stress, data not shown). Thus, values of Ca^{2+} wave propagation speed as fast as 0.5–0.6 mm/s can be resolved (**Figure 9**, **Tables 1**, **2**).

We consider that G5A reporter opens exciting perspectives for the study of cell-to-cell communication in plants. The physiological meaning of Ca^{2+} waves observed within vascular tissues (but not solely there) is one of the interesting aspects which could be investigated. Velocity values observed for these Ca^{2+} signals are of the same order of magnitude than those of "fast" electrical signals (i.e., "action potentials") reported to travel leaf tissues in Arabidopsis (Favre et al., 2011). This substantiates the hypothesis of an interplay between Ca^{2+} and electrical signaling (Król et al., 2011). Recently, glutamate receptor-like putative Ca^{2+} channels were reported to play a role in leaf to leaf signaling after wounding (Mousavi et al., 2013), together with electrical signals. In this context, combining G5A-based imaging of Ca^{2+} with electrophysiological recording of electrical signals might be a powerful method to decipher the molecular basis of electrical signaling in plants upon different types of stress, including wounding.

In conclusion, G5A allows to image free Ca^{2+} elevation in intact plant leaves, making this probe a promising addition in the toolbox of plant cell physiology. Ca^{2+} imaging in intact plant leaves with widely affordable imaging equipment has the potential to boost the investigation of Ca^{2+} signaling in plants.

ACKNOWLEDGMENTS

We thank Dr. T. Nakagawa (Nagoya, Shimane University, Japan) for the pGWB502Ω plasmid, Prof. M. Knight (Durham University, UK) for the *Aeq* line (pMAQ2, Col-0 ecotype), the

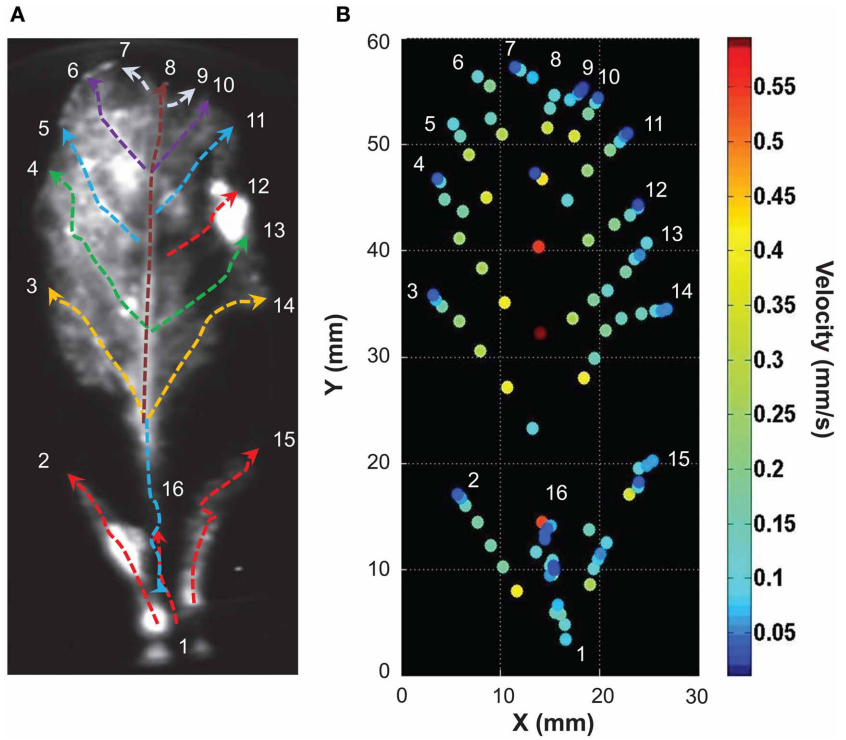

FIGURE 9 | Analysis of the propagation of calcium elevation in detached leaves induced by high salt exposure. (A) Ca^{2+} responses on each vein were analyzed in ImageJ. Velocities (mm/s) of Ca^{2+} signals were determined along paths represented by dashed arrows (details of Ca^{2+} signal velocity, duration and latency are presented on **Table 2**; colors of dashed arrows refer to the latency values so that Ca^{2+} waves that started at similar times are in the same color). **(B)** Propagation speeds along the main leaf vein are indicated for selected points (same space scale as in **A**). False color scale is in mm/s.

Table 2 | Ca^{2+} wave properties in detached leaves upon high salt exposure.

Number of Ca^{2+} responses	Total length (mm)	Velocity mean (mm/s)	Velocity minimum (mm/s)	Velocity maximum (mm/s)	Duration* (s)	Latency* (s)
1	8.62	0.12 ± 0.02	0.06	0.20	75	0
2	17.01	0.16 ± 0.04	0.03	0.41	105	30
3	17.34	0.19 ± 0.05	0.04	0.39	90	150
4	20.33	0.19 ± 0.04	0.03	0.40	105	165
5	13.18	0.22 ± 0.06	0.09	0.36	60	195
6	10.63	0.18 ± 0.04	0.10	0.28	60	195
7	2.88	0.06 ± 0.02	0.04	0.10	45	255
8	32.90	0.31 ± 0.08	0.09	0.60	105	150
9	2.78	0.04 ± 0.01	0.01	0.07	75	240
10	9.94	0.13 ± 0.06	0.02	0.35	75	195
11	10.21	0.11 ± 0.03	0.03	0.23	90	195
12	9.77	0.13 ± 0.04	0.02	0.24	75	195
13	14.41	0.14 ± 0.03	0.04	0.27	105	165
14	17.59	0.15 ± 0.04	0.04	0.40	120	150
15	20.04	0.11 ± 0.03	0.03	0.35	180	0
16	20.25	0.10 ± 0.04	0.02	0.54	195	150

**Time resolution is limited by the time acquisition (15 s).*

late Prof. Philippe Brûlet (CNRS, Gif-sur-Yvette, France) who kindly provided us with the *G5A* construct that we used to build the *G5A* line. This work was supported by a joint CNRS-INRA fellowship to Elsa Ronzier, by the Agropolis Fondation (Grant 0803-022), and by the European Commission's FP7 (Grant IRG 268393). We are grateful to Drs. Cliona Hann and Siobhán Staunton for their helpful comments on the manuscript.

SUPPLEMENTARY MATERIAL

The Supplementary Material for this article can be found online at: http://www.frontiersin.org/journal/10.3389/fpls.2014.00043/abstract

Supplementary video S1 | Light emission from 4 week-old G5A-expressing leaves upon a high salt stimulus applied to roots of the plant presented in Figures 5, 6. The left part **(A)** shows the bright field view of the plant (scale bar is 2 cm). Video in the right part **(B)** is made of frames, each corresponding to photons collected over a 30 s time lapse, displayed at a rate of three frames per second (video rate is ×90). At time zero of the video, the plant has been adapted to dark for 20 min and no Ca^{2+} signals were detected (data not shown). Application of 200 mM NaCl to roots at $t = 5$ min (3.33 s, video time) induced propagation of Ca^{2+} elevation over long distances from roots to leaves over 77 min. NaCl-induced Ca^{2+} waves were different in expanded leaves and in young ones. Propagation of strong Ca^{2+} elevations to fully expanded leaves can be visualized just after the NaCl stress and is followed by slow Ca^{2+} variations in leaves over 77 min. Small young leaves emit strong and transient Ca^{2+} elevation only 3.5–4.5 min after the NaCl stress (5.66–6.66 s, video time).

Supplementary video S2 | Second example of light emission from 4 week-old G5A-expressing leaves upon a high salt stimulus applied to roots of the same plant. The left part **(A)** shows the bright field view of this plant (scale bar is 2 cm). Video in the right part **(B)** is made of frames, each corresponding to photons collected over a 30 s time lapse, displayed at a rate of three frames per second (video rate is ×90). At time zero of the video, the plant has been adapted to dark for 20 min and no Ca^{2+} signals were detected (data not shown). Application of 200 mM NaCl to roots at $t = 5$ min (3.33 s, video time) induced propagation of a Ca^{2+} elevation over long distances from roots to leaves over 150 min. As in video S1, NaCl-induced Ca^{2+} waves were different in expanded leaves and in young ones. In this other plant, however, propagation rates and kinetics of Ca^{2+} changes were different from those in the plant featured in video S1, exemplifying the complex nature of Ca^{2+} responses in intact plants.

Supplementary video S3 | Light emission by a leaf detached from a *G5A* plant upon a high-salt stimulus applied to the petiole. The left part **(A)** shows the bright field view of the leaf (scale bar is 1 cm). Video in the right part **(B)** is made of frames, each corresponding to photons collected over a 15 s time lapse, displayed at a rate of six frames per second (video rate is ×90). At time zero no light is detected. Application of 200 mM NaCl to petiole at $t = 1$ min (0.66 s, video time) induced Ca^{2+} waves from petiole to leaf tips over 7 min.

Supplementary video S4 | Second example of light emission from a detached G5A-expressing leaf upon a high salt stimulus applied to the petiole. The left part **(A)** shows the bright field view of the leaf (scale bar is 1 cm). Video in the right part **(B)** is made of frames, each corresponding to photons collected over a 15 s time lapse, displayed at a rate of six frames per second (video rate is ×90). At time zero no light is detected. Application of 200 mM NaCl to petiole at $t = 1$ min (0.66 s, video time) induced Ca^{2+} waves from the petiole to leaf tips over 17 min. In this leaf from another plant, however, propagation rates and kinetics of Ca^{2+} changes were different from those in the leaf featured in video S3, exemplifying the complex nature of Ca^{2+} responses in excised leaves.

REFERENCES

Allen, G. J., Kwak, J. M., Chu, S. P., Llopis, J., Tsien, R. Y., Harper, J. F., et al. (1999). Cameleon calcium indicator reports cytoplasmic calcium dynamics in Arabidopsis guard cells. *Plant J.* 19, 735–747. doi: 10.1046/j.1365-313x.1999.00574.x

Alonso, M. T., and Garcia-Sancho, J. (2011). Nuclear Ca^{2+} signalling. *Cell Calcium* 49, 280–289. doi: 10.1016/j.ceca.2010.11.004

Baubet, V., Le Mouellic, H., Campbell, A. K., Lucas-Meunier, E., Fossier, P., and Brulet, P. (2000). Chimeric green fluorescent protein-aequorin as bioluminescent Ca^{2+} reporters at the single-cell level. *Proc. Natl. Acad. Sci. U.S.A.* 97, 7260–7265. doi: 10.1073/pnas.97.13.7260

Benikhlef, L., L'Haridon, F., Abou-Mansour, E., Serrano, M., Binda, M., Costa, A., et al. (2013). Perception of soft mechanical stress in Arabidopsis leaves activates disease resistance. *BMC Plant Biol.* 13:133. doi: 10.1186/1471-2229-13-133

Bonza, M. C., Loro, G., Behera, S., Wong, A., Kudla, J., and Costa, A. (2013). Analyses of Ca^{2+} accumulation and dynamics in the endoplasmic reticulum of Arabidopsis root cells using a genetically encoded Cameleon sensor. *Plant Physiol.* 163, 1230–1241. doi: 10.1104/pp.113.226050

Brini, M. (2008). Calcium-sensitive photoproteins. *Methods* 46, 160–166. doi: 10.1016/j.ymeth.2008.09.011

Cassidy, P. J., and Radda, G. K. (2005). Molecular imaging perspectives. *J. R. Soc. Interface* 2, 133–144. doi: 10.1098/rsif.2005.0040

Chiesa, A., Rapizzi, E., Tosello, V., Pinton, P., De Virgilio, M., Fogarty, K. E., et al. (2001). Recombinant aequorin and green fluorescent protein as valuable tools in the study of cell signalling. *Biochem. J.* 355, 1–12. doi: 10.1042/0264-6021:3550001

Clough, S. J., and Bent, A. F. (1998). Floral dip: a simplified method for Agrobacterium-mediated transformation of *Arabidopsis thaliana*. *Plant J.* 16, 735–743. doi: 10.1046/j.1365-313x.1998.00343.x

Dodd, A. N., Jakobsen, M. K., Baker, A. J., Telzerow, A., Hou, S. W., Laplaze, L., et al. (2006). Time of day modulates low-temperature Ca^{2+} signals in Arabidopsis. *Plant J.* 48, 962–973. doi: 10.1111/j.1365-313X.2006.02933.x

Fasano, J. M., Swanson, S. J., Blancaflor, E. B., Dowd, P. E., Kao, T. H., and Gilroy, S. (2001). Changes in root cap pH are required for the gravity response of the Arabidopsis root. *Plant Cell* 13, 907–921. doi: 10.2307/3871348

Favre, P., Greppin, H., and Degli Agosti, R. (2011). Accession-dependent action potentials in Arabidopsis. *J. Plant Physiol.* 168, 653–660. doi: 10.1016/j.jplph.2010.09.014

Fricker, M. D., Plieth, C., Knight, H., Blancaflor, E., Knight, M. R., White, N. S., et al. (1999). "Chapter forty-two - fluorescence and luminescence techniques to probe ion activities in living plant cells," in *Fluorescent and Luminescent Probes for Biological Activity, 2nd Edn,* ed W. T. Mason (London: Academic Press), 569–596.

Gjetting, K. S., Ytting, C. K., Schulz, A., and Fuglsang, A. T. (2012). Live imaging of intra- and extracellular pH in plants using pHusion, a novel genetically encoded biosensor. *J. Exp. Bot.* 63, 3207–3218. doi: 10.1093/jxb/ers040

Gorokhovatsky, A. Y., Marchenkov, V. V., Rudenko, N. V., Ivashina, T. V., Ksenzenko, V. N., Burkhardt, N., et al. (2004). Fusion of Aequorea victoria GFP and aequorin provides their Ca^{2+}-induced interaction that results in red shift of GFP absorption and efficient bioluminescence energy transfer. *Biochem. Biophys. Res. Commun.* 320, 703–711. doi: 10.1016/j.bbrc.2004.06.014

Iwano, M., Ngo, Q. A., Entani, T., Shiba, H., Nagai, T., Miyawaki, A., et al. (2012). Cytoplasmic Ca^{2+} changes dynamically during the interaction of the pollen tube with synergid cells. *Development* 139, 4202–4209. doi: 10.1242/dev.081208

Johnson, C. H., Knight, M. R., Kondo, T., Masson, P., Sedbrook, J., Haley, A., et al. (1995). Circadian oscillations of cytosolic and chloroplastic free calcium in plants. *Science* 269, 1863–1865. doi: 10.1126/science.7569925

Knight, M. R., Campbell, A. K., Smith, S. M., and Trewavas, A. J. (1991). Transgenic plant aequorin reports the effects of touch and cold-shock and elicitors on cytoplasmic calcium. *Nature* 352, 524–526. doi: 10.1038/352524a0

Krebs, M., Held, K., Binder, A., Hashimoto, K., Den Herder, G., Parniske, M., et al. (2012). FRET-based genetically encoded sensors allow high-resolution live cell imaging of Ca^{2+} dynamics. *Plant J.* 69, 181–192. doi: 10.1111/j.1365-313X.2011.04780.x

Król, E., Płachno, B. J., Adamec, L., Stolarz, M., Dziubińska, H., and Trębacz, K. (2011). Quite a few reasons for calling carnivores 'the most wonderful plants in the world'. *Ann. Bot.* 109, 47–64. doi: 10.1093/aob/mcr249

Marti, M. C., Stancombe, M. A., and Webb, A. A. (2013). Cell- and stimulus type-specific intracellular free Ca^{2+} signals in Arabidopsis. *Plant Physiol.* 163, 625–634. doi: 10.1104/pp.113.222901

Martin, J. R., Rogers, K. L., Chagneau, C., and Brulet, P. (2007). *In vivo* bioluminescence imaging of Ca^{2+} signalling in the brain of Drosophila. *PLoS ONE* 2:e275. doi: 10.1371/journal.pone.0000275

Mithofer, A., and Mazars, C. (2002). Aequorin-based measurements of intracellular Ca^{2+}-signatures in plant cells. *Biol. Proced. Online* 4, 105–118. doi: 10.1251/bpo40

Miwa, H., Sun, J., Oldroyd, G. E., and Downie, J. A. (2006). Analysis of calcium spiking using a cameleon calcium sensor reveals that nodulation gene expression is regulated by calcium spike number and the developmental status of the cell. *Plant J.* 48, 883–894. doi: 10.1111/j.1365-313X.2006.02926.x

Monshausen, G. B., Messerli, M. A., and Gilroy, S. (2008). Imaging of the Yellow Cameleon 3.6 indicator reveals that elevations in cytosolic Ca^{2+} follow oscillating increases in growth in root hairs of Arabidopsis. *Plant Physiol.* 147, 1690–1698. doi: 10.1104/pp.108.123638

Monshausen, G. B., Miller, N. D., Murphy, A. S., and Gilroy, S. (2011). Dynamics of auxin-dependent Ca^{2+} and pH signaling in root growth revealed by integrating high-resolution imaging with automated computer vision-based analysis. *Plant J.* 65, 309–318. doi: 10.1111/j.1365-313X.2010.04423.x

Mousavi, S. A., Chauvin, A., Pascaud, F., Kellenberger, S., and Farmer, E. E. (2013). GLUTAMATE RECEPTOR-LIKE genes mediate leaf-to-leaf wound signalling. *Nature* 500, 422–426. doi: 10.1038/nature12478

Nakagawa, T., Suzuki, T., Murata, S., Nakamura, S., Hino, T., Maeo, K., et al. (2007). Improved Gateway binary vectors: high-performance vectors for creation of fusion constructs in transgenic analysis of plants. *Biosci. Biotechnol. Biochem.* 71, 2095–2100. doi: 10.1271/bbb.70216

Naumann, E. A., Kampff, A. R., Prober, D. A., Schier, A. F., and Engert, F. (2010). Monitoring neural activity with bioluminescence during natural behavior. *Nat. Neurosci.* 13, 513–520. doi: 10.1038/nn.2518

Perez Koldenkova, V., and Nagai, T. (2013). Genetically encoded Ca^{2+} indicators: Properties and evaluation. *Biochim. Biophys. Acta.* 1833, 1787–1797. doi: 10.1016/j.bbamcr.2013.01.011

Rivadossi, A., Zucchelli, G., Garlaschi, F. M., and Jennings, R. C. (2004). Light absorption by the chlorophyll a-b complexes of photosystem II in a leaf with special reference to LHCII. *Photochem. Photobiol.* 80, 492–498. doi: 10.1562/0031-8655(2004)080<0492:LABTCA>2.0.CO;2

Rogers, K. L., Martin, J. R., Renaud, O., Karplus, E., Nicola, M. A., Nguyen, M., et al. (2008). Electron-multiplying charge-coupled detector-based bioluminescence recording of single-cell Ca^{2+}. *J. Biomed. Opt.* 13, 031211. doi: 10.1117/1.2937236

Rogers, K. L., Stinnakre, J., Agulhon, C., Jublot, D., Shorte, S. L., Kremer, E. J., et al. (2005). Visualization of local Ca^{2+} dynamics with genetically encoded bioluminescent reporters. *Eur. J. Neurosci.* 21, 597–610. doi: 10.1111/j.1460-9568.2005.03871.x

Sai, J., and Johnson, C. H. (2002). Dark-stimulated calcium ion fluxes in the chloroplast stroma and cytosol. *Plant Cell* 14, 1279–1291. doi: 10.1105/tpc.000653

Schneider, C. A., Rasband, W. S., and Eliceiri, K. W. (2012). NIH Image to ImageJ: 25 years of image analysis. *Nat. Methods* 9, 671–675. doi: 10.1038/nmeth.2089

Steinhorst, L., and Kudla, J. (2013). Calcium and reactive oxygen species rule the waves of signaling. *Plant Physiol.* 163, 471–485. doi: 10.1104/pp.113.222950

Taylor, K. L., Brackenridge, A. E., Vivier, M. A., and Oberholster, A. (2006). High-performance liquid chromatography profiling of the major carotenoids in *Arabidopsis thaliana* leaf tissue. *J. Chromatogr. A* 1121, 83–91. doi: 10.1016/j.chroma.2006.04.033

Verrillo, F., Occhipinti, A., Kanchiswamy, C. N., and Maffei, M. E. (2014). Quantitative analysis of herbivore-induced cytosolic calcium by using a Cameleon (YC 3.6) calcium sensor in *Arabidopsis thaliana*. *J. Plant Physiol.* 171, 136–139. doi: 10.1016/j.jplph.2013.09.020

Ward, W. W., and Cormier, M. J. (1976). *In vitro* energy transfer in *Renilla* bioluminescence. *J. Phys. Chem.* 80, 2289–2291. doi: 10.1021/j100561a030

Webb, S. E., Rogers, K. L., Karplus, E., and Miller, A. L. (2010). The use of aequorins to record and visualize Ca^{2+} dynamics: from subcellular microdomains to whole organisms. *Methods Cell Biol.* 99, 263–300. doi: 10.1016/B978-0-12-374841-6.00010-4

Zhu, X., Feng, Y., Liang, G., Liu, N., and Zhu, J. K. (2013). Aequorin-based luminescence imaging reveals stimulus- and tissue-specific Ca2+ dynamics in Arabidopsis plants. *Mol. Plant.* 6, 444–455. doi: 10.1093/mp/sst013

Conflict of Interest Statement: The authors declare that the research was conducted in the absence of any commercial or financial relationships that could be construed as a potential conflict of interest.

Received: 12 December 2013; accepted: 29 January 2014; published online: 18 February 2014.

Citation: Xiong TC, Ronzier E, Sanchez F, Corratgé-Faillie C, Mazars C and Thibaud J-B (2014) Imaging long distance propagating calcium signals in intact plant leaves with the BRET-based GFP-aequorin reporter. Front. Plant Sci. ***5****:43. doi: 10.3389/fpls.2014.00043*

This article was submitted to Plant Cell Biology, a section of the journal Frontiers in Plant Science.

Copyright © 2014 Xiong, Ronzier, Sanchez, Corratgé-Faillie, Mazars and Thibaud. This is an open-access article distributed under the terms of the Creative Commons Attribution License (CC BY). The use, distribution or reproduction in other forums is permitted, provided the original author(s) or licensor are credited and that the original publication in this journal is cited, in accordance with accepted academic practice. No use, distribution or reproduction is permitted which does not comply with these terms.

frontiers in
PLANT SCIENCE

ORIGINAL RESEARCH ARTICLE
published: 30 June 2014
doi: 10.3389/fpls.2014.00292

Photosynthesis in a different light: spectro-microscopy for *in vivo* characterization of chloroplasts

Sébastien Peter[1], Martina B. Zell[2], Christian Blum[3], Alexander Stuhl[4], Kirstin Elgass[1], Marcus Sackrow[4†], Vinod Subramaniam[3,5], Alfred J. Meixner[4], Klaus Harter[1], Veronica G. Maurino[2,6] and Frank E. Schleifenbaum[1,4]*

[1] Department of Plant Physiology, Center for Plant Molecular Biology (ZMBP), University of Tübingen, Tübingen, Germany
[2] Biocenter Cologne, Botanical Institute, University of Cologne, Cologne, Germany
[3] Nanobiophysics Group and MESA+ Institute for Nanotechnology, University of Twente, Enschede, Netherlands
[4] Department of Nano Optics, Insitute of Physical and Theoretical Chemistry, University of Tübingen, Tübingen, Germany
[5] Department of Nanoscale Biophysics, FOM Institute AMOLF, Amsterdam, Netherlands
[6] Plant Molecular Physiology and Biotechnology Group, Institut of Developmental and Molecular Biology of Plants, Cluster of Excellence on Plant Sciences, Heinrich-Heine-Universität, Düsseldorf, Germany

Edited by:
George R. Littlejohn, University of Exeter, UK

Reviewed by:
Suleyman I. Allakhverdiev, Russian Academy of Sciences, Russia
Tomas Morosinotto, Università di Padova, Italy
Thomas Paul Howard, University of Exeter, UK
Cornelia Spetea, University of Gothenburg, Sweden

***Correspondence:**
Frank E. Schleifenbaum, University of Tübingen, Auf der Morgenstelle 18,72076 Tübingen, Germany
e-mail: frank.schleifenbaum@uni-tuebingen.de

†Present address:
Marcus Sackrow, Picoquant GmbH, Rudower Chaussee 29, 12489 Berlin, Germany

During photosynthesis, energy conversion at the two photosystems is controlled by highly complex and dynamic adaptation processes triggered by external factors such as light quality, intensity, and duration, or internal cues such as carbon availability. These dynamics have remained largely concealed so far, because current analytical techniques are based on the investigation of isolated chloroplasts lacking full adaptation ability and are performed at non-physiologically low temperatures. Here, we use non-invasive *in planta* spectro-microscopic approaches to investigate living chloroplasts in their native environment at ambient temperatures. This is a valuable approach to study the complex function of these systems, because an intrinsic property—the fluorescence emission—is exploited and no additional external perturbations are introduced. Our analysis demonstrates a dynamic adjustment of not only the photosystemI/photosystemII (PSI/PSII) intensity ratio in the chloroplasts but also of the capacity of the LHCs for energy transfer in response to environmental and internal cues.

Keywords: fluorescence, spectroscopy, photochemistry, chloroplast, photosystem, spectromicroscopy

INTRODUCTION

Photosynthesis of plants still sets the benchmark in light-to-energy conversion regarding efficiency, stability and the ability to adapt to dynamic surrounding conditions. Photosynthesis is a highly complex process, involving multi-step energy migration within and between the two photosystems (PS) I and II, which are located in adaptable ratios in the grana and the stroma thylakoids of chloroplasts. The PSs are highly ordered functional and structural units that perform the primary photochemistry of photosynthesis: the absorption of light and the conversion of energy by charge separation. Especially the light harvesting complexes (LHCs) are responsible for the high efficiency of the whole process of photosynthesis due to the broad spectral absorption of ambient light by the LHCs, which is directed to the reaction center via a complex and efficient energy migration chain.

To optimize the use of available light-energy, higher plants undergo highly complex adaptation processes, which are mainly concerned with a structural rearrangement of the chloroplasts (Anderson et al., 1988, 2008; Anderson, 1999).The thylakoid membranes of chloroplasts, which are organized in stacked (grana thylakoids) and non-stacked (stromathylakoids) membranes, comprise different amounts of PSI and PSII. Ultrastructural studies of chloroplasts reveal an accumulation of PSII predominantly in the grana thylakoids, whereas PSI is found mainly in the stroma thylakoids (Anderson, 1986; Allen and Forsberg, 2001). Plants that experience changes in ambient light conditions offer an altered photosynthesis efficiency, which most likely is believed to be connected to a reorganization of the chloroplasts and, hence, a change in the PSI/PSII ratio (Anderson et al., 1988).

Accordingly, it is desirable to determine this ratio *in vivo* at ambient conditions as a measure of the plant ability to adapt its photosynthesic apparatus to the changing light environment. Non-invasive analyses of chloroplasts use the inherent autofluorescence of these compartments, which generally makes them accessible to optical studies. The emission spectrum of chloroplasts exhibits a maximum at 680 nm, which can be assigned to the fluorescence of the reaction center of PSII. Additionally, a spectral shoulder between 700 and 750 nm in the emission

spectrum arising from the PSI reaction center is observed (Krause and Weis, 1991). However, a straightforward determination of the PSI/PSII ratio is hampered using conventional fluorescence microscopy due to the strong overlap of the spectral signatures of PSI and PSII. Hence, fluorescence spectroscopic measurements up to now have mostly been carried out at low temperatures (77 K and below) using isolated chloroplasts, where a differentiation between PSI and PSII is possible (Krause and Weis, 1991). However, similar to ultrastructural studies, plant adaptation processes in a living cell context remain obscured with these methods, since the composition of the photosynthetic apparatus reacts highly sensitive to sample treatments (Andersen et al., 1972). Furthermore, the influence of environmental and endogenous cues on the photosynthetic capacity cannot be explored using isolated chloroplasts. Here, we present two strategies using optical spectro-microscopy to overcome these limitations. These non-invasive techniques provide access to the composition of the photosynthesis apparatus and its adaptation to environmental changes at ambient conditions. To this end, we analyzed the PSI/PSII intensity ratio in chloroplasts at room temperature and in their cellular context by applying high spatial resolution fluorescence spectroscopy. We show that in a high-resolution fluorescence emission spectrum, the contributions of the distinct photosystems can be derived from the spectral shape, which depends on the relative contributions of PSI and PSII, respectively, and hence, the two subpopulations can be identified and compared. A careful statistical analysis of the room temperature emission spectra (SART) enables for monitoring global adaptations in the chloroplasts (i.e., the PSI/PS II intensity ratio).

Using conventional fluorescence-based techniques, however, only the final chromophore of an energy transfer cascade in the photosystems (**Figure 1A**) can be monitored, while the individual steps and composition of the energy transfer systems are not accessible (**Figure 1B**). This is because the energy absorbed by the LHCs is very efficiently funneled to chlorophyll *a* in the reaction centers as the last component of the energy migration chain (Butler and Kitajima, 1975) (**Figure 1A**). Accordingly, any detected fluorescence light originates from the emission of the reaction centers and information about the upstream energy cascade is not available (**Figure 1C**). The crystal structures of LHCs suggest a rigid, uniform assembly of these complexes (Liu et al., 2004).Variations are known to involve different supramolecular organizations of PSs and LHCs detected by electron microscopy (Yakushevska et al., 2001) as well as alterations in the total pigment amount and ratio in the chloroplasts (Bailey et al., 2004). Pigment analysis is usually based on the isolation of pigments using organic solvents followed by chromatographic separation. However, a technique that enables the observation of the photosynthetic efficiency *in vivo* has been missing so far. To overcome this restriction and get access to the composition of the energy transfer complexes *in vivo*, we established a novel *in planta* approach by disentangling the distinct energy transfer steps at ambient temperature. This was achieved by recording the fluorescence excitation spectra (FExS) in the diffraction limited focal spot by confocal fluorescence microscopy.

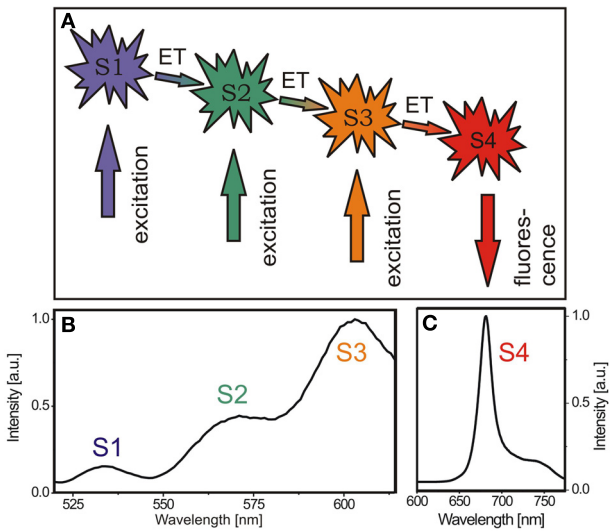

FIGURE 1 | Energy migration pathway in chloroplasts can be visualized by spatially resolved fluorescence excitation spectroscopy (FExS). **(A)** Energy migration scheme in chloroplasts. S1 to S3 indicate states in the LHC energy transfer cascade, from which excitation energy is transferred downstream to the reaction center (S4). **(B)** Representative confocal fluorescence excitation spectrum of an *A. thaliana* chloroplast recorded by sweeping the excitation wavelength while recording the fluorescence intensity at 680 nm. **(C)** Typical chloroplast fluorescence emission spectrum of an *A. thaliana* chloroplast excited at 633 nm.

METHODS

PLANT MATERIAL AND GROWTH CONDITIONS

Arabidopsis (*Arabidopsis thaliana*) ecotype Columbia-0 (wild type, wt) and transgenic plants overexpressing the maize photosynthetic NADP-malic enzyme (MEm2 and MEm5 Fahnenstich et al., 2007) were grown in pots containing three parts of soil (Gebr. Patzer KG, Sinntal-Jossa, Germany) and one part of vermiculite (Basalt Feuerfest, Linz, Germany) at 22°C day temperature under long days (LD, 16 h light/8 h darkness) or short days (SD, 8 h light/16 h darkness). The light intensity (photosynthetic active radiation) was 110 µmol quanta $m^{-2}s^{-1}$. Maize plants were grown in soil with temperatures ranging from 23 to 26°C and a 16 h light/8 h darkness cycle at a photon flux density of 350 µmol quanta $m^{-2}s^{-1}$. Mature (12 week-old plants) and immature (2 week-old seedlings) maize plants were used for the measurements.

STATISTICAL ANALYSIS OF ROOM TEMPERATURE EMISSION SPECTRA (SART)

Data acquisition for SART was accomplished by initially recording a fluorescence intensity map of the plant tissue to identify the chloroplasts using a custom-built confocal fluorescence microscope based on a Zeiss Axiovert 135TV (Carl Zeiss, Germany, Detector: PDM avalanche photodiode, Picoquant, Germany). The custom-built setup was equipped with a 633 nm excitation source (PL-610, Polytec, Germany) and a raster scanning stage (P517, Physik instrumente, Germany). Fluorescence emission spectra with diffraction-limited spatial resolution were acquired

from chloroplasts to determine the relative contributions of PSI and PSII to the spectral signature using a polychromator spectrograph (Acton 300i, Roper Scientific, US, Pixis 100B, Princeton Instruments, US). To reduce the data volume, this spectral shape was analyzed by studying the intensity ratio at characteristic wavelengths. The PSI to PSII intensity ratio was directly deduced by calculating the intensity ratio $\lambda_{emPSI(730\,nm)}$:$\lambda_{emPSII(680\,nm)}$. To account for individual differences in the composition within and among single chloroplasts, we recorded five spectra per chloroplast and averaged the PSI/PSII intensity ratio of numerous chloroplasts ($n = 140$–200). Based on this statistical analysis of chloroplast emission spectra at room temperature (SART), the average PSI/PSII intensity ratio of living plants was determined as a function of external conditions.

FLUORESCENCE EXCITATION SPECTRO-MICROSCOPY (FExS)

To record fluorescence excitation spectra with a diffraction limited spatial resolution, our custom-built confocal microscope (details above) was combined with a supercontinuum laser (SC-400pp, Fianium, UK) as an excitation source. To sequentially scan the excitation wavelength, the supercontinuum source was coupled into a grating monochromator (Acton 300i, Roper Scientific, US), which was synchronized with the data acquisition by a custom-built software protocol. The fluorescence emission was recorded in a spectral window between 655 and 685 nm, matching the fluorescence emission of the PS II reaction center. Excitation spectra were recorded by sweeping the excitation wavelength from 500 to 620 nm, covering the absorption of the LHC pigments while recording the fluorescence emission. Using this fluorescence excitation spectroscopy (FExS) arrangement, intense fluorescence emission is observed for excitation waengths in resonance with the absorbance of one of the LHC pigments. Simultaneously, the energy migration pathway is intact so that the excitation energy is funneled downstream to the reaction center. Accordingly, the intensity of the distinct bands is proportional to the relative amount of energy guided to the reaction center (**Figure 1**). A detailed description of the experimental realization by the combination of confocal microscopy with a feedback-controlled supercontinuum laser source is given elsewhere (Blum et al., 2011).

RESULTS

USING STATISTICAL ANALYSIS OF ROOM TEMPERATURE EMISSION SPECTRA (SART) TO MONITOR THE PSI/PSII INTENSITY RATIO OF INDIVIDUAL CHLOROPLASTS

At room temperature, the emission spectra of PSI and PSII show significant spectral overlap and cannot be distinguished using band-pass filtering as a straightforward approach. However, in a high-resolution fluorescence emission spectrum, the obtained spectral shape depends on the relative contributions of PSI and PSII, and hence the two subpopulations can be identified, compared, and distinguished from each other (**Figure 2A**). To survey the suitability of the SART approach for PSI/PSII intensity ratio determination, chloroplasts of immature and mature leaves of maize (*Zea mays*), a canonical C4 plant with Kranz anatomy consisting of mesophyll and bundle sheath cells, were used as model system. Maize chloroplasts of immature bundle sheath cells exhibit a high PSII activity (Lozier et al., 1971) while those of mature bundle sheath cells have established the characteristic agranal or only rudimentary grana morphology and show a low PSII activity (Woo et al., 1970). Using the *in vivo* SART approach we determined a low PSI/PSII ratio in bundle sheath cells of immature maize leaves, whereas this ratio rose substantially for

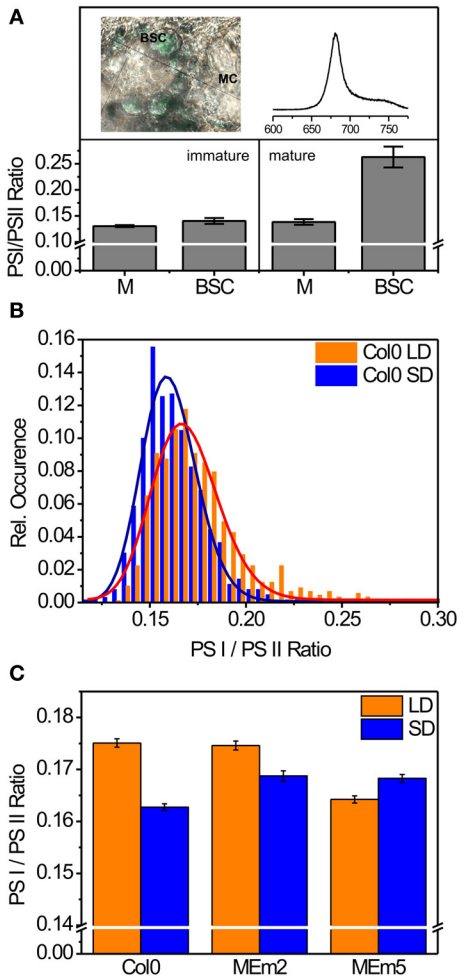

FIGURE 2 | PSI/PSII ratio in chloroplasts of living plant cells determined by SART. (A) Average PSI/PSII ratio of chloroplasts in immature maize leaf tissue [left; calculated from 19 spectra recorded from mesophyll cells (MC) and 19 spectra recorded in bundle sheath cells (BSC), ($n = 38$, $p = 0.1$)] and in mature leaf tissue (right; calculated from 38 spectra recorded in MC and 59 spectra recorded in BSC). The upper left shows a brightfield image of a maize leaf section with MS and BSC cells. The upper right depicts a typical fluorescence intensity spectrum recorded from MC (x axis: emission wavelength [nm]). **(B)** Histogram of the calculated PSI/PSII intensity ratio of *A. thaliana* grown under long day (LD) and short day (SD) conditions. The histograms were calculated from 893 spectra in case of LD plants and 630 spectra in case of SD conditions. The histograms were fit with lognormal model functions with an adjusted R^2-value of at least 0.95 (solid lines). **(C)** Average PSI/PSII intensity ratios in chloroplasts of *A. thaliana* wild type (Col0) and transgenic plants expressing maize plastidic NADP malic enzyme at different levels (MEm2 and MEm5 plants with 6 and 33 times increased NADP ME activity with regards to the wild type, respectively) grown under short day (SD) or long day (LD) conditions.

bundle sheath cells of mature plants (**Figure 2A**). Based on this data, we validated that SART enables the determination of the PSI/PSII ratio in living plants. We therefore used SART to investigate the ability of the prototypical C3 plant *Arabidopsis thaliana* (Arabidopsis; *A. thaliana*) to adjust the PSI/PSII ratio to external and environmental cues.

To check the influence of the duration of the light period on the relative PSI/PSII luminescence, we grew *A.thaliana* ecotype Columbia-0 (Col0) under long day (LD) and short day (SD) conditions (16/8 and 8/16 h photoperiod, respectively). Spectra were recorded from plants at the same growth stadium in the second half of the light period. To prevent any adulteration of the results by spectra close to the noise or saturation limit of the spectrograph, we disregarded the most and least intense 5% of the recorded spectra for downstream processing. The calculated PSI/PSII ratios show a monomodal distribution that can be well explained by a lognormal model in both LD- and SD-grown plants (**Figure 2B**). As a *t*-test analysis might be misleading to identify whether the means of these distributions differ significantly, we performed a Z-score test using unbiased estimators (Zhou et al., 1997) to calculate the significance level for this lognormal distributions according to

$$\alpha = 2\varphi(Z);\ Z < 0$$

with

$$\varphi(Z) = \frac{1}{\sqrt{2\pi}} \int_{-\infty}^{Z} exp\left(\frac{-x^2}{2}\right) dx$$

Plants grown under LD conditions show an overall significantly increased PSI/PSII ratio compared to plants grown under the more restrictive SD conditions. We calculated a Z-Score of $Z = -12.57$ translating into a significance level of $2.9{*}10^{-36}$. These results indicate that *A. thaliana* plants adapt their photosynthesis apparatus, namely the apparent PSI/PSII ratio, depending on the available amount of light.

To investigate the capability of the *in vivo* adjustment to changes in internal cues, we compared the PSI/PSII ratio of *A. thaliana* wild type plants with that of two independent transgenic lines overexpressing the maize photosynthetic NADP-malic enzyme (MEm2 and MEm5 with 6 and 33 times higher NADP-ME activity Fahnenstich et al., 2007). As shown previously, the MEm plants present a sustained low level of the organic acids malate and fumarate, especially when grown in SD (Fahnenstich et al., 2007; Zell et al., 2010). As a consequence of the impairment in the supply of carbon in SD, the MEm plants show a dwarf growth phenotype, which is accompanied by more crowded thylakoid membrane systems and a lower PSII quantum yield compared to the wild type. The intensity of the changes described follows a dose response relationship with the level of NADP-ME activity (Zell et al., 2010). However, no differences in phenotype and all the above-mentioned parameters were found when the MEm plants were grown under LD conditions (Zell et al., 2010). For the determination of the PSI/PSII intensity ratio by SART, we grew the plants at both LD and SD conditions and recorded several hundred emission spectra per condition and plant. Again, the histograms of the calculated PSI/PSII intensity ratios obtained are monomodal and plausibly explained by a lognormal model (Supplemental Figure S1). Comparing the means of the PSI/PSII distributions, we found that MEm2 plants show no significant change in their PSI/PSII intensity ratio compared to wild type plants under LD conditions (significance level: 0.64). Furthermore, the MEm2 plants have a moderately enhanced PSI/PSII intensity ratio compared to wild type plants under SD conditions (significance level: $6.5{*}10^{-8}$). This indicates that the slight overexpression of the plastidic NADP-malic enzyme has, if at all, only a moderate effect on the PSI/PSII intensity ratio in SD conditions. In contrast, the MEm5 plants show a pronounced drop in the PSI/PSII intensity ratio under LD conditions and slight increase under SD conditions (**Figure 2C**; significance level of $5.3{*}10^{-27}$ and $5.8{*}10^{-9}$ at LD and SD, respectively). This indicates that the chloroplasts of the MEm5 plants adapt to the carbon shortage by lowering the PSI/PSII intensity ratio under LD conditions. Since the quantum yield of PSII does not depend on the NADP-malic enzyme expression level when grown under LD conditions (Zell et al., 2010), this change in the PSI/PSII intensity ratio reflects an alteration in the relative PSI amount. Possibly, the alteration of the PSI/PSII intensity ratio in LD is one compensatory mechanism that enables the MEm5 plants to prevent a dwarfed growth phenotype.

USING FLUORESCENCE EXCITATION SPECTRO-MICROSCOPY (FExS) TO INVESTIGATE THE EFFICIENCY OF LIGHT HARVESTING COMPLEXES IN AN INDIVIDUAL CHLOROPLAST

To investigate the individual efficiency of LHCs and their ability to adapt to changing environmental conditions, we applied FExS to 5-weeks-old *A. thaliana* wild type and MEm5 plants grown under SD conditions. The emission passband was chosen to match the PSII-emission. As shown in **Figure 3**, wild type and MEm5 plants showed three fluorescence excitation peaks between 520 nm and 620 nm ($\lambda_{peak1} = 534$ nm; $\lambda_{peak2} = 568$ nm; $\lambda_{peak3} = 604$ nm). We initially assumed these three peaks to originate in different pigments; however, there are no three pigments exhibiting their absorbance maxima in this wavelength regime. Rather, the peaks are assigned to the $Q_x(0, 0)$ and higher vibronic Q_x and Q_y transitions of the chlorophylls (Breton and Vermeglio, 1988; Fragata et al., 1988). The excitation spectra shown here reflect how much light is funneled to the PSII reaction centers upon absorbance at a given wavelength. Assuming that the LHCs and PSs form highly optimized functional units one expects that there is little variation in the composition of these cellular compounds and, as a consequence, this is expected to be reflected in a very constant excitation spectrum.

To establish if there is any adaptation of plants not only in the PIR but also inside the light harvesting apparatus, we recorded chloroplast excitation spectra *in planta* from wild type and from MEm5 plants. For data analysis, three Gaussians were fit to every spectrum as shown in **Figure 3** and the areas under the peaks were calculated in relation to the area under the first peak at 534 nm (peak S1).

As shown in **Figure 4A**, the spectra of wild type plants showed a rather broad distribution of the peak area ratios ($2\sigma_{(S2:S1)} = 0.73 \pm 0.05$, $\sigma_{(S3:S1)} = 1.60 \pm 0.14$, $2\sigma_{(S3:S2)} = 0.96 \pm 0.24$). This indicates that light harvesting

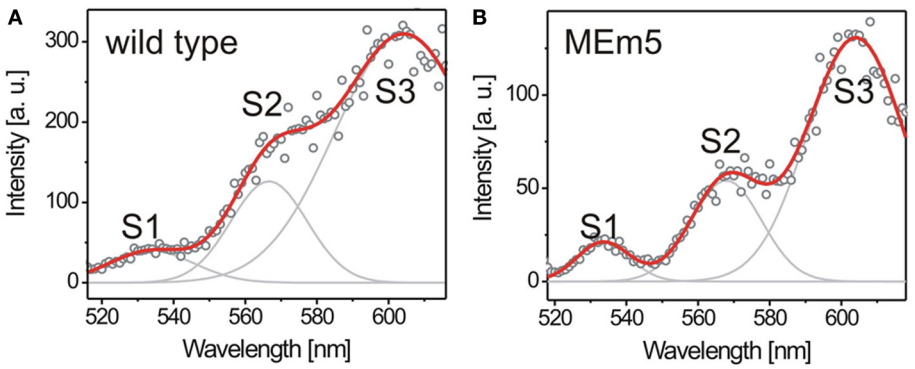

FIGURE 3 | Fluorescence excitation spectra of chloroplasts recorded from 5-week-old *A. thaliana* wild type (100 spectra) (A) and MEm5 (150 spectra) (B). The plants were grown at white light (50 μmol quanta m^2s^{-1}) under SD conditions. Three transitions contributing to the energy migration chain are visible as distinct bands. The spectral envelope was fitted by three Gaussians (gray lines) to determine the relative contribution of the respective pigments to the excitation spectrum. The red curve depicts the summation of the three Gaussian distributions; round circles represent the raw data. Fluorescence intensity at the red region of the spectrum is slightly overrepresented due to higher excitation power at that edge of the spectrum.

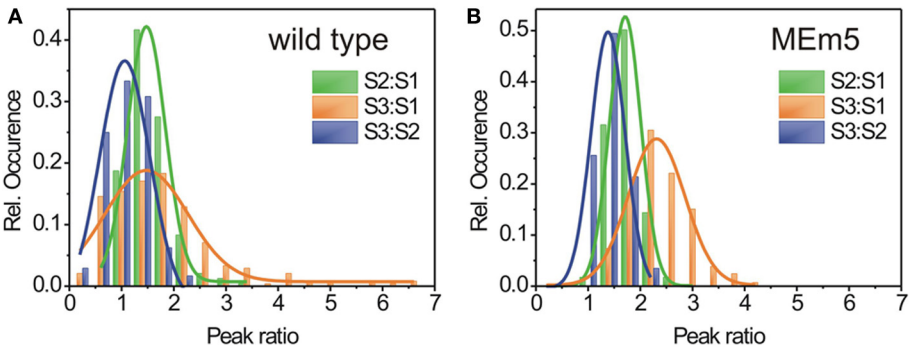

FIGURE 4 | FExS reveals characteristic composition for different carotenoids of the LHCs in chloroplasts of *A. thaliana* wild type (A) and MEm (B) plants. Every FExS spectrum was fitted by three Gaussians and the area under the peaks was calculated relative to the peak representing the highest transition energy (S1). Histograms of the peak ratio distribution of the excitation peak areas for wild type **(A)** and MEm5 plants **(B)**. Red: peak ratio S2:S1, green: peak ratio S3:S1; blue: peak ratio S3:S2. The histograms were fit by Gaussians (solid lines) and show normal distribution.

in living plants is by no means due to a rigid, uniform machinery but rather exhibits variations in terms of efficiency on a local basis. In contrast, for the MEm5 plants, the peak ratio distributions were significantly narrowed compared to the wild type $[2\sigma_{(S2:S1)} = 0.60 \pm 0.01, \quad \sigma_{(S3:S1)} = 1.09 \pm 0.08, 2\sigma_{(S3:S2)} = 0.65 \pm 0.04)$ (**Figure 4B**). Furthermore, the peak ratios exhibit an overall shift toward larger values for MEm5 plants compared to their wt counterparts. This means that overall, a higher fraction of fluorescence is excited at higher wavelength regions in MEm5 plants than in Col0.

DISCUSSION

The results reported in this manuscript offer several insights into the adaptation potential of the photosynthetic apparatus of higher plants. First, our SART data substantiate previous findings that differences in the length of the light period in live plants lead to a reprogramming of the PSI/PSII ratio. We believe that the measured change in the PSI/PSII intensity ratio of LD- and SD-grown plants can be translated into a readjustment in the PSI/PSII ratio in plants because the quantum yield of Col0 plants grown in the applied light conditions does not change significantly (Zell et al., 2010). In contrast to previous studies, our data were obtained applying a non-invasive approach at ambient temperature conditions. As our data support the results of ultrastructural experiments, we consider our technique valid to monitor the PSI/PSII intensity ratio in living plant cells. We showed that SART can be used to investigate adaptation processes in chloroplasts of plants with changes in carbon homoeostasis with high sensitivity.

In LD conditions, MEm2 plants show no distinguishable growth and PSI/PSII intensity ratio phenotype from wild type plants, although they exhibit slightly lower levels of CO_2 assimilation (Zell et al., 2010). Under this photoperiod, it appears that the photosynthetic productivity can still compensate for the physiological carbon depletion. Therefore, a significant adjustment of the PSI/PSII intensity ratio in MEm2 and wild type plants grown under LD conditions is not required. Contrarily, MEm5 plants, which exhibit a much higher level of NADP-ME,

show clear changes in the PSI/PSII intensity ratio under LD conditions. Apparently, the carbon deficit under these conditions is already severe enough to provoke an effect in the composition of the photosynthetic apparatus. Interestingly, other parameters related to photosynthesis such as the total chlorophyll content and the PSII quantum yield are not different between MEm5 and wild type plants (Zell et al., 2010). Under SD conditions, there is a clear growth phenotype for both MEm2 and MEm5 plants. This is accompanied by a change in the PSI/PSII intensity ratio in MEm plants compared to wild type. MEm plants grown under SD conditions furthermore experience a decreased PSII quantum yield compared to wt plants which is progressive with the NADP-ME activity (Zell et al., 2010). Interestingly, the difference in the PSI/PSII intensity ratio of MEm2 and MEm5 plants is not linear with the NADP-ME activity. We observed that the PSI/PSII intensity ratio of MEm2 plants decreases from LD- to SD-grown plants whereas in MEm5 plants there is an increase. The altered PSII quantum yield might well affect the measured PSI/PSII intensity ratio. However, the fact that these two effects are not correlated is a strong indication that the observed change in the PSI/PSII intensity ratio originates in a relative amount of PSI/PSII. This finding is interpreted as follows: Under sufficient light conditions—as is the case in LD—there is enough energy supply to compensate for the carbon deficit allowing normal growth. In case of MEm2, there is no adaptation necessary due to the moderate overexpression of the NADP-ME. In MEm5, however, a detrimental growth phenotype may be avoided by physiological/molecular compensatory changes, being one of them the large reorganization of the photosynthetic apparatus. In SD conditions, the photosynthetic productivity of MEm chloroplasts can no longer overcome the reduced CO_2 assimilation due to a large carbon starvation. Even a possible re-adjustment of the PSI/PSII ratio, which might reflect a general, adaptive response to limiting light conditions, cannot compensate for the carbon deficit.

A deeper insight into the LHCs of chloroplasts is obtained by application of the FExS approach, which allows identifying the direct observation of the amount of light that is funneled to the downstream excitation centers after excitation of a specific energy state. Our FExS data revealed that the energy transfer to the PSII reaction centers upon excitation in different wavelength regimes is not constant but exhibits significant variations within a plant. The three excitation peaks described in this study do not translate into the amounts of different pigments involved in light harvesting. Rather, we interpret the energy cascade in LHCs as complex multi-level entities. If the LHCs were uniformly assembled, no variations at all would be observed in the excitation peak ratios, just like in the excitation spectra of fluorophores in solution. The fact that we observe strong variations here means that the efficiency of downstream energy transfer upon excitation of a distinct energy level is not constant. As a consequence, a varying fraction of the collected light might migrate by pathways different than energy transfer to the PSII reaction center upon excitation, arguably by non-radiative deactivation of the excited state. The fluctuations observed here essentially reflect a different nano-environment of the excited pigments not observable in isolated systems. This indicates that the chlorophylls of the energy cascade involved in light harvesting are not rigidly embedded into the protein scaffold but rather represent a highly dynamic system *in vivo*. Interestingly, we found that MEm5 plants suffering from carbon starvation exhibit an overall altered photosynthetic efficiency in the probed spectral regime *in vivo* along with a narrowed distribution of the excitation peak ratios. This indicates an overall altered, more uniform composition of MEm5 chloroplasts compared to wild type plants. On microscopic level, wild-type plants seemingly maximize the light absorption and the subsequent energy transfer to the reaction centers. The MEm5 plants obviously present a limitation of this ability. Likely, the MEm5 plants are not able to dynamically re-organize their LHCs like the wild type due to the lack of sufficient carbon supply during the extended night period (Zell et al., 2010). This may reduce the capacity of the MEm5 plants to optimize the photosynthetic energy generation process. Together with the de-regulation of the PSI/PSII ratio, this could contribute to the carbon starvation phenotype of the MEm5 plants under SD conditions.

Taken together, our results suggest the potential for adaptations within the LHCs of land plants such the *A. thaliana* based on a different interaction network of the pigments involved in light harvesting, a mechanism differing from the chromatic adaptation previously reported to be due to alterations of the overall LHC pigment composition incyanobacteria (Kehoe and Gutu, 2006; Mascle-Allemand et al., 2010).

CONCLUDING REMARKS

In this work, we presented two spectro-microscopic approaches, namely SART and FExS, to investigate for the first time photosynthetic adaptation processes in single chloroplasts of living plant cells in their native milieu at ambient temperature. Our data show that SART is a sensitive method for detecting and quantifying externally- (light conditions) and internally- (carbon homoeostasis changes) regulated adaptation processes of chloroplasts. This method is highly sensitive and is thus well suited to investigate the dynamics of PSI/PSII ratio of chloroplasts *in vivo*. Whereas SART spectroscopy enables the determination of the relative PSI/PSII amounts, FExS allows the disentanglement of the energy transfer processes in the LHCs. Both the PSI/PSII fluorescence intensity ratio and the energy transfer are demonstrated to be adjustable to external conditions such as light intensity and internal to cues, such as C_4 acid deficiency, in a highly flexible manner.

ACKNOWLEDGMENT

We acknowledge the support by the Deutsche Forschungsgemeinschaft (DFG) and the Open Access Publishing Fund of the University of Tübingen.

SUPPLEMENTARY MATERIAL

The Supplementary Material for this article can be found online at: http://www.frontiersin.org/journal/10.3389/fpls.2014.00292/abstract

REFERENCES

Allen, J. F., and Forsberg, J. (2001). Molecular recognition in thylakoid structure and function. *Trends Plant Sci.* 6, 317–326. doi: 10.1016/S1360-1385(01)02010-6

Andersen, K. S., Bain, J. M., Bishop, D. G., and Smillie, R. M. (1972). Photosystem II activity in agranal bundle sheath chloroplasts from zea mays. *Plant Physiol.* 49, 461–466. doi: 10.1104/pp.49.4.461

Anderson, J., Chow, W., and Goodchild, D. (1988). Thylakoid membrane organization in sun shade acclimation. *Aust. J. Plant Physiol.* 15, 11–26. doi: 10.1071/PP9880011

Anderson, J. M. (1986). Photoregulation of the composition, function, and structure of thylakoid membranes. *Annu. Rev. Plant Physiol.* 37, 93–136. doi: 10.1146/annurev.pp.37.060186.000521

Anderson, J. M. (1999). Insights into the consequences of grana stacking of thylakoid membranes in vascular plants: a personal perspective. *Aust. J. Plant Physiol.* 26, 625–639. doi: 10.1071/PP99070

Anderson, J. M., Chow, W. S., and De Las Rivas, J. (2008). Dynamic flexibility in the structure and function of photosystem II in higher plant thylakoid membranes: the grana enigma. *Photosyn. Res.* 98, 575–587. doi: 10.1007/s11120-008-9381-3

Bailey, S., Horton, P., and Walters, R. G. (2004). Acclimation of *Arabidopsis thaliana* to the light environment: the relationship between photosynthetic function and chloroplast composition. *Planta* 218, 793–802. doi: 10.1007/s00425-003-1158-5

Blum, C., Schleifenbaum, F., Stopel, M., Peter, S., Sackrow, M., Subramaniam, V., et al. (2011). Room temperature excitation spectroscopy of single quantum dots. *Beilstein J. Nanotechnol.* 2, 516–524. doi: 10.3762/bjnano.2.56

Breton, J., and Vermeglio, A. (1988). *The Photosynthetic Bacterial Reaction Center*. New York, NY; London: Plenum Press. doi: 10.1007/978-1-4899-0815-5

Butler, W. L., and Kitajima, M. (1975). Energy transfer between photosystem II and photosystem I in chloroplasts. *Biochim. Biophys. Acta* 396, 72–85. doi: 10.1016/0005-2728(75)90190-5

Fahnenstich, H., Saigo, M., Niessen, M., Drincovich, M., Zanor, M., Fernie, A., et al. (2007). Low levels of malate and fumarate cause accelerated senescence during extended darkness in *Arabidopsis thaliana* overexpressing maize C 4 NADP-malic enzyme. *Plant Physiol.* 145, 640–652. doi: 10.1104/pp.107.104455

Fragata, M., Nordén, B., and Kurucsev, T. (1988). Linear dichroism (250–700 nm) of chlorophyll a and pheophytin a oriented in a lamellar phase of glyceryl-monooctanoate/H2O. Characterization of electronic transitions. *Photochem. Photobiol.* 47, 133–143. doi: 10.1111/j.1751-1097.1988.tb02703.x

Kehoe, D. M., and Gutu, A. (2006). Responding to color: the regulation of complementary chromatic adaptation. *Annu. Rev. Plant Biol.* 57, 127–150. doi: 10.1146/annurev.arplant.57.032905.105215

Krause, G. H., and Weis, E. (1991). Chlorophyll fluorescence and photosynthesis - the basics. *Annu. Rev. Plant Physiol. Plant Mol. Biol.* 42, 313–349. doi: 10.1146/annurev.pp.42.060191.001525

Liu, Z., Yan, H., Wang, K., Kuang, T., Zhang, J., Gui, L., et al. (2004). Crystal structure of spinach major light-harvesting complex at 2.72 Å resolution. *Nature* 428, 287–292. doi: 10.1038/nature02373

Lozier, R., Baginsky, M., and Butler, W. L. (1971). Inhibition of electron transport in chloroplasts by chaotropic agents and the use of manganese as an electron donor to photosystem II. *Photochem. Photobiol.* 14, 323–328. doi: 10.1111/j.1751-1097.1971.tb06176.x

Mascle-Allemand, C., Duquesne, K., Lebrun, R., Scheuring, S., and Sturgis, J. N. (2010). Antenna mixing in photosynthetic membranes from Phaeospirillum molischianum. *Proc. Natl. Acad. Sci. U.S.A.* 107, 5357–5362. doi: 10.1073/pnas.0914854107

Woo, K. C., Anderson, J. M., Boardman, N. K., Downton, W. J. S., Osmond, C. B., and Thorne, S. W. (1970). Deficient photosystem II in agranal bundle sheath chloroplasts of C4 plants. *Proc. Natl. Acad. Sci. U.S.A.* 67, 18–25. doi: 10.1073/pnas.67.1.18

Yakushevska, A. E., Jensen, P. E., Keegstra, W., Van Roon, H., Scheller, H. V., Boekema, E. J., et al. (2001). Supermolecular organization of photosystem II and its associated light−harvesting antenna in *Arabidopsis thaliana*. *Eur. J. Biochem.* 268, 6020–6028. doi: 10.1046/j.0014-2956.2001.02505.x

Zell, M. B., Fahnenstich, H., Maier, A., Saigo, M., Voznesenskaya, E. V., Edwards, G. E., et al. (2010). Analysis of arabidopsis with highly reduced levels of malate and fumarate sheds light on the role of these organic acids as storage carbon molecules. *Plant Physiol.* 152, 1251–1262. doi: 10.1104/pp.109.151795

Zhou, X.-H., Gao, S., and Hui, S. L. (1997). Methods for comparing the means of two independent log-normal samples. *Biometrics* 53, 1129–1135. doi: 10.2307/2533570

Conflict of Interest Statement: The authors declare that the research was conducted in the absence of any commercial or financial relationships that could be construed as a potential conflict of interest.

Received: 02 July 2013; accepted: 04 June 2014; published online: 30 June 2014.
*Citation: Peter S, Zell MB, Blum C, Stuhl A, Elgass K, Sackrow M, Subramaniam V, Meixner AJ, Harter K, Maurino VG and Schleifenbaum FE (2014) Photosynthesis in a different light: spectro-microscopy for in vivo characterization of chloroplasts. Front. Plant Sci. **5**:292. doi: 10.3389/fpls.2014.00292*
This article was submitted to Plant Cell Biology, a section of the journal Frontiers in Plant Science.
Copyright © 2014 Peter, Zell, Blum, Stuhl, Elgass, Sackrow, Subramaniam, Meixner, Harter, Maurino and Schleifenbaum. This is an open-access article distributed under the terms of the Creative Commons Attribution License (CC BY). The use, distribution or reproduction in other forums is permitted, provided the original author(s) or licensor are credited and that the original publication in this journal is cited, in accordance with accepted academic practice. No use, distribution or reproduction is permitted which does not comply with these terms.

frontiers in
PLANT SCIENCE

ORIGINAL RESEARCH ARTICLE
published: 18 February 2014
doi: 10.3389/fpls.2014.00039

Spectral analysis combined with advanced linear unmixing allows for histolocalization of phenolics in leaves of coffee trees

Geneviève Conéjéro[1], Michel Noirot[2]*, Pascale Talamond[3] and Jean-Luc Verdeil[1]

[1] *Plant Cell Imaging platform PHIV UMR AGAP (Cirad, SupAgro, INRA), UMR B&PMP (INRA, CNRS, UM2, SupAgro), Montpellier, France*
[2] *UMR PVBMT, (CIrad, IRD) La Réunion, France*
[3] *Institut des Sciences de l'Evolution, UMR ISE-M (CNRS, IRD, UM2), Montpellier, France*

Edited by:
Tobias Meckel, Technische Universität Darmstadt, Germany

Reviewed by:
Andreas Nebenführ, University of Tennessee, USA
Hirokazu Tanaka, Osaka University, Japan

****Correspondence:***
Michel Noirot, Institut de Recherche pour le Développement, 911 Avenue Agropolis, 34394 Montpellier, France
e-mail: michel.noirot@ird.fr

An imaging method using spectral analysis combined with advanced linear unmixing was used to allow histolocalization of natural autofluorescent compounds such as hydroxycinnamic acid (chlorogenic acid) and xanthone (mangiferin) in living cells and tissues (mature coffee leaves). The tested method included three complementary steps: 1/ visualization of natural autofluorescence and spectrum acquisition with a multiphoton microscope; 2/ identification of some compounds using previous information on the chemical composition of the tissue, obtained from litterature; and 3/ localization of candidate compounds by spectral imaging. The second part of the study consisted of describing the histochemical structure of leaves during their development. This revealed very fast histochemical differentiation of leaves during the first week after their emergence. Lastly, young leaves of *Coffea pseudozanguebariae* (PSE), *C. eugenioides* (EUG), *C. arabica* (ARA) and *C. canephora* (CAN) were compared. This confirmed the presence of xanthone in PSE and EUG, but especially its precise tissue localization. This also highlighted the paternal CAN origin of the leaf structure in the allotetraploid species ARA. The limits and advantages of the method without staining are discussed relative to classical epifluorescence microscopy under UV light. This non-invasive optical technique does not require pretreatment and is an effective experimental tool to differentiate multiple naturally-occuring fluorochores in living tissues.

Keywords: spectral analysis, multiphotonic microscope, autofluorescence, caffeoylquinic acids, xanthone, *Coffea*

INTRODUCTION

Plants produce a vast array of secondary metabolites such as phenolics that are estimated to comprise at least 8000 different chemicals (Jones et al., 2013). Many of them include low molecular weight phenolics, but also condensation products such as lignins and flavonoids. It is estimated that phenolics represent about 40% of all organic compounds circulating in the biosphere. These contribute to hardiness, color, taste, odor and many of them are of high economic value.

In the *Coffea* genus, caffeoylquinic acids (CQA) and dicaffeoylquinic acids (diCQA)-two secondary metabolites from the phenylpropanoid pathway-are of major economic importance in coffee production via two major species: *Coffea arabica* L. (ARA) (65–70% of the worldwide coffee production) and *C. canephora* Pierre ex Froehner (CAN). CQA and diCQA are indeed the most abundant soluble hydroxycinnamic acids (HQA) present in leaves and seeds (Clifford, 1985; Ky et al., 2001; Campa et al., 2012). Three isomers occur in each class according to the acylating residue positions, but the most important in terms of content is 5-*O*-caffeoylquinic acid, more commonly known as chlorogenic acid (Clifford, 1985) (see **Figure A** in supplementary material).

Another important xanthonoid phenol has been identified in leaves of *C. pseudozanguebariae* Bridson (PSE). This is *C*-glycosyl xanthone, or 2-*C*-β-D-glucopyranosyl–1,3,5,7 tetrahydroxyxanthen-9-one, more commonly known as mangiferin (Talamond et al., 2008, 2011; Campa et al., 2012) (see **Figure A** in supplementary material). As for chlorogenic acid (Bertrand et al., 2003; Mondolot et al., 2006), its content was found to decrease from young to mature leaves (Campa et al., 2012). Lastly, it has also been detected in other *Coffea* species such as *C. eugenioides* S. Moore (EUG) and ARA, but is absent in CAN leaves (Campa et al., 2012).

Great progress has been made in understanding the regulation of the expression of genes involved in phenol metabolism, but less is known about their spatial distribution at the tissular and cellular level. To date, phenol histolocalization is generally done using Neu's reagent, which binds with phenolics, emitting a specific greenish-white epifluorescence under UV light (Neu, 1956). As expected, the most intense greenish-white fluorescence is observed in juvenile coffee leaf blades (Mondolot et al., 2006; Campa et al., 2012), but its specificity toward HQA is low. By contrast, mangiferin histolocalization by epifluorescence does not require any reagents and has been directly observed through its autofluorescence (Talamond et al., 2011; Campa et al., 2012). As phenolics are autofluorescent compounds, it was suggested that microspectrometry allowing fluorescence spectra recording from ROI could be used to confirm their fluorescence signature (Hutzler et al., 1998). This can be achieved using either confocal

(Hutzler et al., 1998) or two-photon microscopy (Talamond et al., 2011). The latter has the advantage of providing excellent three-dimensional spatial resolution of the location from which the fluorescence spectra can be obtained (Saadi et al., 1998). This imaging approach is not commonly used to localize phenolic compounds since fluorescence spectra obtained from plant samples are generated by the emission of many fluorophores with overlapping emission peaks. Fortunately, spectral unmixing methods using computer algorithms provide an opportunity to separate a spectral signal recorded from a single or a group of pixels containing a number of fluorophores into separate intensity signals of each of them.

In this paper, a new imaging approach was carried out to localize phenols *in situ* using a multiphoton microscope combined with spectral analysis and linear unmixing. This allows the differentiation of distinct fluorophores with highly overlapping emission spectra (Zimmermann et al., 2003; Garini et al., 2006). We developed such a method to localize 5-CQA and mangiferin, which are fluorescent compounds, in fresh mature coffee leaves. Nevertheless, it is important to choose plant material with a high proportion of 5-CQA in HQAs in order to minimize noise due to other HQAs. As the highest CQA/HQA ratio (93%) was found to characterize mature ARA leaves (estimated from Campa et al., 2012), we opted to use this material in the first part of the present study. The second part involved describing the differentiation of the histochemical structure of ARA leaves over time. Lastly, the histochemical structure of young leaves was compared between four *Coffea* species, i.e., PSE, EUG, ARA, and CAN. PSE was selected for its very low 5-CQA content (Bertrand et al., 2003) and high mangiferin content in leaves (Talamond et al., 2011; Campa et al., 2012). EUG and CAN were taken into account because they are putative parents of ARA (Lashermes et al., 1999). In addition, the four species constitutes a gradient for the chlorogenic acid content (Campa et al., 2012).

MATERIALS AND METHODS

PLANT MATERIAL

For *Coffea pseudozanguebariae* (PSE), *C. eugenioides* (EUG), *C. arabica* L (cv Bourbon, ARA) and *C. canephora* (CAN), leaves were sampled on coffee trees growing in the field at St Pierre, Réunion (France). Mature leaves were sampled on the third node from the branch tips, whereas young leaves were sampled at phase φ2 and φ3 (Lécolier et al., 2009).

HISTOLOGICAL AND IMAGING METHODS

Leaf cross-sections (50 µm) were obtained using an HM 650 V vibrating blade microtome (Microm, Waldorf, Germany) and then dipped in a glycerol/water (50:50) solution saturated with ascorbic acid to prevent oxidation. A multiphoton Zeiss 510 META NLO microscope (Zeiss, Iena, Germany), equipped with a laser Chameleon Ultra II Ti-Sapphire (Coherent, Santa Clara, California) and a 25x/0.8 Plan-Neofluar immersion objective, was used to obtain galleries of spectral images and emission spectra from fresh leaf sections. Spectral imaging was carried out with laser optimal excitation at 720 nm, reproducing laser UV monophotonic excitation in the 365–700 nm emission range. A set of 32 images was obtained, with each image being acquired with a separate narrow bandwidth (10.7 nm), representing the complete spectral distribution of the fluorescence signals for every point of the microscopic image. This procedure was performed on leaf cross-sections, as well as on pure chlorogenic acid (5-CQA) and mangiferin powders (Sigma-Aldrich, St Quentin Fallavier, France and Extrasynthese, Genay, France, respectively).

To check a possible impact of pH on spectral emission, some experiments using different pH (between pH = 5.5 and 10.5) were carried out in the case of the 5-CQA. There was no impact on the results (data not shown).

The spectral analysis was carried out using the advanced linear unmixing function (LSM 510 software) which separates mixed signals pixel by pixel using the entire emission spectrum of each defined autofluorescent compound in the sample. This function requires at least two spectra and was applied with the advanced iterative option and one residual channel. After spectral imaging acquisitions on leaf cross-sections, the advanced linear unmixing function allowed visualization with coded colors of the fluorescence of chlorogenic acid (5-CQA), mangiferin, and chlorophyll in cells based on their reference spectra.

Each experiment was repeated with 3–5 leaves per different stages or species.

RESULTS

CHARACTERIZATION OF LEAF ANATOMY UNDER FLUORESCENCE

The first step involved obtaining spectral images from mature leaf cross-sections of the ARA (*C. arabica* L cv Bourbon) (**Figure 1**). This image was the result of merging 32 images (channels) obtained between 365 and 700 nm and shows the whole fluorescence detectable in the leaf section without staining. The autofluorescence of cell walls, pigments and cuticle enabled visualization of the leaf anatomical structure.

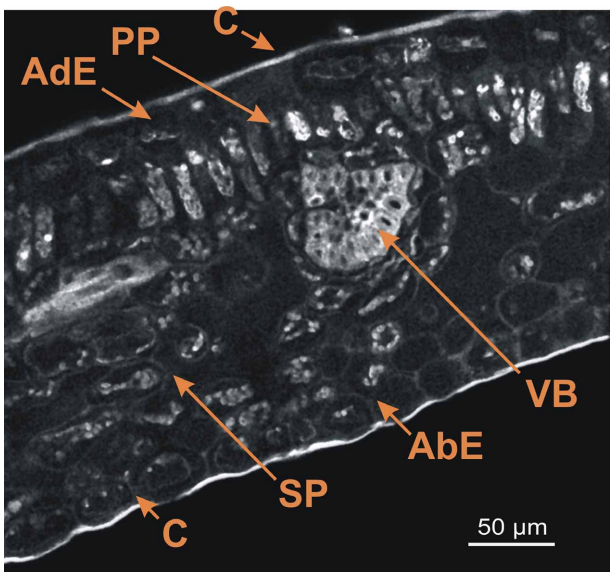

FIGURE 1 | Spectral image on leaf cross-section of the *C. arabica* cv. Bourbon obtained using a multiphoton microscope at 720 nm excitation. AdE, adaxial epidermis; AbE, abaxial epidermis; C. cuticule; PP, palisade parenchyma; SP, spongy parenchyma; VB, vascular bundles. Scale bar = 50 µm.

As described by Dedecca (1957), leaf cross-sections showed the classical foliar structure with the adaxial epidermis, palisade parenchyma, spongy parenchyma, and abaxial epidermis. Each epidermis was covered by a thin cuticle. Lastly, vascular bundles were also present on this cross-section.

The autofluorescence software coding function was then applied, thus generating the central part of **Figure 2**. Coding consisted of giving a wavelength-dependent color to each pixel with a proportional intensity to the pixel fluorescence intensity (Garini et al., 2006). This encoding clearly brought out the previously described leaf structure (**Figure 1**). Three groups of tissues were distinguished according to the autofluorescence intensity and color: 1/both epidermal tissues (adaxial and abaxial), which had low fluorescence; 2/parenchyma (palisade and spongy) was characterized by strong red fluorescence; and 3/vascular bundles showing strong blue fluorescence. Cuticles also showed high orange fluorescence. Lastly some small yellow fluorescent zones were observed within the palisade parenchyma.

The next step consisted of obtaining spectra from red, blue, yellow and orange zones (on the left and right parts of **Figure 2**). In the present case, each spectrum was characteristic of one pixel, symbolized by a cross on the figure, but it was also possible to define each emission spectrum from a small number of pixels, giving identical results. The next step involved looking for compounds that could explain the autofluorescence of these different ROI.

IDENTIFICATION AND LOCALIZATION OF 5-CQA, MANGIFERIN AND CHLOROPHYLL

Reference spectral signatures were acquired on the microscope using controls of products known to be present in mature leaves, i.e., pure 5-CQA and mangiferin powders and chlorophyll extracts. **Figure 3** represents the reference spectra of 5-CQA, mangiferin and chlorophyll. Each molecule could be characterized by its absorption and emission spectra. Spectral signatures of 5-CQA, mangiferin, and chlorophyll were then stored in the Spectra Database. The emission spectrum of 5-CQA obtained with the laser system had the same profile and λ_{max} emission (457 nm) as that obtained with a conventional spectofluorometer with a 300 nm excitation wavelength. Spectral signature of chlorophyll presented λ_{max} at 670 nm, as expected. 5-CQA and mangiferin presented a wide spectral range with peaks at about 455 and 590 nm, respectively.

For the last step, the advanced linear unmixing process was carried out using chlorophyll, 5-CQA and mangiferin reference spectra (**Figure 4**). The composite image (V) was generated from four base images (I–IV), corresponding to the localization of chlorophyll (I), 5-CQA (II), mangiferin (III), and residual fluorescence (IV), respectively. Similarity is striking when comparing **Figures 2**, **4V**.

In fact, chlorophyll, 5-CQA and mangiferin spectra looked like ROI1, ROI2, and ROI3 of the **Figure 2**, respectively. Differences were nevertheless observed due to the fact that several autofluorescent compounds were present at a given pixel. For example, mangiferin spectra did not show a peak at 670 nm, suggesting that ROI3 resulted from both mangiferin and chlorophyll spectra.

High chlorophyll fluorescence was observed in chloroplasts of parenchyma cells (palisade and spongy), but not in the epidermis and leaf veins. 5-CQA fluorescence was mainly distributed in vascular bundles and in the cuticle of the abaxial epidermis, and to a lesser extent in some cells of the adaxial epidermis. It was not detected on the adaxial cuticle. Mangiferin fluorescence appeared in all parenchyma cells and in cuticles (adaxial and abaxial).

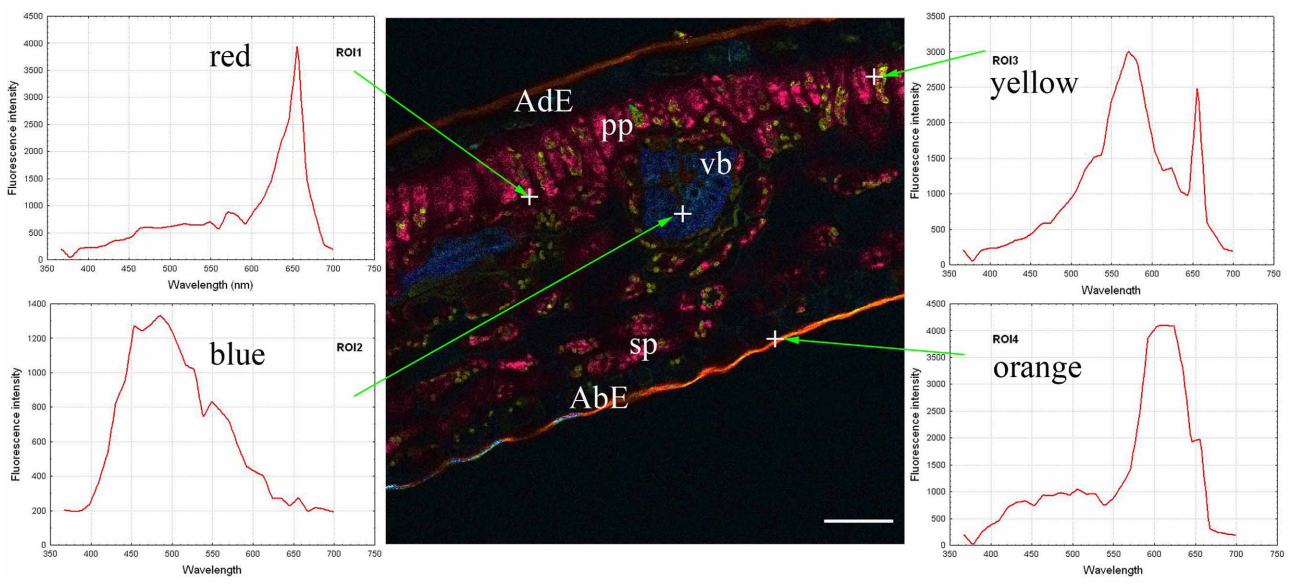

FIGURE 2 | Coded autofluorescence in a *C. arabica* cv. Bourbon leaf blade cross-section observed using a multiphoton microscope at 720 nm excitation. Four spectra emissions were recorded, corresponding to red (ROI1), blue (ROI2), yellow (ROI3) and orange (ROI4) colors, respectively on chloroplasts, vascular bundle, unknow cellular structure and cuticle. AdE, adaxial epidermis; AbE, abaxial epidermis; C, cuticule; PP, palisade parenchyma; SP, spongy parenchyma; VB, vascular bundles. Scale bar = 50 μm

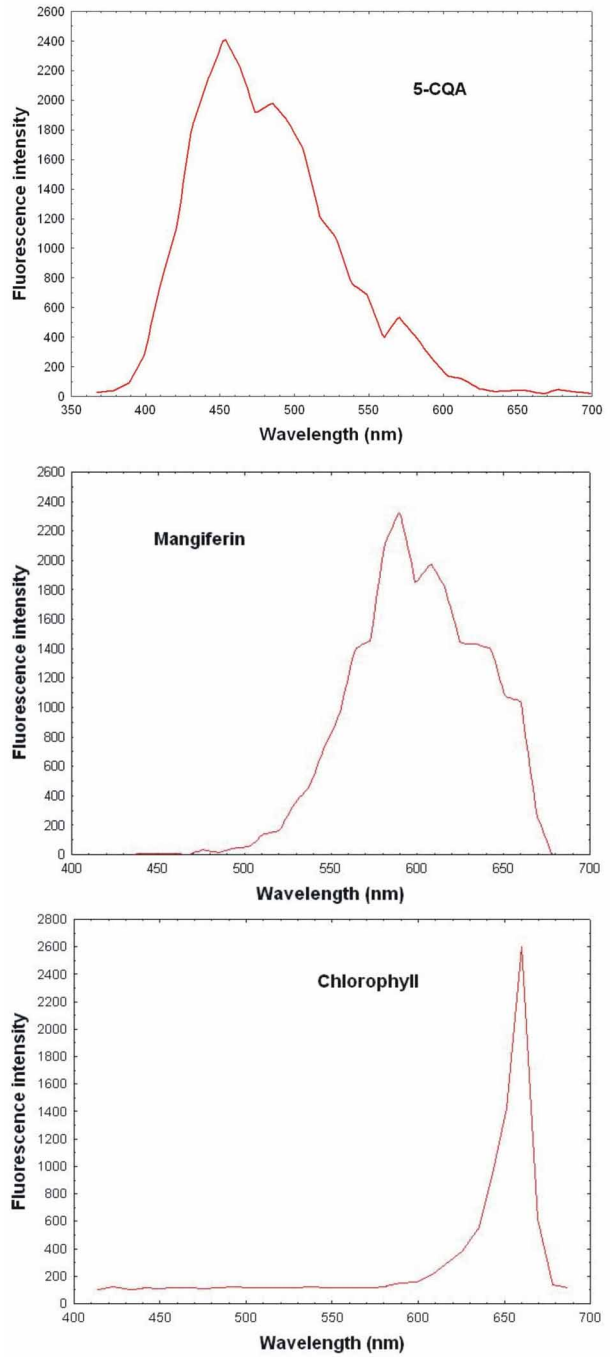

FIGURE 3 | Reference spectrum of controls (5-CQA, chlorophyll, and mangiferin purified porducts) obtained with 720 nm excitation using multiphoton microscope emission from 365 to 700 nm.

HISTOCHEMICAL STRUCTURE VARIATIONS OVER A TIME COURSE IN ARA LEAVES

In very young ARA leaves at the φ2 phase (Lécolier et al., 2009), the classical structure, as seen in **Figure 1**, was not achieved (**Figure 5I**) (see also **Figure BI** in supplementary material). Although the abaxial and adaxial epidermal layers were clearly visible, there was no clear differentiation between palisade and spongy parenchyma. Especially, the absence of clear differentiation characterized the histochemical structure of the leaves. All tissues showed the same blue color in coded autofluorescence (**Figure 5I**). Only the color intensity varied within leaves, thus highlighting the cell boundaries and vacuoles. Spectral analysis using chlorophyll, 5-CQA and mangiferin spectra showed the presence of chlorophyll at a very low level in the parenchyma (**Figure BI,** in supplementary material). Moreover, the three spectra did not explain more than 50% of the fluorescence (intense residual fluorescence). Finally, two main differences characterized the histological distribution of 5-CQA and mangiferin: in the case of 5-CQA, the cell limits were not distinguishable, whereas vacuoles clearly appeared. By contrast, mangiferin was absent from cell walls thus highlighting these latter (**Figure BI** in supplementary material).

The histochemical structure changed very quickly in young leaves over a 4-day period (phase φ3), whereas leaves were always folded at the top of the branch, the classical histochemical structure with two parenchyma (palisade and spongy) became slightly visible (**Figure 5II**). Advanced linear unmixing confirmed the presence of chlorophyll in parenchyma, thus explaining the red zones observed in autofluorescence (see also **Figure BII** in supplementary material). The localisation of 5-CQA in both epidermis was also confirmed. Lastly, mangiferin was also present in vacuoles of both epidermal tissues, but at very low intensity. At maturity, the histochemical structure was definitively acquired, with large intercellular spaces in the spongy parenchyma (**Figure 5III**). The principal effect of age was the lowering of 5-CQA fluorescence in both epidermal layers (**Figure BI,** in supplementary material).

HISTOCHEMICAL COMPARISON BETWEEN SOME COFFEA SPECIES

Histochemical comparison using the advanced linear unmixing process concerned leaves of PSE, EUG, ARA "Bourbon" (ARA) and CAN. In mature leaves, the histochemical structure was similar in the four species (data not shown). This was not the case in young leaves (phase φ3). In this case, two groups of species could be defined, i.e., PSE and EUG vs ARA and CAN. In PSE (**Figure 6I**) and EUG (**Figure 6II**), there was strong histochemical differentiation between adaxial and abaxial epidermal tissues at the vacuole level, based on 5-CQA and mangiferin, respectively (**Figure 6I**). Nevertheless, mangiferin was also present in the spongy parenchyma and, at a lower level, in palisade parenchyma. See also splitted image of PSE leaf in **Figure BII** (supplementary material). In contrast, ARA (**Figure 6III**) and CAN (**Figure 6IV**) did not show mangiferin in adaxial and abaxial epidermal tissues and 5-CQA was strongly present in vacuoles of both of these tissues. In fact, mangiferin was only observable in parenchyma, but as small vesicles.

DISCUSSION

ADVANTAGES AND LIMITS OF THIS NEW IMAGING APPROACH

Spectral analysis, combined with the advanced linear unmixing, provides an efficient tool to localize UV-fluorescent metabolites in living plant tissues. Based on the biochemical results obtained on total leaf extracts, i.e., the strong presence of 5-CQA and

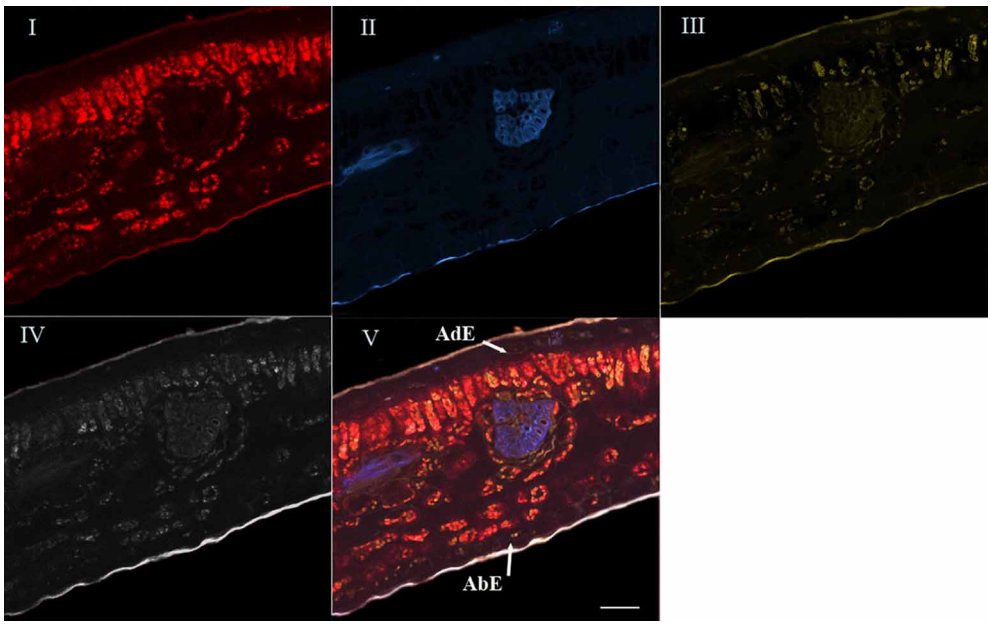

FIGURE 4 | Spectral analysis by linear unmixing method using chlorophyll, 5-CQA and mangiferin spectra. Merged image V was splitted into four base images (I, II, III, and IV). Base image I showed histolocalization of chlorophyll, whereas base images (II) and (III) represented histolocalization of 5-CQA and mangiferin, respectively. Finally, base image (IV) depicted other fluorescent compounds (residual fluorescence). AdE, adaxial epidermis; AbE, abaxial epidermis; Scale bar = 50 μm.

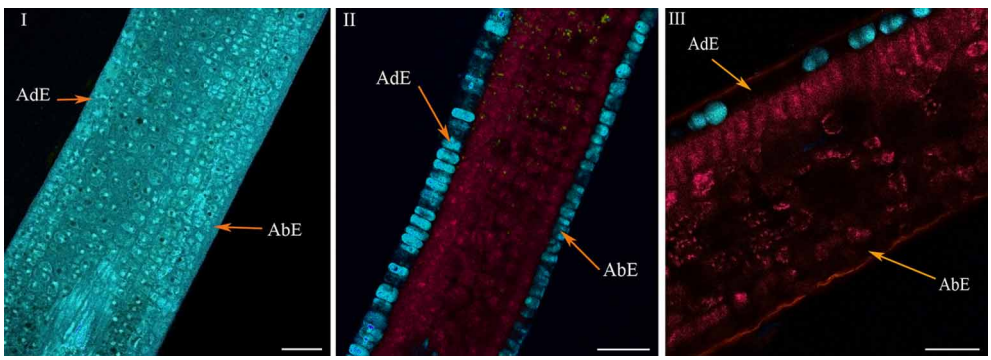

FIGURE 5 | Histochemical structure of ARA (*C.arabica* cv. Bourbon) leaves at very young (I), young (II), and mature (III) stages. All these spectral images showed autofluorescence obtained using a multiphoton microscope at 720 nm excitation. AdE, adaxial epidermis; AbE, abaxial epidermis. Scale bar = 50μm.

mangiferin (Campa et al., 2012), the imaging method allowed their spatial localization in mature and young leaves of several *Coffea* species.

The main advantage of this histological approach was the possibility of reaching intact internal tissues within the cross-section. Images were acquired from selected nascent intact cells and tissues far from superficial layers containing damaged and oxidized cells due to cutting. Consequently, and contrary to standard methods using the Neu's reagent, the superficial oxidation of phenols had no effect on the images. The second advantage was the possibility of localizing, at the tissular and cellular level, a particular chemical species characterized by its own emission spectrum. For example, Neu's reagent cannot discriminate between the different types of phenol, whereas the imaging method permitted specific localization of 5-CQA. Moreover, the method does not require any previous extraction of chlorophyll or other pigments. Especially, as mentioned by Zimmermann et al. (2003) and Berg (2004), spectral imaging, combined with advanced linear unmixing, is a powerful method to simultaneously localize several metabolites showing overlapped spectra.

Nevertheless, some caution is required in the interpretation. As any powerful method, the use of spectral imaging combined with linear unmixing has some limits that must be taken in consideration for image interpretation. For example, if metabolites such as isomers or dimers have similar UV-fluorescent spectra, their specific localization is not possible. This was the case for diCQA (dimer of 5-CQA) that had the same spectral signature than 5-CQA. In such situation results coming from biochemical

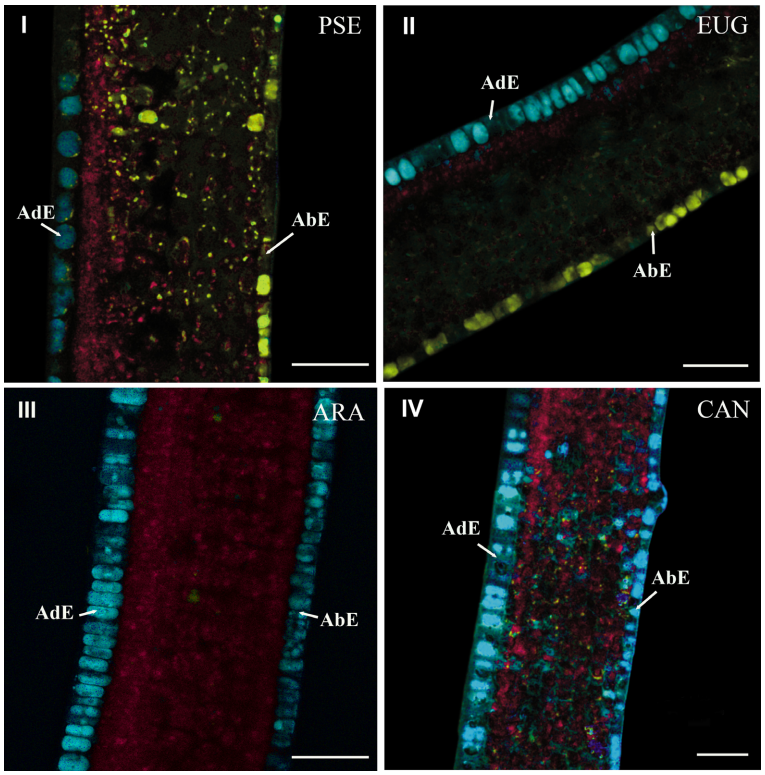

FIGURE 6 | Cross-sections of young leaves of PSE (*C. pseudozanguebariae*) (I), EUG (*C. eugenioides*) (II), ARA (*C. Arabica* "Bourbon") (III) and CAN (*C. canephora*) (IV). The advanced linear unmixing process was carried out using chlorophyll, 5-CQA and mangiferin reference spectra. AdE, adaxial epidermis; AbE, abaxial epidermis. Scale bar = 50μm.

analysis must be considered to support image interpretation. In our study, it was only because quantification by HPLC showed that 5-CQA represented more than 80% of total HQA in mature ARA whose blue zones shown in **Figure 4II** could mainly reflect the 5-CQA localization.

In fact, the present localization of the 5-CQA by spectral analysis could concern both CQA and diCQA which in young leaves constitutes most of HQA. This problem is also true for classical histochemical analysis using Neu's reagent. Nevertheless, the advantages of spectral analysis, as discussed above, were still relevant. Lastly, the absence of HQA or mangiferin in a tissue or cell was an important result. Indeed, spectral imaging allows detection of very low content. This was the case when visualizing 3-CQA and 4-CQA in Sigma-Aldrich powder of 5-CQA, but also using a dilution gradient (data not shown).

PRACTICAL APPLICATION OF SPECTRAL ANALYSIS TO REVEAL THE HISTOCHEMICAL LEAF STRUCTURE AND FOR BETWEEN SPECIES COMPARISONS

The very rapid change in the histochemical leaf structure was the first novel result of the study. In less than 3 days, leaves developed from phase φ2 to phase φ3 (Lécolier et al., 2009) and their histochemical structure changed substantially. Beyond phase φ3, the histological structure was slightly modified and this concerned the spongy parenchyma. In parallel, the blue intensity decreased markedly in both epidermal tissues. This evolution from phase φ3 to leaf maturity has already been observed in CAN using HPLC (Mondolot et al., 2006). In young leaves (phase φ3), 5-CQA and diCQA contents were found to be 2.94 and 2.75% dry matter basis (dmb), respectively, whereas they were 0.58% and 0.14% dmb in mature leaves, respectively.

The differences in 5-CQA and mangiferin histolocalizations between species represented the second novel result of this study. The strong presence of mangiferin in young leaves of PSE was confirmed (Talamond et al., 2008, 2011; Campa et al., 2012). In these leaves (phase φ3), the mangiferin content was 8.6% dmb and decreased up to 5.6% dmb in mature leaves (Campa et al., 2012). Mangiferin has also been localized using UV epifluorescence microscopy (Talamond et al., 2011; Campa et al., 2012). The present results showed a more precise histolocalization of mangiferin in small vesicles of the parenchyma and in vacuoles of the abaxial epidermis, but not in the adaxial epidermis. Conversely, 5-CQA was only localized in the abaxial epidermis. 5-CQA was most abundant and constituted an important reservoir of phenols but its role has not yet been clearly defined. This compound could have at least two different functions, being involved in lignin synthesis, producing the precursor of the lignin structure (guaiacyl and syringyl units), while also being a protective agent against UV or aggressors (Hoffmann et al., 2003). Further experiments are under way to substantiate these assumptions.

The second important result was obtained through the species comparison, highlighting similarities between PSE and EUG, and between CAN and ARA. As EUG and CAN are maternal and paternal parents of ARA (Lashermes et al., 1999), respectively, our work clearly highlighted the paternal origin of the histochemical structure of ARA leaves.

ACKNOWLEDGMENTS

This study was financially supported by the European Union, the Conseil Régional of Réunion and the French Institut pour la Recherche et le Développement (IRD).

SUPPLEMENTARY MATERIAL

The Supplementary Material for this article can be found online at: http://www.frontiersin.org/journal/10.3389/fpls.2014.00039/abstract

Figure A | Chemical structures of 5-CQA and mangiferin.

Figure B | (I) Spectral analysis by linear unmixing method using 5-CQA, mangiferin and chlorophyll spectra on ARA (*C. Arabica* "Bourbon") very young leaf splitted image. **(II)** Spectral analysis by linear unmixing method using 5-CQA, mangiferin and chlorophyll on PSE (*C. pseudozanguebariae*) leaf: splitted image.

REFERENCES

Berg, R. H. (2004). Evaluation of spectral imaging for plant cell analysis. *J. Microsc.* 214, 174–181. doi: 10.1111/j.0022-2720.2004.01347.x

Bertrand, C., Noirot, M., Doulbeau, S., de Kochko, A., Hamon, S., and Campa, C. (2003). Chlorogenic acid content swap during fruit maturation in coffea pseudozanguebariae. qualitative comparison with leaves. *Plant Sci.* 165, 1355–1361. doi: 10.1016/j.plantsci.2003.07.002

Campa, C., Mondolot, L., Rakototondravao, A., Bidel, L. P. R., Gargadennec, A., Couturon, E., et al. (2012). A survey of mangiferin and hydroxycinnamic acid ester accumulation in coffee (*Coffea*) leaves: biological implications and uses. *Ann. Bot.* 110, 595–613. doi: 10.1093/aob/mcs119

Clifford, M. N. (1985). "Chlorogenic acids," in *Coffee Chemistry,* Vol. 1, eds R. J. Clarke and R. Macrae (London: Elsevier ASP Ltd), 153–202.

Dedecca, D. M. (1957). Anatomia e desenvolvimento ontogenético de *Coffea arabica L.* var. typica Cramer. *Bragantia* 16, 315–367. doi: 10.1590/S0006-87051957000100023

Garini, Y., Young, I. T., and McNamara, G. (2006). Spectral imaging principles and applications. *Cytometry* 69, 735–747. doi: 10.1002/cyto.a.20311

Hoffmann, L., Maury, S., Martz, F., Geoffroy, P., and Legrand, M. (2003). Purification, cloning, and properties of an acyltransferase controlling shikimate and quinate ester intermediates in phenylpropanoid metabolism. *J. Biol. Chem.* 278, 95–103. doi: 10.1074/jbc.M209362200

Hutzler, P., Fischbach, R., Heller, W., Jungblut, T. P., Reuber, S., Schmitz, R., et al. (1998). Tissue localization of phenolic compounds in plant by confocal laser scanning microscopy. *J. Exp. Bot.* 49, 953–965. doi: 10.1093/jexbot/49.323.953

Jones, R., Ougham, H., Thomas, H., and Waaland, S. (2013)."Environmental interactions," in *The Molecular Life of Plants,* eds R. John, H. Ougham, H. Thomas, and S. Waaland (Oxford: John Wiley and Sons Ldt), 534–582.

Ky, C. L., Louarn, J., Dussert, S., Guyot, B., Hamon, S., and Noirot, M. (2001). Caffeine, trigonelline, chlorogenic acids and sucrose diversity in wild *Coffea arabica* L. and *C. canephora* P. accessions. *Food Chem.* 75, 223–230. doi: 10.1016/S0308-8146(01)00204-7

Lashermes, P., Combes, M. C., Robert, J., Trouslot, P., D'Hont, A., Anthony, F., et al. (1999). Molecular characterization and origin of the *Coffea arabica* L. genome. *Mol. Gen. Genet.* 261, 259–266. doi: 10.1007/s004380050965

Lécolier, A., Noirot, M., Escoute, J., Chrestin, H., and Verdeil, J. L. (2009). Early effects of the mutation *laurina* on the shoot apex functioning of coffee tree and analysis of the plastochron phases: relationships with the dwarfism of leaves. *Trees* 23, 673–682. doi: 10.1007/s00468-008-0311-y

Mondolot, L., La Fisca, P., Buatois, B., Talansier, E., de Kochko, A., and Campa, C. (2006). Caffeoylquinic acid content and histolocalization in *Coffea canephora* developing leaves. *Ann. Bot.* 98, 33–40. doi: 10.1093/aob/mcl080

Neu, R. (1956). A new reagent for differentiating and determining flavones on paper chromatograms. *Naturwissenschaften* 43, 82. doi: 10.1007/BF00631858

Saadi, A., Lempereur, I., Sharonov, S., Autranb, J. C., and Manfaita, M. (1998). Spatial distribution of phenolic materials in durum wheat grain as probed by confocal fluorescence spectral imaging. *J. Cereal Sci.* 28, 107–117. doi: 10.1006/jcrs.1998.0195

Talamond, P., Conéjéro, G., Verdeil, J. L., and Poëssel, J. L. (2011). Isolation of *C*-glycosyl xanthones from *Coffea pseudozanguebariae* and their location. *Nat. Prod. Comm.* 6, 1885–1888.

Talamond, P., Mondolot, L., Gargadennec, A., de Kochko, A., Hamon, S., and Campa, C. (2008). First report on mangiferin (*C*-glucosyl-xanthone) isolated from leaves of a wild coffee plant, *Coffea pseudozanguebariae* (Rubiaceae). *Acta Bot. Gall.* 155, 513–516. doi: 10.1080/12538078.2008.10516130

Zimmermann, T., Rietdorf, J., and Pepperkok, R. (2003). Spectral imaging and its application in live cell microscopy. *FEBS Lett.* 546, 87–92. doi: 10.1016/S0014-5793(03)00521-0

Conflict of Interest Statement: The authors declare that the research was conducted in the absence of any commercial or financial relationships that could be construed as a potential conflict of interest.

Received: 29 November 2013; accepted: 28 January 2014; published online: 18 February 2014.

*Citation: Conéjéro G, Noirot M, Talamond P and Verdeil J-L (2014) Spectral analysis combined with advanced linear unmixing allows for histolocalization of phenolics in leaves of coffee trees. Front. Plant Sci. **5**:39. doi: 10.3389/fpls.2014.00039*

This article was submitted to Plant Cell Biology, a section of the journal Frontiers in Plant Science.

Copyright © 2014 Conéjéro, Noirot, Talamond and Verdeil. This is an open-access article distributed under the terms of the Creative Commons Attribution License (CC BY). The use, distribution or reproduction in other forums is permitted, provided the original author(s) or licensor are credited and that the original publication in this journal is cited, in accordance with accepted academic practice. No use, distribution or reproduction is permitted which does not comply with these terms.

frontiers in
PLANT SCIENCE

METHODS ARTICLE
published: 23 April 2014
doi: 10.3389/fpls.2014.00140

An update: improvements in imaging perfluorocarbon-mounted plant leaves with implications for studies of plant pathology, physiology, development and cell biology

George R. Littlejohn[1]*, Jessica C. Mansfield[2], Jacqueline T. Christmas[3], Eleanor Witterick[1], Mark D. Fricker[4], Murray R. Grant[1], Nicholas Smirnoff[1], Richard M. Everson[3], Julian Moger[2] and John Love[1]*

[1] Division of Plant and Microbial Sciences, School of Biosciences, University of Exeter, Exeter, UK
[2] School of Physics, University of Exeter, Exeter, UK
[3] Computer Science, University of Exeter, Exeter, UK
[4] Department of Plant Sciences, University of Oxford, Oxford, UK

Edited by:
Markus Schwarzländer, University of Bonn, Germany

Reviewed by:
Viktor Zarsky, Charles University, Czech Republic
Jin-Long Qiu, Institute of Microbiology – Chinese Academy of Sciences, China
David C. Logan, Université d'Angers, France

***Correspondence:**
George R. Littlejohn and John Love, Division of Plant and Microbial Sciences, School of Biosciences, University of Exeter, Geoffrey Pope Building, Stocker Road, Exeter EX4 4QD, UK
e-mail: G.R.Littlejohn@exeter.ac.uk; j.love@exeter.ac.uk

Plant leaves are optically complex, which makes them difficult to image by light microscopy. Careful sample preparation is therefore required to enable researchers to maximize the information gained from advances in fluorescent protein labeling, cell dyes and innovations in microscope technologies and techniques. We have previously shown that mounting leaves in the non-toxic, non-fluorescent perfluorocarbon (PFC), perfluorodecalin (PFD) enhances the optical properties of the leaf with minimal impact on physiology. Here, we assess the use of the PFCs, PFD, and perfluoroperhydrophenanthrene (PP11) for *in vivo* plant leaf imaging using four advanced modes of microscopy: laser scanning confocal microscopy (LSCM), two-photon fluorescence microscopy, second harmonic generation microscopy, and stimulated Raman scattering (SRS) microscopy. For every mode of imaging tested, we observed an improved signal when leaves were mounted in PFD or in PP11, compared to mounting the samples in water. Using an image analysis technique based on autocorrelation to quantitatively assess LSCM image deterioration with depth, we show that PP11 outperformed PFD as a mounting medium by enabling the acquisition of clearer images deeper into the tissue. In addition, we show that SRS microscopy can be used to image PFCs directly in the mesophyll and thereby easily delimit the "negative space" within a leaf, which may have important implications for studies of leaf development. Direct comparison of on and off resonance SRS micrographs show that PFCs do not to form intracellular aggregates in live plants. We conclude that the application of PFCs as mounting media substantially increases advanced microscopy image quality of living mesophyll and leaf vascular bundle cells.

Keywords: perfluorocarbon, *Arabidopsis*, multi-photon, confocal, microscopy, imaging, perfluoroperhydrophenanthrene

INTRODUCTION

Advances in microscopy have made *in vivo* biological imaging increasingly important in recent years. A diverse palette of chemical labels and genetically encoded fluorescent reporters and biosensors, coupled with advanced microscopy techniques, including laser scanning confocal microscopy (LSCM), two-photon fluorescence (TPF) microscopy and label-free imaging techniques such as second harmonic generation (SHG) microscopy and stimulated Raman scattering (SRS) microscopy have enabled unprecedented analysis of living cell dynamics (Shaw and Ehrhardt, 2013). Despite these technical advances, tissues that are rich in airspaces, such as those of plant leaves or animal lungs, remain difficult to image because of the optical aberrations that result from the complex structure of such tissues. As these tissues are typically sites of active metabolism and often targets for pathogens, it is essential to develop relatively simple *in vivo* methods to circumvent these imaging problems.

The spongy mesophyll of higher plant leaves is located adjacent to the lower epidermis, contains numerous airspaces and may be several cell layers thick (**Figure 1A**). These characteristics result in light refraction within the mesophyll and a progressive attenuation of light transmission through the tissue, producing optical aberrations that impair confocal image quality (Feijó and Moreno, 2004; Inoue, 2006; Cheng, 2006). When examining fixed leaves these aberrations are minimized because the fixatives infiltrate the tissue and minimize the optical phase transitions within. Previously, we have shown that it is possible to infiltrate living leaves with perfluorodecalin (PFD, **Figure 1B**) and thereby significantly improve the resolution of LCSM images of the mesophyll while affecting only minimally cellular physiology (Littlejohn et al., 2010). We

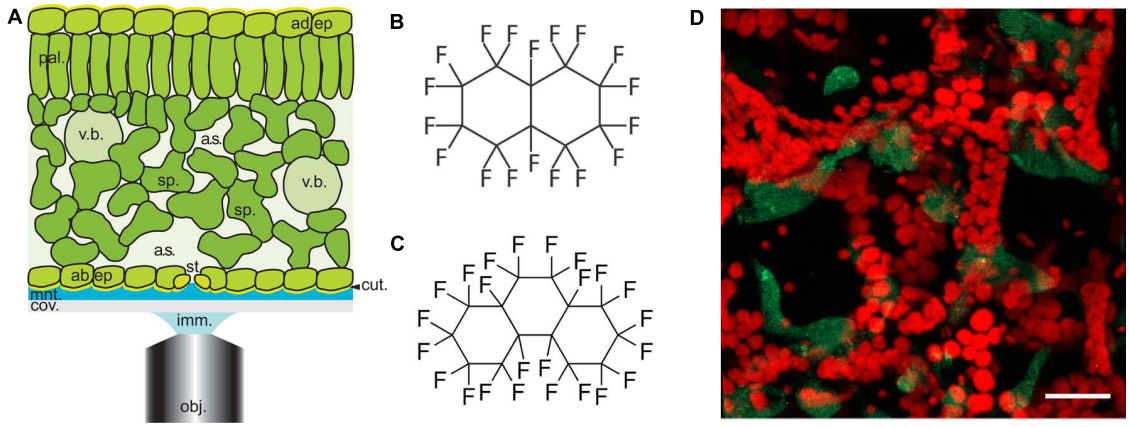

FIGURE 1 | *Arabidopsis* leaf anatomy, chemical structures of perfluorocarbons used in this study and a typical image of *Pseudomonas* infected leaves. (A) Diagrammatical representation showing the anatomical features of the *Arabidopsis* leaf in relation to the optical set-up. Abbreviations used are obj, objective lens; imm, immersion fluid; cov, coverslip; mnt, mountant; cut, cuticle; ad. ep, adaxial epidermis; st, stomatal pore; sp, spongy mesophyll; a.s, airspace; pal, palisade mesophyll; v.b, vascular bundle; ad. ep, adaxial epidermis. Cell walls are indicated by black lines (reproduced with permission from Littlejohn and Love, 2012). **(B,C)** chemical structures of **(A)** PFD and **(B)** PP11. **(D)** Z-stack reconstruction of GFP-expressing *Pseudomonas syringae* pv. tomato DC3000 infected *Arabidopsis* leaf. GFP signal is shown in green and chlorophyll autofluorescence in red. Scale bar is 25 μm.

have had numerous positive reports from users of PFD and some studies have now been published (Johnson et al., 2011; Knapp et al., 2012; Tschiersch et al., 2012; Carrión et al., 2013; Gest et al., 2013; Hoepflinger et al., 2013; Hutt et al., 2013; Mansfield et al., 2013; Wright et al., 2013).

In this paper, we report that the optical qualities of plant mesophyll can be further improved by infiltration with perfluoroperhydrophenanthrene (PP11, **Figure 1C**), a perfluorocarbon (PFC) that has a refractive index that is better matched to that of living cells. To measure the improvement in image quality more objectively, we developed a method of autocorrelation that quantifies the sharpness of the images acquired at varying depths within the leaf. Finally, using SRS microscopy we have shown that both PFD and PP11 are undetectable in living cells, but infiltrate the mesophyll airspaces homogenously. Furthermore, SRS imaging of PFCs *in vivo* may be used to delimit the "negative space" within plant leaves, i.e., the area within the leaf that is involved in gaseous exchange and pathogen invasion. We have advocated the application of PFC mounting of samples to studies of pathogenesis in plants and experiments to date are promising. For example, **Figure 1D** shows an example image of an *Arabidopsis thaliana* leaf infected with the pathogenic bacterium, *Pseudomonas syringae* pv. tomato (DC3000 expressing GFP), taken under the same conditions as those used in Hutt et al. (2013).

MATERIALS AND METHODS

PLANT CULTURE AND SAMPLE MOUNTING

Arabidopsis thaliana (Col-0 ecotype) and transformants that stably and constitutively express a cytoplasmically localized "Venus" yellow fluorescent protein (SEYFP-F46L; Nagai et al., 2002) were used in this study. Seeds were surface sterilized for 3 min with 70% ethanol and then for 5 min with 10% sodium hypochlorite. Seeds were washed five times in water and suspended in 0.1% agar. Seeds were stratified at 4°C, in the dark, for 48 h before being sown on compost and grown at 20°C, in a 16 h/8 h light/dark photoperiod.

Mature leaves were excised from plants aged approximately 3-weeks and sections floated in H_2O, PFD, or PP11 for 5 min according to the methods described in Littlejohn et al. (2010), Littlejohn and Love (2012). Samples were mounted in the same medium and imaged by LSCM, TPF, SHG, and SRS microscopy.

LSCM IMAGING

Confocal imaging was performed using a Zeiss Axiovert 510 Meta LSCM equipped with a 40x/1.30 oil DIC immersion C-Apochromat lens. Immersion medium was Zeiss immersol. Light paths and wavelengths were controlled by a 458/514 nm dichroic mirror. The pinhole was set at 70 μm. Images were integrated and processed using Zeiss 510 software. Images of Venus and chlorophyll fluorescence in intact *Arabidopsis* leaves were collected with excitation at 514 nm using a 30 mW argon laser, 6.1 A, 21.8% transmission intensity. Emission was recorded at 518–604 nm for Venus and at 647–690 nm for chlorophyll. Z-stacks containing 100 z-planes taken with 1 μm step size were collected for each of five samples incubated in PFD, PP11, or H_2O for 5 min before imaging and mounted in the same medium for imaging. Figures were assembled in Adobe Indesign. **Figure 2** LSCM images were generated by using the "cut" function in Zeiss LSM Image Browser software, where the plane presented represents a cut through the entire z-stack from top to bottom taken at an angle of −24°. The images therefore show a progression through the stack from top to bottom. Single z-planes are presented in **Figure 3**. GFP-expressing *Pseudomonas* (made according to Lambertsen et al., 2004) and chlorophyll shown in **Figure 1D** were excited respectively with 488 and 633 nm laser lines and emission captured from 505 to 570 nm (GFP)

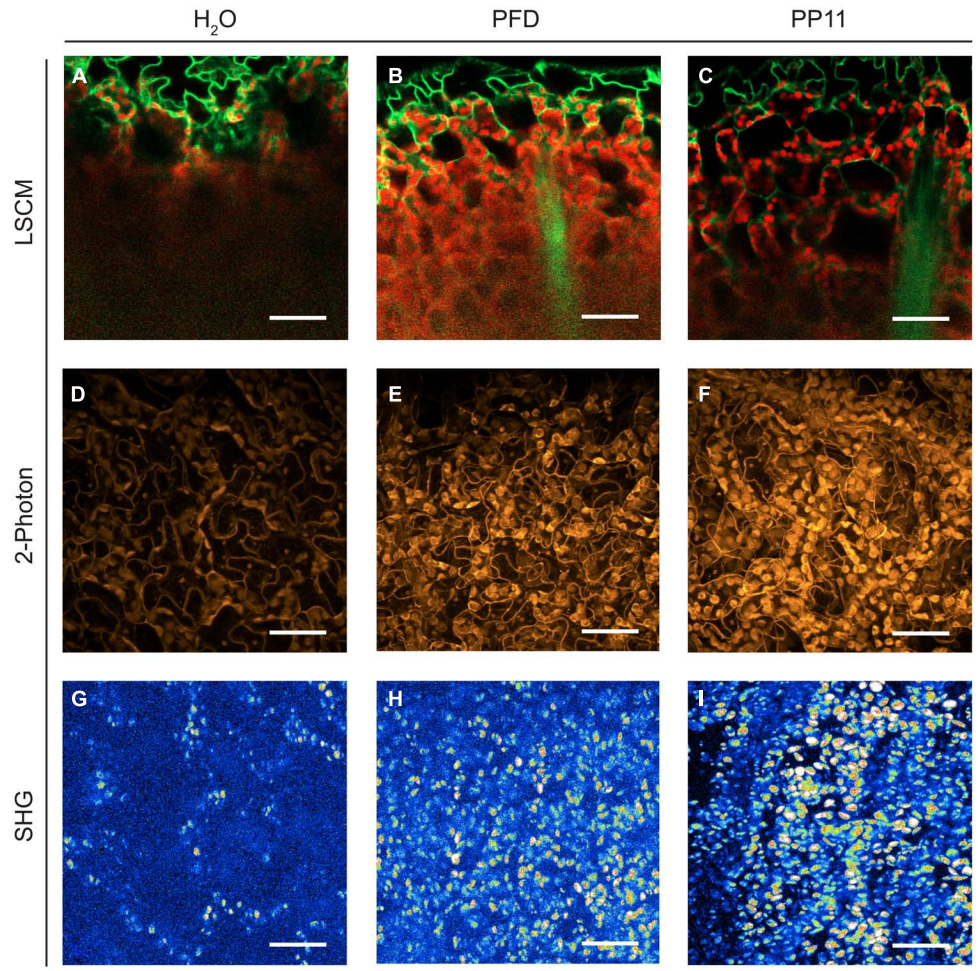

FIGURE 2 | Perfluorocarbon mounting media used with three modes of microscopy. (A–C) LSCM images captured from 1 μm resolution Z-stacks taken of samples mounted in H_2O, PFD and PP11 respectively. Images were generated by using the "cut" function in Zeiss LSM Image Browser software, where the plane presented represents a cut through the entire z-stack from top to bottom taken at an angle of −24°. The images therefore show a progression through the stack from top to bottom. Signal was collected from 518 to 604 nm for Venus, and is displayed in green and at 647–690 nm for chlorophyll, shown in red. **(D–F)** 2-photon micrographs taken of samples mounted in H_2O, PFD, and PP11 respectively. **(G–I)** SHG micrographs taken of samples mounted in H_2O, PFD, and PP11 respectively. **(D–I)** are presented as projections of z-stacks. Scale bars are 50 μm.

and 647–711 nm (chlorophyll). The GFP-*Pseudomonas* Z-stack projected in **Figure 1D** was 30 μm deep, with a 0.25 μm step size and was captured with a C-Apochromat 63x/1.2W Corr M27 lens. The projection was made in Zeiss LSM510 software.

RAMAN SPECTROSCOPY

Prior to SRS imaging the Raman spectra of the PFCs were obtained using a Renishaw RM100 Raman microscope (Renishaw plc, UK), with a 785 nm diode laser and 1200 line/mm spectral grating, giving a spectral resolution of 1 cm^{-1}.

STIMULATED RAMAN SCATTERING MICROSCOPY

Stimulated Raman scattering microscopy required two, pulsed laser beams; one at a longer wavelength (Stokes beam) and the other at a shorter wavelength (pump beam). The difference between the wavelengths of the pulsed lasers was tuned to correspond to the energy of a Raman vibration of interest. In our system a 1064 nm pico-second laser (PicoTrain HighQ laser) provided the Stokes beam and the output from an optical parametrical oscillator OPO (Levante Emerald APE) – pumped by the frequency doubled output of the picoTrain laser – provided the pump beam. The pump beam was tuned to a wavelength of 991.4 nm, which excited the C–F vibrations at 687.5 cm^{-1}.

The amplitude of the Stokes beam was modulated at 1.7 MHz using an EOM. When SRS occurred within the sample, a modulated decrease in pump beam intensity [stimulated Raman loss; Moger et al. (2012)] was detected.

A modified laser scanning confocal microscope (Fluoview 300 IX71 Olympus) was used for imaging the SRS. The objective was a 60x 1.2 NA water immersion objective (UPlanS Apo Olympus). The transmitted light from the sample was collected with a 60x 1.0 NA water-dipping condenser and detected using a photo-diode

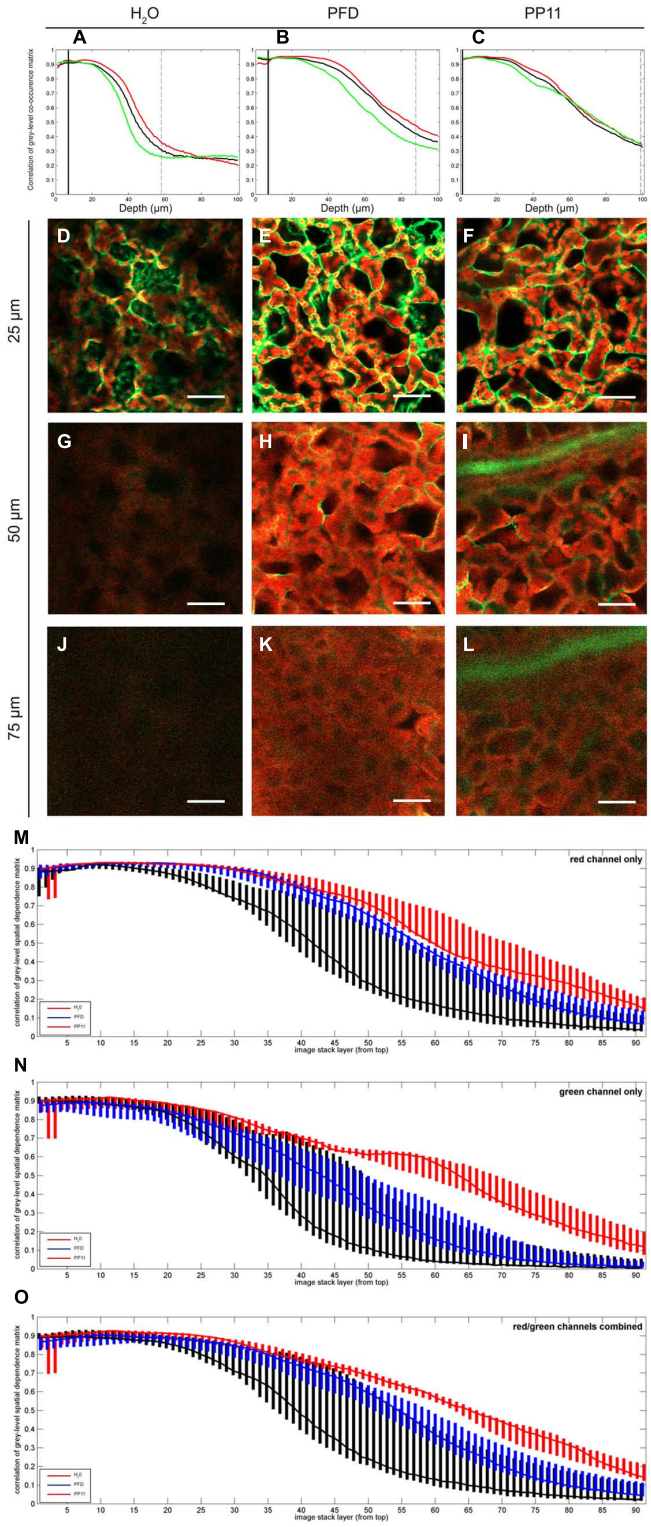

FIGURE 3 | Quantification of image deterioration with depth. **(A–C)** typical autocorrelation results for single samples mounted in H_2O, PFD, and PP11 respectively and imaged as z-stacks 100 µm deep. **(D–F)** representative images taken at a depth of 25 µm from samples mounted in H_2O, PFD, and PP11 respectively **(G–I)** representative images taken at a depth of 50 µm from samples mounted in H_2O, PFD, and PP11 respectively. Signal was collected from 518 to 604 nm for Venus, and is displayed in green and at 647–690 nm for chlorophyll, shown in red. **(J–L)** representative images taken at a depth of 75 µm from samples mounted in H_2O, PFD, and PP11 respectively. **(M–O)** range and median plotted for all samples (n=5) mounted in H_2O, PFD, or PP11 for red, green, and total signal respectively. Scale bars are 50 µm.

with a 70 V reverse bias (FDS1010 thorlabs). The 1064 nm Stokes beam was blocked from reaching the photo-diode using a band pass filter coherent anti-Raman scattering (CARS; 890/220 nm, Chroma technologies). A lockin amplifier was used to separate out the modulated SRL signal and the output from this was connected to the computer and imaging software. Raman Image stacks were acquired at a 512 × 512 pixel resolution and a 256 μm × 256 μm scan area with 1 μm separation between optical slices.

TWO-PHOTON FLUORESCENCE AND SECOND HARMONIC GENERATION MICROSCOPY

Two-photon fluorescence and SHG were performed using the customized microscope described above. Excitation was provided by mode-locked femtosecond Ti:sapphire oscillator (Mira 900D; Coherent, USA) which produced 100-fs pulses at 76 MHz. The central wavelength of the fs beam was 800 nm with an average power at the sample of 5–30 mW. TPF and SHG were spectrally separated from the 800 nm excitation beam by a dichroic mirror (670dcxr; Chroma Technologies). After this, different bandpass filters were used to enable either TPF signal (CG-BG-39-1.00-1 and F70-500-3-PFU; CVI Melles Griot, UK) or SHG signal (F10-400-5-QBL; CVI Melles Griot, UK) to reach the Hamamatsu R3896 photomultiplier tube.

QUANTIFICATION OF IMAGE CLARITY IN THE Z-AXIS

The clarity of each image in relation to its position in the z-axis (i.e., into the tissue) was quantified using textural analysis. For each image, the "green" and "red" color channels were analyzed separately and in combination. A gray-scale spatial dependence matrix (Haralick et al., 1973), labeled "M," was constructed from the intensities (ranging from 0 to 255) of each pixel that composed each image and for each channel. The element $M_{r,c}$, at row r and column c of this matrix is a count of how many times a pixel with intensity r has a pixel of intensity c in its immediate neighborhood, defined as the 8 pixels surrounding the measured pixel. Normalizing this matrix resulted in a set of joint probabilities of pixels with intensities r and c within the neighborhood. The correlation value associated with this normalized matrix (see Haralick et al., 1973) gives a measure of how closely correlated the intensity of a given pixel is with those of its neighboring pixels. The correlation measure was calculated for each image in acquired z-stacks, 100 μm deep, with a 1 μm z-resolution for leaves mounted in H_2O, PP11 and PFD stacks, and separately for the red, green, and combined red/green channels.

RESULTS

PERFLUOROCARBON MOUNTING MEDIA IMPROVE THE OPTICAL RESOLUTION OF DIFFERENT MODES OF LASER SCANNING MICROSCOPY

We compared the image resolution of micrographic z-stacks acquired using LSCM, TPF, and SHG microscopy (**Figure 2**). TPF and SHG are non-linear optical techniques, which involve the simultaneous absorption of two or more photons. All these techniques are intrinsically confocal and generally use infra-red lasers instead of visible or UV lasers to excite fluorophores (Nandakumar et al., 2009). These techniques are considered advantageous compared to single-excitation confocal microscopy because they can deliver improved imaging depths within scattering tissues and reduced photodamage within samples.

Two-photon fluorescence is similar to single photon fluorescence, but it requires the simultaneous absorption of two near infra-red photons, rather than a single UV or visible spectrum photon, to generate a fluorescent signal (Diaspro and Sheppard, 2002).

Second harmonic generation involves the simultaneous absorption of two near infra-red photons and the emission of a single visible photon with half the wavelength of the infra-red photons. This process only occurs in structures which lack inversion symmetry. In plant tissues these structures include cellulose and starch grains (Mizutani et al., 2000; Brown et al., 2003; Cox et al., 2005).

Under all modes of microscopy tested, PP11 and PFD outperformed H2O as an *in vivo* mounting medium, by infiltrating the mesophyll airspaces and smoothing the optical transitions within the mounted leaves. Moreover, we noted that PP11 outperformed PFD, which we ascribe to the refractive index of PP11 being closer to that of living cells compared to PFD. We were routinely able to acquire images from a depth of 100–135 μm within the leaf by LSCM and two photon imaging using PP11 as a mounting medium, which is greater than half the thickness of a leaf of a 3 week-old *Arabidopsis* plant and tests in with rice leaves allow imaging through the entire thickness of the leaf. The use of PFCs as a mounting medium also allowed the acquisition of SHG signals from chloroplast starch, which was not possible for samples mounted in H2O. This may, in itself, represent an important technique for the study of starch in leaves and statoliths in root cells.

To quantify the apparent advantage of using PFC mounting media to image within the mesophyll, we performed autocorrelation analysis on LSCM micrographs acquired at varying depths in *Arabidopsis* leaves. In this case, the fluorescence emission for both cytoplasmically localized Venus (Nagai et al., 2002) and chlorophyll were recorded. The pixel-by-pixel autocorrelation enabled an objective quantification of image quality. Using this method, we noted a wavelength-dependent improvement in resolution when samples were mounted in PFCs, compared to H_2O (**Figure 3**). Images recorded deeper in the sample are more greatly affected by noise, which tends to be uncorrelated, and hence the correlation measure is low compared with the crisper images recorded closer to the surface. Median values for the autocorrelation demonstrate that PP11 and PFD outperform H_2O and PP11 performs better than PFD, with a greater benefit seen in imaging Venus, compared with chlorophyll (**Figures 3M–O**). Most interestingly, the use of PFCs as mounting medium reduced the range of autocorrelation values obtained, showing that the images acquired when samples are mounted in PFD or in PP11 are not only clearer, but more consistent between replicate samples.

Normal cytoplasmic streaming and chloroplast movement was observed in all the experiments performed in this investigation, which is consistent with previous observations that the use of PFCs has a minimal effect on leaf physiology compared to mounting leaf samples in H_2O (Littlejohn et al., 2010). This is also evidenced by the differences in chloroplast position seen between z-stacks represented in **Figures 4G–J**.

STIMULATED RAMAN SCATTERING IMAGING OF PERFLUOROCARBON DISTRIBUTION

TPF and SHG and SRS are non-linear optical techniques, which involve the simultaneous absorption of two or more photons. All these techniques are intrinsically confocal and generally use infrared lasers instead of visible or UV lasers to excite fluorophores.

Stimulated Raman scattering is a chemical-specific technique which relies on stimulating Raman active molecular bond vibrations. SRS requires stimulation by two laser beams at different wavelengths (pump and Stokes beams), with the difference in wavelength between the two beams set to correspond to the energy of the molecular bond vibration of interest. When this condition is met, SRS occurs and results in a loss of intensity in the higher energy pump beam (stimulated Raman loss) and an equal increase in intensity in the Stokes beam (stimulated Raman gain). This process is detected by modulating one of the beams and detecting the modulations in intensity in the second beam using a lockin amplifier (Freudiger et al., 2008).

Perfluorocarbons readily infiltrate leaf airspaces. To ascertain whether PFCs remain localized in the airspaces of the mesophyll or are capable of also penetrating living cells, we imaged the PFC distribution in infiltrated *Arabidopsis* leaves using SRS. Prior to imaging, we demonstrated that Raman spectra may be used to identify specific peaks, which allow the C–F bonds in the PFC and the C–H bonds found in *Arabidopsis* surface waxes, in cellulose and in β-1-3-glucan to be easily distinguished (**Figures 4A–D**). PFC mounting media are therefore compatible with Raman-based imaging of biological molecules (**Figures 4E,F**). Images of the "ON" and "OFF resonance confirmed that PFCs was homogeneously distributed in the airspaces between mesophyll cells (Littlejohn et al., 2010). However, the sensitivity of this technique enables us also to confirm that PFCs do not appear to form intracellular aggregates, and are therefore unlikely to penetrate beyond the apoplast into the protoplasm (**Figures 4G–J**). From a structural perspective, SRS imaging of PFC distribution in leaves has the added advantage of delimiting the mesophyll airspaces, potentially enabling a more intricate understanding and modeling of gas flow dynamics in leaves. The chloroplasts appear in both the on and off resonance SRS images due to their strong two-photon absorption (TPA). In this process they are absorbing one photon originating from the pump beam (either 991 or 989 nm on or off resonance) and one photon

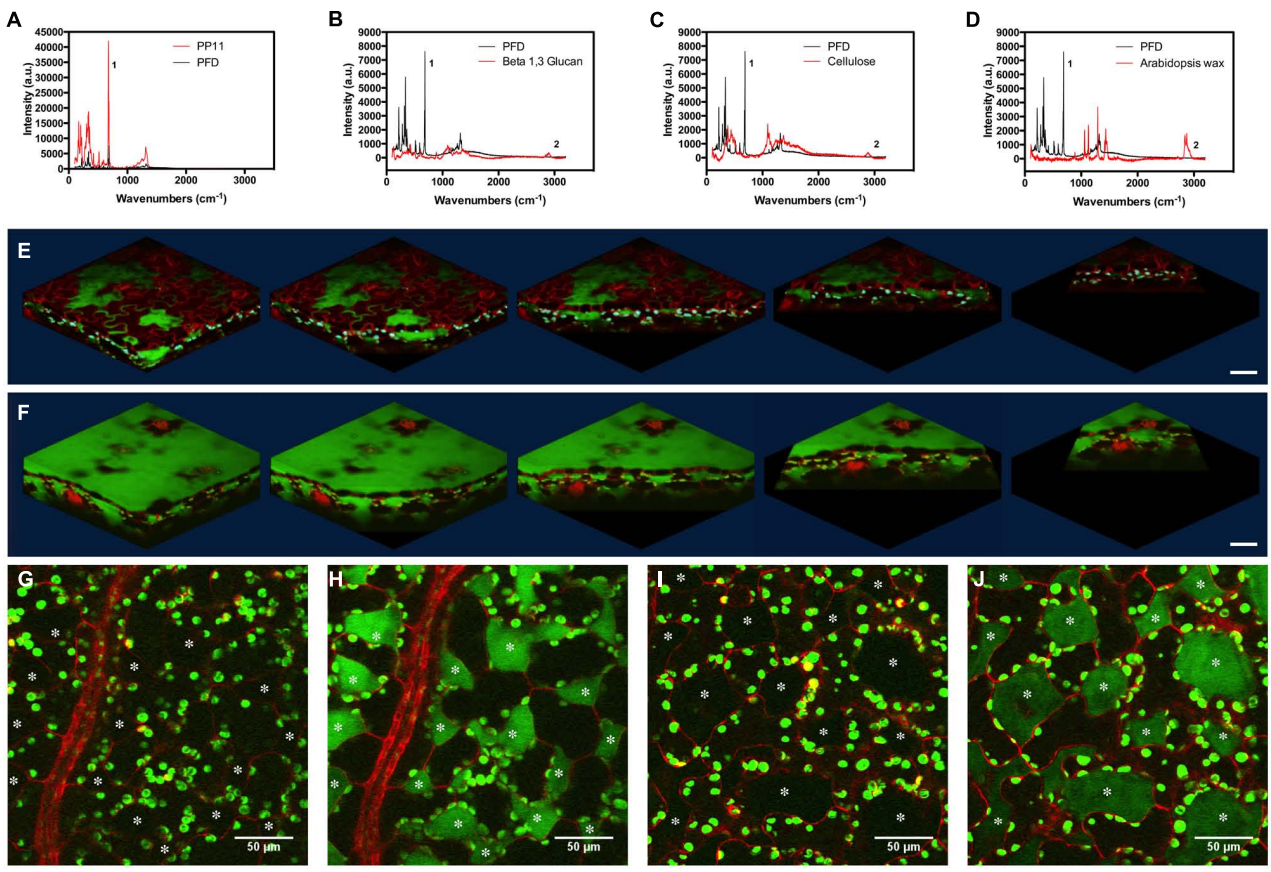

FIGURE 4 | Stimulated Raman scattering imaging of perfluorocarbons *in vivo*. **(A–D)** Raman spectra taken at 785 nm, comparing spectra of PFD and **(A)** PP11, **(B)** Beta 1–3 glucan, **(C)** cellulose, and **(D)** hexane extracted *Arabidopsis* leaf wax. Peaks labeled one and two were used to tune imaging to C–F and C–H bonds respectively. **(E,F)** SRS images representing Z-stacks taken through *Arabidopsis* leaves mounted in **(E)** PFD and **(F)** PP11. **(G,H)** show respectively, off and on resonance images of an *Arabidopsis* leaf mounted in PP11. **(I,J)** show respectively, off and on resonance images of an *Arabidopsis* leaf mounted in PFD. Scale bars are 50 µm. Asterisks denote airspaces.

from the stokes beam (1064 nm). As the absorption spectrum of the chloroplasts is so broad, tuning the wavelength of the excitation laser does not affect the strength of the chloroplast signal.

Some of the chloroplasts may appear to be on the extracellular side of the red lines (cell walls) delineating the cells in the images.

This is due to the strong out-of-focus signal from chloroplasts; normally 2-photon excitation is constricted to a small, defined volume and therefore no pinhole is used to filter out-of-focus information. However, as explained, the absorption of the chloroplasts is so strong that where the chloroplast signal overlaps with that of the PFC, this is most likely an imaging artifact due to the strength of the TPA signal from the chloroplasts compared to the red fluorescence in the cells and the SRS from PFC, particularly as the phenomenon is seen in both on and off images. As the Chloroplast signal is very intense signal from adjacent image frames could be leaked into selected image frame (resolution in z direction is slightly worse than 1 um which is the image step size here). This has the effect of making the chloroplasts appear to be the "wrong" side of the red cell walls.

We cannot categorically exclude the possibility that PFC have penetrated the cells, but consider it to be unlikely as otherwise the TPS from the PFC would be much more ubiquitously distributed.

DISCUSSION

In this investigation, we show that mounting living leaves in the PFCs, PFD, and perfluoroperhydrophenanthrene (PP11) quantifiably improves the clarity and consistency of images acquired from the mesophyll, for a number of laser-based microscopy techniques including LSCM, 2-photon microscopy, SHG, and SRS.

PFD and PP11 are non-toxic and possess a great carrying capacity for O_2 and CO_2. PFCs are not miscible with aqueous solutions, which are a disadvantage when trying to deliver bioactive compounds to cells in the leaf, however, this does suggest that PFCs may be of great use as they will not dilute metabolites or signaling molecules present in the cell wall, which could be easily perturbed by aqueous mounting media.

Both PFCs used in this investigation have low surface tensions (19.3 dyne cm^{-1} for PFD and 21.6 dyne cm^{-1} for PP11 compared to 72.8 dyne cm^{-1} for H_2O; Sargent and Seffl, 1970) that are lower than the 25–30 dyne cm^{-1} required to passively overcome the stomatal barrier (Schönherr and Bukovac, 1972) and readily infiltrate the apoplastic space. This infiltration smooths the optical phase transitions within the mesophyll, resulting in reduced noise and quantifiably clearer images. Moreover, the properties that PFD has displayed for mesophyll – easy infiltration into the tissue, significant improvement in *z*-plane resolution and non-toxicity – may be exploited for more general, *in vivo* imaging of air-filled or heavily vascularised animal tissues, such as insect spiracles or vertebrate lung, where gaseous exchange is also important and which are primary target for microbial infection. Similarly, PFD may be used advantageously for the perfusion and imaging within organ cavities.

The improvement in image clarity obtained by mounting samples in PP11 is greater than for PFD, which we ascribe to a closer matching of the refractive index of PP11 (1.334) with that of leaf tissue, which has been estimated as 1.4–1.6 depending on wavelength of incident light (Paillotin et al., 1998; Feret et al., 2008) compared to that of PFD (1.313). This was shown by autocorrelation analysis of pixel intensities in LSCM images. This analysis also demonstrated that the use of PP11 is particularly advantageous for imaging shorter wavelengths (i.e., the "green" channel; **Figure 3**). Increased fluorescence transmission of shorter wavelengths may have important advantages when more than one fluorophore is imaged simultaneously, for example in analyses that require Forster resonance energy transfer (FRET) or co-localisation.

We anticipate that the general improvement in image quality conferred by mounting in PFC media could be further enhanced through an even closer match between the refractive indices of living cells and the PFC mounting medium. 2,2′-thiodiethanol (TDE) has previously been used in this fashion (Staudt et al., 2007); in aqueous solution at varying concentrations, TDE provides a suite of colorless mounting media with tuned refractive indices from 1.33 to 1.52. Although TDE is not compatible with living samples and used preferentially with fixed specimens, it raises the possibility of a tuneable mounting system composed of two PFCs, each with refractive indices that bracket those of living specimens. These complementary PFCs may then be combined in set proportions to make a mounting medium in which the refractive index is matched to that of any sample.

The presence of C–F bonds in PFCs can be readily distinguished from the C–H bonds found in biological molecules. Consequently, PFCs does not impair the imaging of biological molecules by label-free imaging techniques such as CARS microscopy and SRS microscopy (Mansfield et al., 2013). The C–F bond itself can be exploited to visualize the distribution of PFC in biological material. In this investigation, we have exploited this distinction to generate contrast images of the "negative space" within the mesophyll. Images of the apoplast throughout development will enable a better understanding of leaf expansion and growth. Moreover, is will be possible to use such techniques to develop refined models of the airspaces within leaves, and better understand the constraints of gaseous fluxes within.

CONCLUSION

We have shown that mounting living leaves in PFD and perfluoroperhydrophenanthrene (PP11) improves image resolution for a number of laser-based microscopy techniques including LSCM, TPF, SHG, and SRS microscopy. These compounds allow greater *z*-axis penetration, resulting in clearer micrographs. In addition, PFCs may be used as label-free contrast agents to image the internal architecture of leaves, and enable a more precise understanding of the structural changes that occur during leaf development. As the mesophyll is a primary target for pathogenesis in plants, this technique may also be used to observe the processes of infection deep within the mesophyll. More generally, the use of PFCs as mounting media may be applied to other tissues rich in airspaces, such as animal lungs.

AUTHOR CONTRIBUTIONS

George R. Littlejohn, Mark D. Fricker, Murray R. Grant, Nicholas Smirnoff, Julian Moger, Jacqueline T. Christmas, Richard M. Everson, and John Love designed the research; George R. Littlejohn,

Eleanor Witterick, Jessica C. Mansfield, and Julian Moger performed the experiments; George R. Littlejohn, Eleanor Witterick, Jessica C. Mansfield, Jacqueline T. Christmas, Julian Moger, and John Love analyzed the data; George R. Littlejohn, Jessica C. Mansfield, Jacqueline T. Christmas and Jessica C. Mansfield and John Love wrote the manuscript.

ACKNOWLEDGMENTS

The authors would like to thank John Mansfield and Dawn Arnold for providing GFP-labeled *Pseudomonas*. Funding for this research was from the Biotechnology and Biological Sciences Research Council (BBSRC), UK. We also acknowledge the Exeter Imaging Network.

REFERENCES

Brown, R. M., Millard, A. C., and Campagnola P. J. (2003). Macromolecular structure of cellulose studied by second-harmonic generation imaging microscopy. *Opt. Lett.* 28, 2207–2209. doi: 10.1364/OL.28.002207

Carrión, C. A., Costa, M. L., Martínez, D. E., Mohr, C., Humbeck, K., and Guiamet, J. J. (2013). In vivo inhibition of cysteine proteases provides evidence for the involvement of "senescence-associated vacuoles" in chloroplast protein degradation during dark-induced senescence of tobacco leaves. *J. Exp. Bot.* 64, 4967–4980. doi: 10.1093/jxb/ert285

Cheng, P.-C. (2006). "Interaction of light with botanical specimens," in *Handbook of Biological Confocal Microscopy*, 3rd Edn, ed. J. P. Pawley (New York: Springer Science+Business Media, LLC), 414–441. doi: 10.1007/978-0-387-45524-2_21

Cox, G., Moreno, N., and Feijó, J. (2005). Second-harmonic imaging of plant polysaccharides. *J. Biomed. Opt.* 10:024013. doi: 10.1117/1.1896005

Diaspro, A., and Sheppard, C. J. R. (2002). "Two-photon excitation flouresence microscopy," in *Confocal and Two-Photon Microscopy: Foundations, Applications and Advances*, ed. A. Diaspro (New York, NY: Wiley-Liss Inc.), 39–73.

Feijó, J. A., and Moreno, N. (2004). Imaging plant cells by two-photon excitation. *Protoplasma* 223, 1–32. doi: 10.1007/s00709-003-0026-2

Feret, J.-B., François, C., Asner, G. P., Gitelson, A. A., Martin, R. E., Bidel, L. P. R., et al. (2008). PROSPECT-4 and 5: advances in the leaf optical properties model separating photosynthetic pigments. *Remote Sens. Environ.* 112, 3030–3043. doi: 10.1016/j.rse.2008.02.012

Freudiger, C. W., Min, W., Saar, B. G., Lu, S., Holtom, G. R., He, C. W., et al. (2008). Label-free biomedical imaging with high sensitivity by stimulated raman scattering microscopy. *Science* 322, 1857–1861. doi: 10.1126/science.1165758

Gest, N., Garchery, C., Gautier, H., Jiménez, A., and Stevens, R. (2013). Light-dependent regulation of ascorbate in tomato by a monodehydroascorbate reductase localized in peroxisomes and the cytosol. *Plant Biotechnol. J.* 11, 344–354. doi: 10.1111/pbi.12020

Haralick, R. M., Shanmugam, K., and Dinstein, I. (1973). Textural features for image classification. *IEEE Trans. Syst. Man Cybern.* Vol. SMC-3, No. 6, 610–621. doi: 10.1109/TSMC.1973.4309314

Hoepflinger, M. C., Geretschlaeger, A., Sommer, A., Hoeftberger, M., Nishiyama, T., Sakayama, H., et al. (2013). Molecular and biochemical analysis of the first ARA6 homologue, a RAB5 GTPase, from green algae. *J. Exp. Bot.* 64, 5553–5568. doi: 10.1093/jxb/ert322

Hutt, H., Everson, R., Grant, M., Love, J., and Littlejohn, G. R., (2013). "How clumpy is my image? using citizen science to evaluate crowdsourced annotation tasks," in *Proceedings of the 13th UK Workshop on Computational Intelligence*, Guildford, 136–143, ISBN 978-1-4799-1568-2 (http://clumpy.ex.ac.uk/static/paper.pdf)

Inoue, S. (2006). "Foundations of confocal scanned imaging in light microscopy," in *Handbook of Biological Confocal Microscopy*, 3rd Edn, ed. J. P. Pawley (New York: Springer Science+Business Media, LLC), 1–16.

Johnson, C., Ravichadran, A., Smith, A., Vitha, S., and Holzenburg, A. (2011). Anchoring of FtsZ assemblies to the chloroplast envelope: the role of ARC6. *Microsc. Microanal.* 17(Suppl. 2), 330–331. doi: 10.1017/S1431927611002522

Knapp, E., Flores, R., Scheiblin, D., Modla, S., Czymmek, K., and Yusibov, V. (2012). Materials and methods Plasmid DNA. *Biotechniques* 52, 31–37.

Lambertsen, L., Sternberg, C., and Molin, S. (2004). Mini-Tn7 transposons for site-specific tagging of bacteria with fluorescent proteins. *Environ. Microbiol.* 6, 726–732. doi: 10.1111/j.1462-2920.2004.00605.x

Littlejohn, G. R., Gouveia, J. D., Edner, C., Smirnoff, N., and Love, J. (2010). Perfluorodecalin enhances in vivo confocal microscopy resolution of *Arabidopsis thaliana* mesophyll. *New Phytol.* 186, 1018–1025. doi: 10.1111/j.1469-8137.2010.03244.x

Littlejohn, G. R., and Love, J. (2012). A simple method for confocal imaging of *Arabidopsis* leaves with perfluorodecalin as infiltrative imaging medium. *J. Vis. Exp.* 16, pii: 3394. doi: 10.3791/3394

Mansfield, J., Littlejohn, G., Seymour, M., Lind, R., Perfect, S., and Moger, J. (2013). Label-free chemically specific imaging in-planta with stimulated Raman scattering microscopy. *Anal. Chem.* 85, 5055–5063. doi: 10.1021/ac400266a

Mizutani, G., Sonoda, Y., Sano, H., Sakamoto, M., Takahashi, T., and Ushioda, S. (2000). Detection of starch granules in a living plant by optical second harmonic microscopy. *J. Lumin.* 87–89, 824–826. doi: 10.1016/S0022-2313(99)00428-7

Moger, J., Garrett, N. L., Begley, D., Mihoreanu, L., Lalatsa, A., Lozano, M. V., et al. (2012). Imaging cortical vasculature with stimulated Raman scattering and two-photon photothermal lensing microscopy. *J. Raman Spectrosc.* 43, 668–674. doi: 10.1002/jrs.3156

Nagai, T., Ibata, K., Park, E. S., Kubota, M., Mikoshiba, K., and Miyawaki, A. (2002). A variant of yellow fluorescent protein with fast and efficient maturation for cell-biological applications. *Nat. Biotechnol.* 20, 87–90. doi: 10.1038/nbt0102-87

Nandakumar, P., Kovalev, A., and Volkmer, A. (2009). Vibrational imaging based on stimulated Raman scattering microscopy. *New J. Phys.* 11:033026. doi: 10.1088/1367-2630/11/3/033026

Paillotin, G., Leibl, W., Gapiński, J., Breton, J., and Dobek, A. (1998). Light gradients in spherical photosynthetic vesicles. *Biophys. J.* 75, 124–133 doi: 10.1016/S0006-3495(98)77500-9

Sargent, J. W., and Seffl, R. J. (1970). Properties of perfluorinated liquids. *Fed. Proc.* 29, 1699–1703.

Schönherr, J., and Bukovac, M. J. (1972). Penetration of stomata by liquids. *Plant Physiol.* 49, 813–819. doi: 10.1104/pp.49.5.813

Shaw, S. L., and Ehrhardt, D. W. (2013). Smaller, faster, brighter: advances in optical imaging of living plant cells. *Annu. Rev. Plant Biol.* 64, 351–375. doi: 10.1146/annurev-arplant-042110-103843

Staudt, T., Lang, M. C., Medda, R., Engelhardt, J., and Hell, S. W. (2007). 2,2'-thiodiethanol: a new water soluble mounting medium for high resolution optical microscopy. *Microsc. Res. Tech.* 70, 1–9. doi: 10.1002/jemt.20396

Tschiersch, H., Liebsch, G., Borisjuk, L., Stangelmayer, A., and Rolletschek, H. (2012). An imaging method for oxygen distribution, respiration and photosynthesis at a microscopic level of resolution. *New Phytol.* 196, 926–936. doi: 10.1111/j.1469-8137.2012.04295.x

Wright, K. M., Chapman, S., McGeachy, K., Humphris, S., Campbell, E., Toth, I. K., et al. (2013). The endophytic lifestyle of *Escherichia coli* O157: H7: quantification and internal localization in roots. *Phytopathology* 103, 333–340. doi: 10.1094/PHYTO-08-12-0209-FI

Conflict of Interest Statement: The authors declare that the research was conducted in the absence of any commercial or financial relationships that could be construed as a potential conflict of interest.

Received: 21 December 2013; accepted: 24 March 2014; published online: 23 April 2014.

Citation: Littlejohn GR, Mansfield JC, Christmas JT, Witterick E, Fricker MD, Grant MR, Smirnoff N, Everson RM, Moger J and Love J (2014) An update: improvements in imaging perfluorocarbon-mounted plant leaves with implications for studies of plant pathology, physiology, development and cell biology. Front. Plant Sci. ***5****:140. doi: 10.3389/fpls.2014.00140*

This article was submitted to Plant Cell Biology, a section of the journal Frontiers in Plant Science.

Copyright © 2014 Littlejohn, Mansfield, Christmas, Witterick, Fricker, Grant, Smirnoff, Everson, Moger and Love. This is an open-access article distributed under the terms of the Creative Commons Attribution License (CC BY). The use, distribution or reproduction in other forums is permitted, provided the original author(s) or licensor are credited and that the original publication in this journal is cited, in accordance with accepted academic practice. No use, distribution or reproduction is permitted which does not comply with these terms.

frontiers in
PLANT SCIENCE

ORIGINAL RESEARCH ARTICLE
published: 22 October 2013
doi: 10.3389/fpls.2013.00407

Arabidopsis myosin XI sub-domains homologous to the yeast myo2p organelle inheritance sub-domain target subcellular structures in plant cells

***Amirali Sattarzadeh*[1,2], *Elmon Schmelzer*[2]* *and Maureen R. Hanson*[1]**

[1] *Department of Molecular Biology and Genetics, Cornell University, Ithaca, NY, USA*
[2] *Central Microscopy, Max-Planck-Institute for Plant Breeding Research, Cologne, Germany*

Edited by:
Alex Costa, University of Milan, Italy

Reviewed by:
Sherryl Bisgrove, Simon Fraser University, Canada
Cristina Ruberti, Michigan State University, USA

***Correspondence:**
Elmon Schmelzer, Central Microscopy Max Planck Institute for Plant Breeding Research, Carl-von-Linne-Weg 10, 50829 Köln, Germany
e-mail: schmelze@mpipz.mpg.de

Myosin XI motor proteins transport plant organelles on the actin cytoskeleton. The Arabidopsis gene family that encodes myosin XI has 13 members, 12 of which have sub-domains within the tail region that are homologous to well-characterized cargo-binding domains in the yeast myosin V myo2p. Little is presently known about the cargo-binding domains of plant myosin XIs. Prior experiments in which most or all of the tail regions of myosin XIs have been fused to yellow fluorescent protein (YFP) and transiently expressed have often not resulted in fluorescent labeling of plant organelles. We identified 42 amino-acid regions within 12 Arabidopsis myosin XIs that are homologous to the yeast myo2p tail region known to be essential for vacuole and mitochondrial inheritance. A YFP fusion of the yeast region expressed in plants did not label tonoplasts or mitochondria. We investigated whether the homologous Arabidopsis regions, termed by us the "PAL" sub-domain, could associate with subcellular structures following transient expression of fusions with YFP in *Nicotiana benthamiana*. Seven YFP::PAL sub-domain fusions decorated Golgi and six were localized to mitochondria. In general, the myosin XI PAL sub-domains labeled organelles whose motility had previously been observed to be affected by mutagenesis or dominant negative assays with the respective myosins. Simultaneous transient expression of the PAL sub-domains of myosin XI-H, XI-I, and XI-K resulted in inhibition of movement of mitochondria and Golgi.

Keywords: yeast myo2p, myosin V, transient expression, Golgi, mitochondria, vacuole, confocal microscopy, *Nicotiana benthamiana*

INTRODUCTION

Myosins, molecular motors that move cargo along actin filaments, occur in all eukaryotic organisms. Based on sequence homology, the myosin super family can be divided into 37 classes (Richards and Cavalier-Smith, 2005; Foth et al., 2006). The myosins from higher plants fall within only two classes: class VIII and XI (Hodge and Cope, 2000; Berg et al., 2001). Plant myosins have the domain pattern that is characteristic for most of the myosins: (1) the extremely conserved N-terminal head (motor) domain, which binds to actin filaments and is responsible for force production via ATP hydrolysis (2) the neck (lever arm) domain, including distinctive repeat motifs called IQ repeats and (3) the C-terminal tail domain that facilitates cargo binding. Like most myosins, the tails of plant myosins are highly divergent domains that vary widely in length and in sequence. In addition, the tails of plant myosins have coiled-coil-forming sequences that allow the molecules to dimerize, producing two-headed molecules. In general, the tail domains of myosins are believed to be largely responsible for class-specific functions.

ATM1, which is a class VIII myosin, was the first plant myosin to be characterized, and was implicated in *Arabidopsis thaliana* cell wall formation (Reichelt et al., 1999). Recently, class VIII myosins were shown to be involved in plasmodesmata- mediated intracellular trafficking and endocytosis (Avisar et al., 2008a; Golomb et al., 2008; Sattarzadeh et al., 2008). In contrast to class VIII myosins, class XI myosins are similar to the well-studied myosin V proteins of fungi and animals. In Arabidopsis, a 13-member gene family encodes the myosin XIs (Reddy, 2001; Tominaga and Nakano, 2012). Analysis of insertional mutants of the Arabidopsis myosin XIs revealed considerable redundancy of function, as little effect on plant growth and organelle dynamics was detected (Ojangu et al., 2007; Peremyslov et al., 2008). Single and higher order mutants and RNA silencing have been used to probe functions of the myosin XI family (Ojangu et al., 2007; Prokhnevsky et al., 2008; Sparkes et al., 2008; Avisar et al., 2009). Incomplete myosins have been expressed, carrying putative cargo-binding domains but lacking the motor, so that if such proteins bind a large proportion of the available receptors on a cargo, there should be a dominant negative effect on movement of a particular organelle (Prokhnevsky et al., 2008; Sparkes et al., 2008; Avisar et al., 2009). Replacing the motor domain with fluorescent proteins has resulted in mixed success regarding labeling of particular organelles. Depending on the region of the myosin that has been expressed, sometimes minimal labeling of subcellular structures have been observed, with most fluorescence remaining in the cytoplasm (Reisen and Hanson, 2007; Avisar et al.,

2008b, 2009, 2012). The particular portion of the myosin XI tail that has been used in such experiments has a strong effect on whether or not fluorescent vesicles and subcellular structures are observed.

Class V myosin tails such as yeast myo2p contain two functional domains which harbor vacuole- and mitochondrial-specific and secretory vesicle-specific regions (Pashkova et al., 2005, 2006; Fortsch et al., 2011). Regions homologous to the two domains exist in the Arabidopsis myosin XI family. Previously we have described the labeling of subcellular locations by YFP fusions to the DIL (dilute) domain (similar to the yeast secretory vesicle-specific domain) of 12 Arabidopsis myosin XIs (Sattarzadeh et al., 2011). Peroxisomes were labeled by YFP fusions to DIL domains of 8 different myosin XIs, three labeled Golgi, and others labeled the plasma membrane, endoplasmic reticulum (ER), nuclear envelope, and unidentified vesicles, but none interacted with mitochondria (Sattarzadeh et al., 2011). Inspection of the members of the Arabidopsis myosin XI gene family revealed that except for XI-J, Arabidopsis myosin XI genes encode a 42 amino-acid region within the tail region that is homologous to the yeast myo2p region known to affect vacuole and mitochondrial inheritance (**Figure 1**). All of these regions in Arabidopsis exhibit the sequence PAL in this region; therefore we will refer to these 42 amino acids as the Arabidopsis myosin XI PAL sub-domains. We have previously expressed a YFP fusion to the PAL sub-domain of myosin XI-F and have shown that it localizes to plastids, stromules, peroxisomes, and Golgi in particular cells (Sattarzadeh et al., 2009). Here we report that YFP fusions of the PAL domain from 11 additional Arabidopsis myosin XIs localize to Golgi, mitochondria, nuclear envelope, the plasma membrane and/or to unidentified vesicles. While Golgi and mitochondrial mobility continued in cells transiently expressing the PAL sub-domains of either myosin XI-H, XI-I, and XI-K, simultaneous expression of all three PAL sub-domains resulted in cells with minimal or negligible movement of the two organelles.

RESULTS

ARABIDOPSIS MYOSIN XI TAIL DOMAIN HOMOLOGOUS TO A YEAST MYOSIN V DOMAIN

In the yeast myosin ScMyo2p, there is a 11 amino acid section that has been shown by mutagenesis to be critical for vacuole inheritance (Catlett et al., 2000). Mutations in this region also affect mitochondrial inheritance (Fortsch et al., 2011). A 42 amino acid region encompassing the 11 amino acids is highly conserved between yeast and plants and among the 12 different plant myosin XIs (**Figure 1B**). Based on the ScMyo2p structure template (PDB code2F6HX), homology models of globular tails of all *A. thaliana* class XI myosins were built. The three- dimensional structures that were obtained indicate that the predicted general architecture of the PAL sub-domain in class XI myosins is very similar to that of ScMyo2p (**Figure S1**; **Figure 1C**). The models indicate that the 11 amino-acid sections homologous to the corresponding yeast sections are predicted to be exposed on the surface of the polypeptides when the 42-amino acid regions we expressed are modeled.

LOCALIZATION OF YFP::AT MYOSIN XI PAL SUB-DOMAIN FUSIONS

Previously we have fused the PAL sub-domain from Arabidopsis myosin XI-F to YFP and have shown that the fusion protein labels plastids and stromules (Sattarzadeh et al., 2009). We have now made constructs with the remaining 11 PAL sub-domains from the Arabidopsis class XI myosins fused to YFP at the N-terminus. We report YFP fusion information for XI-C and XI-E together because the PAL domains of these two myosin XIs are identical. The localization of the YFP fusion proteins was examined by confocal laser scanning microscopy (CLSM) in leaf epidermal cells of *N. benthamiana* following agroinfiltration.

Except for the YFP::At XI-2 PAL fusion, all tested fusions labeled vesicles in the same size range as the Golgi, endosomes, and mitochondria (**Figures 2A–E**). The YFP fusions with myosin XI-2 failed to localize to any vesicular structures and strongly labeled the plasma membrane (**Figure 2A**; **Figure S2**). The YFP fusion with the At XI-A PAL sub-domain was usually seen also in the cytoplasm; however, some unidentified vesicular structures were sometimes observed in a few cells (**Figure 2B**). YFP fusion with the homologous region in yeast (RVI: Required for Vacuole Inheritance) resulted in diffuse cytoplasmic labeling in plant cells, but some punctate loci could be discerned at the plasma membrane (**Figure 2F**).

In order to identify the YFP-labeled organelles, we performed co-localization studies by co-expressing the myosin YFP-PAL fusions transiently with CFP or mCherry organelle markers in leaf epidermal cells of *N. benthamiana*. The YFP fusions with the PAL sub-domain of myosins XI-1, XI-D, XI-G, XI-H, XI-I and XI-K co-localized with the Golgi marker (**Figure 3**). Some but not all Golgi were labeled by the YFP::PAL fusion of myosin XI-B (**Figures 3D–F**). Vesicles labeled by YFP fusions with the PAL sub-domain of XI-C and XI-E did not coincide with the Golgi marker (data not shown).

YFP fusions with the PAL sub-domain from myosins XI-C, XI-E, XI-G, XI-H, XI-I, and XI-K co-localized with a mitochondrial marker (**Figure 4**). YFP::PAL fusions with myosins XI-B (**Figure 5**) and XI-D (data not shown) did not coincide with the mitochondrial signal. When YFP::PAL fusions of myosin XI-B, XI-H, XI-I, and XI-K were expressed along with a peroxisomal marker, no co-localization was observed (**Figure 5**).

Eight of the YFP fusions to PAL sub-domain (AtXI-1,B,C,D,E,G,I and K) appear to label the nuclear envelope in epidermal cells (**Figures 6A–I**). Even though the homologous region in yeast interacts with vacuoles, we observed only one plant PAL sub-domain, from XI-B, that label structures that are characteristic of tonoplast membranes in appearance (Xu et al., 2006) (**Figure 7**). Most cells expressing XI-B exhibited fluorescent Golgi, vesicles, and nuclear envelopes (**Figure 7**). The positive and negative co-localizations are summarized in **Table 1**.

MOTILITY OF THE VESICLES LABELED WITH YFP::PAL SUB-DOMAIN FUSIONS

High levels of expression are often achieved following agroinfiltration. When a myosin tail domain lacking the motor function is expressed, a dominant negative effect on motility can sometimes be detected. However, when we examined the vesicles labeled by the 11 YFP::At PAL sub-domains, we found that rapid motility

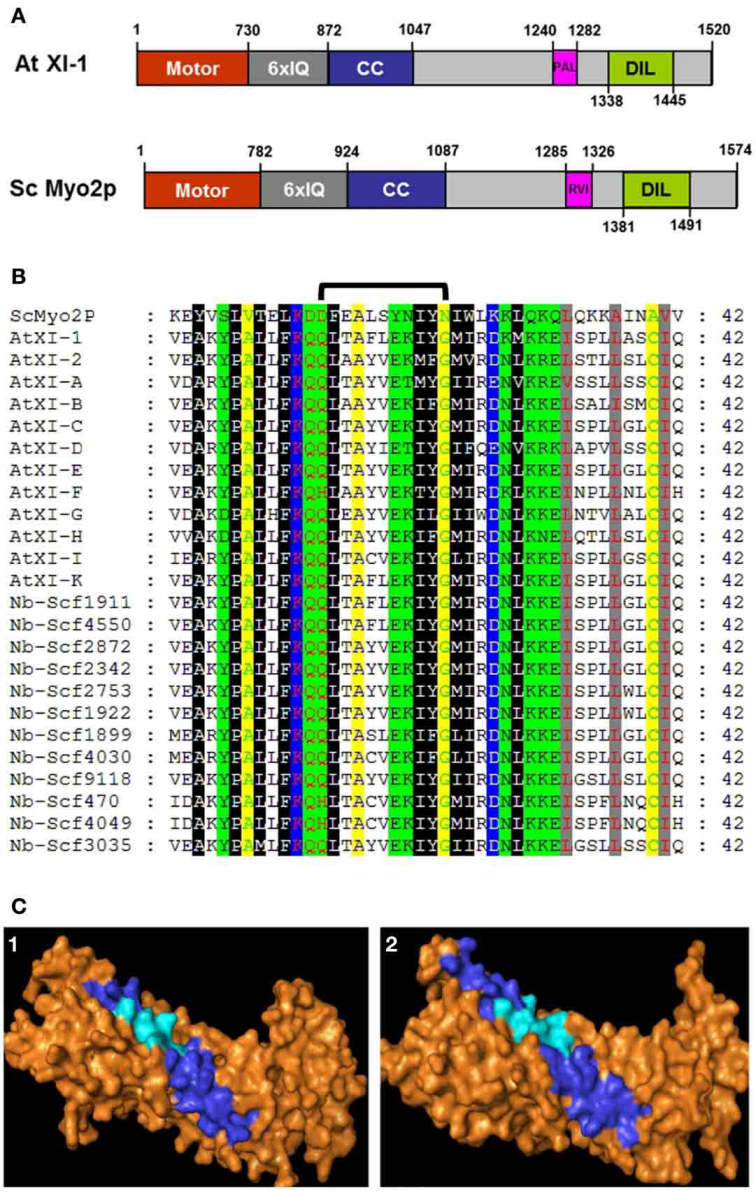

FIGURE 1 | Comparison of At XI-1 and yeast myo2p. (A) Diagram of *A. thaliana* myosin At XI-1 and yeast myosin V ScMyo2p. Motor domain, IQ repeats, coiled-coil (CC) regions and domains in globular tail of both proteins are shown. The PAL sub-domain, the cargo binding site from At XI-1 identified as homologous to ScMyo2p vacuole binding site (signified with RVI), and DIL domains are shown. Drawn approximately to scale except for the motor domain. **(B)** Alignment of the PAL sub-domains from *A. thaliana* class and *N. benthamiana* XI myosins to the homologous domain in the yeast Sc Myo2p. The 11 a.a region critical for vacuole binding (Catlett et al., 2000) in ScMyo2p is indicated by a bracket. **(C)** Homology structural modeling of myosin XI globular tail based on similarity to the myosin V ScMyo2p. Predicted three-dimensional structures of the globular tail of *A. thaliana* class XI-K myosin is illustrated. (1) At XI-K, (2) ScMyo2p. Surface residues are shown in orange. The 11 amino acids critical for the vacuole binding site in ScMyo2p tail (Catlett et al., 2000) and the corresponding amino acids in PAL sub-domains are shown in cyan, while the entire 42-amino acid PAL domain is shown in dark blue.

was retained, in contrast to our prior observation of stationary vesicles following agroinfiltration of YFP::At DIL domain fusions. Motility is documented in **Figures 8A–C** and **Movies S1**– **S4** in Supplementary Material. In order to determine whether a dominant negative effect on movement might occur if multiple PAL sub-domains were expressed, we agroinfiltrated simultaneously four strains, containing YFP-PAL sub-domain fusions from myosins XI-H, XI-I, and XI-K, along with a strain carrying either a mCherry marker for Golgi or for mitochondria. About a third of the cells expressing YFP exhibited YFP-labeled vesicles that were stationery or poorly motile (**Figures 8D–F**). Agroinfiltration does not result in all cells in a leaf expressing the transgenes, so some cells may be expressing only one or two of the PAL sub-domain fusions. We show an example of two adjacent cells, one of which is expressing one or more YFP-labeled PAL sub-domains localized to nearly immobile vesicles, while an adjacent cell is

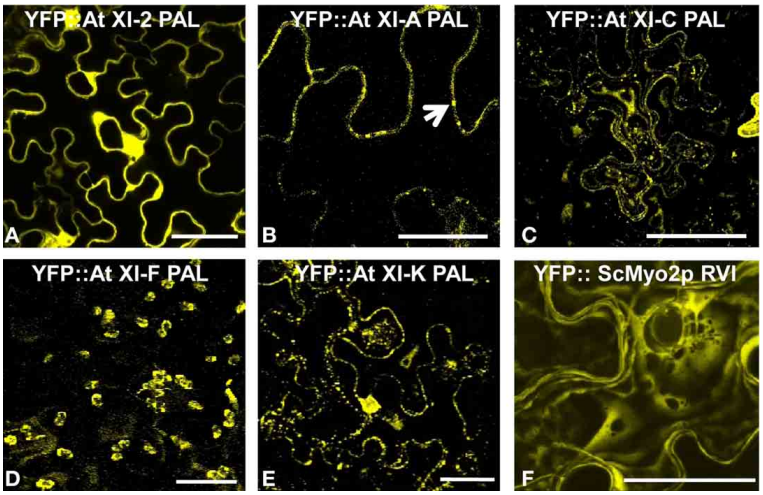

FIGURE 2 | Transient expression of YFP:: Myosin PAL sub-domains. Agrobacterium-mediated transient expression of YFP fusions of PAL sub-domains in epidermal cells of *N. benthamiana* **(A)** At XI-2. **(B)** At XI-A. **(C)** At XI-C. **(D)** At XI-F. **(E)** XI-K. **(F)** ScMyo2p RVI (Required for Vacuole Inheritance). An arrow marks some of the vesicles observed with YFP:: At XI-A PAL. Scale bar = 50 μm.

expressing only the mCherry mitochondrial marker and therefore exhibits motile mitochondria (**Movie S5**). We provide an example of a cell expressing mCherry-Golgi and YFP:: PAL sub-domains located on immobile vesicles in **Movie S6**. When the mCherry Golgi marker is infiltrated by itself, the Golgi exhibit high motility (**Movie S7**). We also observed minimal motility of YFP-labeled vesicles in many cells when we co-infiltrated three strains containing YFP-PAL sub-domain fusions from myosins XI-H, XI-I, and XI-K, without simultaneous co-infiltration of a strain carrying an organelle marker (**Movie S8**). In **Figure 8**, we provide three panels (A–C) from a movie that illustrate movement of vesicles labeled with YFP:: XI-K PAL when it is expressed alone; however, in (**Figures 8D–F**), no movement of vesicles occurs following co-infiltration of XI-H, XI-I, and XI-K. We conclude that expression of multiple PAL sub-domains can impair movement of Golgi and mitochondria by a dominant negative effect.

DISCUSSION

We have observed that 42-amino acid portions of 12 Arabidopsis myosin XI tail regions (the PAL sub-domain) are targeted to different subcellular organelles and membranes. Previously Li and Nebenfuhr (2007) expressed larger regions of the Arabidopsis XI-1 and XI-2 tails that encompass the PAL sub-domain and found they were targeted to peroxisomes, unidentified vesicles, or remained in the cytoplasm (**Figure 9**). We recently reported that the DIL domain of Arabidopsis myosin XIs, which is C-terminal to the PAL sub-domain and also encompassed by the constructs used by Li and Nebenfuhr (2007), targets YFP to several organelles and membranes (Sattarzadeh et al., 2011). PAL and DIL regions from particular myosin XIs can target YFP to Golgi, nuclear envelope, and/or plasma membrane. However, no DIL domains resulted in localization of YFP to mitochondria or tonoplast. Conversely, none of the PAL sub-domain fusions resulted in labeling of ER nor peroxisomes, while 8 DIL domains targeted YFP to peroxisomes and two labeled ER (Sattarzadeh et al., 2011). Thus there are some general differences in the localization information provided by the two different tail regions.

Although the PAL sub-domains among the *A. thaliana* class XI myosins are quite similar, there are some sequence differences in this 42 amino acid region of individual tail domains that could explain the different subcellular localizations (**Table 2**). While the PAL sub- domains of XI-C and XI-E are completely identical, other myosin XI PAL regions are less similar; nevertheless, it is not possible to consult the table of identity to predict which PAL sub-domains are likely to label one organelle vs. another. For example, of the PAL sub-domains that label mitochondria, XI-C/E PAL is 71, 80, 85, and 95% identical, respectively, to XI-G, XI-H, XI-I, and XI-K PAL. However, XI-C/E PAL is 85, 83, and 85%, identical, respectively to XI-1, XI-B, and XI-F, which do not label mitochondria but do label Golgi (**Table 2**). Unidentified aspects of the protein tertiary structure may be important for selective labeling.

The PAL sub-domain of the myosin XIs was selected for study because it is homologous to a sub-domain in yeast myo2p required for vacuole inheritance (Catlett et al., 2000). Recently, (Fortsch et al., 2011) have shown that the same yeast myo2p region is important for mitochondrial inheritance. Furthermore, Li and Nebenfuhr (2007) demonstrated that the structure of myosin XI-1 could be modeled with structural data available for yeast myo2p. Ancestral myosin XIs may have duplicated and diverged in the tail domains to interact with a variety of subcellular structures, including mitochondria, Golgi, and peroxisomes. The yeast PAL sub-domain did not label plant mitochondria or tonoplast (**Figure 2F**), though the yeast DIL domain was able to label plant peroxisomes (Sattarzadeh et al., 2011).

High-level expression of defective motor proteins in various organisms have often been observed to create a dominant-negative effect on organelle movement, possibly because saturation of receptors with the motorless protein prevents intact motors from binding. When we transiently expressed YFP::DIL fusions of 12 Arabidopsis myosin XI proteins, we found that

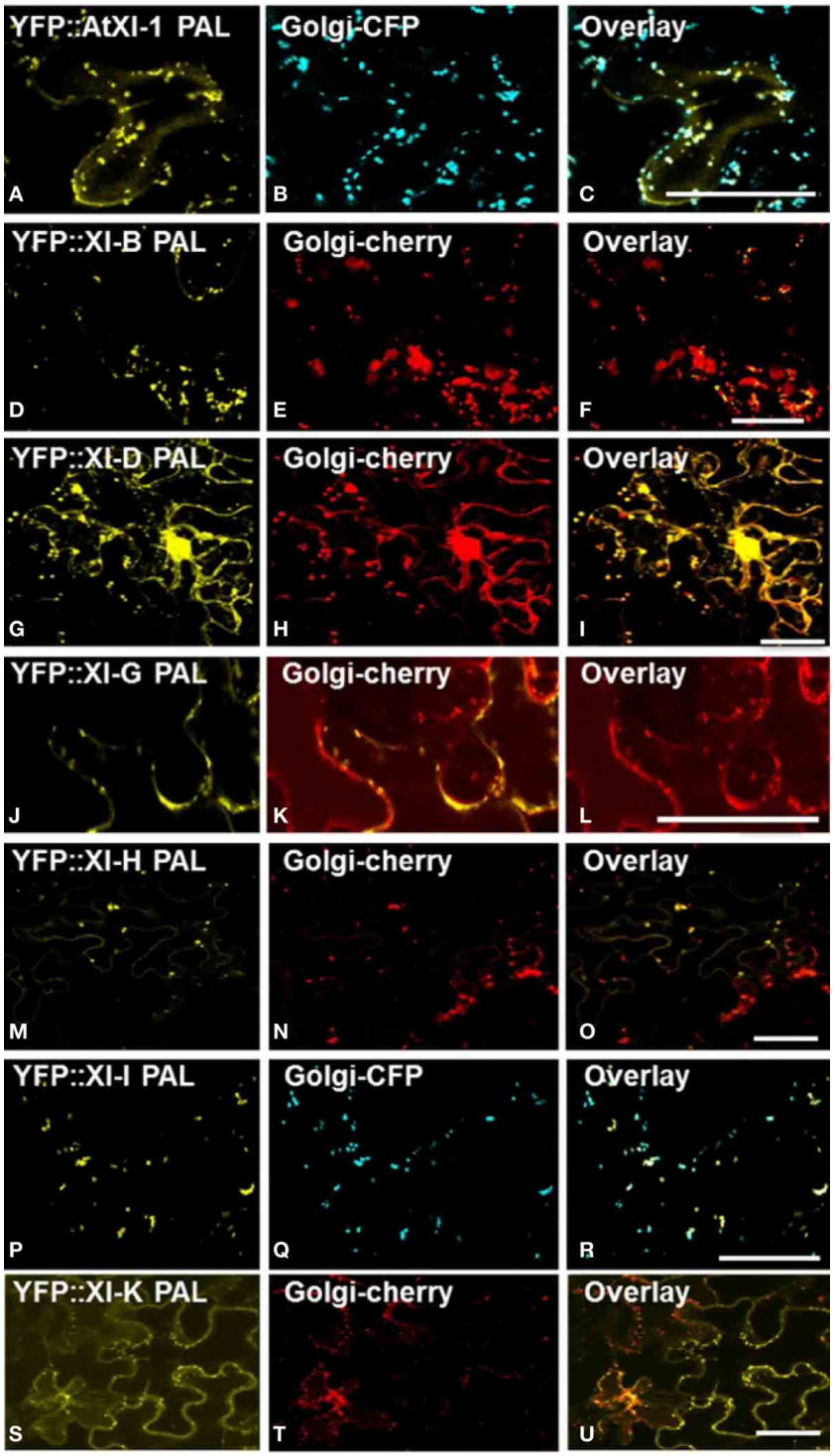

FIGURE 3 | Co-expression of YFP::Myosin XI PAL sub-domain with CFP and mCherry markers for Golgi in epidermal leaf cells of *N. benthamiana* (A) At XI-1. (D) At XI-I B. **(G)** At XI-D. **(J)** At XI-G. **(M)** At XI-H. **(P)** At XI-I **(S)** At XI-K. **(B,E,H,K,N,Q,T)** Golgi marker. **(C,F,I,L,O,R,U)** Merged images of YFP (yellow) and mCherry (red) or CFP (blue). Scale bar = 50 μm

expression of all but one of the fusions resulted in loss of motility of YFP-labeled vesicles and organelles (Sattarzadeh et al., 2011). Expression of various portions of fluorescent protein fusions to myosin XI tails have sometimes resulted in detectable effects on motility even though the affected organelles were not visibly fluorescently labeled. For example, Avisar et al. (2009) did not document localization of GFP::myosin XI tail regions to Golgi or mitochondria, but did detect inhibition of movement of both

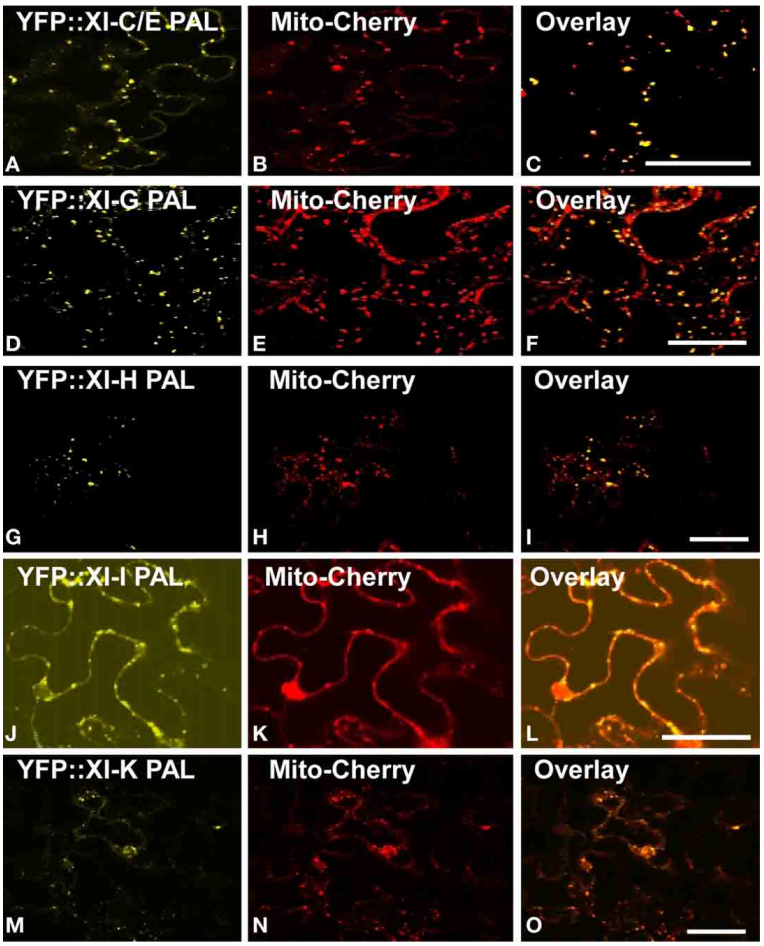

FIGURE 4 | Co-Expression of YFP::Myosin XI PAL sub-domain with mCherry markers for mitochondria in epidermal leaf cells of *N. benthamiana*. **(A)** At XI-C. **(D)** At XI-I G. **(G)** At XI-H. **(J)** At XI-I **(M)** At XI-K. **(B,E,H,K,N)** mCherry mitochondrial marker. **(C,F,I,L,O)** Merged images of YFP (yellow) and mCherry (red). Scale bar = 50 μm.

of the organelles when fusions to XI-1, XI-2, XI-C, XI-E, XI-I, and XI-K were expressed in *N. benthamiana*. Vick and Nebenfuhr (2012) have pointed out that expression of myosin tail regions might result in non-specific inhibition of motility as well as receptor-specific inhibition. We detected no Golgi or mitochondrial labeling with either the PAL or DIL regions of XI-2, but YFP::PAL of XI-C and E labeled mitochondria, YFP: DIL of XI-E labeled peroxisomes and YFP::DIL of XI-1 labeled Golgi (**Figure 3** and Sattarzadeh et al., 2011).

We have expressed Arabidopsis PAL domains in a heterologous plant system, namely *N. benthamiana*. The PAL domains in this species are highly similar to those in Arabidopsis (**Figure 1**; **Figure S3**). In fact, there are *N. benthamiana* PAL domains that are identical to those in Arabidopsis XI-K and XI-C/E (**Figure S3**). Thus proteins present in *N. benthamiana* that bind to PAL domains of endogenous myosin XIs are likely to be able to interact strongly with expressed Arabidopsis PAL domains. However, divergence between some of the Arabidopsis and Nicotiana PAL domains may result in weaker or absent interaction with Nicotiana endogenous proteins, potentially explaining why expression of a single Arabidopsis PAL domain is not sufficient for a strong dominant-negative effect. Furthermore, we may not have detected all the subcellular structures that interact with Arabidopsis PAL domains in Arabidopsis, if they are so divergent that they cannot interact with the myosin receptor proteins in Nicotiana.

Sparkes et al. (2008) were able to observe fluorescent puncta when YFP fusions to tail regions of Arabidopsis XI-E and XI-K were expressed in *N. tabacum* epidermal cells. Although not all peroxisomes, mitochondria, and Golgi were labeled by the YFP fusions to XI-E and XI-K, inhibition of their movement was detected in the cells (Sparkes et al., 2008). We observed that the YFP::PAL sub-domain fusions of XI-I and XI-K labeled mitochondria and Golgi in *N. benthamiana*, but YFP::PAL XI-H also labeled both organelles. Our YFP::PAL XI-B, XI-F, and XI-H fusions labeled Golgi. This is consistent with the observations of Avisar et al. (2009), who observed inhibition of Golgi movement by fusions with XI-B, XI-F, and XI-H; however, the inhibition occurred only in *N. tabacum* and not in

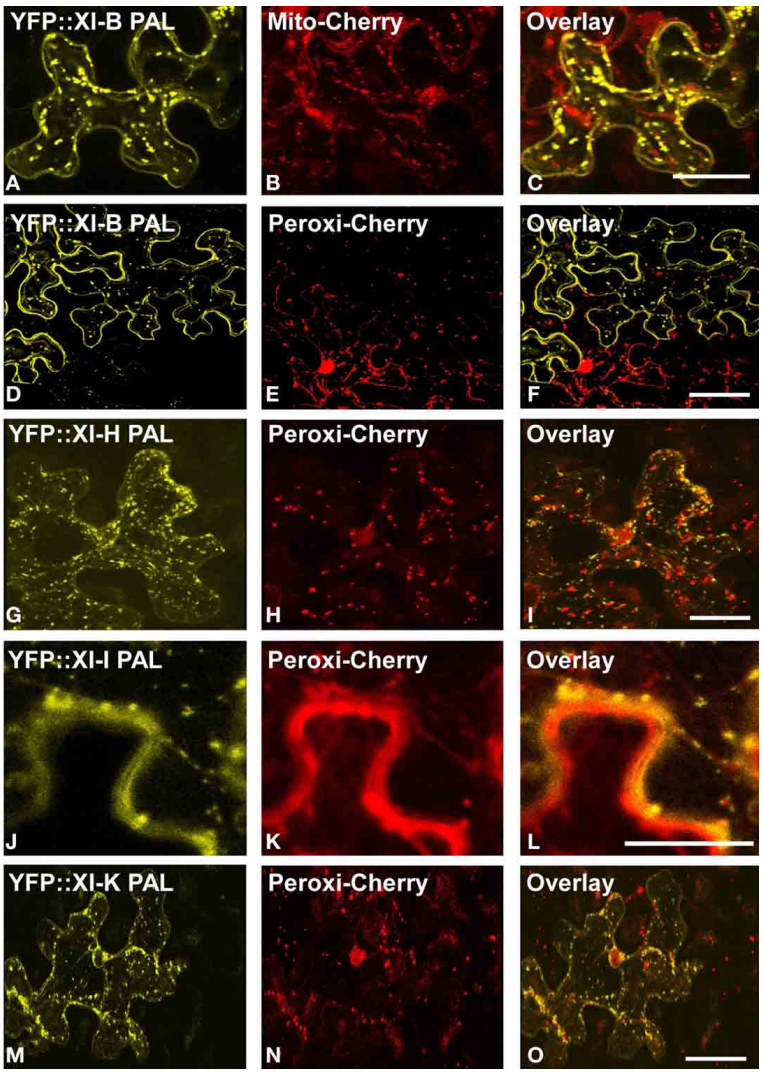

FIGURE 5 | Lack of co-localization with mitochondrial and peroxisome markers. Co-expression of YFP::Myosin XI PAL sub-domains with mCherry markers for mitochondria and peroxisomes in epidermal leaf cells of *N. benthamiana*. **(A** and **D)** At XI-B. **(G)** At XI-H. **(J)** At XI-I **(M)** At XI-K. **(B)** mCherry mitochondrial marker. **(E,H,K,N)** mCherry peroxisomes. **(C,F,I,L,O)** Merged images of YFP (yellow) and mCherry (red). Scale bar = 50 μm

N. benthamiana. Thus if a PAL sub-domain labels a particular motile organelle, the larger constructs expressed by others have often resulted in effects on motility of that organelle. But the correlation is not perfect, as we did not detect labeling of all organelles whose movement was affected by expression of a particular myosin tail. For example, although Sparkes et al. (2008) observed inhibition of Golgi by expression of YFP::XI-E tail fusions, neither the PAL nor DIL regions of XI-E labeled Golgi, even though the XI-E PAL sub-domains in *A. thaliana* and *N. benthamiana* are identical. Possibly other sequences we have not analyzed are able to interact with Golgi and mitochondria; however, abnormal conformation of myosin fragments may also prevent interactions that would normally occur with the intact myosin.

Single myosin XI insertional mutants do not exhibit major phenotypes, though XI-2 and XI-K knockouts are affected in root hair elongation and in Golgi, mitochondrial, and peroxisome motility (Peremyslov et al., 2008). While we have not been able to observe labeling of these three organelles with YFP fusions with XI-2 PAL sub-domains, all three organelles are labeled by either the PAL sub-domain (mitochondria, Golgi) or the DIL domain (peroxisomes) of XI-K fused to YFP. In plants containing single knockouts of XI-1, XI-2, XI-C, XI-E, and XI-I, Avisar et al. (2012) detected minor effects on Golgi movement, while an XI-K knockout greatly inhibited Golgi motility. Of these myosins, we found that YFP::PAL sub-domain fusions of XI-1, XI-I, and XI-K and the YFP::DIL fusion of XI-C labeled Golgi (Sattarzadeh et al., 2011).

Of the Arabidopsis myosin XIs, XI-1, XI-2, XI-H, XI-I, and XI-K are the most highly and ubiquitously expressed (Peremyslov et al., 2011; Sparkes, 2011). Much attention has been focused on myosin XI-K. Avisar et al. (2008b) observed that transient

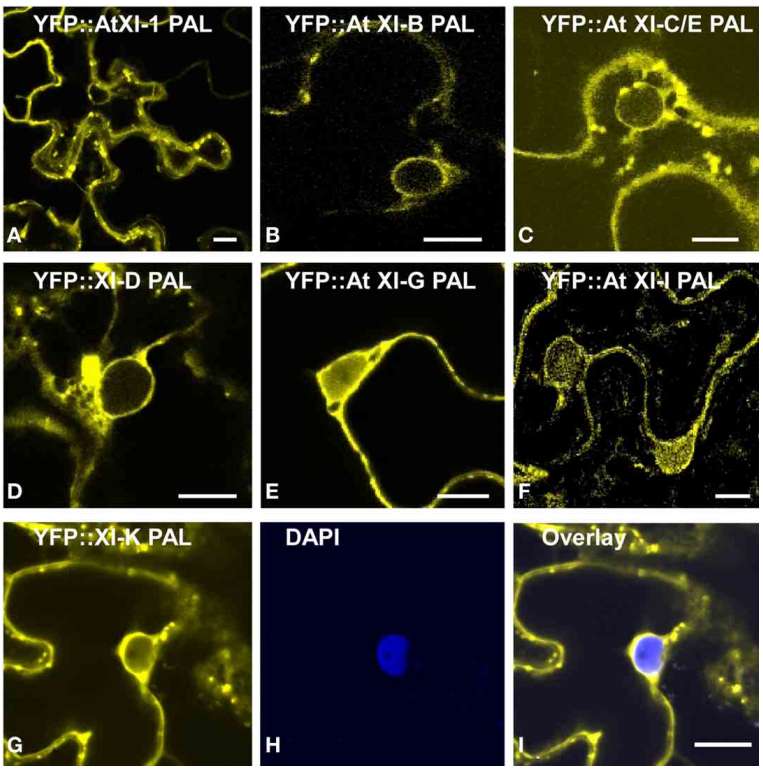

FIGURE 6 | Transient expression of YFP fusions of *A. thaliana* class XI myosin PAL sub-domains in epidermal leaf cells of *N. benthamiana*. YFP fusions of At XI-1 PAL **(A)**, At XI-B PAL **(B)**, At XI-C/E PAL **(C)**, At XI-D PAL **(D)**, At XI-G **(E)**, At XI-I PAL **(F)** and At XI-K PAL **(G)** are shown in yellow. **(H)** DAPI staining of epidermal leaf cells of N. benthamiana expressing YFP:: At XI-K PAL. **(I)** Merged images of YFP (yellow) and DAPI staining (blue). Scale bar = 15 μm.

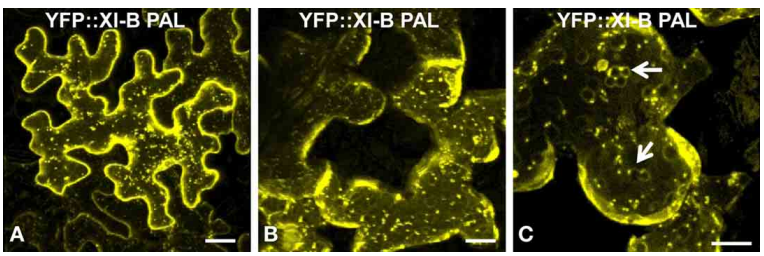

FIGURE 7 | Transient expression of YFP::At XI-B PAL in epidermal leaf cells of *N. benthamiana*. (A) In most cells, this YFP pattern was observed. **(B and C)** Occasionally, structures characteristic of tonoplasts (Xu et al., 2006) were observed. Examples of the putative tonoplasts are indicated with arrows. Scale bar = 25 μm.

silencing or expression of dominant negative constructs of myosin XI-K resulted in impaired movement of Golgi, peroxisomes, and mitochondria. More recent experiments with the XI-K tail region of *N. benthamiana* demonstrated that the particular myosin fragment that is expressed greatly influences how much vesicle motility is affected (Avisar et al., 2012). When Avisar et al. (2012) expressed two globular tail regions that encompass the corresponding Arabidopsis XI-K PAL and DIL domains that we have utilized, they observed inhibition of Golgi movement, but a third construct with a C-terminal extension, and two single amino-acid mutations in the DIL domain resulted in retention of Golgi motility (Avisar et al., 2012). When the entire XI-K sequence was fused to YFP, a small fraction of the Golgi, some regions of the ER, and many endomembrane vesicles were labeled (Peremyslov et al., 2012). The importance of myosin XI-K is also indicated in our YFP fusion experiments, as XI-K PAL or DIL regions fused to YFP resulted in labeling of many locations: Golgi, mitochondria, peroxisomes, nuclear envelope, plasma membrane, and ER (**Figures 3**, **4**; Sattarzadeh et al., 2011).

Even though expression of 12 different Arabidopsis YFP::PAL sub-domain fusions resulted in readily detectable fluorescent labeling of various subcellular structures, the labeled Golgi and

mitochondria move rapidly (**Movies S1–S4**). We have identified 6 different myosin XIs whose PAL sub-domains can interact with mitochondria, and 7 myosin XIs whose PAL sub-domains can interact with Golgi. When certain tail regions of 6 myosin XIs were labeled in transient assays, we previously observed that the motility of vesicles was retained (Reisen and Hanson, 2007). In contrast, when we expressed YFP::DIL fusions in *N. benthamiana*, movement of Golgi and peroxisomes ceased (Sattarzadeh et al., 2011). We cannot rule out the possibility that some of the targeting of YFP::PAL sub-domains to organelles may be due to chance function of the 42 amino-acid sequence as a transit peptide or secretory signal, as C-terminal fusions can sometimes unexpectedly result in labeling of peroxisomes and other vesicles (Cutler et al., 2000). However, targeting programs do not predict any of the PAL sub-domains to be effective transit or signal sequences (**Table S1** in Supplementary Material), though we recognize that such predictions are not perfect. The organelles labeled by the myosin XI PAL sub-domains are largely consistent with a role for the individual myosin XIs in organelle motility, according to the results of mutant, silencing, and dominant negative analysis. Possibly the YFP::PAL sub- domains do not accumulate to the same levels as the YFP::DIL fusion, thus not saturating receptors, allowing a sufficient number of intact motors to attach and transport the organelles. Alternatively, there may be differences in the Golgi and mitochondrial receptors that interact with the multiple PAL sub-domains, so that even if one receptor is saturated with a defective myosin, other receptors can interact with other myosins. Different myosin XIs may vary in affinity for particular cargoes, especially in a heterologous system. Less than 7% of the Golgi were labeled with a full-length myosin XI-K::YFP fusion (Peremyslov et al., 2012). We did not observe a dominant negative effect on Golgi and mitochondrial motility until we expressed three PAL sub-domains (XI-H, XI-I, XI-K) simultaneously (**Movies S5**, **S6**, **S8**). Further inquiry into the role of the PAL sub-domains is needed in order to determine whether motility of Golgi and mitochondria is affected as a result of saturation of receptors on the cargo or because of unknown non-specific effects on myosin function.

Table 1 | Summary of localization of PAL sub-domains of *A. thaliana* class XI myosins N-terminally fused to YFP and transiently expressed in leaves epidermal cells of *N. benthamiana*.

Class XI	PAL sub-domain colocalization	PAL domain No colocalization
At XI-1	Golgi Nuclear envelope	
At XI-2	Plasma membrane	
At XI-A	Cytoplasm, Vesicles	
At XI-B	Golgi Nuclear envelope Vesicles Plasma membrane Tonoplast	*Golgi (some),* *Mitochondria,* *Peroxisomes*
At XI-C/E	Mitochondria Nuclear envelope	*Golgi*
At XI-D	Golgi, Nuclear envelope	*Mitochondria*
At XI-F	Plastids, Stromules Nuclear envelope Golgi, Peroxisomes	
At XI-G	Mitochondria, Golgi Nuclear envelope	
At XI-H	Golgi, Mitochondria	*Peroxisome*
At XI-I	Golgi, Mitochondria Nuclear envelope	*Peroxisome*
At XI-K	Golgi, Mitochondria, Nuclear envelope	*Peroxisome*

Organelles that were observed not to co-localize with a particular myosin are shown in italics.

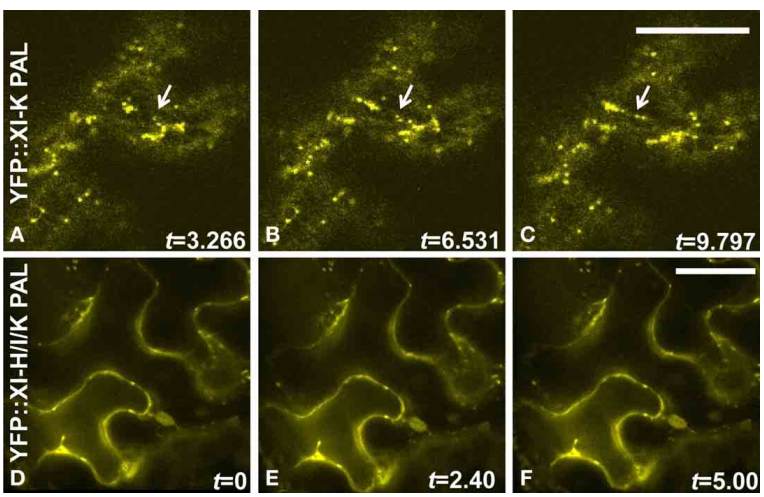

FIGURE 8 | Sequential images indicating movement YFP::At XI-K PAL sub-domain-labeled organelles but lack of movement when multiple domains are infiltrated simultaneously. (A–C) *N. benthamiana* leaves were infiltrated with an Agrobacterium strain carrying a YFP::At XI-K PAL sub-domain. **(D–F)** Leaves were infiltrated simultaneously with three Agrobacterium strains (YFP::At XI-H, YFP::At XI-I, and YFP::At XI-K PAL sub-domains), each of which contained a transgene with one PAL sub-domain fused to YFP. Time-lapse series were obtained by confocal microscope. Only three frames are shown. Time (*t*) is indicated in seconds. Bar = 50 um. An arrow marks an organelle that is in different positions in **A–C**.

Table 2 | Pairwise comparison of the amino acid sequences of the PAL sub-domain from *A. thaliana* class XI myosins and vacuole binding site in the yeast class V myosin Myo2p.

	Myo2P	AtMYA1	AtMYA2	AtXI-A	AtXI-B	AtXI-C	AtXI-D	AtXI-E	AtXI-F	AtXI-G	AtXI-H	AtXI-I	AtXI-K
Myo2P	42	16%	11%	9%	16%	16%	14%	16%	16%	19%	14%	19%	16%
AtMYA1	7	42	69%	66%	73%	85%	59%	85%	76%	61%	69%	78%	90%
AtMYA2	5	29	42	71%	85%	80%	59%	80%	73%	69%	83%	71%	76%
AtXI-A	4	28	30	42%	66%	71%	78%	71%	59%	59%	66%	71%	66%
AtXI-B	7	31	36	28	42	83%	57%	83%	73%	69%	80%	76%	78%
AtXI-C	7	36	34	30	35	42	61%	100%	83%	71%	80%	85%	95%
AtXI-D	6	25	25	33	24	26	42	61%	50%	59%	59%	64%	59%
AtXI-E	7	36	34	30	35	42	26	42	83%	71%	80%	85%	95%
AtXI-F	7	32	31	25	31	35	21	35	42	64%	69%	69%	78%
AtXI-G	8	26	29	25	29	30	25	30	27	42	76%	64%	66%
AtXI-H	6	29	35	28	34	34	25	34	29	32	42	71%	76%
AtXI-I	8	33	30	30	32	36	27	36	29	27	30	42	83%
AtXI-K	7	38	32	28	33	40	25	40	33	28	32	35	42

The identity is shown in percent and the number of identical amino acids are listed.

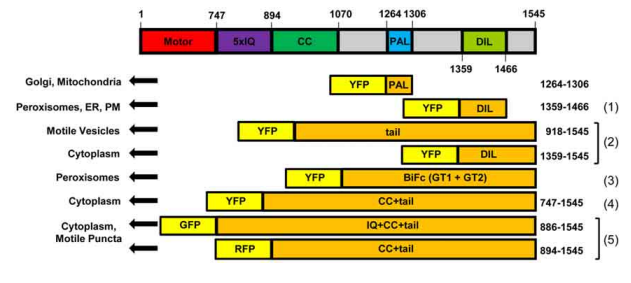

FIGURE 9 | Diagram of At XI-K constructs that have been expressed in Nicotiana. Constructs diagramed are (1) from Sattarzadeh et al. (2011), (2) from Reisen and Hanson (2007), (3) from Li and Nebenfuhr (2007), (4) from Sparkes et al. (2008), and (5) from Avisar et al. (2009). CC: coiled-coil. IQ: IQ repeats. BiFC: construct for Bimolecular Fluorescence Complementation. PM: Plasma Membrane.

MATERIALS AND METHODS

GENERATION OF YFP::MYOSIN CONSTRUCTS, PLANT GROWTH AND AGROINFILTRATION

Generation of the YFP::myosin constructs was performed as described (Sattarzadeh et al., 2009) using standard TOPO and Gateway cloning system (*Invitrogen*, Carlsbad, CA). The primers used are listed in **Table S2** in Supplementary Material. Plant growth and agroinfiltration was done as described (Sattarzadeh et al., 2011). When multiple strains were infiltrated, the same total concentration of bacteria was used as for single infiltration.

FLUORESCENT LABELING OF ORGANELLES AND CONFOCAL LASER SCANNING MICROSCOPY

For labeling of mitochondria, peroxisomes, Golgi stacks and plasma membrane with mCherry fluorescent protein, binary vectors, CD3-991, CD3-984, CD3-967, and CD3-1008 (Nelson et al., 2007) were used, respectively. According to Nelson et al. (2007), the mitochondrial marker was made by fusing the first 29 amino acids from the N-terminus of yeast COXIV (Köhler et al., 1997) to mCherry, the peroxisomal targeting signal Ser-Lys-Leu (Reumann, 2004) to mCherry, and the Golgi marker resulted from fusion of the first 49 amino acids of soybean α-1,2-mannosidase I (Saint-Jore-Dupas et al., 2006) to mCherry. The Golgi CFP marker was made by Sattarzadeh et al. (2011) by fusing the first 52 N-terminal amino acids of a rat 2, 6-sialyl transferase (Boevink et al., 1998). For DNA staining by 4′,6-diamidino-2-phenylindole (DAPI), leaves were immersed in a solution of 2.5% mannitol/0.01%silwet/300 nM DAPI.

CSLM was performed on a Leica microscope equipped with a TCS-SP2 confocal scanning head (Leica Microsystems, Heidelberg, Germany) as described (Sattarzadeh et al., 2009). **Movies S5–S7** were captured by using an Andor XD revolution spinning disc confocal microscope. Infiltrations of each YFP::PAL fusion were performed at 3 separate times and approximately 100 cells in total were observed for each YFP::PAL fusion. The images shown represent the appearance of the majority of the labeling patterns for each fusion. We note in the text if an image is provided of labeling pattern that was only rarely observed.

BIOINFORMATIC ANALYSIS AND STRUCTURAL HOMOLOGY MODEL ANALYSIS

GeneDoc was used for generation of alignments (Nicholas and Nicholas, 1997). Percent identity and divergence between Arabidopsis and *N. benthamiana* myosin XI PAL domains was generated with the LASERGENE MEGALIGN program (DNAstar, Madison, WI). Structure homology models for the tail domain of class XI mysoins were built by SWISSMODEL (Arnold et al., 2006) based on the Myo2p structure template (2f6hX). PyMol (Delano Scientific) was used for drawing the structural homology models.

ACKNOWLEDGMENTS

This work was supported by the Chemical Sciences, Geosciences and Biosciences Division, Office of Basic Energy Sciences, Office of Science, U.S. Department of Energy grant DE-FG02-09ER16070 to Maureen R. Hanson. We thank Rainer Franzen for excellent technical assistance and Rebecca Williams at the Cornell Life Sciences Core Laboratories Center for Microscopy and

Imaging for numerous helpful suggestions regarding the spinning disc confocal microscope.

SUPPLEMENTARY MATERIAL

The Supplementary Material for this article can be found online at: http://www.frontiersin.org/Journal/10.3389/fpls.2013.00407/abstract

Supplementary Figure 1 | Homology structural modeling of myosin XI globular tail based on similarity to the myosin V ScMyo2p. Predicted three-dimensional structures of the globular tail of *A. thaliana* class XI myosins are illustrated. **(A)** XI-1. **(B)** XI-2. **(C)** XI-A. **(D)** XI-B. **(E)** XI-C. **(F)** XI-D. **(G)** XI-E. **(H)** XI-F. **(I)** XI-G. **(J)** XI-H. **(K)** XI-I. **(L)** XI-K. Surface residues are shown in orange. The 11 amino acids critical for the vacuole binding site in ScMyo2p tail (Catlett et al., 2000) and the corresponding amino acids in PAL sub-domains are shown in cyan.

Supplementary Figure 2 | Co-expression of YFP::Myosin XI-2 PAL domain with mCherry markers for the plasma membrane in epidermal leaf cells of *N. benthamiana* (A) At XI-2 (B) Plasma membrane marker. (C) Merged images of YFP (yellow) and mCherry (red). Scale bar = 10 μm.

Supplementary Figure 3 | Pairwise comparison of the amino acid sequences identity and divergence between Arabidopsis and *N. benthamiana* myosin XI PAL domains. Table of identity and divergence was generated with the LASERGENE MEGALIGN program(DNAstar, Madison, WI).

Movies S1–S4 | Movement of YFP::At XI-PAL sub-domain-labeled organelles. *N. benthamiana* leaves were infiltrated with an Agrobacterium strain carrying a YFP::AtXI-PAL sub-domain **(S1)** XI-1 **(S2)** XI-C/E **(S3)** XI-D and **(S4)** XI-K.

Movie S5 | Co-expression of YFP::At XI-H, YFP::At XI-I and YFP::AT XI-K PAL sub-domains with mCherry markers) for mitochondria in epidermal leaf cells of *N. benthamiana* leaves. Leaves were infiltrated simultaneously with four Agrobacterium strains, each of which contained either contained a transgene with one PAL sub-domain fused to YFP (yellow) or a mCherry protein (red) targeted to mitochondria. Time-lapse series (25 frames, 0.2 s intervals) were obtained with an Andor spinning disc confocal microscope using a 60X objective. To the right of the yellow-labeled cell is a cell with motile mCherry-labeled mitochondria that is not exhibiting expression of the YFP-labeled PAL sub-domains.

Movie S6 | Co-expression of YFP::At XI-H, YFP::At XI-I and YFP::AT XI-K PAL sub-domains with mCherry markers (red) for Golgi in epidermal leaf cells of *N. benthamiana* leaves. Leaves were infiltrated simultaneously with four Agrobacterium strains, each of which contained either contained a transgene with one PAL sub-domain fused to YFP (yellow) or a mCherry protein (red) targeted to mitochondria. Time-lapse series (25 frames, 0.2 s intervals) were obtained with an Andor spinning disc confocal microscope using a 60X objective.

Movie S7 | Movement of mCherry-labeled Golgi bodies in epidermal cells of *N. benthamiana* leaves. Time-lapse series (20 frames, 3 s intervals) were obtained by the Leica CSLM. The movie is shown at 5 frames per second.

Movie S8 | Co-expression of YFP::At XI-H, YFP::At XI-I and YFP::AT XI-K PAL sub-domains in epidermal leaf cells of *N. benthamiana* leaves. Leaves were infiltrated simultaneously with three Agrobacterium strains, each of which contained a transgene with one PAL sub-domain fused to YFP. Time-lapse series (25 frames, 0.2 s intervals) were obtained with an Andor spinning disc confocal microscope using a 60X objective.

Table S1 | Predicted subcellular localization of *A. thaliana* class XI myosin PAL sub-domains. The prediction was generated using Target P (Brunak et al., 2007) based on the predicted presence of any of the N-terminal presequences: chloroplast transit peptide (cTP), mitochondrial targeting peptide (mTP) or secretory pathway signal peptide (SP).

Table S2 | List of primers used in this study.

REFERENCES

Arnold, K., Bordoli, L., Kopp, J., and Schwede, T. (2006). The SWISS-MODEL workspace: a web-based environment for protein structurehomology modelling. *Bioinformatics* 22, 195–201. doi: 10.1093/bioinformatics/bti770

Avisar, D., Abu-Abied, M., Belausov, E., and Sadot, E. (2012). Myosin XIK is a major player in cytoplasm dynamics and is regulated by two amino acids in its tail. *J. Exp. Bot.* 63, 241–249. doi: 10.1093/jxb/err265

Avisar, D., Abu-Abied, M., Belausov, E., Sadot, E., Hawes, C., and Sparkes, I. A. (2009). A comparative study of the involvement of 17 Arabidopsis myosin family members on the motility of Golgi and other organelles. *Plant Physiol.* 150, 700–709. doi: 10.1104/pp.109.136853

Avisar, D., Prokhnevsky, A. I., and Dolja, V. V. (2008a). Class VIII myosins are required for plasmodesmatal localization of a closterovirus Hsp70 homolog. *J. Virol.* 82, 2836–2843. doi: 10.1128/JVI.02246-07

Avisar, D., Prokhnevsky, A. I., Makarova, K. S., Koonin, E. V., and Dolja, V. V. (2008b). Myosin XI-K Is required for rapid trafficking of Golgi stacks, peroxisomes, and mitochondria in leaf cells of Nicotiana benthamiana. *Plant Physiol.* 146, 1098–1108. doi: 10.1104/pp.107.113647

Berg, J. S., Powell, B. C., and Cheney, R. E. (2001). A millennial myosin census. *Mol. Biol. Cell* 12, 780–794. doi: 10.1091/mbc.12.4.780

Boevink, P., Oparka, K., Cruz, S. S., Martin, B., Betteridge, A., and Hawes, C. (1998). Stacks on tracks: the plant Golgi apparatus traffics on an actin/ER network. *Plant J.* 15, 441–447. doi: 10.1046/j.1365-313X.1998.00208.x

Brunak, S., Von Jeijne, G., and Nielsen, H. (2007). Locating proteins in the cell using TargetP, SignalP, and related tools. *Nat. Protoc.* 2, 953–971. doi: 10.1038/nprot.2007.131

Catlett, N. L., Duex, J. E., Tang, F., and Weisman, L. S. (2000). Two distinct regions in a yeast myosin-V tail domain are required for the movement of different cargoes. *J. Cell Biol.* 150, 513–525. doi: 10.1083/jcb.150.3.513

Cutler, S. R., Ehrhardt, D. W., Griffitts, J. S., and Somerville, C. R. (2000). Random GFP::cDNA fusions enable visualization of subcellular structures in cells of Arabidopsis at a high frequency. *Proc. Natl. Acad. Sci. U.S.A.* 97, 3718–3723. doi: 10.1073/pnas.97.7.3718

Fortsch, J., Hummel, E., Krist, M., and Westermann, B. (2011). The myosin-related motor protein Myo2 is an essential mediator of bud-directed mitochondrial movement in yeast. *J. Cell Biol.* 194, 473–488. doi: 10.1083/jcb.201012088

Foth, B. J., Goedecke, M. C., and Soldati, D. (2006). New insights into myosin evolution and classification. *Proc. Natl. Acad. Sci. U.S.A.* 103, 3681–3686. doi: 10.1073/pnas.0506307103

Golomb, L., Abu-Abied, M., Belausov, E., and Sadot, E. (2008). Different subcellular localizations and functions of Arabidopsis myosin VIII. *BMC Plant Biol.* 8:3. doi: 10.1186/1471-2229-8-3

Hodge, T., and Cope, M. J. (2000). A myosin family tree. *J. Cell Sci.* 113(Pt 19), 3353–3354.

Köhler, R. H., Zipfel, W. R., Webb, W. W., and Hanson, M. R. (1997). The green fluorescent protein as a marker to visualize plant mitochondria *in vivo*. *Plant J.* 11, 613–621. doi: 10.1046/j.1365-313X.1997.11030613.x

Li, J. F., and Nebenfuhr, A. (2007). Organelle targeting of myosin XI is mediated by two globular tail subdomains with separate cargo binding sites. *J. Biol. Chem.* 282, 20593–20602. doi: 10.1074/jbc.M700645200

Nelson, B. K., Cai, X., and Nebenfuhr, A. (2007). A multicolored set of *in vivo* organelle markers for co-localization studies in Arabidopsis and other plants. *Plant J.* 51, 1126–1136. doi: 10.1111/j.1365-313X.2007.03212.x

Nicholas, K. B., and Nicholas, H. B. J. (1997). Gene Doc: a tool for editing and annotating multiple sequence alignments. *Embnew. News* 4:14.

Ojangu, E. L., Jarve, K., Paves, H., and Truve, E. (2007). Arabidopsis thaliana myosin XIK is involved in root hair as well as trichome morphogenesis on stems and leaves. *Protoplasm*a 230, 193–202. doi: 10.1007/s00709-006-0233-8

Pashkova, N., Catlett, N. L., Novak, J. L., and Weisman, L. S. (2005). A point mutation in the cargo-binding domain of myosin V affects its interaction with multiple cargoes. *Eukaryot. Cell* 4, 787–798. doi: 10.1128/EC.4.4.787-798.2005

Pashkova, N., Jin, Y., Ramaswamy, S., and Weisman, L. S. (2006). Structural basis for myosin V discrimination between distinct cargoes. *EMBO J.* 25, 693–700. doi: 10.1038/sj.emboj.7600965

Peremyslov, V. V., Klocko, A. L., Fowler, J. E., and Dolja, V. V. (2012). Arabidopsis Myosin XI-K localizes to the motile endomembrane vesicles associated with F-actin. *Front. Plant Sci.* 3:184. doi: 10.3389/fpls.2012.00184

Peremyslov, V. V., Mockler, T. C., Filichkin, S. A., Fox, S. E., Jaiswal, P., Makarova, K. S., et al. (2011). Expression, splicing, and evolution of the myosin gene family in plants. *Plant Physiol.* 155, 1191–1204. doi: 10.1104/pp.110.170720

Peremyslov, V. V., Prokhnevsky, A. I., Avisar, D., and Dolja, V. V. (2008). Two class XI myosins function in organelle trafficking and root hair development in Arabidopsis. *Plant Physiol.* 146, 1109–1116. doi: 10.1104/pp.107.113654

Prokhnevsky, A. I., Peremyslov, V. V., and Dolja, V. V. (2008). Overlapping functions of the four class XI myosins in Arabidopsis growth, root hair elongation, and organelle motility. *Proc. Natl. Acad. Sci. U.S.A.* 105, 19744–19749. doi: 10.1073/pnas.0810730105

Reddy, A. S. N. (2001). Molecular motors and their functions in plants. *Int. Rev. Cytol.* 204, 97–178. doi: 10.1016/S0074-7696(01)04004-9

Reichelt, S., Knight, A. E., Hodge, T. P., Baluska, F., Samaj, J., Volkmann, D., et al. (1999). Characterization of the unconventional myosin VIII in plant cells and its localization at the post-cytokinetic cell wall. *Plant J.* 19, 555–567. doi: 10.1046/j.1365-313X.1999.00553.x

Reisen, D., and Hanson, M. R. (2007). Association of six YFP-myosin XI-tail fusions with mobile plant cell organelles. *BMC Plant Biol.* 7:6. doi: 10.1186/1471-2229-7-6

Reumann, S. (2004). Specification of the peroxisome targeting signals type 1 and type 2 of plant peroxisomes by bioinformatics analyses. *Plant Physiol.* 135, 783–800. doi: 10.1104/pp.103.035584

Richards, T. A., and Cavalier-Smith, T. (2005). Myosin domain evolution and the primary divergence of eukaryotes. *Nature* 436, 1113–1118. doi: 10.1038/nature03949

Saint-Jore-Dupas, C., Nebenfuhr, A., Boulaflous, A., Follet-Gueye, M. L., Plasson, C., Hawes, C., et al. (2006). Plant N-glycan processing enzymes employ different targeting mechanisms for their spatial arrangement along the secretory pathway. *Plant Cell* 18, 3182–3200. doi: 10.1105/tpc.105.036400

Sattarzadeh, A., Franzen, R., and Schmelzer, E. (2008). The Arabidopsis class VIII myosin ATM2 is involved in endocytosis. *Cell Motil. Cytoskeleton* 65, 457–468. doi: 10.1002/cm.20271

Sattarzadeh, A., Krahmer, J., Germain, A. D., and Hanson, M. R. (2009). A myosin XI tail domain homologous to the yeast myosin vacuole-binding domain interacts with plastids and stromules in Nicotiana benthamiana. *Mol. Plant* 2, 1351–1358. doi: 10.1093/mp/ssp094

Sattarzadeh, A., Schmelzer, E., and Hanson, M. R. (2011). Analysis of organelle targeting by DIL domains of the Arabidopsis myosin XI family. *Front. Plant Sci.* 2:72. doi: 10.3389/fpls.2011.00072

Sparkes, I. (2011). Recent advances in understanding plant myosin function: life in the fast lane. *Mol. Plant* 4, 805–812. doi: 10.1093/mp/ssr063

Sparkes, I. A., Teanby, N. A., and Hawes, C. (2008). Truncated myosin XI tail fusions inhibit peroxisome, Golgi, and mitochondrial movement in tobacco leaf epidermal cells: a genetic tool for the next generation. *J. Exp. Bot.* 59, 2499–2512. doi: 10.1093/jxb/ern114

Tominaga, M., and Nakano, A. (2012). Plant-specific myosin XI, a molecular perspective. *Front. Plant Sci.* 3:211. doi: 10.3389/fpls.2012.00211

Vick, J. K., and Nebenfuhr, A. (2012). Putting on the breaks: regulating organelle movements in plant cells. *J. Integr. Plant Biol.* 54, 868–874. doi: 10.1111/j.1744-7909.2012.01180.x

Xu, Y., Ishida, H., Reisen, D., and Hanson, M. R. (2006). Upregulation of a tonoplast-localized cytochrome P450 during petal senescence in Petunia inflata. *BMC Plant Biol.* 6:8. doi: 10.1186/1471-2229-6-8

Conflict of Interest Statement: The authors declare that the research was conducted in the absence of any commercial or financial relationships that could be construed as a potential conflict of interest.

Received: 01 July 2013; accepted: 26 September 2013; published online: 22 October 2013.

*Citation: Sattarzadeh A, Schmelzer E and Hanson MR (2013) Arabidopsis myosin XI sub-domains homologous to the yeast myo2p organelle inheritance sub-domain target subcellular structures in plant cells. Front. Plant Sci. **4**:407. doi: 10.3389/fpls.2013.00407*

This article was submitted to Plant Cell Biology, a section of the journal Frontiers in Plant Science.

Copyright © 2013 Sattarzadeh, Schmelzer and Hanson. This is an open-access article distributed under the terms of the Creative Commons Attribution License (CC BY). The use, distribution or reproduction in other forums is permitted, provided the original author(s) or licensor are credited and that the original publication in this journal is cited, in accordance with accepted academic practice. No use, distribution or reproduction is permitted which does not comply with these terms.

frontiers in
PLANT SCIENCE

REVIEW ARTICLE
published: 19 November 2013
doi: 10.3389/fpls.2013.00439

Plant cell shape: modulators and measurements

Alexander Ivakov* and Staffan Persson*

Max-Planck-Institute of Molecular Plant Physiology, Potsdam, Germany

Edited by:
Alex Costa, University of Milan, Italy

Reviewed by:
Laurie Smith, University of California San Diego, USA
Ying Fu, China Agricultural University, China

****Correspondence:***
Alexander Ivakov and Staffan Persson, Max-Planck-Institute of Molecular Plant Physiology, Am Muehlenberg 1, 14476 Potsdam, Germany
e-mail: Ivakov@mpimp-golm.mpg.de;Persson@mpimp-golm.mpg.de

Plant cell shape, seen as an integrative output, is of considerable interest in various fields, such as cell wall research, cytoskeleton dynamics and biomechanics. In this review we summarize the current state of knowledge on cell shape formation in plants focusing on shape of simple cylindrical cells, as well as in complex multipolar cells such as leaf pavement cells and trichomes. We summarize established concepts as well as recent additions to the understanding of how cells construct cell walls of a given shape and the underlying processes. These processes include cell wall synthesis, activity of the actin and microtubule cytoskeletons, in particular their regulation by microtubule associated proteins, actin-related proteins, GTP'ases and their effectors, as well as the recently-elucidated roles of plant hormone signaling and vesicular membrane trafficking. We discuss some of the challenges in cell shape research with a particular emphasis on quantitative imaging and statistical analysis of shape in 2D and 3D, as well as novel developments in this area. Finally, we review recent examples of the use of novel imaging techniques and how they have contributed to our understanding of cell shape formation.

Keywords: Microtubules, actin, auxin, pavement cell, shape tools, Arabidopsis, hypocotyl

INTRODUCTION

In immature organs where cell division is actively taking place, cells are small and the shapes of cells are largely defined by the most recent cell divisions where new cell walls have been laid down along previous division planes. The walls in such cells are straight and the cells are largely iso-diametric, bearing little resemblance to the shapes commonly observed in mature organs. To acquire their final shapes, cells must change their proportions while increasing in size. For changes in proportions to occur some parts of the cell surface must grow differently to other parts. This model of cell shape formation was proposed by Paul Green in 1965 on the basis of observations of the growth of giant internodal cells of *Nitella* and is still relevant today (Green, 1965).

In this review we aim to dissect how simple and complex cell shapes, such as those of cylindrical hypocotyl cells and leaf epidermal pavement cells, respectively, are thought to be established. A largely neglected area in the field of plant cell shape is the usage of quantitative means to define shape. We therefore also put an emphasis on how certain tools and algorithms may be used to quantify and compare shapes.

GENERAL CONCEPTS

The shape of the cell is bounded and defined by the cell wall and it follows that cell wall expansion must be differentially regulated around the cell to generate the final cell morphology. Cell walls expand through irreversible deformation under a turgor-driven cell wall stress in a process called "creep." Creep involves the breaking of hydrogen bonds between cell wall polymers and the reversible and irreversible breakage of covalent bonds (Cosgrove, 2005). Cell wall expansion is promoted by cell wall loosening factors, such as expansin proteins, and xyloglucan endotransglycosylases/hydrolases (XTHs) (Cosgrove, 2000; Van Sandt et al., 2007). Expansins are thought to promote cell wall creep by breaking hydrogen bonds between cellulose and xyloglucan chains (Cosgrove, 2000). XTH is able to hydrolyse covalently-bonded xyloglucan chains and re-attach them at a later time, weakening the wall (Fry et al., 1992). Cell wall stiffening may also occur. Agents proposed to stimulate cell wall stiffening include pectin methylesterase (Micheli, 2001), extensin proteins, peroxidases (Passardi et al., 2004), and reactive oxygen species (Schopfer, 1996). Creep is typically measured in isolated cell walls in an extensiometer, where the wall is loaded with a constant load and the irreversible lengthening of the wall is measured (Cosgrove, 2000).

Differential cell wall expansion underlying shape formation can include growth rates varying locally as some parts of the wall expand faster than others, as well as growth anisotropy, where the rates of expansion of a given segment of the wall are different in different directions. Anistropy is distinguished from isotropy, where the rates of expansion are equal in all directions. Cell wall anisotropy is determined by the structure of the cell wall and the arrangement of cellulose within it. Cellulose consists of high molecular weight glucan chains arranged in partially-crystalline bundles held together by numerous hydrogen bonds. These structures, termed microfibrils, have a high tensile strength and strongly resist deformation in the presence of a stretching force. The strong microfibrils are embedded in a pliant gel-like matrix consisting of hemicelluloses and pectin polysaccharides. This fiber and matrix configuration of the cell wall has been likened to a composite material (e.g., fiber-glass) and cell walls have been shown to behave mechanically like such material (Kerstens et al., 2001; Fratzl et al., 2004). The orientation of the cellulose microfibrils within the cell wall is therefore an important determinant of the behavior of the wall during growth as well

as in mature tissues (Burgert and Fratzl, 2009). Microfibrils resist expansion most strongly parallel to themselves and less strongly in other directions and thus form the basis for anisotropy.

Cellulose is produced by cellulose synthase (CesA) complexes which are mobile in the plasma membrane and extrude glucan chains into the cell wall. Cellulose microfibrils have long been observed to co-align with microtubules in the cell cortex (Green, 1962). More recently, observations of fluorescently-labeled CesA complexes in the plasma membrane showed that their movement is guided by cortical microtubules (Paredez et al., 2006). Hence, by controlling microtubule organization plant cells can control the arrangements of cellulose microfibrils, and therefore the pattern of wall expansion and cell morphogenesis (Wymer and Lloyd, 1996; Lloyd, 2011). Plant microtubules are mobile and highly dynamic structures which exhibit a treadmilling movement generated by a fast rate of net polymerization at the plus end and a slower rate of depolymerisation at the minus end (Shaw et al., 2003). Microtubules interacting with each other have emergent self-organizing properties and spontaneously organize into parallel bundles or arrays (Wasteneys and Ambrose, 2009). These microtubule arrays have the ability to rapidly re-organize to new orientations. Such re-organization control CesA trajectories and microfibril arrangements, which in turn influence cell shape.

CYLINDRICAL CELLS

Anisotropic expansion has been shown to be responsible for the formation of shape in cylindrical cells, such as those of *Nitella* and *Chara*, but also of expanding root and hypocotyls cells in Arabidopsis. When cells in a multicellular organ grow in this manner, cylindrical organs such as stems, roots and hypocotyls are produced. Quantification of local strain rates in growing roots indicate a high degree of anisotropy in the expansion zone which contributes to the elongated cylindrical shape of the cells and of the entire organ and observations of microfibril orientations can largely explain the observed anisotropy (Baskin et al., 1999; Anderson et al., 2010).

CELLULOSE DEPOSITION

Genetic and pharmacological experiments have shown that anisotropic expansion is greatly compromised in plants with decreased levels of cellulose (See Table S1 for an overview of mutants affecting cell shape). Cellulose-deficient mutants and plants treated with the cellulose synthesis inhibitor isoxaben exhibit radial swelling and dramatic decreases in cell elongation in hypocotyls and roots (Arioli et al., 1998; Fagard et al., 2000; Refrégier et al., 2004; Fujita et al., 2013). Presumably, in the presence of insufficient amounts of cellulose the cell wall is unable to resist the force of turgor and expands uncontrollably.

However, radial swelling is also sometimes observed in mutants with normal amounts of cellulose and with unaltered cellulose microfibril orientations, such as the temperature-sensitive microtubule organization mutant *mor1-1* (Sugimoto et al., 2003). Observations of this mutant led Wasteneys (2004) to propose the "microfibril length regulation hypothesis" (Wasteneys, 2004) whereby microtubules also control the length of deposited cellulose microfibrils. According to this hypothesis, in certain states of microtubule disruption, cellulose microfibrils are short and unable to resist the expansion of the cell wall due to insufficient hydrogen bonding with the cell wall matrix. These defects would then lead to radial swelling of the cells and decreased anisotropy.

MICROTUBULE ORGANIZATION

Various mutants with defects in microtubule organization or stability have defects in establishing anisotropic expansion and exhibit isotropic, swollen cells, as well as various degrees of helical twisting of cylindrical organs. Right-handed twisting has been observed in the *spiral1* (Furutani et al., 2000; Hashimoto, 2002; Nakajima et al., 2004; Sedbrook et al., 2004) and *spiral2/tortifolia1* mutants (Buschmann et al., 2004; Shoji et al., 2004). These mutants had altered microtubule orientations in hypocotyl cells. The products of these genes were identified as novel plant microtubule-associated proteins. When α- and β-tubulin were modified through the addition of GFP or other tags, right-handed growth was observed (Abe and Hashimoto, 2005), while left handed twisting is observed in the semi-dominant α-tubulin mutants *lefty1* and *lefty2* (Hashimoto, 2002; Thitamadee et al., 2002; Abe et al., 2004) and in the conditional microtubule organization mutant *mor-1* (Whittington et al., 2001), which exhibits severely disorganized microtubules at restrictive temperatures. Moreover, Ishida et al. (2007) examined a collection of missense and deletion mutants in α- and β-tubulin and observed both right and left-handed helical growth, depending on the position of the mutation (Ishida et al., 2007). In addition, helical twisting can be observed when microtubules are impaired with microtubule-directed drugs (Furutani et al., 2000; Nakamura et al., 2004).

It has been suggested that helical twisting and radial swelling in microtubule-related mutants may be caused by an altered pattern of CesA movement and a consequent alteration in the orientations of cellulose microfibrils in the cell wall (Wada, 2012). Helical patterns of microfibril deposition have been predicted to produce torsion in cylindrical *Nitella* cells growing anisotropically (Probine, 1963). Interestingly, right handed twisting has recently been described in the *pom2/csi1* mutant (Bringmann et al., 2012). POM2/CSI1 is a large microtubule-associated protein which also interacts with the CesA complex and was shown to be essential for the attachment of CesA complexes to microtubules. In its absence, CesA complexes lose their microtubule guidance and this leads to a partial loss of growth anisotropy and right-handed helical twisting of cylindrical organs (Bringmann et al., 2012; Li et al., 2012; Landrein et al., 2013). Closer examination of the pattern of cellulose deposition in cell walls revealed that the typical transverse cellulose orientation observed in wild type cells had given way to a tilted helical pattern (Landrein et al., 2013). The authors suggested that cellulose deposition in the absence of microtubule guidance may have a natural preponderance to occur in a curved, helical manner at an angle to the cell axis, thus producing twisted growth, and plants may use microtubule guidance of CesA complexes to counteract this tendency. Hence, microtubule organization dictates the arrangements of cellulose microfibrils, which is essential for directed growth of cylindrical cells.

ACTIN CYTOSKELETON AND CELLULAR TRAFFICKING

In contrast to animal cells, where the microtubule cytoskeleton is primarily involved in intra-cellular transport, plant cells rely almost exclusively on the actin cytoskeleton as a transport network in interphase cells. The efficient transport of materials throughout the cell is crucial for cell growth and cell wall synthesis. Unlike cellulose, most cell wall matrix polysaccharides (with the exception of callose) are produced in the Golgi apparatus, and all plasma membrane and cell wall proteins are produced in the ER and subsequently trafficked through the Golgi apparatus, and secreted into the wall. The synthesis and the regulation of cell wall expansion thus depend on the efficient delivery of new wall material and growth-regulating factors to all cellular locations.

The importance of actin-based movement for cell growth and cell shape control is evident from drug experiments and mutants with disrupted actin networks. The resulting phenotypes, e.g., growth retardation and loss of anisotropy, are presumably caused by decreased delivery of new material to growing cellular locations (e.g., the cell wall). CesA complexes are assembled in the Golgi on their way to the plasma membrane and fluorescently-labeled CesA proteins have recently been used to probe the role of actin in cell wall synthesis. CesA-containing Golgi were seen to be less mobile upon actin depolymerisation and in the *act2act7* double mutant with impaired actin cytoskeleton, while rates of exocytosis of new CesA particles and endocytosis of CesA and FM4-64 dye were also compromised (Crowell et al., 2009; Sampathkumar et al., 2013). Drug-treated and mutant plants had cell wall defects and exhibited cellulose deficiency, accompanied by cell swelling and more isotropic growth of root cells (Gilliland et al., 2002; Kandasamy et al., 2009). Thus, the actin cytoskeleton appears to be a crucial factor in cell wall assembly and directed cell growth.

Interestingly, the *act2act7* mutant has also been shown to exhibit helical twisting (Gilliland et al., 2002; Kandasamy et al., 2009; Sampathkumar et al., 2013), a phenotype traditionally observed in microtubule-related mutants. It has recently been shown that actin filaments and microtubules transiently interact in living plant cells and a crosstalk between the actin and microtubule cytoskeleton was implicated (Sampathkumar et al., 2011). The actin cytoskeleton is further needed for re-assembly of the microtubules (Sampathkumar et al., 2011), while stabilization, and partial disruption, of actin using jasplakinolide disorganized the cortical microtubules and the movement patterns of CesAs in the plasma membrane (Sampathkumar et al., 2013). Thus, while the actin cytoskeleton may also have direct effects on cell wall synthesis independently of its transport role, it is still unclear whether this occurs through the effect of actin on microtubule organization.

PAVEMENT CELLS

Leaf epidermal pavement cells are an example of a cell type where multipolar growth patterns emerge to generate complex irregular cell shapes (**Figure 1**). Pavement cells have attracted much interest in recent years as a model of shape formation that goes beyond the simple scheme observed in cylindrical cells. In some species, pavement cells form a regular undulating pattern of lobes and indentations in their anticlinal cell wall which has been likened to a jigsaw puzzle.

CYTOSKELETAL COORDINATION

Just like in cylindrical cells, the cytoskeleton is thought to be central to the formation of shape in pavement cells. However, the picture seems to be more complex than in cylindrical cells, and interactions between the two cytoskeleton components appear to be required for pattern formation which establishes multi-polar growth.

Microtubules have been observed to aggregate into parallel bundles arranged transversely across future indentation regions (Fu et al., 2005; Zhang et al., 2011), restricting local growth there, presumably through their control of the ordered deposition of cellulose microfibrils (**Figure 2**). Between the indentation regions, the outgrowth of lobes is associated with the aggregation of cortical fine actin filaments that are thought to promote

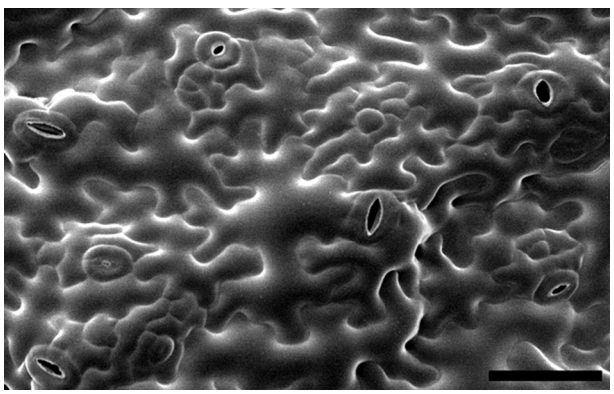

FIGURE 1 | Leaf epidermal pavement cells on the abaxial surface (underside) of an Arabidopsis cotyledon. Image is reproduced with permission from Dolan and Langdale (2004). Scale bar: 50 μm.

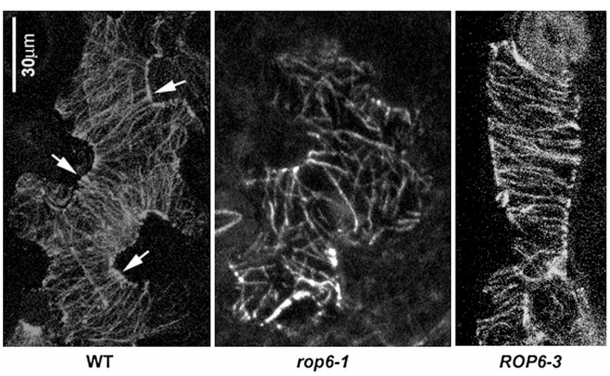

FIGURE 2 | Organization of cortical microtubules in leaf epidermal pavement cells. Typical organization of microtubules in wild-type (left panel), *rop6-1* (mid panel) and *ROP6-3* over-expressor (right panel) leaf epidermal pavement cells visualized by an anti-tubulin antibody. Arrows indicate ordered transverse microtubules in the neck regions of wild-type cells. Image is reproduced with permission from Fu et al. (2009). Scale bar: 30 μm.

local growth, possibly through the stimulation of vesicular trafficking and the preferential targeting of growth-promoting factors to these regions.

The regular organization of microtubules interspersed with fine actin has been shown to be generated through regulatory interactions between the cytoskeleton and the switch-like RAC/ROP-GTP'ase proteins (Fu et al., 2005, 2009). In particular ROP2 and ROP4, when in their active GTP-bound form, act redundantly to stimulate the aggregation of fine actin filaments by activating the ROP effector RIC4, while locally inhibiting the assembly of ordered microtubule arrays. Through a counteracting pathway, the ROP-interacting, microtubule-binding RIC1 protein inhibits the local assembly of fine actin where microtubules are abundant through inactivation of ROP2 and promotes microtubule assembly, thus making cortical fine actin and microtubules mutually-inhibiting and the microtubules self-activating. More recently, another pathway involving ROP6 GTP'ase was shown to promote the assembly of ordered microtubule arrays by activating the RIC1 protein, adding another piece to the puzzle (Fu et al., 2009). In such a system the two cytoskeletal components may be expected to self-organize into a pattern of mutually-exclusive local domains which then generate a regular lobed pattern through their opposing effects on local cell wall expansion. Over-activation of either pathway causes a complete loss of lobe formation as one component completely displaces the other around the entire cell periphery. This is exemplified in plants overexpressing RIC1 under the 35S promoter that causes dense transverse arrays of microtubules to form throughout the cell, resulting in block-like cells (Fu et al., 2005). This is also similar to constitutive activation of ROP2 (Fu et al., 2002, 2005) and constitutive over-expression of ROP6 (Fu et al., 2009; Lin et al., 2013). These results put an emphasis on precise coordination between the microtubule and actin cytoskeleton during complex cell shape formation.

Disruptions of the cytoskeleton and cytoskeleton-related genes further underscore its importance in pavement cell shape formation. Dual mutants of any two of the three actin protein iso-variants expressed in vegetative tissues in Arabidopsis disrupt pavement cell morphology, with the strongest reported effect in *act2act7*, where lobe formation is severely suppressed (Kandasamy et al., 2009). A number of genes encoding plant homologs of the ACTIN RELATED PROTEIN 2/3 (ARP2/3) complex have recently been identified in morphological screens with defects in cell shape formation. The ARP2/3 complex is known in other organisms as an actin modulator and appears to promote the nucleation, polymerization and cross-linking of actin and the assembly of fine cortical actin networks (Machesky and Gould, 1999). Mutants in the ARP2/3 complex genes ARP2/WURM, ARP3/DISTORTED, and ARPC5/CROOKED (Hülskamp et al., 1994; Li et al., 2003; Mathur et al., 2003a,b) all show severe defects in pavement cell shape, with a near-total absence of lobes. A mutant affecting another ARP2/3 subunit, *distorted2*, did not have a dramatic pavement cell shape phenotype, but exhibited cell adhesion defects between pavement cell lobes (El-Din El-Assal et al., 2004).

The ARP2/3 complex is known to function co-ordinately with the WAVE protein complex which appears to be required for its activation (Frank et al., 2004; Gautreau et al., 2004). Similar to ARP2/3 mutants, WAVE complex mutants exhibit cell shape abnormalities in pavement cells and trichomes. Components in this complex known to affect pavement cell shape include PIROGI/SRA1 (Basu et al., 2004), GNARLED/NAP1 (Brembu et al., 2004; Deeks et al., 2004; El-Assal et al., 2004), PIRP1 (Brembu et al., 2004), IRREGULAR TRICHOME BRANCH 1/SCAR2/DISTORTED3 (Basu et al., 2005; Zhang et al., 2005) and BRICK1 in maize (Frank and Smith, 2002) and in Arabidopsis (Djakovic et al., 2006; Le et al., 2006). In addition, several links underlying the stimulation of actin polymerization by ROP's have been identified, with the WAVE complex as a central player. The WAVE subunit PIROGI/SRA1 protein interacts with active ROP's and promotes the stimulation of ARP2/3 (Szymanski, 2005). SPIKE1, a known trichome morphogenesis modulator (Qiu et al., 2002), was recently identified as a guanine nucleotide exchange factor (GEF) which interacts with and promotes the activation of ROP's, as well as interacting with the WAVE complex subunit NAP1/GNARLED and promoting the activation of actin polymerization through the ARP2/3 complex (Basu et al., 2008).

Microtubule disruptions also severely affect pavement cell morphogenesis. The microtubule plus-end binding protein CLASP has been shown to be important for proper microtubule organization and stability (Ambrose et al., 2007; Kirik et al., 2007). In the *clasp1* mutant cortical microtubules exhibit an increased frequency of detachment from the cortex, are less dense and hyper-parallel and the pavement cell shape defective (Kirik et al., 2007; Wasteneys and Ambrose, 2009). MOR1 was identified in a screen for defective microtubule organization and the mutant exhibited severely defective pavement cell shapes, with a near-absence of lobes (Whittington et al., 2001; Kotzer and Wasteneys, 2006). The dynamic reorganization of microtubules involves targeted microtubule severing mediated by the protein katanin (Bichet et al., 2001). The katanin mutants *fra2* and *ktn1-3* have defective pavement cell shapes (Burk et al., 2001; Lin et al., 2013). Katanin was recently shown to be a downstream component of the ROP6-RIC1 pathway and was activated by its interaction with RIC1 (Hamant, 2013; Lin et al., 2013). RNAi and overexpression of MAP18, a novel microtubule associated protein proposed to destabilize microtubules, also caused defective lobe formation (Wang et al., 2007). Taken together, the organization and coordination of the cytoskeletal components are highly influential on the differential growth of a cell.

ANISOTROPY

It has often been assumed that cell wall anisotropy must be involved in the generation of the shapes of pavement cells (Fu et al., 2005). However, to what extent this is true has been unclear as there has been little experimental verification. Kerstens et al. (2001) used extensiometry to show that the lobed leaf epidermis of *Kalanchoe blossfeldiana* expands isotropically in response to wall stress as a tissue. The authors used polarization confocal microscopy and determined that the tissue does not exhibit a predominant orientation of cellulose microfibrils, being essentially isotropic (Kerstens et al., 2001). This was contrasted from block-like onion epidermal cells, which had a net

longitudinal orientation of cellulose microfibrils and expanded highly anisotropically, with higher expansion rates perpendicular to the orientation of cellulose microfibrils (Kerstens et al., 2001; Suslov and Verbelen, 2006; Suslov et al., 2009).

Attempts to address questions of differential growth and growth anisotropy have traditionally followed the approach of kinematic analysis (Silk and Erickson, 1979). In its simplest form it is exemplified by the classic experiment where ink dots are painted onto a root at regular intervals and their position examined over time to estimate local growth rates and directions. More recently sophisticated kinematic approaches have been applied in 2D and even 3D to infer the growth patterns of plant leaves and roots. These experiments have used exogenously-applied dots as landmarks (Poethig and Sussex, 1985; Basu et al., 2007; Remmler and Rolland-Lagan, 2012) or have tracked features present in the material being observed, such as local gray-level image structure (Schmundt et al., 1998; van der Weele et al., 2003) and mutationally-induced clonal cells which can be distinguished from their surroundings (Rolland-Lagan et al., 2003, 2005).

A result of kinematic experiments conducted on plant leaves was the surprising finding that growing dicot leaves exhibit little growth anisotropy (Erickson, 1966; Poethig and Sussex, 1985), even though local growth rates vary strongly both spatially and temporally (Poethig and Sussex, 1985; Schmundt et al., 1998). A limitation of these studies was the use of relatively mature leaves, while it is known that many developmental decisions are made early in development (Cookson et al., 2005). More recently Remmler and Rolland-Lagan (2012) tracked fluorescent micro-particles applied to the surface of young leaves to estimate local expansion rates in three dimensions and found high degrees of growth anisotropy only during short, initial stages of leaf development and largely isotropic growth for the remainder of leaf expansion (Remmler and Rolland-Lagan, 2012). The results of the experiments with leaves illustrate that varying growth rates alone may be sufficient to alter shape even in the absence of anisotropy. However, lobe formation is a cellular phenomenon and, even though the properties of individual cells may be expected to define the behavior of a tissue to some extent, local variation may cancel out over a collection of cells, particularly if it is adaptive for it to do so. Thus, the behavior of an entire tissue may not be indicative of cellular-level processes. Therefore, growth and cell wall properties must be examined at the cellular level. It is only very recently that this has been attempted and some studies are beginning to shed light on this subject.

Again, kinematic analysis is proving a useful tool, even though it is challenging to conduct kinematic analysis at the level of a cell wall in a single cell, as intra-cellular landmarks are usually non-stationary, while cell walls are largely uniform in texture and lack landmarks themselves. Zhang et al. (2011) attempted to quantify the expansion of the anticlinal cell wall in pavement cells of growing Arabidopsis cotyledons by defining the junctions between cells as landmarks and observing the cells as they expanded over a period of several days. Surprisingly, it was found that different segments of the sinusoidally-curved anticlinal wall grew at largely-equal relative rates throughout the cell, indicating isotropy. The cells also expanded essentially isometrically and changed little in shape while increasing in size, following an initial period during which lobes were initiated.

Zhang et al. (2011) pointed out that the lateral growth of pavement cells through which lobes are created cannot be explained simply by turgor-driven yielding of the anticlinal wall because there is no pressure gradient between adjacent cells. In addition, the authors speculated that the anticlinal wall may respond uniformly to tensions generated in the periclinal walls. The outer periclinal wall is subject to "tissue tension" and is strongly reinforced to resist this force (Kutschera and Niklas, 2007; Kutschera, 2008). As a "stress skin," the outer wall is thought to provide a mechanical constraint to expansion in plant stems, thus exerting a control on the growth not only of cells, but of entire organs, forming the basis of the "epidermal growth control theory" (Kutschera and Niklas, 2007). In a similar manner, the epidermis of leaves has also been shown to limit leaf expansion (Marcotrigiano, 2010). It is thus logical that differential growth of the underlying tissue must be accompanied by differential growth in the growth-limiting outer periclinal wall. At the cellular level, anisotropic growth of this wall could generate lobes and indentations in the anticlinal walls beneath. In addition, Armor and Overall. (personal communication; University of Sydney) tracked fluorescent microparticles on growing Arabidopsis cotyledon pavement cells and concluded that the upper periclinal cell wall expands anisotropically and that this could explain lobe formation, confirming the above predictions (Armour et al., pers. Commun.).

Partial loss of anisotropy is commonly observed in cell wall-related mutants and the contribution of anisotropy to pavement cell formation can thus be assessed. Various cellulose-related mutants have been shown to exhibit simpler pavement cell morphologies with wider indentations and shorter lobes or a complete absence of lobes (Williamson et al., 2001). The *rsw2* mutant, defective in the KORRIGAN endo-1,4-β-glucanase involved in cell wall remodeling, exhibits swollen pavement cells with dramatically simplified shape (Lane et al., 2001), similar to *rsw3*, a cellulose-deficient mutant impaired in a putative glucosidase II, involved in N-glycan processing in the ER (Burn et al., 2002). More recently the *anisotropy1* mutant was identified as an allele of AtCesA1 which decreased cellulose crystallinity without affecting cellulose content and caused the loss of pavement cell lobing (Fujita et al., 2013). These data highlight the importance of ordered microfibril deposition for anisotropic growth patterns observed in complex cell shapes, such as those in pavement cells.

OTHER EFFECTORS

HORMONES

Auxin

A relatively new, but anticipated, addition to the pavement cell puzzle is the role of plant hormones in the generation of pavement cell shapes. Various hormones are involved in almost all aspects of plant morphogenesis and may also be expected to be important in highly-polar pavement cells. From the point of view of cell shape control, auxin signaling is interesting because auxin stimulates cell expansion and has long been known to be important for the establishment of cell and organ polarity. Treatment of plants with the synthetic auxin naphthalene acetic acid (NAA) was shown to cause an increase in the frequency of anticlinal wall oscillation

and the cells produce a larger number of shallow lobes (Xu et al., 2010; Li et al., 2011), while quadruple *yucca* mutants with defects in auxin biosynthesis exhibit reduced interdigitation. The latter may be rescued by supplying external auxin (Xu et al., 2010), providing the first indication that auxin may also be involved in the establishment of polarity in pavement cells.

Various auxin transporters exhibit polar localization on the plasma membrane and contribute to establishing and maintaining directional auxin flow. An example is the PIN1 auxin-efflux transporter, which localizes to the basal surface of cylindrical root stele cells, contributing to auxin flow toward the root meristem (Blilou et al., 2005). The polar targeting of PIN1 protein is strongly dependent on its phosphorylation status, where phosphorylation by PINOID kinase promotes apical localization, and de-phosphorylation by a PP2A phosphatase promotes targeting to the basal end (Friml et al., 2004; Michniewicz et al., 2007; Kleine-Vehn et al., 2009; Huang et al., 2010). PIN1 also localizes to the tips of growing lobes in pavement cells (Xu et al., 2010; Li et al., 2011). Li et al. (2011) demonstrated that the PINOID/PP2A phosphorylation switch also regulates the targeting of PIN1 in pavement cells in a strikingly similar manner to that observed in roots. Hyper-phosphorylation of PIN1 through the over-expression of PINOID, or in the knockout of the FYPP1 gene encoding a PP2A phosphatase, caused PIN1 to localize to indentations instead of lobes, suppressing lobe formation. Over-expression of PIN1 stimulated lobe formation in a similar manner to auxin treatment, while the *pin1* mutant produces pavement cells devoid of lobes (Xu et al., 2010).

It has been assumed that lobe formation in pavement cells is mediated by intra-cellular interactions between the actin and microtubule cytoskeleton, with the crosstalk mediated by ROP GTP'ase switches (Fu et al., 2005, 2009; Mathur, 2006). However, pavement cells do not develop in isolation and the outgrowth of lobes must be coordinated with the in-growth of indentations in neighboring cells. Such prefect coordination implies the existence of inter-cellular signaling between pavement cells. Auxin is again a good candidate as it is a mobile morphogen.

Significant bi-directional crosstalk between auxin signaling and RAC/ROP GTP'ases is also known (Wu et al., 2011). Xu et al. (2010) explored the connection between auxin signaling and the ROP2 and ROP6 GTP'ases involved in pavement cell formation. It was demonstrated that auxin activates ROP2 and ROP6 in protoplasts in a dose-dependent manner, as well as stimulating both the ROP2/RIC4 and the ROP6/RIC1 pathways, previously known to activate fine actin and microtubule assembly respectively. This activation was dependent on a functional AUXIN BINDING PROTEIN1, which has been proposed to function as a cell-surface auxin receptor (Badescu and Napier, 2006; Xu et al., 2010). The results taken together allowed the authors to propose auxin as a local intercellular signal coordinating lobe outgrowth with the generation of indentations in neighboring cells by stimulating the assembly of microtubule arrays across the anticlinal cell wall (Xu et al., 2010, 2011). Other recently identified mutants further strengthen the role of auxin in pavement cell development. In a yeast two-hybrid screen using constitutively-active ROP proteins as a bait the INTERACTOR OF CONSTITUTIVE ACTIVE ROPs 1 (ICR1) protein was identified (Lavy et al., 2007). The protein is a novel RAC/ROP effector which is thought to function as a scaffold for the interactions of ROP's with their interaction targets. The *icr1* and the somewhat-related *icr2* mutants exhibit a complete absence of lobes in their adaxial pavement cells.Hazak et al. (2010) subsequently showed that the polarized localization of multiple PIN proteins is impaired in the *icr1* mutant, resulting in abnormal auxin distribution and severe developmental phenotypes throughout the plant. Auxin also stimulated *ICR1* expression and ICR1 is thought to function in an auxin-regulated positive feedback loop and functions to integrate auxin signaling with ROP-based cell polarity regulation (Hazak et al., 2010). These reports thus nicely link auxin signaling to modulations of the cytoskeletal components.

Cytokinin

While auxin appears to promote pavement cell interdigitation by activating ROPs, cytokinin has recently been shown to act antagonistically to auxin and suppress interdigitation (Li et al., 2013). Mutants with suppressed cytokinin signaling and cytokinin receptor mutants exhibited enhanced interdigitation while over-stimulation of cytokinin signaling suppressed or abolished lobe formation. The suppression of intedigitation appears to again involve the ROPs, as activation of cytokinin signaling was shown to counteract the auxin-induced activation of ROP2 (Li et al., 2013).

CELLULAR TRAFFICKING

Vesicular trafficking has long been implicated in pavement cell development. It is often assumed that cortical fine actin filaments stimulate the outgrowth of lobes by promoting the delivery of vesicles, similar to what is known in tip-growing cells such as root hairs (Yang, 2008). The entire non-cellulose component of plant cell walls is delivered through secretion, while CesA localization at the plasma membrane depends on more specialized vesicular trafficking. In addition, wall loosening agents such as expansins and XTHs must also be delivered through vesicles. More localized secretion of these agents may be involved in generating differential growth. The establishment of a bulge on Arabidopsis root hair initials is accompanied by local up-regulation of the activity of XTHs (Vissenberg et al., 2001) and expansins (Baluska et al., 2000) and such a mechanism may also be involved in the formation of pavement cell lobes, although this has not been demonstrated.

The ICR1 protein, known to be involved in pavement cell formation as discussed above, has been shown to be important for the regulation of vesicle trafficking by ROPs and the *icr1* mutant has decreased rates of exocytosis of PIN2, while endocytosis is unaffected (Hazak et al., 2010). ICR1 is also known to interact with the plant homolog of the Exocyst complex subunit Sec3 (Lavy et al., 2007), important for the tethering of secretory vesicles to the plasma membrane in preparation for fusion (Terbush et al., 1996) and the polarized targeting of exocytic events to growing buds in budding yeast (Wiederkehr et al., 2003). Active ROPs could recruit ICR1-Sec3 complexes to the plasma membrane (Lavy et al., 2007), while the *icr1* mutant had generally compromised exocytosis in root cells (Hazak et al., 2010). One of the viable mutants defective in Exocyst function, *exo84b-2* exhibits

a mildly reduced complexity of pavement cell shape (Selbach, 2012). In addition, mutants in proteins of the Transport Protein Particle II (TRAPPII) complex, involved in post-Golgi vesicle trafficking and exocytosis, exhibit severe pavement cell phenotypes, with almost complete loss of lobbing, as well as defective and incomplete cell walls between cells (Qi et al., 2011).

Endocytosis appears to also be important in cell wall synthesis and modification and cell shape formation. Cell wall-derived pectin is reportedly endocytosed into endosomal compartments, perhaps for re-mobilization to other parts of the cell wall (Baluška et al., 2002). Endocytosis is also important for the regulation of cellulose synthesis by regulating CesA abundance at the plasma membrane through removal. Although it is unclear whether clathrin or a clathrin-independent mechanism is involved (Dhonukshe et al., 2007; Crowell et al., 2009), recent work suggest that one of the proteins in the adaptor complex AP2 may interact with primary wall CesA proteins *in vitro* (Bashline et al., 2013). Furthermore, the *rsw9* mutant, deficient in DYNAMIN RELATED PROTEIN 1A, has severely compromised clathrin-mediated endocytosis and exhibits cellulose deficiency, altered cell wall composition and other cell wall-related phenotypes, including cell swelling in roots (Collings et al., 2008). Furthermore, ROP2 was recently shown to promote the polar localization of PIN1 in lobe tips of pavement cells by inhibiting its endocytosis, thus adding another link to the bi-directional interactions between auxin and ROP signaling (Nagawa et al., 2012). Thus, ROP-mediated cell polarization not only affects the cytoskeleton but appears to also be crucial in the pattern forming processes determining polarized vesicular trafficking.

POST-IMAGING: QUANTITATIVE ANALYSIS OF SHAPE

The recent use of complex cell shapes, such as pavement cells and trichomes, as model systems for cell shape formation has increased the difficulty in describing and comparing their phenotypes. Such shapes are irregular, highly variable and exhibit a high level of complexity which is often too great to establish a clear phenotypic description in an objective, quantitative manner. Thus, methods are required to quantify and compare shapes. The broad field of morphometrics concerns itself with the quantitative analysis of shape and morphology. Numerous methods to quantify and compare shapes have been devised and are reviewed here, with a particular emphasis on their relevance to shapes commonly observed in plants.

Shape consists of geometric information. Lengths and widths, the coordinate positions of defined feature points and ratios between object dimensions are all examples of such information. Some geometric information also carries information not related to the shape itself, for example the coordinates of specific points are influenced by the shape's location and would change if the shape were moved or rotated. By its formal definition, shape is the geometric information which is independent of size, location and rotation and must thus be separated from these factors.

Distance methods

Distance methods are the simplest and one of the earliest forms of morphometrics. Distance methods attempt to describe a shape by measuring the distances between defined shape features, such as the lengths of limbs. Distance data is easy to collect and readily interpretable. The lengths of lobes, the widths of indentations and the lengths of trichome branches have been used to quantify the shape phenotypes of these complex cells (Fu et al., 2005, 2009; Le et al., 2006).

A chief disadvantage of such methods is their dependence on size. In plant cells, changes in shape are typically accompanied by an increase in size, however, the converse is not always true and increasing size may not be accompanied by differential growth. Thus, shape does not always change with increasing size, even in complex cells such as pavement cells. Growth of pavement cells can be isometric, as kinematic studies have shown (Zhang et al., 2011). Many mutants have defects in plant and leaf size and grow at a slower rate. Furthermore, Arabidopsis leaves do not appear to have a clear cessation of growth and continue to expand asymptotically throughout their lives (Cookson et al., 2005). It has been shown that the duration of cell and leaf expansion is also an important factor in the regulation of leaf growth, with leaves of slow-growing mutants often continuing to grow for a longer time (Cookson et al., 2005). Using measures which reflect cell size can potentially appear to pick up differences in shape which may be driven simply by capturing cells of the same shape at a different point in their development when they are simply smaller or larger.

Ratio methods

The problem of size dependence can be overcome by normalizing the distances to each other or to other measures of size and expressing them as ratios or proportions. Such ratios are true descriptors of shape as they are independent of size, location and rotation. The ratio of length to width is a classic shape measure, often used to describe the shapes of leaves (Tsukaya, 2003). For simple shapes, such as cylindrical cells, the length/width ratio may describe the bulk of the shape variation and is thus a very appropriate measure for their comparison. In pavement cells, the number of lobes has been normalized on cell area (Xu et al., 2010; Li et al., 2011, 2013) to obtain a quantitative indicator of interdigitation.

Other ratio-based shape descriptors attempt to compare a shape with simple reference shapes such as a circle. For this, the area of the shape is expressed as a ratio of the area of the smallest reference shape that can enclose it. These measures are easy to calculate and do not require the manual marking of shape features, such as lobes. There have been several examples of their use on pavement cells and trichomes, e.g., circularity (Le et al., 2006; Zhang et al., 2011), and new measures of this type have been devised to quantify specific aspects of cellular morphology, such as "swelling factor," defined by comparing the area of a shape to an enclosing equilateral triangle (Basu et al., 2008), shape factor (Kirik et al., 2007) and form factor (Djakovic et al., 2006).

Distance and ratio methods suffer from their lack of uniqueness. Thus, two very differently-shaped cells may have the same circularity and will not be distinguished. A different measure may be used to distinguish these cells, however, this choice of measure is largely arbitrary, and such a measure may not always be found. Comparing the results of different studies is hampered if different measures have been used. Generally, such measures reflect a particular aspect of shape to some degree, while ignoring

other aspects. These measures thus carry only limited information about a shape and may not always be informative, especially when the complexity of the shapes is high.

Landmark methods

Landmark morphometrics, also known as geometric morphometrics, attempts to compare shapes by comparing the coordinate positions of a set of defined common points, usually obtained by manual marking. As coordinates are typically influenced by position, rotation and size, they may first be brought into *registration* to superimpose the shapes in such a way as to make the landmark positions comparable. This is generally done by minimizing the sum of squared distances between all corresponding landmarks through scaling, translation and rotation to remove information on size, location and orientation respectively. The aggregate sum of distances between all pairs of corresponding points then represents how dissimilar the shapes are. Generalized Procrustes Analysis is a commonly-used method of achieving registration and extracting shape similarity measures from landmarks and can be applied in two, three or more dimensions (Gower, 1975; Rohlf and Slice, 1990).

Landmark methods are much used in comparative morphological studies of animals, where a variety of anatomical structures may be used to define landmarks, e.g., bones, wing structure in insects. In plants it is often difficult to define common points between structures. In leaves, the tips and bases and the junctions between veins may be used (Sinclair and Hoffmann, 2003), but this is not always applicable, e.g., in leaves which have only one tip and base. Recently MicroCT scanning was used to extract 3D models of entire orchid flowers, which were then analyzed using three-dimensional landmark methods (Van Der Niet et al., 2010). Most cell shapes in plants lack common landmarks, except a tip and base in some cases. It may be supposed that the tips of pavement cell lobes or trichome branches may be used as landmarks, however, cells differ widely in the number of lobes and trichome tips. It is also impossible to decide which lobe on one cell corresponds to a lobe on another cell, as the cells usually have no symmetry and no tip and base. Pseudolandmarks, defined by arbitrary sampling of a cell outline or surface at regular intervals, may be used in some cases and have been shown to perform well on some cell shapes (Pincus and Theriot, 2007).

Outline methods

The use of distance and landmark methods often requires manual measurement of shape features or marking of landmarks. Such techniques inherently suffer from bias and inaccuracy as they are influenced by skill and training level, personal preferences, fatigue and emotional and motivational factors such as experimenter's bias, as well as being time-consuming and limited in throughput. In some cases landmarks can also be difficult or impossible to identify (see above). For these reasons it may sometimes be desirable to extract and process shape information independently of landmarks. Morphometric techniques for the comparison of 2D outlines and 3D surfaces attempt to describe the entire outline or surface in the form of continuous mathematical functions and then compare the parameters of these functions, thus obviating the need to identify landmarks. Such methods typically operate on data of a low dimension (such as 2D or 3D coordinates) and transform it to a vector representation in a higher number of dimensions, thus providing a multivariate descriptor where the variables typically carry information about the entire shape, rather than specific points on it.

Examples of outline methods for continuous 2D outlines are elliptic Fourier analysis (Granlund, 1972; Kuhl and Giardina, 1982; Rohlf and Archie, 1984) and eigenshape analysis (Lohmann, 1983). The first method decomposes the shape outline as a Fourier series of trigonometric harmonic functions of increasing frequency, generating a series of Fourier coefficients which represent the shape, while the second method provides an angular representation of the outline which is then represented by a series of eigenvectors. Both methods do not strictly depend on landmark points, however, they do require digitized outline coordinates and a starting point on the outline, which may be arbitrary. The descriptors are also variant with respect to rotation and some form of registration is required. Approaches to normalize for rotational effects include Procrustes alignment of pseudolandmarks on the outline before analysis (Frieß and Baylac, 2003) and rotation of harmonics after encoding as Fourier coefficients to align the first harmonic between all shapes (Kuhl and Giardina, 1982).

The subsequent encoding in a high-dimensional morphospace provides a unique and complete representation which contains all the information which describes the shape. This is evident from the fact that the entire shape can be re-constructed and visualized from the multivariate descriptor with a desired level of precision. These methods thus allow a large amount of shape information to be collected and encoded without human participation and this permits objective, unbiased comparisons of complex shapes to be made. Even though the numerical shape representations are not readily human-interpretable, they are amenable to multivariate analysis techniques and can be used for unsupervised or supervised data mining approaches such as clustering, regression and machine learning. Such approaches have the potential to pick up patterns and differences in the data which may not be readily obvious to the human eye on the background of high shape variation, especially in complex cells like pavement cells. A number of software implementations for outline analysis are available (Slice, 1998; Hammer et al., 2001; Iwata and Ukai, 2002; Perugini, 2002).

While originally devised for computer vision shape-matching applications (Granlund, 1972; Kuhl and Giardina, 1982; Chen and Ho, 1991), the use of elliptic Fourier analysis in plant biology has been increasing in recent years, and it is becoming a popular tool for the analysis of leaf and petal shapes (Iwata and Ukai, 2002; Yoshioka et al., 2004, 2005; Andrade et al., 2008, 2010), however, its use for the analysis of plant cell shape has not been published to date.

3D methods

A criticism of outline methods is their ignorance of shape detail in the interior of the outline and the lack of recognition of 3D structure. They are thus not well suited to the comparison of complex 3D organs and cells, such as flowers, trichomes and spongy mesophyll cells. To this end, landmark-free methods for 3D shapes and 2D surfaces in 3D spaces have been developed.

An extension of elliptic Fourier analysis to three dimensions first encodes a stack of orthoslices of the shape using conventional elliptic Fourier analysis and then subjects the profile of each Fourier coefficient through the "depth" of the shape to another Fourier transform (Niculescu et al., 2002) or interpolates the depth profiles using spline curves (Jeong and Radke, 2007). Another recent method uses conformal geometry to represent 3D surfaces and defines several new distance measures for their comparison independently of landmarks (Boyer et al., 2011; Lipman and Daubechies, 2011). Although three-dimensional landmark-free outline and surface methods have attracted interest in the medical imaging and paleontological community, they are yet to be applied to plants.

One of the challenges in 3D shape comparison is obtaining three-dimensional geometric data of sufficient resolution and the extraction of the objects of interest from it. It has been possible to obtain confocal depth-stacks of plant tissues for some time, however, automated methods for processing such imagery have been limiting. Recent years have seen a profusion of such approaches published and the capabilites are rapidly increasing. Confocal stacks have been used to reconstruct the 3D structure of leaves (Wuyts et al., 2010, 2012) and parenchyma tissue in grape berries (Gray et al., 1999). Multi-angle image acquisition was used to reconstruct three-dimensional models of whole plant organs at cellular resolution and the temporal progression of flower development in Arabidopsis could be followed in unprecedented detail (Fernandez et al., 2010). Even more recently, three-dimensional cell segmentation was used to measure *in vivo* gene expression on a cell by cell basis by detecting the signal of fluorescent markers within cells (Federici et al., 2012).

A recent implementation, called TrichEratops, reconstructs plant surfaces in three dimensions from depth-stacks acquired on a light microscope and contains tools for the analysis of trichome patterning (Failmezger et al., 2013).

Morphological screening

Shape is the global output of the action of numerous cellular components and can thus be used to investigate them. Using multivariate shape data as a basis for screening allows it to be used as readout for many processes simultaneously. Untangling the effects of the various components on the readout can be achieved using data mining techniques. For example cluster analysis may group diverse shape phenotypes into separate groups which may share common causal mechanisms. This notion has been used in various approaches which have aimed to identify novel cellular components or small molecule inhibitors by using shape as an output.

Teixeira et al. (2002) used the shapes of yeast nuclei to identify novel proteins involved in nuclear architecture and gene silencing (Teixeira et al., 2002). The study used manual observation of images to identify defective phenotypes. However, another study conducted an unbiased image-based screen using automated microscopy and an image processing pipeline which automatically quantified 40 parameters in human cancer cell lines, including 10 descriptors of shape, to identify two new inhibitors of protein kinases (Tanaka et al., 2005). Morphological data was also used to identify RhoGAP/GTP'ase signaling interactions in *Drosophilla* cells (Nir et al., 2010). Both commercial and open-source automated image analysis pipelines are becoming increasingly popular. CellProfiler is a powerful open-source implementation, able to extract and analyse a large array of data from a variety of images (Carpenter et al., 2006). CellProfiler was recently used in a supervised machine learning approach where a classifier was trained by human users to automatically identify particular subtle cellular phenotypes (Jones et al., 2009). However, systematic screening approaches using objective image-derived morphological data are yet to be conducted in plants.

PERSPECTIVE

It is becoming increasingly clear that hormonal regulation, chiefly auxin and cytokinin, is an important cue for cell shape formation. This input may then impact on the activity of small GTP'ases that organize the cytoskeleton, which in turn affect the location and direction of the cell wall architecture. While some of the regulatory aspects therefore are beginning to emerge, much remains to be investigated. For example, how are hormonal gradients interacting and then being translated to recruitments of certain factors to one side of the cell but not another? In addition, the behavior of certain components within the cell is largely interpreted without considering effects from neighboring cells nor from the tissue that the cell is embedded in. Hence, it will be important to understand the behavior of the cell in these types of contexts, especially with regards to the mechanical stresses that are generated when a tissue is expanding. In a wider perspective, different plant species have different developmental programs that in the end lead to great variations in cell shape. It is anticipated that we can translate some of the knowledge gleaned in Arabidopsis to understand processes in other species, but it is currently unclear how this will play out. Lastly, integrative platforms using quantitative tools to measure cell shape variations and modeling of intracellular processes will certainly be very useful to a more complete understanding of how cells obtain their shapes.

SUPPLEMENTARY MATERIAL

The Supplementary Material for this article can be found online at: http://www.frontiersin.org/journal/10.3389/fpls.2013.00439/abstract

REFERENCES

Abe, T., and Hashimoto, T. (2005). Altered microtubule dynamics by expression of modified α-tubulin protein causes right-handed helical growth in transgenic Arabidopsis plants. *Plant J.* 43, 191–204. doi: 10.1111/j.1365-313X.2005.02442.x

Abe, T., Thitamadee, S., and Hashimoto, T. (2004). Microtubule defects and cell morphogenesis in the lefty1lefty2 tubulin mutant of *Arabidopsis thaliana*. *Plant Cell Physiol.* 45, 211–220. doi: 10.1093/pcp/pch026

Ambrose, J. C., Shoji, T., Kotzer, A. M., Pighin, J. A., and Wasteneys, G. O. (2007). The arabidopsis CLASP gene encodes a microtubule-associated protein involved in cell expansion and division. *Plant Cell Online* 19, 2763–2775. doi: 10.1105/tpc.107.053777

Anderson, C. T., Carroll, A., Akhmetova, L., and Somerville, C. (2010). Real-time imaging of cellulose reorientation during cell wall expansion in arabidopsis roots. *Plant Physiol.* 152, 787–796. doi: 10.1104/pp.109.150128

Andrade, I., Mayo, S., Kirkup, D., and Van Den Berg, C. (2008). Comparative morphology of populations of Monstera Adans. (Araceae) from natural forest fragments in Northeast Brazil using elliptic Fourier Analysis of leaf outlines. *Kew Bull.* 63, 193–211. doi: 10.1007/s12225-008-9032-z

Andrade, I., Mayo, S., Kirkup, D., and Van Den Berg, C. (2010). Elliptic fourier analysis of leaf outline shape in forest fragment populations of *anthurium sinuatum* and A. pentaphyllum (araceae) from northeast brazil. *Kew Bull.* 65, 3–20. doi: 10.1007/s12225-010-9188-1

Arioli, T., Peng, L., Betzner, AS., Burn, J., Wittke, W., Herth, W., et al. (1998). Molecular analysis of cellulose biosynthesis in arabidopsis. *Science* 279, 717–720. doi: 10.1126/science.279.5351.717

Badescu, G. O., and Napier, R. M. (2006). Receptors for auxin: will it all end in TIRs? *Trends Plant Sci.* 11, 217–223. doi: 10.1016/j.tplants.2006.03.001

Baluška, F., Hlavacka, A., Šamaj, J., Palme, K., Robinson, D. G., Matoh, T., et al. (2002). F-actin-dependent endocytosis of cell wall pectins in meristematic root cells. insights from brefeldin a-induced compartments. *Plant Physiol.* 130, 422–431. doi: 10.1104/pp.007526

Baluska, F., Salaj, J., Mathur, J., Braun, M., Jasper, F., Samaj, J., et al. (2000). Root hair formation: F-actin-dependent tip growth is initiated by local assembly of profilin-supported F-actin meshworks accumulated within expansin-enriched bulges. *Dev. Biol.* 227, 618–632. doi: 10.1006/dbio.2000.9908

Bashline, L., Li, S., Anderson, C. T., Lei, L., and Gu, Y. (2013). The endocytosis of cellulose synthase in arabidopsis is dependent on μ2, a clathrin-mediated endocytosis adaptin. *Plant Physiol.* 163, 150–160. doi: 10.1104/pp.113.221234

Baskin, T. I., Meekes, H. T. H. M., Liang, B. M., and Sharp, R. E. (1999). Regulation of growth anisotropy in well-watered and water-stressed maize roots. II. role of cortical microtubules and cellulose microfibrils. *Plant Physiol.* 119, 681–692. doi: 10.1104/pp.119.2.681

Basu, D., El-Assal, S. E.-D., Le, J., Mallery, E. L., and Szymanski, D. B. (2004). Interchangeable functions of Arabidopsis PIROGI and the human WAVE complex subunit SRA1 during leaf epidermal development. *Development* 131, 4345–4355. doi: 10.1242/dev.01307

Basu, D., Le, J., El-Essal, S. E.-D., Huang, S., Zhang, C., Mallery, E. L., et al. (2005). DISTORTED3/SCAR2 is a putative arabidopsis WAVE complex subunit that activates the Arp2/3 complex and is required for epidermal morphogenesis. *Plant Cell Online* 17, 502–524. doi: 10.1105/tpc.104.027987

Basu, D., Le, J., Zakharova, T., Mallery, E. L., and Szymanski, D. B. (2008). A SPIKE1 signaling complex controls actin-dependent cell morphogenesis through the heteromeric WAVE and ARP2/3 complexes. *Proc. Natl. Acad. Sci. U.S.A.*105, 4044–4049. doi: 10.1073/pnas.0710294105

Basu, P., Pal, A., Lynch, J. P., and Brown, K. M.(2007). A novel image-analysis technique for kinematic study of growth and curvature. *Plant Physiol.* 145, 305–316. doi: 10.1104/pp.107.103226

Bichet, A., Desnos, T., Turner, S., Grandjean, O., and Höfte, H. (2001). BOTERO1 is required for normal orientation of cortical microtubules and anisotropic cell expansion in Arabidopsis. *Plant J.* 25, 137–148. doi: 10.1046/j.1365-313x.2001.00946.x

Blilou, I., Xu, J., Wildwater, M., Willemsen, V., Paponov, I., Friml, J., et al. (2005). The PIN auxin efflux facilitator network controls growth and patterning in Arabidopsis roots. *Nature* 433, 39–44. doi: 10.1038/nature03184

Boyer, D. M., Lipman, Y., St. Clair, E., Puente, J., Patel, B. A., Funkhouser, T., et al. (2011). Algorithms to automatically quantify the geometric similarity of anatomical surfaces. *Proc. Natl. Acad. Sci. U.S.A.* 108, 18221–18226. doi: 10.1073/pnas.1112822108

Brembu, T., Winge, P., Seem, M., and Bones, A. M. (2004). NAPP and PIRP encode subunits of a putative wave regulatory protein complex involved in plant cell morphogenesis. *Plant Cell Online* 16, 2335–2349. doi: 10.1105/tpc.104.023739

Bringmann, M., Li, E., Sampathkumar, A., Kocabek, T., Hauser, M.-T., and Persson, S. (2012). POM-POM2/cellulose synthase interacting1 is essential for the functional association of cellulose synthase and microtubules in arabidopsis. *Plant Cell Online* 24, 163–177. doi: 10.1105/tpc.111.093575

Burgert, I., and Fratzl, P. (2009). Plants control the properties and actuation of their organs through the orientation of cellulose fibrils in their cell walls. *Integr. Comp. Biol.* 49, 69–79. doi: 10.1093/icb/icp026

Burk, D. H., Liu, B., Zhong, R., Morrison, W. H., and Ye, Z.-H. (2001). A katanin-like protein regulates normal cell wall gbiosynthesis and cell elongation. *Plant Cell Online* 13, 807–827. doi: 10.1105/tpc.13.4.807

Burn, J. E., Hurley, U. A., Birch, R. J., Arioli, T., Cork, A., and Williamson, R. E. (2002). The cellulose-deficient Arabidopsis mutant rsw3 is defective in a gene encoding a putative glucosidase II, an enzyme processing N-glycans during ER quality control. *Plant J.* 32, 949–960. doi: 10.1046/j.1365-313X.2002.01483.x

Buschmann, H., Fabri, C. O., Hauptmann, M., Hutzler, P., Laux, T., Lloyd, C. W., et al. (2004). Helical growth of the arabidopsis mutant tortifolia1 reveals a plant-specific microtubule-associated protein. *Curr. Biol.* 14, 1515–1521. doi: 10.1016/j.cub.2004.08.033

Carpenter, A., Jones, T., Lamprecht, M., Clarke, C., Kang, I., Friman, O., et al. (2006). CellProfiler: image analysis software for identifying and quantifying cell phenotypes. *Genome Biol.* 7:R100. doi: 10.1186/gb-2006-7-10-r100

Chen, Z., and Ho, S.-Y. (1991). Computer vision for robust 3D aircraft recognition with fast library search. *Pattern Recogn.* 24, 375–390. doi: 10.1016/0031-3203(91)90051-6

Collings, D. A., Gebbie, L. K., Howles, P. A., Hurley, U. A., Birch, R. J., Cork, A. H., et al. (2008). Arabidopsis dynamin-like protein DRP1A: a null mutant with widespread defects in endocytosis, cellulose synthesis, cytokinesis, and cell expansion. *J. Exp. Bot.* 59, 361–376. doi: 10.1093/jxb/erm324

Cookson, S. J., Van Lijsebettens, M., and Granier, C. (2005). Correlation between leaf growth variables suggest intrinsic and early controls of leaf size in *Arabidopsis thaliana*. *Plant Cell Environ.* 28, 1355–1366. doi: 10.1111/j.1365-3040.2005.01368.x

Cosgrove, D. J. (2000). Loosening of plant cell walls by expansins. *Nature* 407, 321–326. doi: 10.1038/35030000

Cosgrove, D. J. (2005). Growth of the plant cell wall. *Nat. Rev. Mol. Cell Biol.* 6, 850–861. doi: 10.1038/nrm1746

Crowell, E. F., Bischoff, V., Desprez, T., Rolland, A., Stierhof, Y.-D., Schumacher, K., et al. (2009). Pausing of golgi bodies on microtubules regulates secretion of cellulose synthase complexes in arabidopsis. *Plant Cell Online* 21, 1141–1154. doi: 10.1105/tpc.108.065334

Deeks, M. J., Kaloriti, D., Davies, B., Malhó, R., and Hussey, P. J. (2004). Arabidopsis NAP1 Is Essential for Arp2/3-Dependent Trichome Morphogenesis. *Curr. Biol.* 14, 1410–1414. doi: 10.1016/j.cub.2004.06.065

Dhonukshe, P., Aniento, F., Hwang, I., Robinson, D. G., Mravec, J., Stierhof, Y.-D., et al. (2007). Clathrin-mediated constitutive endocytosis of PIN auxin efflux carriers in arabidopsis. *Curr. Biol.* 17, 520–527. doi: 10.1016/j.cub.2007.01.052

Djakovic, S., Dyachok, J., Burke, M., Frank, M. J., and Smith, L. G. (2006). BRICK1/HSPC300 functions with SCAR and the ARP2/3 complex to regulate epidermal cell shape in Arabidopsis. *Development* 133, 1091–1100. doi: 10.1242/dev.02280

Dolan, L., and Langdale, J. A. (2004). New insights into plant development in New England. *Dev.* 131, 5215–5220. doi: 10.1242/dev.01439

El-Assal, S. E.-D., Le, J., Basu, D., Mallery, E. L., and Szymanski, D. B. (2004). Arabidopsis GNARLED Encodes a NAP125 Homolog that Positively Regulates ARP2/3. *Curr. Biol.* 14, 1405–1409. doi: 10.1016/j.cub.2004.06.062

El-Din El-Assal, S., Le, J., Basu, D., Mallery, E. L., and Szymanski, D. B. (2004). DISTORTED2 encodes an ARPC2 subunit of the putative Arabidopsis ARP2/3 complex. *Plant J.* 38, 526–538. doi: 10.1111/j.1365-313X.2004.02065.x

Erickson, R. O. (1966). Relative elemental rates and anisotropy of growth in area: a computer programme. *J. Exp. Bot.* 17, 390–403. doi: 10.1093/jxb/17.2.390

Fagard, M., Desnos, T., Desprez, T., Goubet, F., Refregier, G., Mouille, G., et al. (2000). PROCUSTE1 encodes a cellulose synthase required for normal cell elongation specifically in roots and dark-grown hypocotyls of arabidopsis. *Plant Cell Online* 12, 2409–2423. doi: 10.1105/tpc.12.12.2409

Failmezger, H., Jaegle, B., Schrader, A., Hülskamp, M., and Tresch, A. (2013). Semi-automated 3D leaf reconstruction and analysis of trichome patterning from light microscopic images. *PLoS Comput. Biol.* 9:e1003029. doi: 10.1371/journal.pcbi.1003029

Federici, F., Dupuy, L., Laplaze, L., Heisler, M., and Haseloff, J. (2012). Integrated genetic and computation methods for in planta cytometry. *Nat. Meth.* 9, 483–485. doi: 10.1038/nmeth.1940

Fernandez, R., Das, P., Mirabet, V., Moscardi, E., Traas, J., Verdeil, J.-L., et al. (2010). Imaging plant growth in 4D: robust tissue reconstruction and lineaging at cell resolution. *Nat. Meth.* 7, 547–553. doi: 10.1038/nmeth.1472

Frank, M., Egile, C., Dyachok, J., Djakovic, S., Nolasco, M., Li, R., et al. (2004). Activation of Arp2/3 complex-dependent actin polymerization by plant proteins distantly related to Scar/WAVE. *Proc. Natl. Acad. Sci. U.S.A.* 101, 16379–16384. doi: 10.1073/pnas.0407392101

Frank, M. J., and Smith, L. G. (2002). A small, novel protein highly conserved in plants and animals promotes the polarized growth and division of maize leaf epidermal cells. *Curr. Biol.* 12, 849–853. doi: 10.1016/S0960-9822(02)00819-9

Fratzl, P., Burgert, I., and Gupta, H. S. (2004). On the role of interface polymers for the mechanics of natural polymeric composites. *Phys. Chem. Chem. Phys.* 6, 5575–5579. doi: 10.1039/b411986j

Frieß, M., and Baylac, M. (2003). Exploring artificial cranial deformation using elliptic Fourier analysis of procrustes aligned outlines. *Am. J. Phys. Anthropol.* 122, 11–22. doi: 10.1002/ajpa.10286

Friml, J., Yang, X., Michniewicz, M., Weijers, D., Quint, A., Tietz, O., et al. (2004). A PINOID-dependent binary switch in apical-basal PIN polar targeting directs auxin efflux. *Science* 306, 862–865. doi: 10.1126/science.1100618

Fry, S. C., Smith, R. C., Renwick, K. F., Martin, D. J., Hodge, S. K., and Matthews, K. J. (1992). Xyloglucan endotransglycosylase, a new wall-loosening enzyme activity from plants. *Biochem. J.* 282, 821–828.

Fu, Y., Gu, Y., Zheng, Z., Wasteneys, G., and Yang, Z. (2005). Arabidopsis interdigitating cell growth requires two antagonistic pathways with opposing action on cell morphogenesis. *Cell* 120, 687–700. doi: 10.1016/j.cell.2004.12.026

Fu, Y., Li, H., and Yang, Z. (2002). The ROP2 GTPase controls the formation of cortical fine F-actin and the early phase of directional cell expansion during arabidopsis organogenesis. *Plant Cell Online* 14, 777–794. doi: 10.1105/tpc.001537

Fu, Y., Xu, T., Zhu, L., Wen, M., and Yang, Z. (2009). A ROP GTPase signaling pathway controls cortical microtubule ordering and cell expansion in arabidopsis. *Curr. Biol.* 19, 1827–1832. doi: 10.1016/j.cub.2009.08.052

Fujita, M., Himmelspach, R., Ward, J., Whittington, A., Hasenbein, N., Liu, C., et al. (2013). The anisotropy1 D604N mutation in the arabidopsis cellulose synthase1 catalytic domain reduces cell wall crystallinity and the velocity of cellulose synthase complexes. *Plant Physiol.* 162, 74–85. doi: 10.1104/pp.112.211565

Furutani, I., Watanabe, Y., Prieto, R., Masukawa, M., Suzuki, K., Naoi, K., et al. (2000). The SPIRAL genes are required for directional control of cell elongation in A*arabidopsis thaliana*. *Development* 127, 4443–4453. Available online at: http://dev.biologists.org/content/127/20/4443.long

Gautreau, A., Ho, H.-Y. H., Li, J., Steen, H., Gygi, S. P., and Kirschner, M. W. (2004). Purification and architecture of the ubiquitous Wave complex. *Proc. Natl. Acad. Sci. U.S.A.* 101, 4379–4383. doi: 10.1073/pnas.0400628101

Gilliland, L. U., Kandasamy, M. K., Pawloski, L. C., and Meagher, R. B. (2002). Both vegetative and reproductive actin isovariants complement the stunted root hair phenotype of the arabidopsisact2-1 mutation. *Plant Physiol.* 130, 2199–2209. doi: 10.1104/pp.014068

Gower, J. (1975). Generalized procrustes analysis. *Psychometrika* 40, 33–51. doi: 10.1007/BF02291478

Granlund, G. H. (1972). Fourier preprocessing for hand print character recognition. *Comp. IEEE Trans.* 21, 195–201. doi: 10.1109/TC.1972.5008926

Gray, J. D., Kolesik, P., Høj, P. B., and Coombe, B. G. (1999). Confocal measurement of the three-dimensional size and shape of plant parenchyma cells in a developing fruit tissue. *Plant J.* 19, 229–236. doi: 10.1046/j.1365-313X.1999.00512.x

Green, P. B. (1962). Mechanism for plant cellular morphogenesis. *Science* 138, 1404–1405. doi: 10.1126/science.138.3548.1404

Green, P. B. (1965). Pathways of cellular morphogenesis: a diversity in nitella. *J. Cell Biol.* 27, 343–363. doi: 10.1083/jcb.27.2.343

Hamant, O. (2013). Integrative cell biology: katanin at the crossroads. *Curr. Biol.* 23: R206–R208. doi: 10.1016/j.cub.2013.01.031

Hammer, Ø., Harper, D., and Ryan, P. (2001). PAST: paleontological statistics software package for education and data analysis. *Palaeontol. Electron.* 4, 9. Available online at: http://palaeo-electronica.org/2001_1/past/issue1_01.htm

Hashimoto, T. (2002). Molecular genetic analysis of left–right handedness in plants. *Philos. Trans. R. Soc. Lond. B Biol. Sci.* 357, 799–808. doi: 10.1098/rstb.2002.1088

Hazak, O., Bloch, D., Poraty, L., Sternberg, H., Zhang, J., Friml, J., et al. (2010). A Rho scaffold integrates the secretory system with feedback mechanisms in regulation of auxin distribution. *PLoS Biol.* 8:e1000282. doi: 10.1371/journal.pbio.1000282

Huang, F., Kemel Zago, M., Abas, L., Van Marion, A., Galván-Ampudia, C. S., and Offringa, R. (2010). Phosphorylation of conserved PIN motifs directs arabidopsis PIN1 polarity and auxin transport. *Plant Cell Online* 22, 1129–1142. doi: 10.1105/tpc.109.072678

Hülskamp, M., Miséra, S., and Jürgens, G. (1994). Genetic dissection of trichome cell development in Arabidopsis. *Cell* 76, 555–566. doi: 10.1016/0092-8674(94)90118-X

Ishida, T., Kaneko, Y., Iwano, M., and Hashimoto, T. (2007). Helical microtubule arrays in a collection of twisting tubulin mutants of *Arabidopsis thaliana*. *Proc. Natl. Acad. Sci. U.S.A.* 104, 8544–8549. doi: 10.1073/pnas.0701224104

Iwata, H., and Ukai, Y. (2002). SHAPE: a computer program package for quantitative evaluation of biological shapes based on elliptic fourier descriptors. *J. Hered.* 93, 384–385. doi: 10.1093/jhered/93.5.384

Jeong, Y., and Radke, R. J. (2007). Reslicing axially sampled 3D shapes using elliptic Fourier descriptors. *Med. Image Anal.* 11, 197–206. doi: 10.1016/j.media.2006.12.003

Jones, T. R., Carpenter, A. E., Lamprecht, M. R., Moffat, J., Silver, S. J., Grenier, J. K., et al. (2009). Scoring diverse cellular morphologies in image-based screens with iterative feedback and machine learning. *Proc. Natl. Acad. Sci. U.S.A.* 106, 1826–1831. doi: 10.1073/pnas.0808843106

Kandasamy, M. K., McKinney, E. C., and Meagher, R. B. (2009). A single vegetative actin isovariant overexpressed under the control of multiple regulatory sequences is sufficient for normal arabidopsis development. *Plant Cell Online* 21, 701–718. doi: 10.1105/tpc.108.061960

Kerstens, S., Decraemer, W. F., and Verbelen, J.-P. (2001). Cell walls at the plant surface behave mechanically like fiber-reinforced composite materials. *Plant Physiol.* 127, 381–385. doi: 10.1104/pp.010423

Kirik, V., Herrmann, U., Parupalli, C., Sedbrook, J. C., Ehrhardt, D. W., and Hülskamp, M. (2007). CLASP localizes in two discrete patterns on cortical microtubules and is required for cell morphogenesis and cell division in Arabidopsis. *J. Cell. Sci.* 120, 4416–4425. doi: 10.1242/jcs.024950

Kleine-Vehn, J., Huang, F., Naramoto, S., Zhang, J., Michniewicz, M., Offringa, R., et al. (2009). PIN auxin efflux carrier polarity is regulated by PINOID kinase-mediated recruitment into GNOM-independent trafficking in arabidopsis. *Plant Cell Online* 21, 3839–3849. doi: 10.1105/tpc.109.071639

Kotzer, A. M., and Wasteneys, G. O. (2006). Mechanisms behind the puzzle: microtubuleâ€"microfilament cross-talk in pavement cell formationThis review is one of a selection of papers published in the special issue on plant cell biology." *Can. J. Bot.* 84, 594–603. doi: 10.1139/b06-023

Kuhl, F. P., and Giardina, C. R. (1982). Elliptic Fourier features of a closed contour. *Comp. Graph. Image Process.* 18, 236–258. doi: 10.1016/0146-664X(82)90034-X

Kutschera, U. (2008). The growing outer epidermal wall: design and physiological role of a composite structure. *Ann. Bot.* 101, 615–621. doi: 10.1093/aob/mcn015

Kutschera, U., and Niklas, K. J. (2007). The epidermal-growth-control theory of stem elongation: an old and a new perspective. *J. Plant Physiol.* 164, 1395–1409. doi: 10.1016/j.jplph.2007.08.002

Landrein, B., Lathe, R., Bringmann, M., Vouillot, C., Ivakov, A., Boudaoud, A., et al. (2013). Impaired cellulose synthase guidance leads to stem torsion and twists phyllotactic patterns in arabidopsis. *Curr. Biol.* 23, 895–900. doi: 10.1016/j.cub.2013.04.013

Lane, D. R., Wiedemeier, A., Peng, L., Höfte, H., Vernhettes, S., Desprez, T., et al. (2001). Temperature-sensitive alleles of RSW2 Link the KORRIGAN Endo-1, 4-β-Glucanase to cellulose synthesis and cytokinesis in arabidopsis. *Plant Physiol.* 126, 278–288. doi: 10.1104/pp.126.1.278

Lavy, M., Bloch, D., Hazak, O., Gutman, I., Poraty, L., Sorek, N., et al. (2007). A novel ROP/RAC effector links cell polarity, root-meristem maintenance, and vesicle trafficking. *Curr. Biol.* 17, 947–952. doi: 10.1016/j.cub.2007.04.038

Le, J., Mallery, E. L., Zhang, C., Brankle, S., and Szymanski, D. B. (2006). Arabidopsis BRICK1/HSPC300 is an essential WAVE-complex subunit that selectively stabilizes the Arp2/3 Activator SCAR2. *Curr. Biol.* 16, 895–901. doi: 10.1016/j.cub.2006.03.061

Li, H., Lin, D., Dhonukshe, P., Nagawa, S., Chen, D., Friml, J., et al. (2011). Phosphorylation switch modulates the interdigitated pattern of PIN1 localization and cell expansion in Arabidopsis leaf epidermis. *Cell Res.* 21, 970–978. doi: 10.1038/cr.2011.49

Li, H., Xu, T., Lin, D., Wen, M., Xie, M., Duclercq, J., et al. (2013). Cytokinin signaling regulates pavement cell morphogenesis in Arabidopsis. *Cell Res.* 23, 290–299. doi: 10.1038/cr.2012.146

Li, S., Blanchoin, L., Yang, Z., and Lord, E. M. (2003). The putative arabidopsis Arp2/3 complex controls leaf cell morphogenesis. *Plant Physiol.* 132, 2034–2044. doi: 10.1104/pp.103.028563

Li, S., Lei, L., Somerville, C. R., and Gu, Y. (2012). Cellulose synthase interactive protein 1 (CSI1) links microtubules and cellulose synthase complexes. *Proc. Natl. Acad. Sci. U.S.A.* 109, 185–190. doi: 10.1073/pnas.1118560109

Lin, D., Cao, L., Zhou, Z., Zhu, L., Ehrhardt, D., and Yang, Z. (2013). Rho GTPase signaling activates microtubule severing to promote microtubule ordering in arabidopsis. *Curr. Biol.* 23, 290–297. doi: 10.1016/j.cub.2013.01.022

Lipman, Y., and Daubechies, I. (2011). Conformal wasserstein distances: comparing surfaces in polynomial time. *Adv. Math.* 227, 1047–1077. doi: 10.1016/j.aim.2011.01.020

Lloyd, C. (2011). Dynamic microtubules and the texture of plant cell walls. *Int. Rev. Cell Mol. Biol.* 287, 287–329. doi: 10.1016/B978-0-12-386043-9.00007-4

Lohmann, G. P. (1983). Eigenshape analysis of microfossils: a general morphometric procedure for describing changes in shape. *J. Int. Assoc. Math. Geol.* 15, 659–672. doi: 10.1007/BF01033230

Machesky, L. M., and Gould, K. L. (1999). The Arp2/3 complex: a multifunctional actin organizer. *Curr. Opin. Cell Biol.* 11, 117–121. doi: 10.1016/S0955-0674(99)80014-3

Marcotrigiano, M. (2010). A role for leaf epidermis in the control of leaf size and the rate and extent of mesophyll cell division. *Am. J. Bot.* 97, 224–233. doi: 10.3732/ajb.0900102

Mathur, J. (2006). Local interactions shape plant cells. *Curr. Opin. Cell Biol.* 18, 40–46. doi: 10.1016/j.ceb.2005.12.002

Mathur, J., Mathur, N., Kernebeck, B., and Hülskamp, M. (2003a).Mutations in actin-related proteins 2 and 3 affect cell shape development in arabidopsis. *Plant Cell Online* 15, 1632–1645. doi: 10.1105/tpc.011676

Mathur, J., Mathur, N., Kirik, V., Kernebeck, B., Srinivas, B. P., and Hülskamp, M. (2003b). Arabidopsis CROOKED encodes for the smallest subunit of the ARP2/3 complex and controls cell shape by region specific fine F-actin formation. *Development* 130, 3137–3146. doi: 10.1242/dev.00549

Micheli, F. (2001). Pectin methylesterases: cell wall enzymes with important roles in plant physiology. *Trends Plant Sci.* 6, 414–419. doi: 10.1016/S1360-1385(01)02045-3

Michniewicz, M., Zago, M. K., Abas, L., Weijers, D., Schweighofer, A., Meskiene, I., et al. (2007).Antagonistic regulation of PIN phosphorylation by PP2A and PINOID directs auxin flux. *Cell* 130, 1044–1056. doi: 10.1016/j.cell.2007.07.033

Nagawa, S., Xu, T., Lin, D., Dhonukshe, P., Zhang, X., Friml, J., et al. (2012).ROP GTPase-dependent actin microfilaments promote PIN1 polarization by localized inhibition of clathrin-dependent endocytosis. *PLoS Biol.* 10:e1001299. doi: 10.1371/journal.pbio.1001299

Nakajima, K., Furutani, I., Tachimoto, H., Matsubara, H., and Hashimoto, T. (2004). SPIRAL1 encodes a plant-specific microtubule-localized protein required for directional control of rapidly expanding arabidopsis cells.*Plant Cell Online* 16, 1178–1190. doi: 10.1105/tpc.017830

Nakamura, M., Naoi, K., Shoji, T., and Hashimoto, T. (2004). Low concentrations of propyzamide and oryzalin alter microtubule dynamics in arabidopsis epidermal cells. *Plant Cell Physiol.* 45, 1330–1334. doi: 10.1093/pcp/pch300

Niculescu, G., Toni, L., Foran, D., Nosher, J., and Demarco, J. (2002).A dynamic imaging database for 3-D morphologic analysis and clinical assessment in diagnostic radiology. *Proc. AMIA Symp.* 1115. Available online at: http://www.ncbi.nlm.nih.gov/pmc/articles/PMC2244582/?page=1

Nir, O., Bakal, C., Perrimon, N., and Berger, B. (2010). Inference of RhoGAP/GTPase regulation using single-cell morphological data from a combinatorial RNAi screen. *Genome Res.* 20, 372–380. doi: 10.1101/gr.100248.109

Paredez, A. R., Somerville, C. R., and Ehrhardt, D. W. (2006). Visualization of cellulose synthase demonstrates functional association with microtubules. *Science* 312, 1491–1495. doi: 10.1126/science.1126551

Passardi, F., Penel, C., and Dunand, C. (2004). Performing the paradoxical: how plant peroxidases modify the cell wall. *Trends Plant Sci.* 9, 534–540. doi: 10.1016/j.tplants.2004.09.002

Perugini, D. (2002). MorphoUt 1.0: utilities for closed shape morphometry. *Comput. Geosci.* 28, 73–79. doi: 10.1016/S0098-3004(01)00055-3

Pincus, Z., and Theriot, J. A. (2007). Comparison of quantitative methods for cell-shape analysis. *J. Microsc.* 227, 140–156. doi: 10.1111/j.1365-2818.2007.01799.x

Poethig, R. S., and Sussex, I. M. (1985). The developmental morphology and growth dynamics of the tobacco leaf. *Planta* 165, 158–169. doi: 10.1007/BF00395038

Probine, M. C. (1963). Cell growth and the structure and mechanical properties of the wall in internodal cells of nitella opaca: III. SPIRAL GROWTH AND CELL WALL STRUCTURE. *J. Exp. Bot.* 14, 101–113. doi: 10.1093/jxb/14.1.101

Qi, X., Kaneda, M., Chen, J., Geitmann, A., and Zheng, H. (2011). A specific role for Arabidopsis TRAPPII in post-Golgi trafficking that is crucial for cytokinesis and cell polarity. *Plant J.* 68, 234–248. doi: 10.1111/j.1365-313X.2011.04681.x

Qiu, J. L., Jilk, R., Marks, M. D., and Szymanski, D. B. (2002). The arabidopsis SPIKE1 gene is required for normal cell shape control and tissue development. *Plant Cell Online* 14, 101–118. doi: 10.1105/tpc.010346

Refrégier, G., Pelletier, S., Jaillard, D., and Höfte, H. (2004). Interaction between wall deposition and cell elongation in dark-grown hypocotyl cells in arabidopsis. *Plant Physiol.* 135, 959–968. doi: 10.1104/pp.104.038711

Remmler, L., and Rolland-Lagan, A.-G. (2012).computational method for quantifying growth patterns at the adaxial leaf surface in three dimensions. *Plant Physiol.* 159, 27–39. doi: 10.1104/pp.112.194662

Rohlf, F. J., and Archie, J. W. (1984). A comparison of fourier methods for the description of wing shape in mosquitoes (Diptera: Culicidae). *Syst. Biol.* 33, 302–317. doi: 10.2307/2413076

Rohlf, F. J., and Slice, D. (1990). Extensions of the procrustes method for the optimal superimposition of landmarks. *Syst. Biol.* 39, 40–59. doi: 10.2307/2992207

Rolland-Lagan, A.-G., Bangham, J. A., and Coen, E. (2003).Growth dynamics underlying petal shape and asymmetry. *Nature* 422, 161–163. doi: 10.1038/nature01443

Rolland-Lagan, A.-G., Coen, E., Impey, S. J., and Bangham, J. A. (2005).A computational method for inferring growth parameters and shape changes during development based on clonal analysis.*J. Theor. Biol.* 232, 157–177. doi: 10.1016/j.jtbi.2004.04.045

Sampathkumar, A., Gutierrez, R., McFarlane, H. E., Bringmann, M., Lindeboom, J., Emons, A.-M., et al. (2013). Patterning and lifetime of plasma membrane-localized cellulose synthase is dependent on actin organization in arabidopsis interphase cells. *Plant Physiol.* 162, 675–688. doi: 10.1104/pp.113.215277

Sampathkumar, A., Lindeboom, J. J., Debolt, S., Gutierrez, R., Ehrhardt, D. W., Ketelaar, T., et al. (2011). Live cell imaging reveals structural associations between the actin and microtubule cytoskeleton in arabidopsis. *Plant Cell Online* 23, 2302–2313. doi: 10.1105/tpc.111.087940

Schmundt, D., Stitt, M., Jahne, B., and Schurr, U. (1998). Quantitative analysis of the local rates of growth of dicot leaves at a high temporal and spatial resolution, using image sequence analysis. *Plant J.* 16, 505–514. doi: 10.1046/j.1365-313x.1998.00314.x

Schopfer, P. (1996). Hydrogen peroxide-mediated cell-wall stiffening *in vitro* in maize coleoptiles. *Planta* 199, 43–49. doi: 10.1007/BF00196879

Sedbrook, J. C., Ehrhardt, D. W., Fisher, S. E, Scheible, W. R., and Somerville, C. R. (2004). The Arabidopsis SKU6/SPIRAL1 gene encodes a plus end–localized microtubule-interacting protein involved in directional cell expansion. *Plant Cell Online* 16, 1506–1520. doi: 10.1105/tpc.020644

Selbach, K. (2012). *Funktionelle Analyse des SCAR/WAVE- und Exocyst-Komplexes hinsichtlich der Zellmorphogenese in Arabidopsis thaliana*. Ph.D. thesis, Universität zu Köln, Köln.

Shaw, S. L., Kamyar, R., and Ehrhardt, D. W. (2003). Sustained microtubule treadmilling in arabidopsis cortical arrays. *Science* 300, 1715–1718. doi: 10.1126/science.1083529

Shoji, T., Narita, N. N., Hayashi, K., Asada, J., Hamada, T., Sonobe, S., et al. (2004). Plant-specific microtubule-associated protein SPIRAL2 is required for anisotropic growth in arabidopsis. *Plant Physiol.* 136, 3933–3944. doi: 10.1104/pp.104.051748

Silk, W. K., and Erickson, R. O. (1979). Kinematics of plant growth. *J. Theor. Biol.* 76, 481–501. doi: 10.1016/0022-5193(79)90014-6

Sinclair, C., and Hoffmann, A. A. (2003). Monitoring salt stress in grapevines: are measures of plant trait variability useful? *J. Appl. Ecol.* 40, 928–937. doi: 10.1046/j.1365-2664.2003.00843.x

Slice, D. (1998). *Morpheus et al.: Software for Morphometric Research*. Stony Brook, NY: Department of Ecology and Evolution, State University of New York.

Sugimoto, K., Himmelspach, R., Williamson, R. E., and Wasteneys, G. O. (2003). Mutation or drug-dependent microtubule disruption causes radial swelling without altering parallel cellulose microfibril deposition in arabidopsis root cells. *Plant Cell Online* 15, 1414–1429. doi: 10.1105/tpc.011593

Suslov, D., and Verbelen, J.-P. (2006). Cellulose orientation determines mechanical anisotropy in onion epidermis cell walls. *J. Exp. Bot.* 57, 2183–2192. doi: 10.1093/jxb/erj177

Suslov, D., Verbelen, J.-P., and Vissenberg, K. (2009).Onion epidermis as a new model to study the control of growth anisotropy in higher plants. *J. Exp. Bot.* 60, 4175–4187. doi: 10.1093/jxb/erp251

Szymanski, D. B. (2005). Breaking the WAVE complex: the point of Arabidopsis trichomes. *Curr. Opin. Plant Biol.* 8, 103–112. doi: 10.1016/j.pbi.2004.11.004

Tanaka, M., Bateman, R., Rauh, D., Vaisberg, E., Ramachandani, S., Zhang, C., et al. (2005).An unbiased cell morphology–based screen for new, biologically active small molecules. *PLoS Biol.* 3:e128. doi: 10.1371/journal.pbio.0030128

Teixeira, M. T., Dujon, B., and Fabre, E. (2002).Genome-wide nuclear morphology screen identifies novel genes involved in nuclear architecture and Gene-silencing in Saccharomyces cerevisiae. *J. Mol. Biol.* 321, 551–561. doi: 10.1016/S0022-2836(02)00652-6

Terbush, D. R., Maurice, T., Roth, D., and Novick, P. (1996). The Exocyst is a multiprotein complex required for exocytosis in Saccharomyces cerevisiae. *EMBO J.* 15, 6483–6494.

Thitamadee, S., Tuchihara, K., and Hashimoto, T. (2002). Microtubule basis for left-handed helical growth in Arabidopsis. *Nature* 417, 193–196. doi: 10.1038/417193a

Tsukaya, H. (2003). Organ shape and size: a lesson from studies of leaf morphogenesis. *Curr. Opin. Plant Biol.* 6, 57–62. doi: 10.1016/S1369526602000055

Van Der Niet, T., Zollikofer, C. P. E., León, M. S. P. D., Johnson, S. D., and Linder, H. P. (2010). Three-dimensional geometric morphometrics for studying floral shape variation. *Trends Plant Sci.* 15, 423–426. doi: 10.1016/j.tplants.2010.05.005

van der Weele, C. M., Jiang, H. S., Palaniappan, K. K., Ivanov, V. B., Palaniappan, K., and Baskin, T. I. (2003). A new algorithm for computational image analysis of deformable motion at high spatial and temporal resolution applied to root growth. roughly uniform elongation in the meristem and also, after an abrupt acceleration, in the elongation zone. *Plant Physiol.* 132, 1138–1148. doi: 10.1104/pp.103.021345

Van Sandt, V. S. T., Suslov, D., Verbelen, J.-P., and Vissenberg, K. (2007).Xyloglucan endotransglucosylase activity loosens a plant cell wall. *Ann. Bot.* 100, 1467–1473. doi: 10.1093/aob/mcm248

Vissenberg, K., Fry, S. C., and Verbelen, J. P. (2001). Root hair initiation is coupled to a highly localized increase of xyloglucan endotransglycosylase action in arabidopsis roots. *Plant Physiol.* 127, 1125–1135. doi: 10.1104/pp.010295

Wada, H. (2012). Hierarchical helical order in the twisted growth of plant organs. *Phys. Rev. Lett.* 109, 128104. doi: 10.1103/PhysRevLett.109.128104

Wang, X., Zhu, L., Liu, B., Wang, C., Jin, L., Zhao, Q., et al. (2007). Arabidopsis MICROTUBULE-ASSOCIATED PROTEIN18 functions in directional cell growth by destabilizing cortical microtubules. *Plant Cell Online* 19, 877–889. doi: 10.1105/tpc.106.048579

Wasteneys, G. O. (2004). Progress in understanding the role of microtubules in plant cells. *Curr. Opin. Plant Biol.* 7, 651–660. doi: 10.1016/j.pbi.2004.09.008

Wasteneys, G. O., and Ambrose, J. C. (2009). Spatial organization of plant cortical microtubules: close encounters of the 2D kind. *Trends Cell Biol.* 19, 62–71. doi: 10.1016/j.tcb.2008.11.004

Whittington, A. T., Vugrek, O., Wei, K. J., Hasenbein, N. G., Sugimoto, K., Rashbrooke, M. C. et al. (2001). MOR1 is essential for organizing cortical microtubules in plants. *Nature* 411, 610–613. doi: 10.1038/35079128

Wiederkehr, A., Du, Y., Pypaert, M., Ferro-Novick, S., and Novick, P. (2003).Sec3p is needed for the spatial regulation of secretion and for the inheritance of the cortical endoplasmic reticulum. *Mol. Biol. Cell* 14, 4770–4782. doi: 10.1091/mbc.E03-04-0229

Williamson, R. E., Burn, J. E., Birch, R., Baskin, T. I., Arioli, T., Betzner, A. S., et al. (2001).Morphology of rsw1, a cellulose-deficient mutant of *Arabidopsis thaliana*. *Protoplasma* 215, 116–127. doi: 10.1007/BF01280308

Wu, H.-M., Hazak, O., Cheung, A. Y., and Yalovsky, S. (2011).RAC/ROP GTPases and auxin signaling. *Plant Cell Online* 23, 1208–1218. doi: 10.1105/tpc.111.083907

Wuyts, N., Massonnet, C., Dauzat, M., and Granier, C. (2012). Structural assessment of the impact of environmental constraints on *Arabidopsis thaliana* leaf growth: a 3D approach. *Plant Cell Environ.* 35, 1631–1646. doi: 10.1111/j.1365-3040.2012.02514.x

Wuyts, N., Palauqui, J.-C., Conejero, G., Verdeil, J.-L., Granier, C., and Massonnet, C. (2010).High-contrast three-dimensional imaging of the Arabidopsis leaf enables the analysis of cell dimensions in the epidermis and mesophyll. *Plant Methods* 6, 17. doi: 10.1186/1746-4811-6-17

Wymer, C., and Lloyd, C. (1996). Dynamic microtubules: implications for cell wall patterns. *Trends Plant Sci.* 1, 222–228.

Xu, T., Nagawa, S., and Yang, Z. (2011).Uniform auxin triggers the Rho GTPase-dependent formation of interdigitation patterns in pavement cells. *Small GTPases* 2, 227–232. doi: 10.4161/sgtp.2.4.16702

Xu, T., Wen, M., Nagawa, S., Fu, Y., Chen, J.-G., Wu, M.-J., et al. (2010). Cell surface- and Rho GTPase-based auxin signaling controls cellular interdigitation in arabidopsis. *Cell* 143, 99–110. doi: 10.1016/j.cell.2010.09.003

Yang, Z. (2008). Cell Polarity signaling in arabidopsis. *Annu. Rev. Cell Dev. Biol.* 24, 551–575. doi: 10.1146/annurev.cellbio.23.090506.123233

Yoshioka, Y., Iwata, H., Ohsawa, R., and Ninomiya, S. (2004). Analysis of petal shape variation of primula sieboldii by elliptic fourier descriptors and principal component analysis. *Ann. Bot.* 94, 657–664. doi: 10.1093/aob/mch190

Yoshioka, Y., Iwata, H., Ohsawa, R., and Ninomiya, S. (2005).Quantitative evaluation of the petal shape variation in Primula sieboldii caused by breeding process in the last 300 years. *Heredity* 94, 657–663. doi: 10.1038/sj.hdy.6800678

Zhang, C., Halsey, L., and Szymanski, D. (2011).The development and geometry of shape change in *Arabidopsis thaliana* cotyledon pavement cells. *BMC Plant Biol.* 11:27. doi: 10.1186/1471-2229-11-27

Zhang, X., Dyachok, J., Krishnakumar, S., Smith, L. G., and Oppenheimer, D. G. (2005). IRREGULAR TRICHOME BRANCH1 in arabidopsis encodes a plant homolog of the Actin-Related Protein2/3 Complex Activator Scar/WAVE that regulates actin and microtubule organization. *Plant Cell Online* 17, 2314–2326. doi: 10.1105/tpc.104.028670

Conflict of Interest Statement: The authors declare that the research was conducted in the absence of any commercial or financial relationships that could be construed as a potential conflict of interest.

Received: 02 September 2013; accepted: 14 October 2013; published online: 19 November 2013.

*Citation: Ivakov A and Persson S (2013) Plant cell shape: modulators and measurements. Front. Plant Sci. **4**:439. doi: 10.3389/fpls.2013.00439*

This article was submitted to Plant Cell Biology, a section of the journal Frontiers in Plant Science.

Copyright © 2013 Ivakov and Persson. This is an open-access article distributed under the terms of the Creative Commons Attribution License (CC BY). The use, distribution or reproduction in other forums is permitted, provided the original author(s) or licensor are credited and that the original publication in this journal is cited, in accordance with accepted academic practice. No use, distribution or reproduction is permitted which does not comply with these terms.